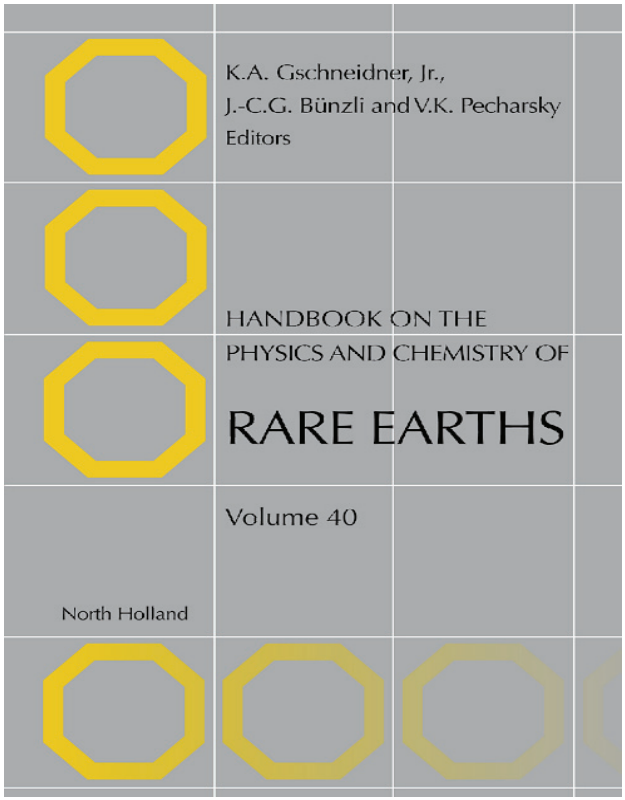

From: Claude Piguet* and Jean-Claude G. Bu¨nzli†,
Self-Assembled Lanthanide Helicates: From Basic Thermodynamics to Applications
In Karl Gschneidner Jr, Jean-Claude G. BU¨ NZLI, Vitalij K. PECHARSKY editor:
Handbook on the Physics and
Chemistry of Rare Earths, Vol. 40,
The Netherlands: 2010, pp.301-553.
ISBN: 978-0-444-53220-6,

CHAPTER **247**

Self-Assembled Lanthanide Helicates: From Basic Thermodynamics to Applications

Claude Piguet* and **Jean-Claude G. Bünzli†**

Contents

* Department of Inorganic, Analytical and Applied Chemistry, University of Geneva, 30 quai E. Ansermet, CH-1211 Geneva 4, Switzerland
† Laboratory of Lanthanide Supramolecular Chemistry, École Polytechnique Fédérale de Lausanne, BCH 1402, CH-1015 Lausanne, Switzerland and Department of Advanced Materials Sciences, Korea University, Sejong Campus, Jochiwon, Korea (WCU project R31-10035)

Handbook on the Physics and Chemistry of Rare Earths, Volume 40
ISSN 0168-1273, DOI: 10.1016/S0168-1273(10)40007-0

List of Symbols and Acronyms

1D	one-dimensional
2D	two-dimensional
3D	three-dimensional
5D10	mouse hybridoma cell line
χ	magnetic susceptibility tensor
χ_0	isotropic part of the magnetic susceptibility tensor
δ_i^{dia}	diamagnetic shift in ppm for a nucleus i
$\delta_{ij}^{\mathrm{exp}}$	hyperfine chemical shift for a nucleus i in a complex of a lanthanide j
$\delta_{ij}^{\mathrm{para}}$	paramagnetic hyperfine chemical shift in ppm for a nucleus i in a complex of a lanthanide j
ϕ_i	spherical coordinate of nucleus i
γ	gyromagnetic ratio
η_{et}	efficiency of the ligand-to-metal energy transfer
η_{ISC}	efficiency of intersystem crossing
η_{sens}	efficiency of the sensitization process
μ_{B}	Bohr magneton
μ_{eff}	effective electronic magnetic momentum in μ_{B}
θ_i	spherical coordinate of nucleus i
τ_{c}	characteristic correlation time
τ_{e}	electron spin relaxation characteristic time
τ_{m}	chemical exchange characteristic time
τ_{r}	rotational characteristic time
ω	Larmor precession frequency in Hz
A_i	Fermi hyperfine constant for a nucleus i
B_q^k	crystal-field parameters of rank k
bipy	bipyridine
bp	base pair
BSA	bovine serum albumin
C_j	Bleaney's factor of lanthanide j, scaled to -100 for Dy^{III}
CD	circular dichroism
cDNA	circular DNA
CN	coordination number
COSY	correlated spectroscopy
CPL	circularly polarized luminescence
CY	cyanine dye
Delfia©	dissociation-enhanced fluoroimmunoassay
Dlbt	double-lanthanide-binding tag
DMF	dimethylformamide

DNA	deoxyribonucleic acid
DO2A	1,4,7,10-tetraazacyclododecane-1,7-diacetate
DPA	dipicolinate
dpbt	2-(*N*,*N*-diethylamin-4-yl)-bis(3,5-dimethylpyrazol-1-yl)-1,3,5-triazine
$dppeO_2$	diphenylphosphineethane dioxide
dsDNA	double-stranded DNA
DTPA	diethylenetrinitrilopentaacetate
EB	ethidium bromide
EDC	1-ethyl-3-(3-dimethylaminopropyl) carbodiimide hydrochloride
EDTA	ethylenediaminetetraacetate
ER	endoplasmatic reticulum
ES-MS	electrospray (ion spray) mass spectrometry
eu	electrostatic unit ($1\ \text{eu} = 1.602 \times 10^{-19}\ \text{C}$)
F_i	contact term of the nucleus *i*
fac	facial
fod	6,6,7,7,8,8,8-heptafluoro-2,2-dimethyl-3,5-octanedionate
FRET	Förster resonance energy transfer
g_e	Landé factor
G_i	axial geometrical factor of the nucleus *i*
GM	Göppert-Mayer unit (two-photon absorption cross section)
H_0	applied magnetic field
HeLa	cervix cancer cell line
hfa	hexafluoroacetylacetonate
HHH	head-to-head-to-head
HHT	head-to-head-to-tail
HOPO	1-methyl-2,3-dihydroxypyridone
HS	high spin
HSQC	heteronuclear single quantum coherence
IC	internal conversion
IC_{50}	half-maximal inhibitory concentration
ILCT	intraligand charge-transfer state
Jurkat	human T leukemia cell line
k	Boltzmann's constant
LDH	lactase dehydrogenase
LMCT	ligand-to-metal charge-transfer state
LS	low spin
MCF-7	breast cancer cell line
mer	meridional
Mk	Mischler's ketone

MOF	metal-organic framework
MRI	magnetic resonance imaging
N_A	Avogadro's number
NHE	normal hydrogen electrode
NIR	near-infrared light
NLO	nonlinear optic
NMP	*N*-methyl-2-pyrrolidinone
NOEDIF	nuclear Overhauser effect difference spectroscopy
NOESY	nuclear Overhauser enhancement spectroscopy
OAc	acetate
PCR	polymerase chain reaction
PCS	pseudocontact shift
phen	phenanthroline
PLDS	polylysine dicarboxylate succinate polymer
Q_L^R	overall quantum yield obtained upon ligand excitation
Q_R^R	metal-centered (intrinsic) quantum yield.
r_i	*R*-nucleus *i* distance
rac	racemic
RDC	residual dipolar coupling
RPMI-1640	Rosswell Park Memorial Institute cell culture medium
S	spin quantum number
$\langle S_z \rangle$	expectation value of S_z
SA	streptavidin
SCE	saturated calomel electrode
SMM	single molecule magnet
ssDNA	single-stranded DNA
T_1	longitudinal nuclear relaxation time
T_2	transversal nuclear relaxation time
TAM	2,3-dihydroxyterephthalamide
TL	total luminescence
TPA	two-photon (or biphotonic) absorption
TRD	time-resolved detection
TRLM	time-resolved luminescence microscopy
Tr(χ)	trace of the magnetic susceptibility tensor
tta	thenoyltrifluoroacetylacetonate
UV	ultraviolet light
WST-1	cell proliferation and viability assay [4-(3-(4-iodophenyl)-2-(4-nitrophenyl)-2*H*-5-tetrazolio)-1,3-benzene disulfonate
YAG	yttrium aluminum garnet
ZINDO	Zeners's intermediate neglect of differential overlap

1. INTRODUCTION

1.1 The fascination for molecular helical edifices

The fascination for helical edifices is as old as the human civilization and the Tower of Babel, erected during the first dynasty of the Babylonian (− 1895 to − 1595 BC) represents an archetype of a single-stranded helical pattern (Figure 1A). Interestingly, the Bible (Genesis 11: 1–5) mentions the Tower of Babel for the particular combination of rotation and linear progressions, which is characteristic of a helical structure and which illustrates the creation of several different languages (i.e., the rotation) preventing the ascent (i.e., the linear progression) of the unified mankind toward heaven and God.

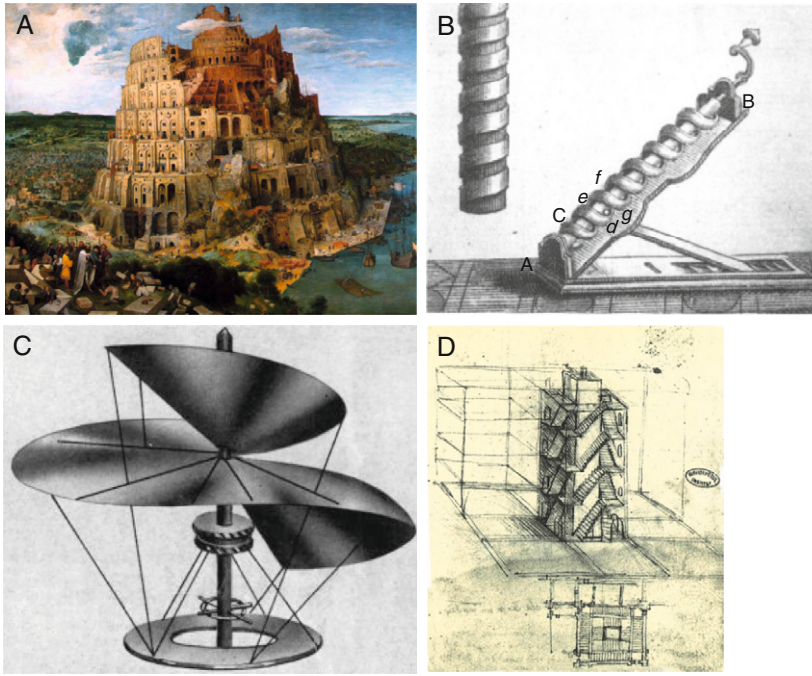

FIGURE 1 (A) Representation of the Tower of Babel by Pieter Bruegel the Elder (1525–1569), from http://artcess.files.wordpress.com. (B) A scheme of Archimedes' screw in *Leçons de Physique Expérimentale*, Jean-Antoine Nollet, Leçon IX, Fig. 12, 1743 (http://chem.ch.huji.ac.il./history/nollet.html). (C) The original scheme of a helicopter by Leonardo Da Vinci (1452–1519), from http://www.century-of-flight.net. (D) Da Vinci's sketch of a quadruple-stranded staircase, which inspired the double-stranded helical staircase built in the center of the castle of Chambord (France, sixteenth century); Léonard Da Vinci, Institut de France, Ms B, fol. 47v, http://www.maat-ingenierie.fr.

Mechanically speaking, these two characteristics were successfully exploited by the ancient Greeks and Egyptians for the pumping of fluids (Archimedes' screw, −287 to −212 BC, Figure 1B), then adapted to the first design of a helicopter by Leonardo Da Vinci (1490), when he realized that air can be considered as a fluid (Figure 1C). The obvious extension of the single-stranded helical pattern toward double-, triple-, and even quadruple-stranded helices made of interpenetrated helical strands rapidly followed (Figure 1D), eventually leading to the development of efficient propellers for boats and airplanes during the last century.

It is thus not surprising that a similar fascination and craze for microscopic helical patterns arose at the molecular level as soon as structural characterization techniques were at hand. The seven seminal contributions of Linus *Pauling* published back-to-back in the *Proceedings of the National Academy of Sciences of the United States of America* in 1951 (Pauling and Corey, 1951a,b,c,d,e,f,g), all dealing with the secondary structure of proteins produced by the three-dimensional helical pattern adopted by linked amino acids, would be the key for understanding biology at the molecular level. The helical structure in proteins is induced by noncovalent intramolecular hydrogen bonds connecting every main-chain carbonyl (C=O) and amino (N–H) groups separated by four amino acid residues (Figure 2A). This produces very regular single-stranded right-handed helices, the so-called α-helices, characterized by a pitch of 5.4 Å, that is, a linear progression of 5.4 Å for a complete turn of the molecular strand containing on average 3.6 amino acids. The subsequent recognition, 1 year later, that (i) the helical structure is also crucial for nucleic acids (Watson and Crick, 1953) and (ii) intermolecular hydrogen bonds are also responsible for the formation of deoxyribonucleic acids (DNAs), greatly contributed to make these helical edifices familiar among molecular scientists (Sayre, 1975; Watson, 1968; Wilkins, 2003).

1.2 Nanoscopic metal-containing helices: The helicates

The chemists involved during the last two decades in the manipulation of weak noncovalent interactions as a new tool for the rational building of nanoscopic supramolecular architectures, logically considered the formation of (supra)molecular helical structures as an undeniable demonstration of the validity of their approach for the synthetic preparation of novel micro- and nanoscopic objects (Lehn, 1995). Inspired by previous investigations on the electrochemical behavior of intertwinned dimeric Cu(I) complexes (Lehn et al., 1983), *Lehn* and coworkers selected the noncovalent Cu(I)–N bonds for the programmed connection of two covalent helical strands around a central axis defined by a line of regularly spaced metal ions in the complex $[Cu_3(\mathbf{L1})_2]^{3+}$ (Figure 3; Lehn et al., 1987). This double-stranded helix was the first recognized member of what has

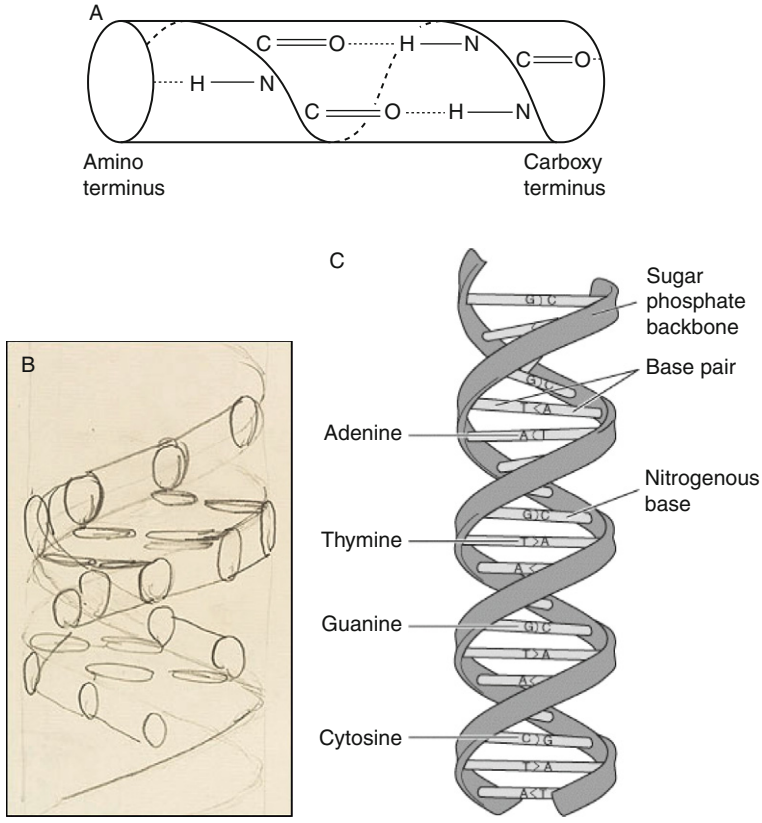

FIGURE 2 (A) Toilet roll representation of the main-chain intramolecular hydrogen bonding in a protein α-helix, from http://cryst.bbk.ac.uk/PPS2/course/section3. (B) An early sketch (1952) representing the double-stranded helical structure of DNA, from http://genome.wellcome.ac.uk. (C) Modern representation of the double-stranded helix in DNA, from http://www.ocean.udel.edu.

become later a novel and large family of polynuclear coordination complexes, termed *helicates*, a contraction of the word helix (Greek: $\varepsilon\lambda\iota\xi$ = winding, convolution, spiral) with the suffix *-ate*, characterizing host–guest complexes between (pre)organized receptors and metal ions (compare for instance coronate, cryptate, etc.; Lehn, 1995; Lehn et al., 1987; Vögtle, 1991). A helicate is thus defined as a discrete helical supramolecular complex constituted by one or more covalent organic strands wrapped about and coordinated to a series of at least two ions defining the helical axis (Lehn et al., 1987; Piguet et al., 1997a).

Though the complexes $[Fe_2(\mathbf{L2}\text{-}2H)_3]$, an analogue of rhodotorulic acid (Figure 4A; Carrano and Raymond, 1978; Carrano et al., 1979; Scarrow

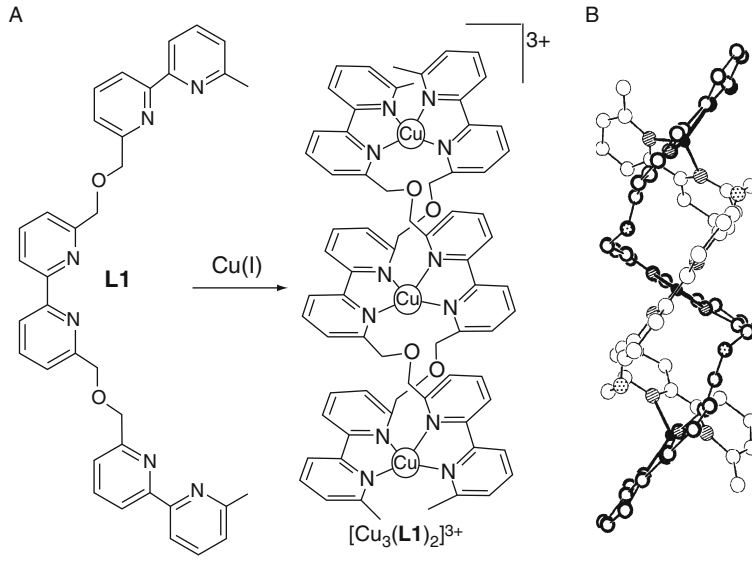

FIGURE 3 (A) Self-assembly and (B) X-ray crystal structure of the trinuclear saturated homotopic double-stranded helicate $[Cu_3(\mathbf{L1})_2]^{3+}$ (reproduced by permission from Hamacek et al., 2006, © 2006 Royal Society of Chemistry; Lehn et al., 1987, © 1987 The National Academy of Sciences USA).

et al., 1985), and $[Cu_2(\mathbf{L3})_3]^{4+}$ (Figure 4B; Harris and McKenzie, 1969) clearly correspond to triple-stranded helicates according to the above definition, they were considered as standard binuclear coordination complexes at the time of their publication. Therefore, the justification for a novel terminology for these complexes entirely relies on some additional rational programming of the final complexes thanks to a judicious match between the stereoelectronic properties of the metal ions and the ligand-binding possibilities (Piguet et al., 1997a,b). In this context, the planned preparation of the complete family of bi- ($[Cu_2(\mathbf{L4})_2]^{2+}$), tri- ($[Cu_3(\mathbf{L1})_2]^{3+}$), tetra- ($[Cu_4(\mathbf{L5})_2]^{4+}$), and pentanuclear ($[Cu_5(\mathbf{L6})_2]^{2+}$) helicates unambiguously confirmed the great potential of the supramolecular approach in coordination chemistry (Figure 5; Lehn and Rigault, 1988). In these complexes, the match between ligand and metal stereochemical requirements is based on the oxopropylene spacers separating the bidentate 2,2′-bipyridine segments, which are short enough to prevent the connection of two bipyridines to the same metal ion, but long enough to allow the wrapping of the organic ligand strands about the helical axis defined by the aligned metals. Moreover, the connection of both oxopropylene spacers and terminal methyl groups at the 6,6′-positions of the bipyridine units in **L1** and **L4–L6** strictly limits their coordination to tetrahedral metal ions.

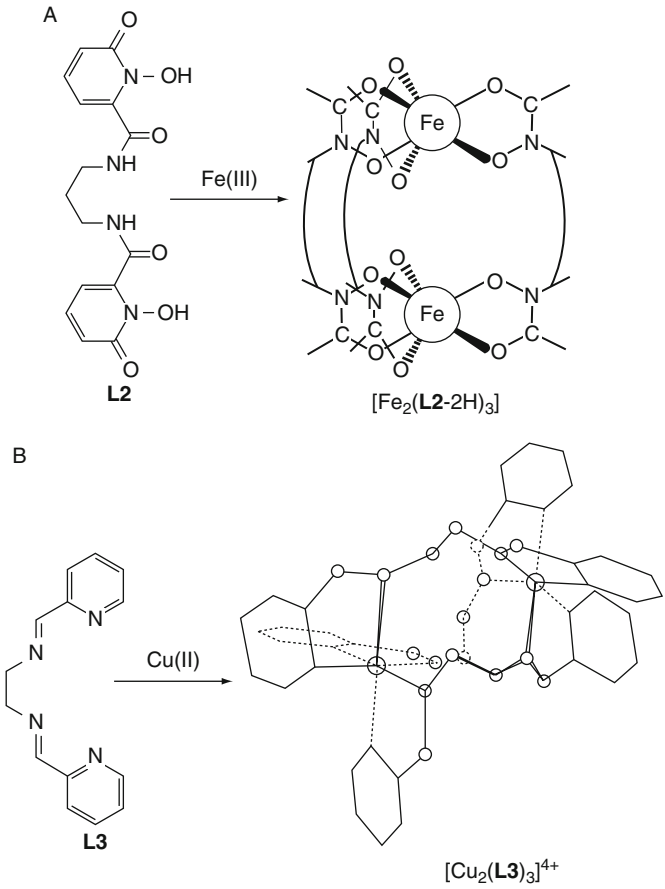

FIGURE 4 The formation of early binuclear triple-stranded helicates with (A) Fe(II) and (B) Cu(II) metal ions (redrawn after (A) Scarrow et al., 1985 and (B) Harris and McKenzie, 1969).

The spherical Cu(I) cation (d^{10} electronic configuration) is thus ideally suited for the formation of double-stranded helicates with **L1** and **L4–L6,** because of its lack of directional coordination bonds and its limited electrostatic factor $z^2/R = 1.30$ eu $Å^{-1}$ (z is the charge of the cation and R is its ionic radius; Shannon, 1976), which is compatible with $CN = 4$ (Figure 5). The demonstration of this novel concept in coordination chemistry, combined with the undeniable aesthetic appeal of helical structures, were at the origin of a considerable enthusiasm leading to the isolation and structural characterization of a plethora of binuclear double-, triple-, and quadruple-stranded helicates during the past two decades (for comprehensive reviews, see Albrecht, 2001; Constable, 1992, 1994, 1996;

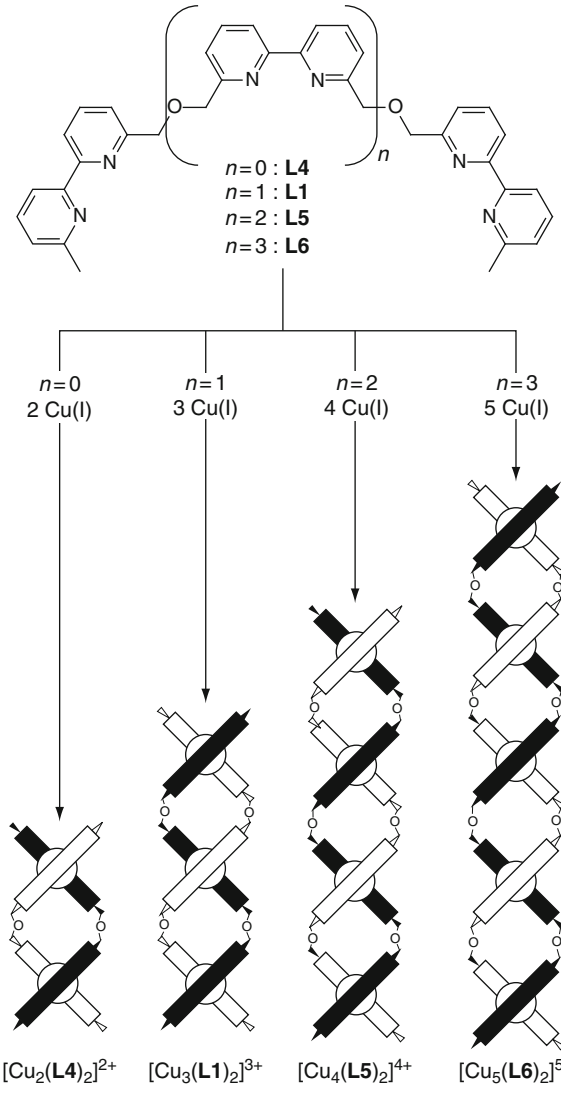

FIGURE 5 Programmed assemblies of bi- to pentanuclear double-stranded helicates (redrawn after Lehn and Rigault, 1988).

Piguet et al., 1997a). However, the preparation of helicates containing three metal ions such as $[Cu_3(\mathbf{L1})_2]^{3+}$ (Lehn et al., 1987) is less common (for selected examples, see Capo et al., 2002; Constable et al., 1991; Garrett et al., 1992; Greenwald et al., 1999; Hutin et al., 2006; Koert et al., 1990; Pfeil and Lehn, 1992; Smith and Lehn, 1996; Zong and Thummel, 2005),

while those with four or more metals are rare (Krämer et al., 2002; Lehn and Rigault, 1988; Marquis-Rigault et al., 1996; Matthews et al., 2003; Maurizot et al., 2004; Potts et al., 1993; Wang et al., 1998).

Probably because it was not clearly identified as standard thermodynamic complexation process for a long time, the formation of supramolecular helicates was accompanied by the emergence of a novel flourishing semantics, often borrowed from biology, whereby noncovalent interactions are crucial. The terms *self-assembly* and *self-organization*, first introduced in 1987 (Lehn et al., 1987), are now among the most used words in chemistry for describing the formation of sophisticated coordination or complexation processes. The competition between different thermodynamic equilibria, often leading to some selectivity depending on the choice of external conditions (stoichiometries, solvent, temperature; see Schneider and Yatsimirsky, 2008), was first termed *self-recognition* (Figure 6; Caulder and Raymond, 1997; Krämer et al., 1993; Lehn, 1995), and slowly evolves to more modern terminologies such as *combinatorial dynamic libraries*, *constitutional dynamic chemistry*, and *adaptative chemistry* (Lehn, 1999, 2007). The thermodynamic origins of these strange coordination behaviors were first tentatively addressed in 1992 with the claim that positive cooperativity drives the assembly processes of the target helicates to completion (Garrett et al., 1992; Pfeil and Lehn, 1992). Although the validity of this proposal was rapidly accepted by the community, the only support for this fundamental explanation relied on two Scatchard plots, which eventually appeared to be inadequate for testing cooperativity in assembly processes mixing intra- and intermolecular processes (Ercolani, 2003; Hamacek and Piguet, 2006; Hamacek et al., 2006; Piguet et al., 2005). The subsequent and remarkable kinetic studies establishing the intimate mechanisms of these assembly processes (Boukhalfa and Crumbliss, 2000; Charbonnière et al., 1997; Fatin-Rouge et al., 2000, 2001; Meyer et al., 1997) indeed remained very elusive on the operation of positive cooperativity, because of the lack, at that time, of clear definition of this concept for multicomponent processes involving intra- and intermolecular connections (Ercolani, 2003; Hamacek et al., 2006). Nevertheless, this belief in a strange and novel driving force favoring the target supramolecular architecture had a deep impact in the community and a large number of discrete 1D (racks, helicates), 2D (grids, circular helicates, metallacrown), and 3D complexes (clusters, boxes, polygons) were obtained thanks to a judicious match between the metal and ligand stereochemical properties (for comprehensive reviews, see Caulder and Raymond, 1999; Fujita et al., 2005; Lawrence et al., 1995; Leininger et al., 2000; Mulder et al., 2004; Piguet, 1999; Stoddart and Philp, 1996).

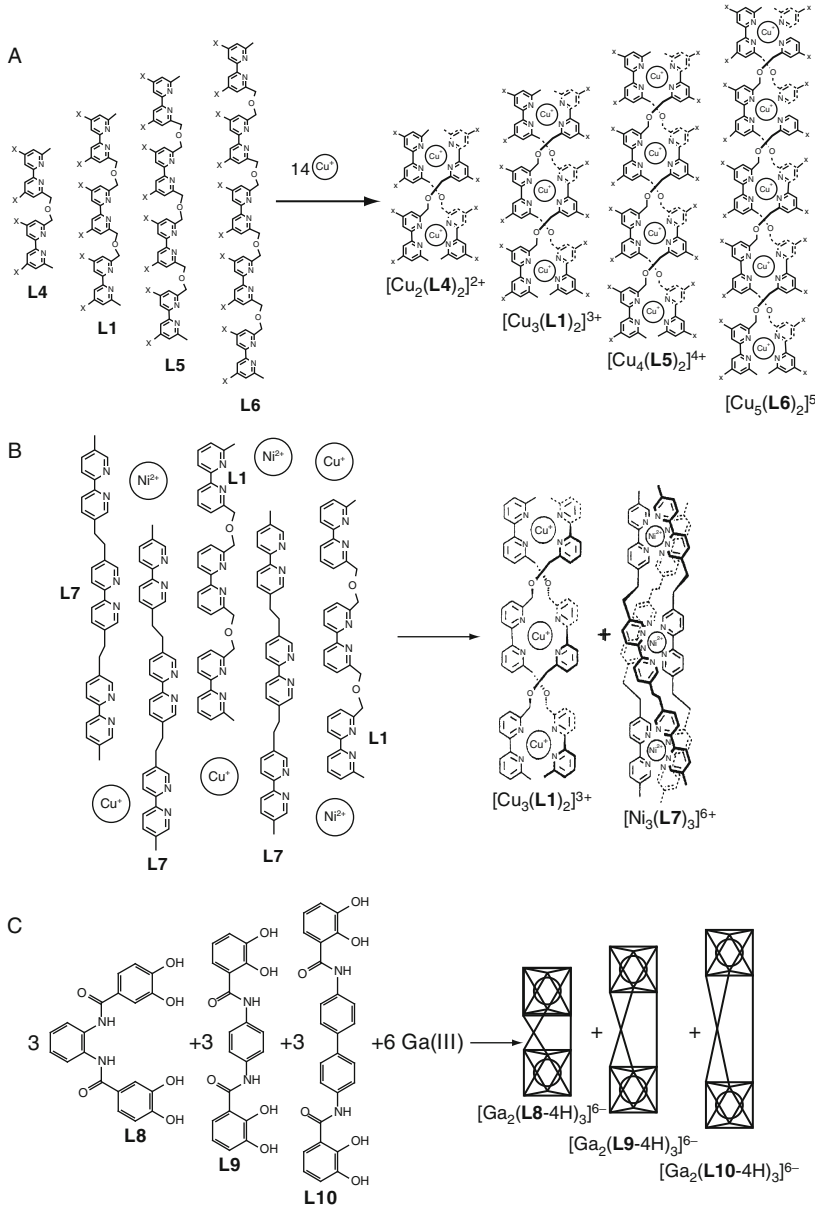

FIGURE 6 Self-recognition of (A) homopolymetallic double-stranded helicates $[Cu_m(\mathbf{L}k)_2]^{m+}$ ($k = 1$, 4–6; Krämer et al., 1993), (B) multiple-stranded helicates $[Cu_3(\mathbf{L1})_2]^{3+}$ and $[Ni_3(\mathbf{L7})_3]^{6+}$ (Krämer et al., 1993), and (C) homoleptic triple-stranded helicates $[Ga_2(\mathbf{L}k\text{-}4H)_3]^{6-}$ ($k = 8$–10; Caulder and Raymond, 1997) (reproduced by permission from Hamacek et al., 2006, © 2006 Royal Society of Chemistry).

1.3 Synthetic strategy, classification, and properties of self-assembled helicates

According to its definition, a helicate can be schematically represented as a series of helical mononuclear coordination complexes multiply linked by spacers and packed along a helical axis passing through the metal ions (Figure 7). Since the dative bonds connecting the peripheral ligand strands to the central metal ions are weak enough to allow reversibility at room temperature, the assembly process may explore the complete potential energy hypersurface, thus systematically providing the thermodynamically most stable complex (a process sometimes termed *self-healing*; Lehn, 1995).

The basic strategy for the generation of one particular helicate therefore relies on three crucial factors: (1) a judicious match between the intrinsic information borne by the metal (size, charge, polarizability, ligand-field stabilization) and the ligand strands (denticity of the binding units, steric constraints, type of donor atoms, nephelauxetic parameters); (2) a suitable set of external constraints, originally termed conditional information (Piguet, 1999), which affects the thermodynamic processes (solvent, stoichiometry, concentration, pressure, temperature); and (3) the free energy driving force brought by the principle of maximum site occupancy (Fyles and Tong, 2007; Hamacek et al., 2005a,b; Krämer et al., 1993; Lehn and Eliseev, 2001). Since 1987, the combinations of hundreds of sophisticated ligand strands with s-block, p-block, and d-block metal ions have been reported (Albrecht, 2001; Piguet et al., 1997a), which can be easily classified according to the simple method illustrated in Figure 8 for a binuclear double-stranded helicate.

Firstly, the total number of helical strands n wrapped about the helical axis defined by the metal ions corresponds to *single-* ($n = 1$), *double-* ($n = 2$), *triple-* ($n = 3$), and *quadruple*-stranded ($n = 4$) helicates. Secondly, ligand strands containing similar successive binding units are termed *homotopic*,

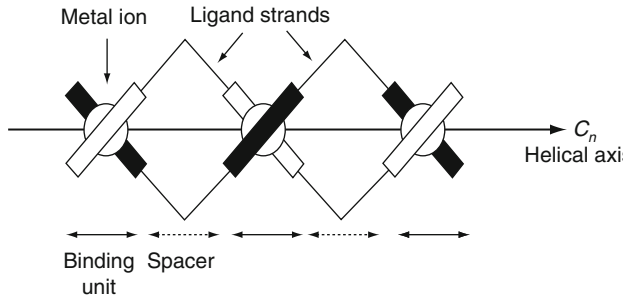

FIGURE 7 Schematic representation of a trinuclear double-stranded helicate.

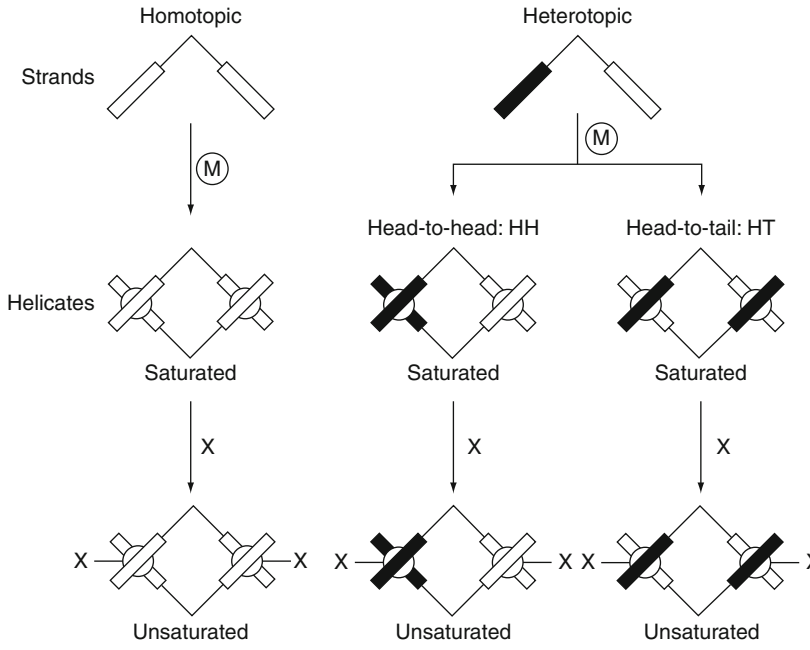

FIGURE 8 Classification of helicates according to their intrinsic information (reproduced by permission from Piguet et al., 1997a, © 1997 American Chemical Society).

while the consideration of different binding units refers to *heterotopic*. In the latter case, the relative orientation of the strands in the helicate is mentioned with the characters *H* (head) and *T* (tail) such as head-to-head and head-to-tail, corresponding to parallel, and, respectively, antiparallel arrangements. Thirdly, the coordination of ancillary ligands to the metal ion transforms a *saturated* helicate into its *unsaturated* counterpart (Figure 8). Finally, the total number of metal ions is indicated by the *multinuclearity* of the helicate, while the presence of different metals along the helical axis is defined by the *multimetallicity* of the helicate. It is, however, worth stressing here the relationship between the wrapping of the strand and the chirality of the final helicate (Cahn et al., 1966). Geometrically speaking, a helix is the figure generated by the motion of a point around and along a line, the helical axis. Ideally, the axis is a straight line and the two kinds of motions are circular at a constant distance *r* and linear, respectively, which eventually produces a cylindrical palindromic helix (i.e., a regular helix with a constant pitch = ratio of axially linear to angular properties; Figure 9; Brewster, 1974).

It may be right-handed (plus, *P*) or left-handed (minus, *M*) according to whether the rotation is clockwise, respectively anticlockwise, when the

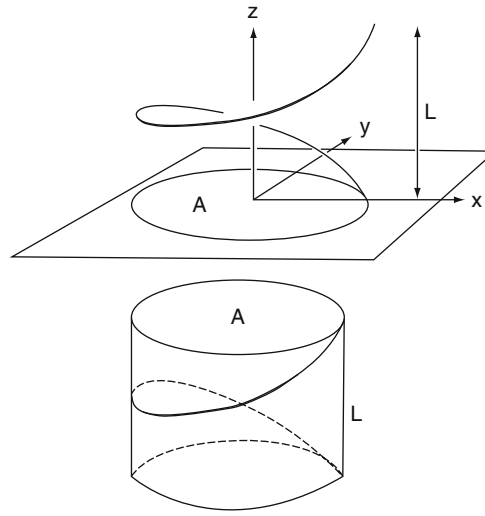

FIGURE 9 A single turn of a right-handed (*P*) circular palindromic single-stranded helix. *L* is the pitch, *z* is the helical axis, and *A* is the area of the subtended circle in the plane *xy* (reproduced by permission from Piguet et al., 1997a,b, © 1997 American Chemical Society).

helix is considered to wind from the viewers' eye toward a point distant from the viewer (Meurer and Vögtle, 1985). Obviously, the application of these theoretical geometrical concepts to a series of atoms connected by covalent bonds forming the strands of the helicate requires some minor adaptations (Piguet et al., 1997a), but the screw direction, measured by *P* or *M* helicities and induced by the wrapping of the strands, is crucial because it prevents the existence of symmetry operation of the second kind, and the helicates are thus potentially chiral objects (Cahn et al., 1966). If we ignore the helical portions produced by the spacers, that is, we neglect the contribution of the spacers to the total helical pitch (Figure 7), the helicity of the final helicate may be simply deduced from the absolute configurations Δ or *Λ* of the metal ions produced by the chelated strands (Figure 10).

For binuclear homotopic helicates with chelated strands, there are only two possibilities. Either the two metal ions possess the same absolute configurations and a pair of enantiomers is formed (*PP* or *MM*), or the metal ions display opposite absolute configurations, thus leading to an achiral side-by-side complex, sometimes called a mesocate (Albrecht, 2001). However, such unambiguous chiral characteristics are rarely met in practice because (i) the helical fractions defined by the spacers are rarely negligible; (ii) heterotopic strands produce helical portions of

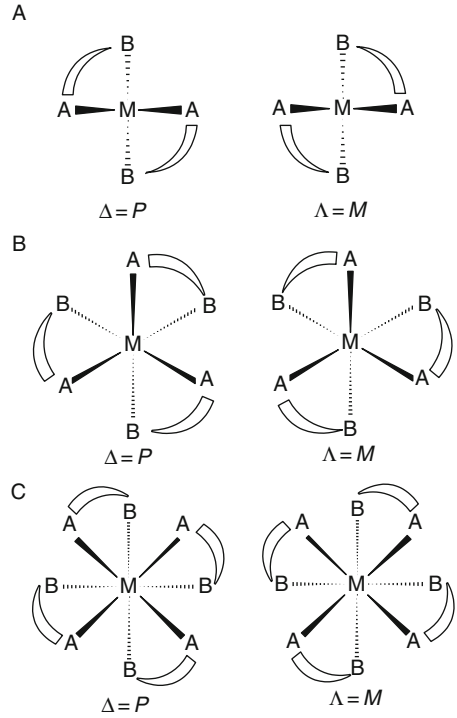

FIGURE 10 Absolute configurations and related helicities of (A) bis-chelate complexes viewed down the C_2-axis, (B) tris-chelate complexes viewed down the C_3-axis, and (C) tetrachelate complexes viewed down the C_4-axis. Bidentate binding units have been selected for the sake of clarity.

different nature, thus leading to chiral pairs of diastereomers for the side-by-side complexes; (iii) monodentate binding units do not induce chiral environments around metal ions; and (iv) for an odd number of metal ions, the side-by-side complexes correspond to amphiverse helices (i.e., helices containing only an excess of one type of helical portion; for a detailed discussion, see Piguet et al., 1997a). However, a more global chiral characteristic of the helices lies in the systematic existence of two opposite helical arrangements, depending on the symmetry axis considered for defining the helical wrapping (Figure 11). This property finds applications in a boat propeller, in which, for technical reasons, it is sometimes more relevant to rotate the helix by 90° while maintaining the same screw direction for the motor.

Please note that the quadruple-stranded helicate shown in Figure 11C is a typical example of a chiral helical object strictly produced by the wrapping of the spacers, while the square-planar Pd–N_4 units are achiral.

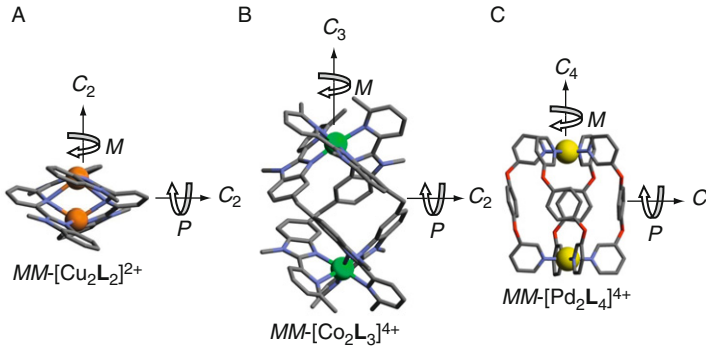

FIGURE 11 Crystal structures of (A) double-stranded (redrawn after Piguet et al., 1989a), (B) triple-stranded (redrawn after Williams et al., 1991), and (C) quadruple-stranded (redrawn after McMorran and Steel, 1998) helicates highlighting the relationship between the helicities about the main axis and the perpendicular twofold axes.

1.4 Introducing lanthanide ions into helicates

Despite their indubitable aesthetic appeal, the helicates severely suffer from the lack of significant applications, except for their confidential use as (i) precursors for topologically nontrivial entangled structures (for a review, see Lukin and Vögtle, 2005) and (ii) structural probes and cleaving agents for DNA (Hannon et al., 2001; Schoentjes and Lehn, 1995). Thanks to their rich metal-centered electronic, magnetic, and optical properties, the trivalent lanthanides, R^{III}, are obvious partners for pushing these supramolecular edifices into the field of nanoscopic functional devices (Bünzli and Piguet, 2002). However, the limited expansion of the valence 4f-orbitals, which are shielded from external perturbations by the filled $5s^2$- and $5p^6$-orbitals, produces R^{III}-ligand coordination bonds displaying faint covalency, and consequently no pronounced stereochemical preferences of electronic origin (Bünzli and Piguet, 2005). The coordination geometry around R^{III} thus results from their large electrostatic factors ($z^2/R = 8.72$–10.45 eu^2 Å^{-1} along the lanthanide series), combined with the minimization of steric interligand repulsions. Coordination numbers $CN = 8 - 10$ are common for complexes in solution (Cotton, 2006), among which $CN = 9$, associated with a D_{3h}-symmetrical tricapped-trigonal prismatic arrangement of the donors atoms, is standard. Consequently, the programming of lanthanide helicates relies almost exclusively on the judicious design of ligand strands possessing either tridentate chelating units to give saturated triple-stranded helicates ($CN = 9$; Figure 12A; Piguet et al., 1992a), or bidentate chelating units to give saturated quadruple-stranded helicates ($CN = 8$; Figure 12B; Basset et al., 2004; Dong et al., 2007; Xu and Raymond, 2006). Though the detailed understanding

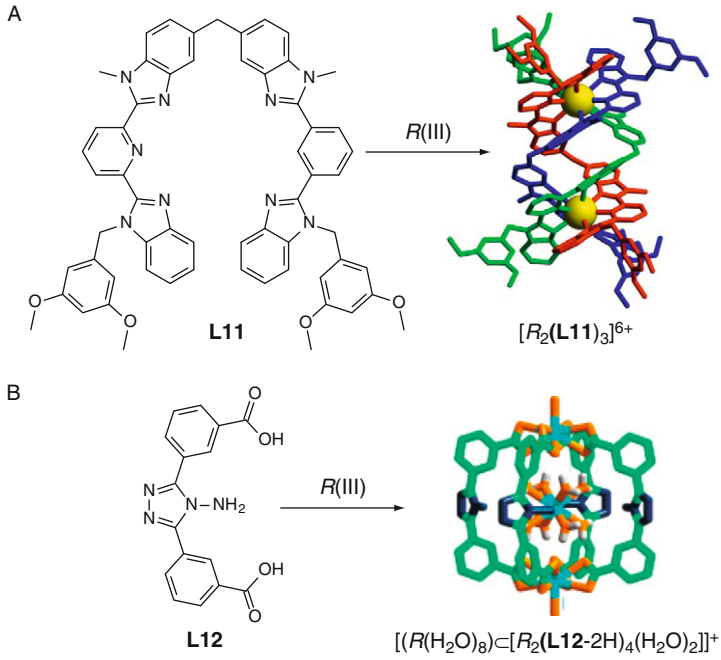

FIGURE 12 Stereochemical match between (A) bis-tridentate (redrawn after Piguet et al., 1992a) and (B) bis-bidentate segmental ligands with trivalent lanthanides to give triple-stranded, respectively, quadruple-stranded helicates (reproduced by permission from Dong et al., 2007, © American Chemical Society).

and control of the self-assembly of lanthanide triple-stranded helicates have been the subject of considerable efforts since their discovery in 1992 (Hamacek et al., 2005a,b), the variable coordination numbers and geometries adopted by R^{III} ions, combined with their entropic affinity for negatively charged oxygen donors, often perturb the assembly process due to the competitive formation of alternative unsaturated complexes. For instance, the bis-bidentate ligand **L13**^{b} reacts with $R(ClO_4)_3$ in acetonitrile to give the expected chiral triple-stranded helicate $[R_2(\mathbf{L13}^{b})_3]^{6+}$ (Figure 13; Martin et al., 1998). However, the use of the slightly more competing triflate anions in $R(CF_3SO_3)_3$ produces the centrosymmetric achiral unsaturated side-by-side complex $[R_2(\mathbf{L13}^{b})_2(H_2O)_4(CF_3SO_3)_4]^{2+}$ with zero net helicity (Figure 13; Martin et al., 1998).

Finally, the choice of the spacer is crucial because minor structural variations may dramatically affect the issue of the thermodynamic assembly process with lanthanides, a situation encountered when the potential free energy hypersurface is rather flat. The bis-tridentate ligand **L14**, which is designed to produce triple-stranded helicates, indeed gives the

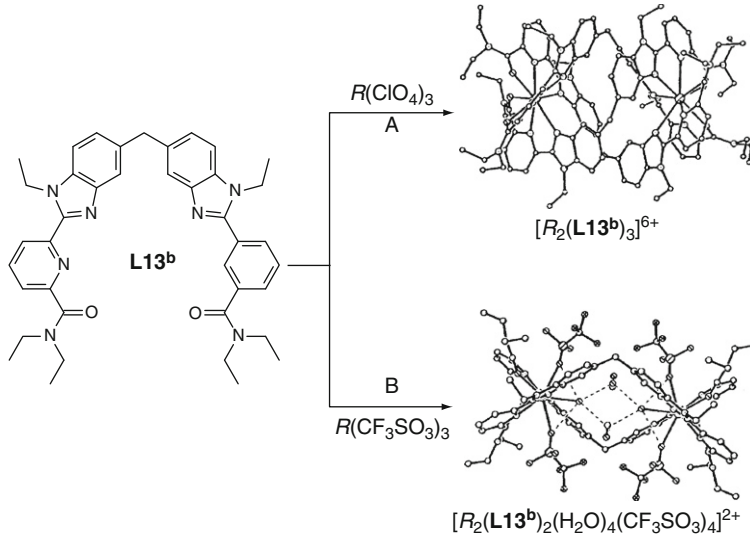

FIGURE 13 Formation of (A) a binuclear saturated triple-stranded lanthanide helicate and (B) a binuclear unsaturated double-stranded side-by-side lanthanide complex (redrawn after Martin et al., 1998).

expected assembly only with diphenylene spacers (Figure 14A), while the use of para-xylyl spacers provides an alternative unsaturated bidimensional circular helicate (Figure 14B; Senegas et al., 2005).

A similar limitation has been recently reported for the synthesis of unsaturated triple-stranded binuclear lanthanide helicates with bis-bidentate acylpyrazolone ligand strands and some analogues of bis-β-diketonate ligands, for which only the ethyl spacer was found to form the targeted helical complex (Semenov et al., 2008).

1.5 Scope of the review

The report on the first lanthanide-containing helicate in 1992 (Figure 12A; Piguet et al., 1992a) established, for more than a decade, the systematic use of 2,6-disubstituted pyridines (N_3, N_2O, and NO_2 donor sites) as the unique building block for the preparation of triple-stranded $[R_m\mathbf{L}_3]^{3m+}$ helicates (Figure 15; Bünzli and Piguet, 2002). The only exception has been the short report by Goodgame et al. (1993) on the triple-helical wrapping of a *p*-xylene-bridged bis(2-pyridone) ligand featuring two monodentate coordination units around two neodymium ions, the inner coordination sphere of the metal ions being completed by three bidentate nitrates. The second deliberate design of a noncontaining pyridine binding unit for the self-assembly of lanthanide helicate has been reported in 2004, whereby

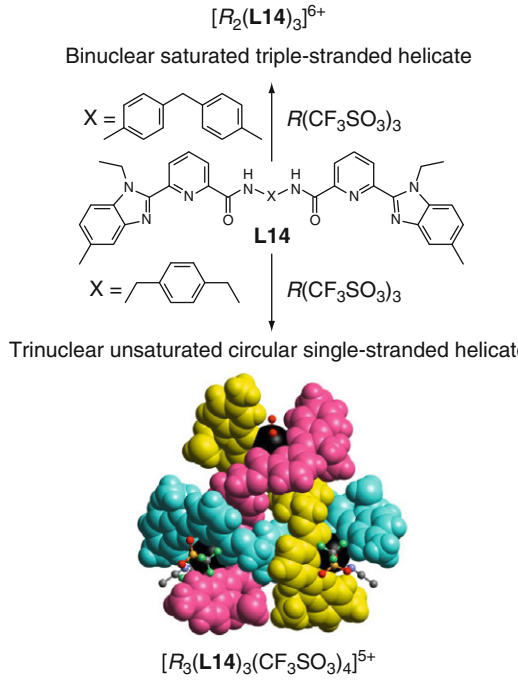

FIGURE 14 Influence of the spacer on the assembly process (bottom structure reproduced by permission from Senegas et al., 2005, © 2005 Royal Society of chemistry).

two bidentate β-diketonates (O_2 donor site) are connected by a spacer to give a bis-bidentate ligand strand, which is able to produce binuclear triple- and quadruple-stranded helicates when reacted with R^{III} (Basset et al., 2004). Later, analogous bidentate O_2 donor sites in bis-acylpyrazolone strands have been reacted with R^{III} to give unsaturated triple-stranded binuclear lanthanide helicates (Semenov et al., 2008), while related bidentate β-diketonates (Xu and Raymond, 2006) or carboxylates (Dong et al., 2007) binding units have been used for the isolation and structural characterization of related actinide and lanthanide quadruple-stranded helicates. More recently, alternative tridentate ligands based on 8-hydroxyquinoline (N_2O donor site) have been described for the design of standard triple-stranded lanthanide helicates (Albrecht et al., 2007a,b; Shavaleev et al., 2008).

After an introductory chapter on mononuclear precursors with benzimidazolepyridine or dipicolinic acid derivatives, this chapter mainly focuses on the rich chemical adventure provided by the systematic exploitation of the 2,6-disubstituted pyridine units for the self-assembly of lanthanide helicates (Sections 2–6). Section 7 aims at opening some

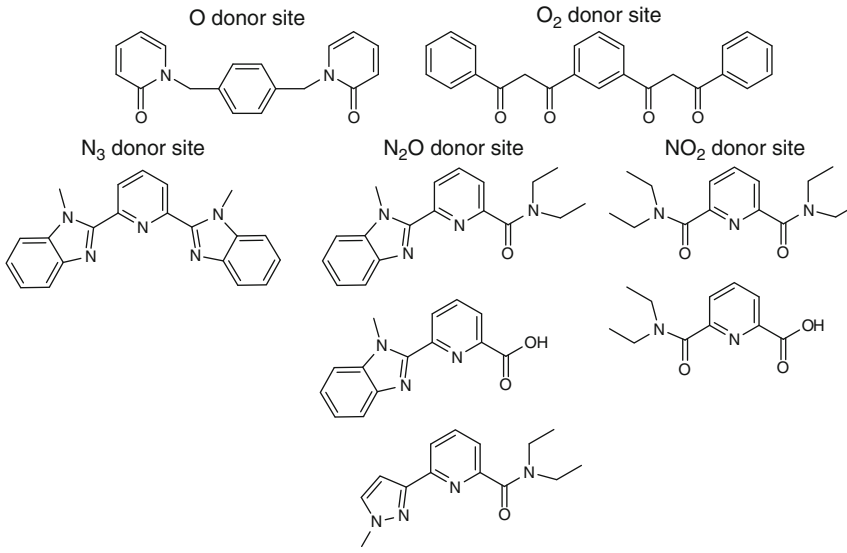

FIGURE 15 Top: oxygen-donor ligands used by Basset et al. (2004) and Goodgame et al. (1993). Bottom: tridentate 2,6-disubstituted pyridines used as binding units for the design of lanthanide helicate since 1992.

perspectives for the design of polymetallic helicates containing at least one trivalent lanthanide, but combined with s-, p-, or d-block metal ions. Finally, Section 8 reports on the few examples of lanthanide or actinide helicates which are built from noncontaining pyridine binding units. In addition to ligand design and structural information, detailed thermodynamic aspects of the self-assembly processes are reviewed, as well as the relationship between the helicate structure and their photophysical properties. Moreover, Section 6 describes practical applications of luminescent binuclear helicates in bioanalyses with emphasis on live cell staining and DNA analysis. Literature is fully covered until the end of October 2008.

Note regarding nomenclature. The term ''nuclear'' (e.g., polynuclear) is used to characterize assemblies into which several metal ions are imbedded while ''metallic'' (e.g., bimetallic, trimetallic) indicates that the molecule contains different metal ions.

2. MONONUCLEAR 4f TRIPLE-HELICAL PRECURSORS

During the last two decades, the supramolecular approach greatly contributed to the rapid evolution of standard coordination chemistry, usually limited to mono- and binuclear complexes, toward more complicated and sophisticated nanometric edifices bearing novel functionalities.

The associated bottom-up process thus relies on the identification of building blocks connected by weak (i.e., noncovalent) interactions and possessing specific physicochemical properties, which can be further tuned by intercomponent communications operating at the (supra)molecular level (Lehn, 1995).

2.1 Choice and synthesis of mononuclear building blocks

Among the different factors controlling the thermodynamic stability of a coordination complex, the free energy change related to the formation of intermolecular metal–ligand bonds, modulated by desolvation, plays a crucial role (see Section 1.3). In view of the apparent preference for nine-coordination in complexes with small unidentate ligands (e.g., water or acetonitrile; see Figure 16, bottom) and given that the resulting tricapped-trigonal prismatic coordination environment both possesses an interesting symmetry (D_{3h}) and usually prevents interaction with additional donor molecules, targeting such a coordinative environment for lanthanide ions results in compounds with intense emissive properties. Because trivalent lanthanides, R^{III}, display no pronounced stereochemical preferences (see Section 1.4), the intrinsic information borne by the ligand entirely controls the structural output of the target mononuclear building blocks. To limit the geometrical and thermodynamic possibilities offered

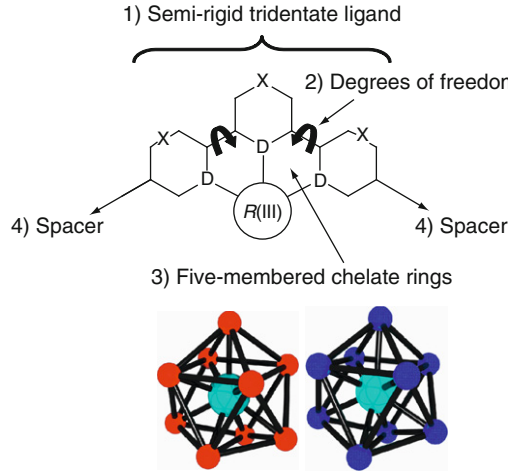

FIGURE 16 Top: stereochemical criteria to be met by a terpyridine-like ligand for the design of regular C_3-symmetrical mononuclear triple-helical building blocks. Bottom: tricapped-trigonal prismatic coordination geometry encountered in (left) R^{III} aquo ions $[Eu(H_2O)_9]^{3+}$ (redrawn after Moret et al., 1991) and (right) $[Eu(MeCN)_9]^{3+}$ (redrawn after Shen et al., 1990).

by the complete exploration of the energy hypersurface, the ligand-binding properties must obey four strict stereochemical requirements (Figure 16):

(1) The use of semirigid tridentate binding units restricts the structural issues to $[R(\mathbf{L}^k)_n]^{3+}$, whereby $n = 1$–3 characterizes the number of strands wrapped about the central metal. The target C_3-symmetrical triple-helical complex $[R(\mathbf{L}^k)_3]^{3+}$ can be further produced as the major species thanks to a strict control of the conditional information expressed in the stoichiometric ratio $R{:}\mathbf{L}^k = 1{:}3$ (i.e., entropic selection).
(2) An optimum set of degrees of freedom must be implemented in the tridentate binding unit in order to allow helical wrapping while forcing meridional tricoordination leading to the exclusive formation of a tricapped-trigonal prismatic arrangement of the nine donor atoms around the central lanthanide in $[R(\mathbf{L}^k)_3]^{3+}$ (Ruiz-Martinez et al., 2008), much as is found in the aquo ions (Bünzli, 1998) or in the acetonitrile solvates (Shen et al., 1990).
(3) For large cations such as R^{III}, the chelate effect is enthalpically optimized for five-membered chelate rings (Motekaitis et al., 1994).
(4) Since each mononuclear building block has to be connected to its neighbors in the final helicate, spacers must be grafted at the end of tridentate binding units, which are able to transmit the helical twist along the complete strand.

Pyridine rings substituted at the 2- and 6-positions by semirigid coordinating side arms, which are further connected to spacers, indeed fit these criteria (Figure 15). Moreover, the low-energy $\pi \rightarrow \pi^*$ electronic transition centered onto the pyridine ring may be exploited for light-harvesting and indirect sensitization of the central lanthanide cation (Sabbatini et al., 1996). Some aspects of this structural pattern can be found in the commercially available tridentate ligand 2,6-dipicolinic acid (Figure 17A; Grenthe, 1961; Harrowfield et al., 1995) and 2,2′:6′,2″-terpyridine (Figure 17B; Durham et al., 1969; Frost et al., 1969; Semenova et al., 1999).

Both types of triple-helical complexes $[R(\mathbf{L15})_3]^{3-}$ and $[R(\mathbf{L16})_3]^{3+}$ display pseudotricapped-trigonal prismatic arrangements of the nine donor atoms in the solid state (N_3O_6 for $[R(\mathbf{L15})_3]^{3-}$ and N_9 for $[R(\mathbf{L16})_3]^{3+}$). Detailed solution studies of $[R(\mathbf{L15})_3]^{3-}$ in water demonstrate that the dynamically average D_3-symmetrical triple-helical structure is maintained at millimolar concentration, but with a significant increase of the amplitude of the fast flip–flop oscillation of the central pyridine rings with the larger lanthanides (Ouali et al., 2002; Piguet and Geraldes, 2003). The tris-chelates $[R(\mathbf{L15^a})_3]^{3-}$ with $R =$ Eu, Tb display intense luminescence thanks to sensitization through the $(\mathbf{L^{15a}})^{2-}$ triplet

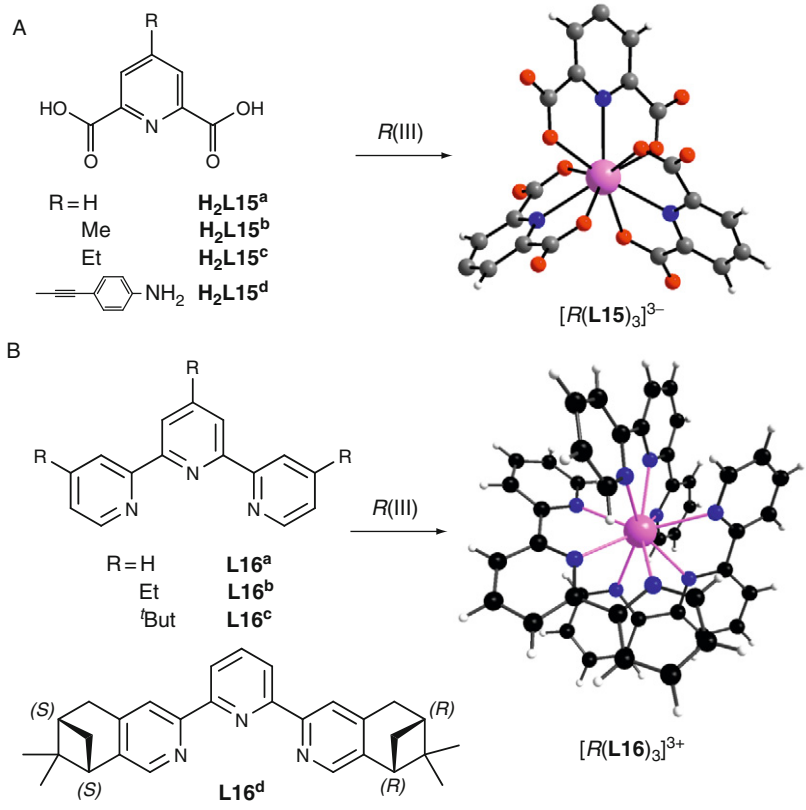

FIGURE 17 Schematic formation of D_3-symmetrical lanthanide triple-helical building blocks with (A) 2,6-dipicolinic acid and (B) 2,2′:6′,2″ terpyridine. Structures of the complexes $[Eu(\mathbf{L15^a})_3]^{3-}$ and $[Eu(\mathbf{L16^a})_3]^{3+}$ are redrawn from Harrowfield et al. (1995) and Semenova et al. (1999), respectively.

state (Aspinall, 2002) or, possibly, as has been suggested for Tb, through the singlet state (Kleinerman, 1969). Because of their strong visible luminescence, the $[R(\mathbf{L15^a})_3]^{3-}$ chelates were thoroughly investigated both in the solid state (Hopkins et al., 1996) and in aqueous solution (An et al., 2000; Chauvin et al., 2004; Huskowska and Riehl, 1995; Meskers and Dekkers, 2001; Werts et al., 2002). Introduction at the 4-position of the pyridine ring of small substituents (e.g., OH, Cl, Br, NH_2, or $NHCOCH_3$) modulates the photophysical properties of Tb complexes (Lamture et al., 1995), while grafting a substituted polyoxyethylene pendant on the same position additionally results in better water solubility and potentiality for conjugation of the helical complexes with biomolecules (see Section 2.5.3; Gassner et al., 2008).

A striking feature of the dipicolinate tris-complexes is the *P*-$[R(\mathbf{L15^a})_3]^{3-} \rightleftharpoons$ *M*-$[R(\mathbf{L15^a})_3]^{3-}$ helical interconversion occurring in the ground state ($k_{rac} = 50$–$200\ s^{-1}$ for $R =$ Eu–Yb; Ouali et al., 2002) and in the excited state ($k_{rac} = 10\ s^{-1}$ for Eu($^5D_0$); Huskowska and Riehl, 1995; Meskers and Dekkers, 2001), which is fast enough to prevent preparative helical separations, but slow enough to evidence Pfeiffer effects or chiral enrichments in the excited state when $[R(\mathbf{L15^a})_3]^{3-}$ interact with chiral substrates (Richardson et al., 1991), respectively, with polarized excitation light beams (Gawryszewska et al., 2006).

Compared with $[R(\mathbf{L15^a})_3]^{3-}$, the stability of the triple-helical cation $[R(\mathbf{L16^a})_3]^{3+}$ is much smaller because of the lack of charge neutralization accompanying the complexation process. Consequently, the triple-helical structure is only observed in the solid state (Semenova et al., 1999). In an aprotic polar solvent such as anhydrous acetonitrile, partial on–off equilibria of the distal pyridine rings gives predominantly eight-coordinated structures at millimolar concentrations (Chapman et al., 1984). Peripheral substitution at the 4-positions of the pyridine rings in $\mathbf{L16^b}$ and $\mathbf{L16^c}$ has only a minor effect on the stability and solution structures of the triple-helical complexes $[R(\mathbf{L16})_3]^{3+}$, but significantly increases metal-centered luminescence upon ligand irradiation (Mürner et al., 2000). Surprisingly, the connection of chiral alkyl six-membered rings at the 4- and 5-positions of the distal pyridine rings in $\mathbf{L16^d}$ improves the stability of the final lanthanide complex to such an extent that a single diastereomer, *P*-$[R(\mathbf{L16^d})_3]^{3+}$ or *M*-$[R(\mathbf{L16^d})_3]^{3+}$, can be detected in 5 mM acetonitrile solution (Muller et al., 2002a). Considering the behavior of the triple-helical lanthanide building blocks with the series of ligands **L15** and **L16**, it is clear that the first series provides final $[R(\mathbf{L15})_3]^{3-}$complexes which are stable enough for the self-assembly process being effective in solution, but which cannot be connected to spacers compatible with the transmission of helical twist in polynuclear helicates. On the other hand, the terpyridine backbone, although more difficult to modify (Cargill Thompson, 1997; Piguet et al., 1993a), is better suited for being incorporated within a segmental helical strand (Hasenknopf et al., 1996; Rapenne et al., 1999). However, the limited thermodynamic stability and the poor kinetic inertness of the triple-helical building blocks $[R(\mathbf{L16})_3]^{3+}$ are severe handicaps for their consideration for the self-assembly of polynuclear helicates. On the other hand, the replacement of the distal pyridine ring in **L16** (Figure 17) with *N*-alkylated benzimidazole rings in **L17** (Figures 18 and 19) leads to semirigid extended aromatic tridentate NNN heterocyclic binding units, which are easy to modify, and well suited for their inclusion into segmental helical ligands (Piguet et al., 1994). Moreover, the basicity of these ligands is comparable to that of terpyridine and the grafting of two five-membered rings at the 2- and 6-positions of the central pyridine ring in **L17** reduces steric crowding

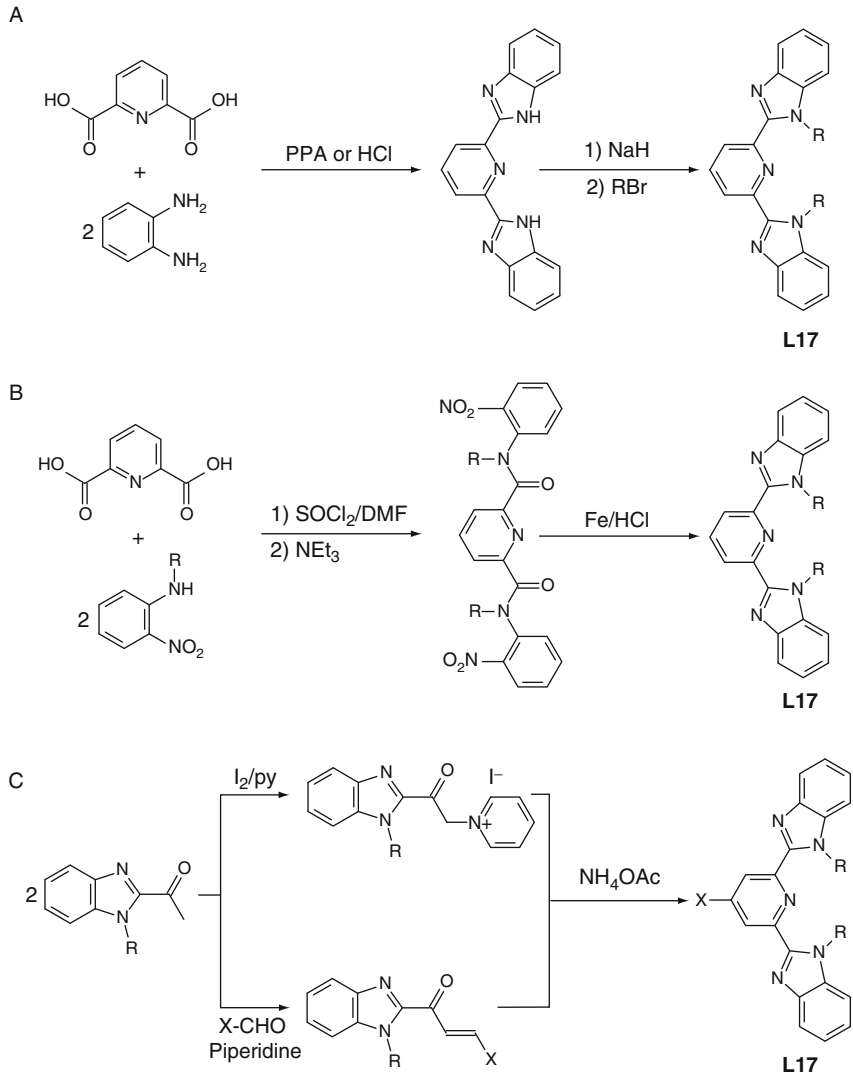

FIGURE 18 Preparation of substituted 2,6-bis(benzimidazol-2-yl)pyridine ligands **L17** following (A) original intermolecular *Phillips* reaction, (B) intramolecular *Piguet* cyclization, and (C) *Kröhnke* methodology.

upon complexation to R^{III} (Piguet et al., 1992b); this eventually produces robust triple-helical building blocks $[R(\mathbf{L17})_3]^{3+}$ for helicate self-assembly in aprotic solvents (Piguet et al., 1993c).

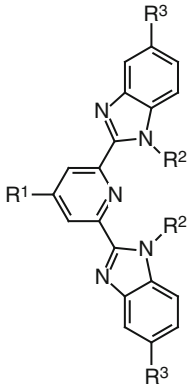

Ligand	R^1	R^2	R^3	References
L17[a]	H	CH_3	H	Piguet et al., 1989b
L17[b]	H	C_2H_5	H	Piguet et al., 1993b
L17[c]	H	C_3H_7	H	Piguet et al., 1993b
L17[d]	H	$(CH_2)_7CH_3$	H	Piguet et al., 1989b
L17[e]	H	$(CH_3O)_2C_6H_3$	H	Piguet et al., 1993b
L17[f]	H	C_2H_5	CH_3	Piguet et al., 1995a
L17[g]	Ph	$(CH_3O)_2C_6H_3$	H	Piguet et al., 1993a
L17[h]	$PhNO_2$	$(CH_3O)_2C_6H_3$	H	Piguet et al., 1993a
L17[i]	$PhNEt_2$	$(CH_3O)_2C_6H_3$	H	Piguet et al., 1993a
L17[j]	$PhNEt_2$	CH_3	H	Petoud et al., 1997a
L17[k]	H		H	Muller et al., 2001a
L17[l]		CH_3	H	Muller et al., 2002b

FIGURE 19 C_2-symmetrical tridentate 2,6-bis(benzimidazol-2-yl)pyridine ligands prepared for the design of lanthanide triple-helical building blocks $[R(\mathbf{L17})_3]^{3+}$.

2.1.1 Synthetic strategy: Benzimidazolepyridine derivatives

A classical intermolecular strategy (Phillips, 1928; Wright, 1951) was first used for preparing 2,6-bis(benzimidazol-2-yl)pyridine (Addison and Burke, 1981; Addison et al., 1983) followed by double *N*-alkylation (Figure 18A; Piguet et al., 1989b). The subsequent development of an intramolecular version of this reaction by Piguet et al. (1994) offers unique perspectives in terms of selectivity and stereochemical control, a crucial point for the preparation of nonsymmetrical tridentate binding units and for the connection of spacers to the terminal benzimidazole rings (Figure 18B). Finally, the central pyridine ring can be modified using either a *Kröhnke* methodology (Kröhnke, 1963) for grafting substituents at the 4-position (Figure 18C; Muller et al., 2002b; Piguet et al., 1993a), or the direct use of adequately 4-substituted dipicolinic acid derivatives **L15** (Chauvin et al., 2001).

Recently, a slightly modified one-pot synthetic approach to 2,6-bis (benzimidazole)pyridine was proposed by reacting aromatic ditopic *o*-nitroamines with aryl diacid chlorides (Figure 20). The noticeable modification from the method proposed by Piguet et al. (Figure 18B) is to run the reaction in *N*-metyl-2-pyrrolidinone (NMP) as solvent while keeping activated iron as the reducing agent in the last step; in this way, a yield of 90% is obtained for the reduction/ring closing reaction. Alternatively, to avoid the disadvantages of activated iron, namely the strong binding of Fe^{II} to the final product, necessitating EDTA treatment to remove it, and its high cost, cheaper sodium dithionite ($Na_2S_2O_4$) can be used as mild

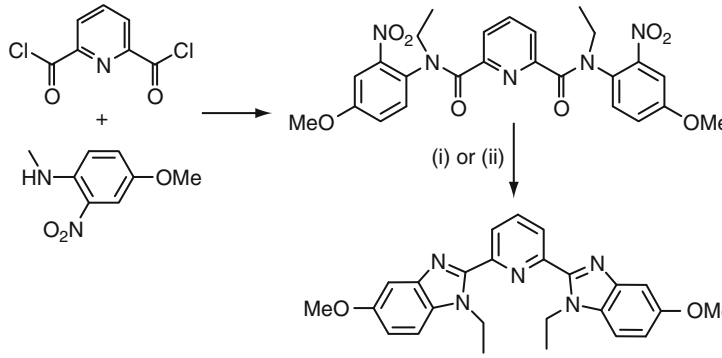

FIGURE 20 One-pot synthetic pathways to 2,6-bis(benzimidazole)pyridines proposed by McKenzie et al. (2008): (i) NMP, 50 °C, 8 h; activated Fe, NMP, HCl, 90 °C; EDTA(aq) and (ii) $Na_2S_2O_4$, DMF, EtOH, H_2O, 85 °C, 18 h.

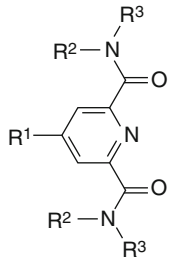

Ligand	R^1	R^2	R^3	References
L18[a]	H	C_2H_5	C_2H_5	Renaud et al., 1997a
L18[b]	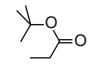	C_2H_5	C_2H_5	Muller et al., 2001b
L18[c]	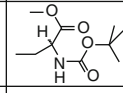	C_2H_5	C_2H_5	Muller et al., 2001b
L18[d]	H	$(CH_3)_2CH$	$(CH_3)_2CH$	LeBorgne et al., 2003
L18[e]	H	C_6H_5-CH_2	C_6H_5-CH_2	LeBorgne et al., 2003
L18[f]	H	C_6H_5-CH_2	H	LeBorgne et al., 2003
L18[g]	H	$C_{10}H_6$-$CH(CH_3)$	H	Leonard et al., 2007

FIGURE 21 C_2-symmetrical tridentate 2,6-bis(carboxamido)pyridine ligands prepared for the design of lanthanide triple-helical building blocks $[R(\mathbf{L18})_3]^{3+}$.

reducing reagent, although to the expense of a reduced yield of about 70% (McKenzie et al., 2008).

Following the endlessly repeated, but questionable assertion that trivalent lanthanide are mainly oxophilic (Jocher et al., 2007; Senegas et al., 2003), the distal benzimidazole groups of **L17** have been replaced with amide groups in **L18** (tridentate ONO donor) to give triple-helical building blocks $[R(\mathbf{L18})_3]^{3+}$ (Figure 21). Whereas the syntheses from dipicolinic acids **L15** are straightforward, the preparation of secondary and tertiary amides ensures the possible connection to spacers and the inclusion of the ONO tridentate binding unit **L18** within helical segmental ligands.

The unsymmetrical tridentate NNO ligands **L19**, in which the central pyridine ring is decorated with one benzimidazole unit and one carboxamide group, have been synthesized by using either 2-carboxamido-6-carboxylatopyridine (Chauvin et al., 2001) or 2-benzimidazole-6-carboxylatopyridine (Le Borgne et al., 2004; Piguet et al., 1994) synthons (Figure 22). Upon reaction with R^{III}, the triple-helical precursors $[R(\mathbf{L19})_3]^{3+}$ exist as mixtures of meridional and facial conformers (see Figure 28 in Section 2.2). Finally, the hydrolysis of the amide group of **L19** produces unsymmetrical 2-benzimidazole-6-carboxylatopyridine ligands, which have been introduced into segmental helical ligands (Chauvin et al., 2007, 2008; Deiters et al., 2008; Edder et al., 1997; Elhabiri et al., 1999, 2004a; Vandevyver et al., 2007) or connected to covalent tripods in order to avoid meridional/facial isomerization (Senegas et al., 2003). It is worth noting that the alternative connection of ester groups at the 2- and 6-position of the pyridine ring gives tridentate ONO ligand whose weak affinity for R^{III} is not compatible with their use in triple-helical complexes (Renaud et al., 1997b).

2.1.2 Synthetic strategy: Dipicolinic acid derivatives

The dipicolinic acid platform has proven to be extremely versatile, leading to numerous applications of its tris-complexes with Eu and Tb, in particular in analytical and bioanalytical chemistry (see Section 2.5 for photophysical properties and Section 6.2 for bioanalytical applications). As a consequence, researchers have invented ways of modulating the photophysical properties, principally by introducing substituents on the para position of the pyridine ring, a relatively easy synthetic procedure. Simple substituents (e.g., Cl, Br, NH_2, $NHCOCH_3$) are introduced by substitution of the hydroxyl function of chelidamic acid under

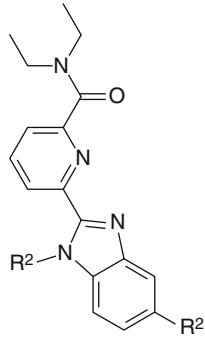

Ligand	R^1	R^2
L19[a]	CH_3	H
L19[b]	C_2H_5	H
L19[c]	$(CH_3O)_2C_6H_3$	H
L19[d]	C_2H_5	CH_3OCH_2

FIGURE 22 C_s-symmetrical tridentate 2-benzimidazole-6-carboxamidopyridine ligands prepared for the design of lanthanide triple-helical building blocks $[R(\mathbf{L19})_3]^{3+}$ (Le Borgne et al., 2004).

appropriate, although harsh, conditions (Figure 23). This substitution is easy in view of the presence of the pyridine electron-withdrawing group in para position with respect to the hydroxyl function. Milder conditions for the synthesis of the 4-bromo derivative **L15^{f}** have been recently proposed which involve reacting chelidamic acid with tetrabutylbromide in toluene and in presence of phosphorus pentoxide (Picot et al., 2008b). One notes, however, that purification of the ligands under their acidic form, either by recrystallization or by ion-exchange chromatography gives poor results. Therefore, a customary procedure is to purify the corresponding ester by silica-gel chromatography and subsequent recrystallization, followed by quantitative hydrolysis under mild conditions (Lamture et al., 1995).

For more elaborate applications, such as bioprobes or nonlinear optical materials, the dipicolinate framework has been considerably expanded and decorated with π-conjugated and/or solubilizing groups (D'Aléo et al., 2008a,b). Introduction of a π-system in the 4-position is meant to induce charge transfer onto the pyridine moiety and is achieved through a

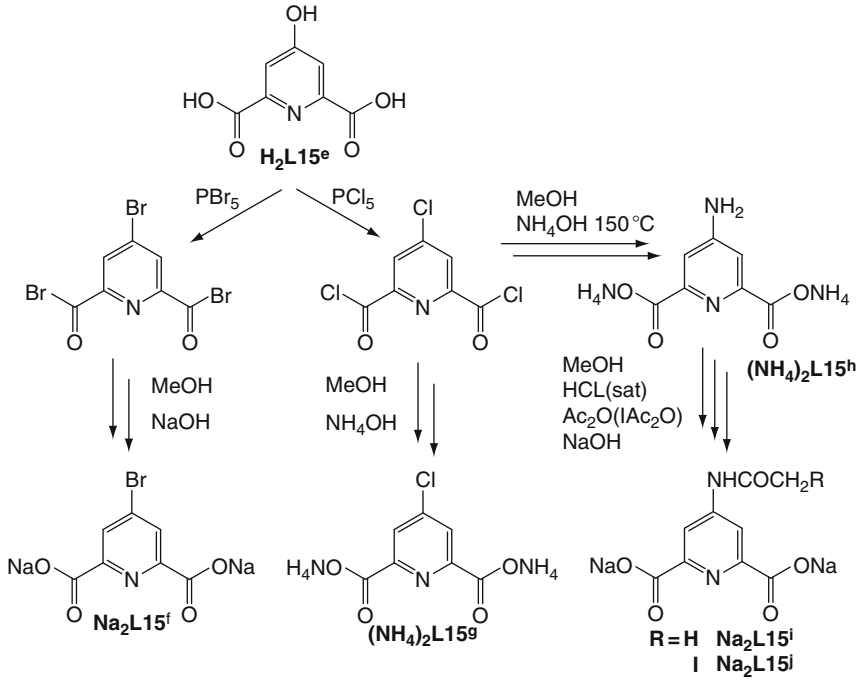

FIGURE 23 Synthetic paths for simple 4-pyridine-substituted dipicolinates (Lamture and Wensel, 1995; Lamture et al., 1995).

Pd-catalyzed Sonogashira cross-coupling reaction (Sonogashira et al., 1975) on 4-bromo or on more reactive iodo-substituted dipicolinic frameworks whereby either the dialkyl (methyl, ethyl) ester or diamide forms can be used (Picot et al., 2008b; Platas-Iglesias et al., 2001). While the bromo derivatives led to deceptively low yields (<45%), the less stable 4-iodo synthons proved to be much more effective with yields for the final ligands larger than 90%. Alternatively, the π-conjugated system can be introduced in the 2- and 6-positions by direct amidation of the carboxylic acid functions (Figure 24; Picot et al., 2008a).

The design of bifunctional chelating agents with a multidentate unit for coordination to R^{III} ions and an additional functionality is essential in bioanalyses, for instance for labeling DNA molecules or targeted proteins with lanthanide luminescent labels. One of the preferred position for the latter functionality is again the 4-position and an early example is $\mathbf{H_2L15^j}$ (Figure 23). Another strategy is to take advantage of the lipophilic properties of polyoxyethylene fragments which, in addition, are amenable to easy derivatization. Ligands $\mathbf{H_2L15^s}$ to $\mathbf{H_2L15^v}$ which bear a $(CH_2–CH_2–O)_3$ short pendant arm functionalized with hydroxyl, methoxy, amine, or phthalimide groups, have been synthesized bearing this idea in mind (Gassner et al., 2008). They were obtained either under the acidic form or as the sodium salt in 45–57% yield, starting from the diethylester of chelidamic acid. The polyoxyethylene pendant was grafted first by using a Mitsunobu reaction (Mitsunobu and Yamada, 1967). Hydrolysis of the resulting ester led to $\mathbf{H_2L15^s}$ whereas treatment with iodotrimethylsilane and subsequent hydrolysis yielded $\mathbf{H_2L15^t}$. For the other two ligands, $\mathbf{H_2L15^u}$ and $\mathbf{H_2L15^v}$, two successive Mitsunobu reactions were used to couple the polyoxyethylene arm onto a phthalimide group and then the resulting product to the dipicolinate framework; hydrolysis under specific conditions yielded either one of the ligands (Figure 25).

2.2 Solid state and solution structures of the mononuclear triple-helical precursors

Upon reaction of hydrated $R(ClO_4)_3$ or $R(CF_3SO_3)_3$ salts with the tridentate ligands **L15** in water and **L17–L19** in organic solvents, the complexes $[R(\mathbf{L15})_n]^{(3-2n)+}$ or $[R(\mathbf{Lk})_n]^{3+}$ ($n = 1$–3) are successively formed. Depending on the specific substituents borne by the ligands, the macroscopic formation constants $\beta_{1,n}^{R,Lk}$ may drastically vary (see Section 2.3), but the large majority of C_2-symmetrical ligands **L15**, **L17**, and **L18** eventually produces D_3-symmetrical triple-helical chelates $[R(\mathbf{L15})_3]^{3-}$ or $[R(\mathbf{Lk})_3]^{3+}$, while the C_1-symmetrical ligands **L19** give mixtures of *mer*-$[R(\mathbf{L19})_3]^{3+}$ (C_1-symmetry) and *fac*-$[R(\mathbf{L19})_3]^{3+}$ (C_3-symmetry) complexes. Numerous crystal and molecular structures have been reported for tris(dipicolinates) $[R(\mathbf{L15})_3]^{3-}$ showing the influence of the counterion on the triple-helical

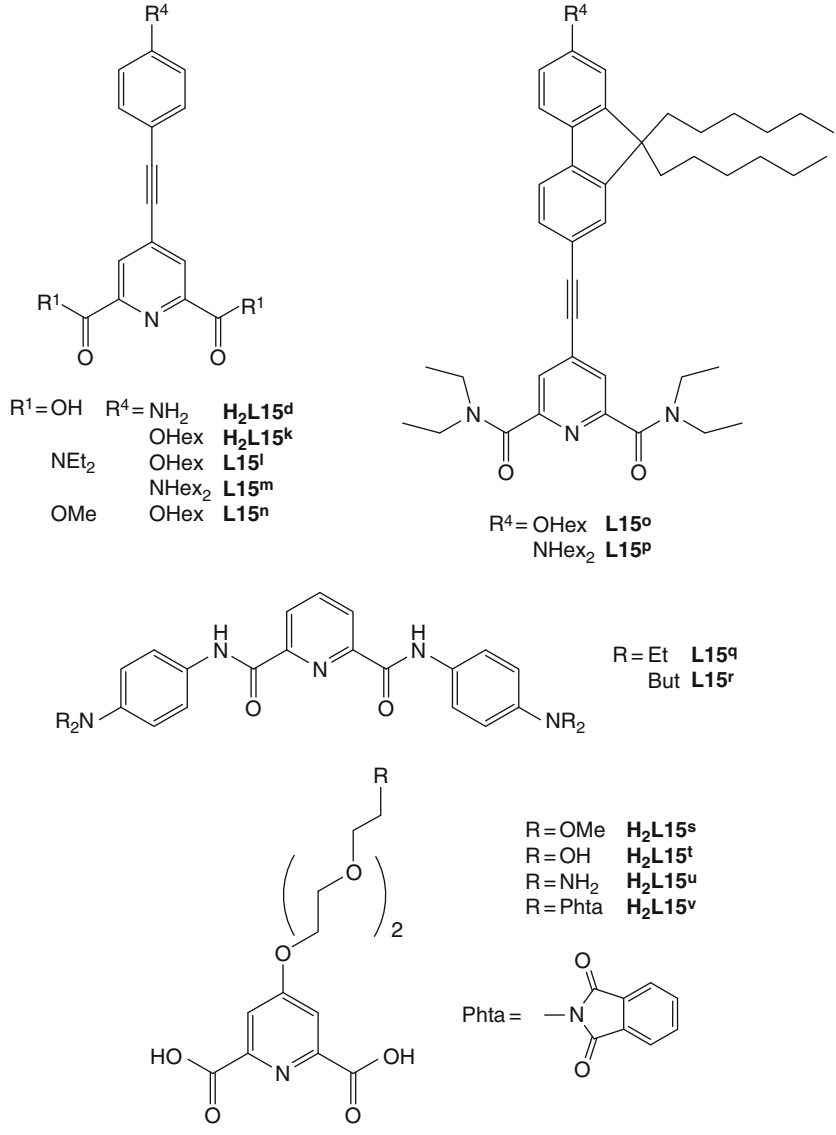

FIGURE 24 π-Conjugated (**L15^{d-r}**; Picot et al., 2008a) and polyoxyethyleneglycol-fitted dipicolinic acid derivatives (**H$_2$L15^{s-v}**; Gassner et al., 2008).

structure with idealized D_3-symmetry (Brayshaw et al., 1995). The crystal structure of [Eu(**L17^a**)$_3$]$^{3+}$ demonstrates the formation of pseudo-D_3-symmetry in the triple-helical complexes with the central lanthanide atom

being nine-coordinated in a pseudotricapped-trigonal prismatic arrangement (Figure 26; Piguet et al., 1993c), a structural pattern previously reported for the analogous complexes $[Eu(\mathbf{L16^a})_3]^{3+}$ (Figure 17B; Durham et al., 1969; Frost et al., 1969; Semenova et al., 1999). The Eu–N bond distances are similar in $[Eu(\mathbf{L17^a})_3]^{3+}$ and $[Eu(\mathbf{L16})_3]^{3+}$, but the extension of the distal aromatic rings in going from $\mathbf{L16^a}$ to $\mathbf{L17^a}$ is responsible for the formation of three intramolecular interstrand π-stacking interactions involving pairs of almost parallel benzimidazole rings in $[Eu(\mathbf{L17^a})_3]^{3+}$ (Figure 26; Piguet et al., 1993c).

At a concentration of 10 mM in acetonitrile, the triple-helical structure found for $[R(\mathbf{L17^a})_3]^{3+}$ in the solid state is maintained for R = Ce–Dy (Petoud et al., 1997a). For smaller lanthanides (R = Ho–Lu), the third

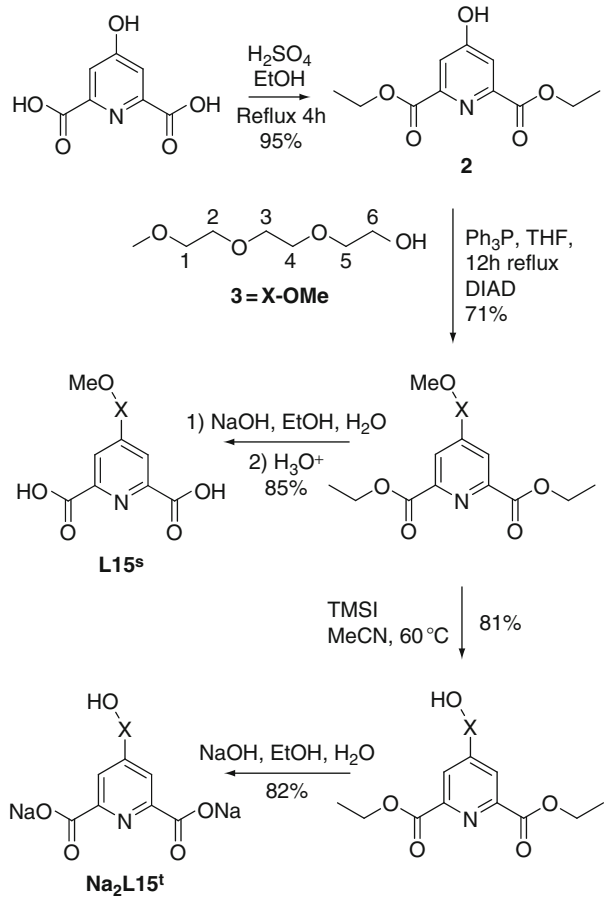

FIGURE 25 Continued

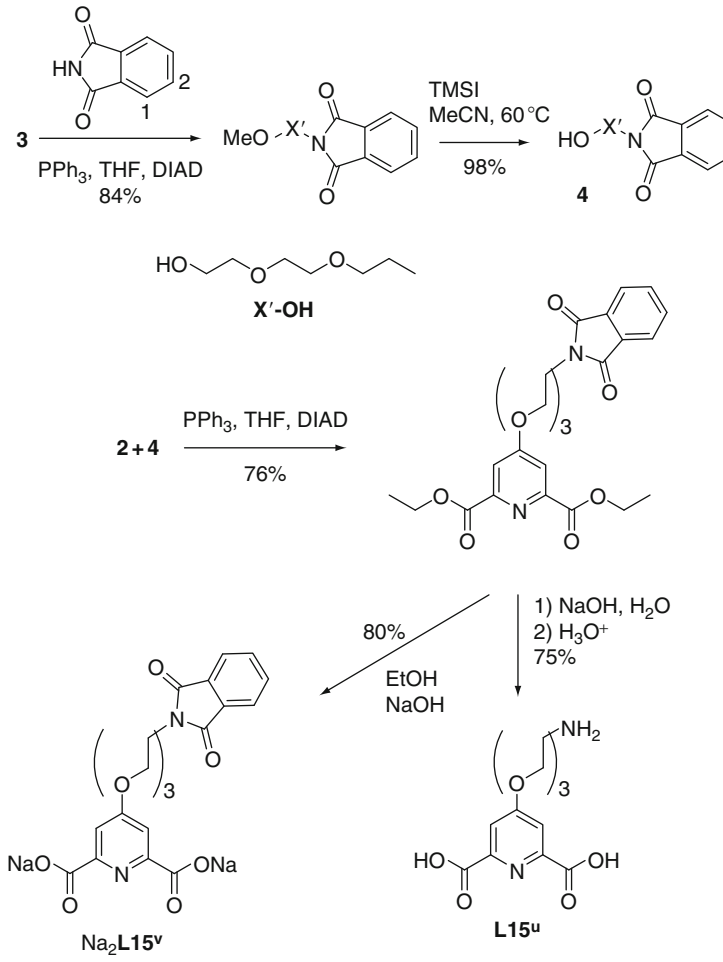

FIGURE 25 Synthesis of the dipicolinic acid derivatives $\mathbf{H_2L15^s}$ to $\mathbf{H_2L15^v}$ fitted with substituted trioxyethyleneglycol pendants (redrawn form Gassner et al., 2008).

successive stability constants measuring the affinity for the coordination of the third tridentate ligand $K_3^{R,L17a} = \beta_{1,3}^{R,L17a}/\beta_{1,2}^{R,L17a}$ is too weak to ensure the quantitative formation of the triple-helical complex under stoichiometric conditions. A mixture of $[R(\mathbf{L17^a})_3]^{3+}$, $[R(\mathbf{L17^a})_2]^{3+}$, and $\mathbf{L17^a}$ in slow exchange on the NMR timescale is thus evidenced in solution (Piguet et al., 1993c). The crystal structure of $[R(\mathbf{L17^f})_3]^{3+}$ confirms the formation of the triple-helical building blocks, but the increased steric congestion produced by the peripheral ethyl groups distorts the regular helical wrapping of the strands and reduces interstrand stacking

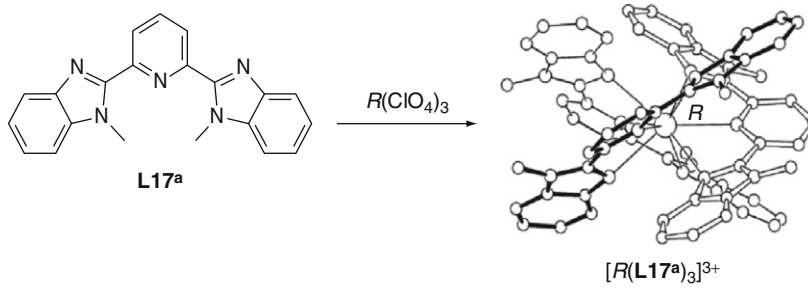

FIGURE 26 Schematic formation of D_3-symmetrical lanthanide triple-helical precursors with 2,6-bis(benzimidazolyl)pyridine **L17**. The representation of the complex corresponds to the crystal structure of $[Eu(\mathbf{L17^a})_3]^{3+}$ (redrawn from Piguet et al., 1993c).

(Piguet et al., 1995b). This trend is stepwise emphasized with $\mathbf{L17^c}$ (R^2 = propyl), $\mathbf{L17^e}$ (R^2 = 3,5-dimethoxybenzyl), and $\mathbf{L17^k}$ (R^2 = neopentyl), which precludes the formation and isolation of triple-helical complexes with these ligands (Muller et al., 2001a; Petoud et al., 1997a). However, the connection of a carboxyl substituent at the 4-position of the pyridine ring in $\mathbf{L17^l}$ has no effect on the complexation process and standard 1:3 triple-helical complexes are formed (Muller et al., 2001b). A very similar structural pattern is found with the amide derivatives **L18**, which lead to the formation of pseudo-D_3-symmetrical triple-helical complexes $[R(\mathbf{L18^a})_3]^{3+}$ (Renaud et al., 1997a), $[R(\mathbf{L18^b})_3]^{3+}$ (Muller et al., 2001b), $[R(\mathbf{L18^f})_3]^{3+}$ (Le Borgne et al., 2003), and $[R(\mathbf{L18^g})_3]^{3+}$ (Leonard et al., 2007) with the poorly constrained tertiary-amide substituents or with secondary-amide groups (Figure 27). However, bulky substituents grafted onto the tertiary-amide functions in $\mathbf{L18^d}$ and $\mathbf{L18^e}$ prevent the formation of triple-helical complexes and only 1:2 complexes $[R(\mathbf{L18^d})_2]^{3+}$ and $[R(\mathbf{L18^e})_2]^{3+}$ can be prepared (Le Borgne et al., 2003).

A thorough paramagnetic NMR study of $[R(\mathbf{L18^a})_3]^{3+}$ in acetonitrile shows the expected dynamically averaged D_3-symmetrical structure corresponding to the existence of a racemic mixture of P-$[R(\mathbf{L18^a})_3]^{3+}$ and M-$[R(\mathbf{L18^a})_3]^{3+}$ blocked on the NMR timescale (Renaud et al., 1997a). When unsymmetrical secondary-amide groups are considered in the ligands $\mathbf{L18^f}$ and $\mathbf{L18^g}$, the three possible blocked arrangements of the terminal alkyl substituents *EE*, *EZ*, and *ZZ* induces the formation of a mixture of 13 different inert isomers for the triple-helical complexes $[R(\mathbf{L18^f})_3]^{3+}$ and $[R(\mathbf{L18^g})_3]^{3+}$, which eventually gives intricate NMR spectra (Le Borgne et al., 2003). Interestingly, the crystal structures of both $[R(\mathbf{L18^f})_3]^{3+}$ (Le Borgne et al., 2003) and $[R(\mathbf{L18^g})_3]^{3+}$ (Leonard et al., 2007) show the selection of a single isomer during the crystallization process with the three ligands adopting *ZZ* conformations. Closely related

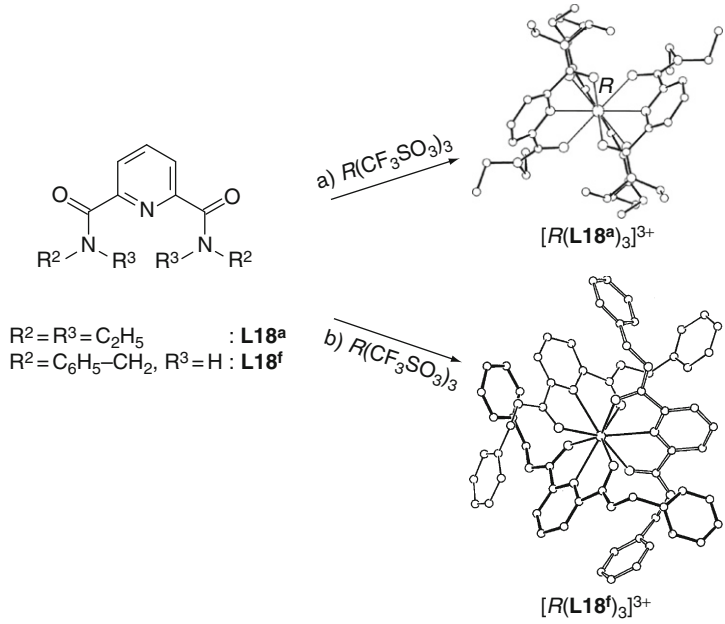

FIGURE 27 Schematic formation of D_3-symmetrical lanthanide triple-helical precursors with (A) 2,6-bis(tertiary-amide)pyridine ligands and (B) 2,6-bis(secondary-amide) pyridine ligands. The representation of the complexes corresponds to the crystal structures of $[Eu(\mathbf{L18^a})_3]^{3+}$ and $[Eu(\mathbf{L18^f})_3]^{3+}$ (redrawn from Le Borgne et al., 2003; Renaud et al., 1997a).

limitations affect the design of triple-helical complexes with the unsymmetrical NNO donor ligands **L19** because of the unavoidable meridional/facial isomerism (Figure 28; Le Borgne et al., 2004). No X-ray quality crystals could be grown from these mixtures, but 1:2 complexes $[Eu(\mathbf{L19^a})_2(CF_3SO_3)_2(H_2O)]^+$ and $[Eu(\mathbf{L19^d})_2(CF_3SO_3)_2(H_2O)]^+$, which possess no conformational isomer, could be fully characterized in the solid state (Le Borgne et al., 2004).

2.3 Thermodynamic stability and size-discriminating effects

Cumulative $\log(\beta_{1,n}^{R,Lk})$ and successive $\log(K_n^{R,Lk})$ stability constants are defined in the following equations:

$$n\mathbf{Lk} + R^{3+} \rightleftharpoons [R(\mathbf{Lk})_n]^{3+} \quad \beta_{1,n}^{R,Lk} \tag{1}$$

$$n\mathbf{Lk} + R^{3+} \rightleftharpoons [R(\mathbf{Lk})_n]^{3+} \quad K_{1,n}^{R,Lk} \tag{2}$$

The initial data of Grenthe (1961) on the mono-, bis-, and tris-complexes with unsubstituted dipicolinate are reported on Figure 29. There is an expected electrostatic trend in the $\log(\beta_{1,3}^{R,L15})$ values which increase from ≈18 to ≈22 up to Dy, corresponding to a free energy difference $\Delta(\Delta G_{1,3}^{R,L15^{\circ}}) \approx 23$ kJ mol^{-1}; the cumulative constants then stay constant up to Tm before slightly decreasing until the end of the series mainly due to the decreasing value of $\log K_1$. With respect to free energy, this eventual decrease corresponds to less than 4 kJ mol^{-1}. With the exception of the first part of the series (up to Nd), the size-discriminating effect is therefore very small. Substitution of the pyridine 4-position by derivatized trioxyethylene fragments does not lead to fundamental changes in thermodynamic stability of the triple-helical chelates, especially if one considers the uncertainties associated with the determination of $\log(\beta_{1,n}^{R,L15})$ values by spectrophotometry (see Table 1; Gassner et al., 2008).

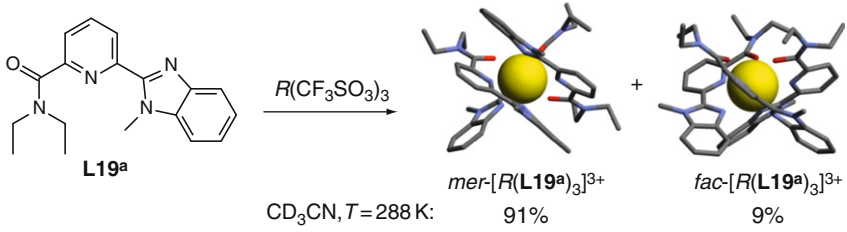

FIGURE 28 Schematic formation of lanthanide triple-helical building precursors with 2-benzimidazole-6-carboxypyridine ligands. The representation of the complexes corresponds to the optimized gas-phase molecular structures obtained for *mer*-[Lu(**L19^{a}**)$_3$]$^{3+}$ and *fac*-[Lu(**L19^{a}**)$_3$]$^{3+}$ (redrawn from Le Borgne et al., 2004).

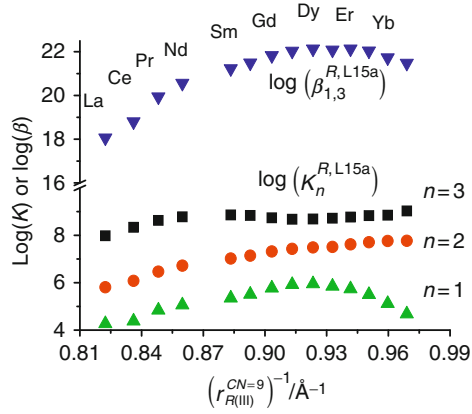

FIGURE 29 Stability constants for [Ln(**L15^{a}**)$_i$]$^{(3-2i)+}$ (data from Grenthe, 1961).

TABLE 1 Cumulative $\log(\beta_{1,n}^{R,Lk})$ and successive $\log(K_n^{R,Lk})$ stability constants reported for the formation of complexes $[R(\mathbf{L15}^j)_n]^{(3-n)+}$ (j = s–v, n = 1–3; see Figure 24) from $R(ClO_4)_3$ in water and of complexes $[R(\mathbf{L}k)_n]^{3+}$ (k = 17–19, n = 1–3; see Figures 19, 21, and 22) from $R(CF_3SO_3)_3$ in acetonitrile; T = 293 K

Ligand	R	$\log(\beta_{1,1}^{R,L})$	$\log(\beta_{1,2}^{R,L})$	$\log(\beta_{1,3}^{R,L})$	$\log(K_2^{R,L})$	$\log(K_3^{R,L})$	References
L15^{s}	La	10.2(6)	16.2(8)	20.9(7)	6.5(1.4)	4.2(1.5)	Gassner et al. (2008)
	Eu	8.9	14.3(2)	20.5(2)	4.4(2)	6.2(4)	Gassner et al. (2008)
	Tb	9.1(6)	15.5(6)	21.4(6)	6.4(1.2)	5.9(1.2)	Gassner et al. (2008)
L15^{t}	La	7.9(4)	14.2(5)	20.2(6)	6.3(9)	6.0(1.1)	Gassner et al. (2008)
	Eu	8.8(2)	15.1(2)	20.3(3)	6.3(4)	5.2(5)	Gassner et al. (2008)
	Tb	8.7(1)	15.1(2)	20.3(3)	6.4(3)	5.2(5)	Gassner et al. (2008)
	Lu	8.8	16.6(1)	22.8(2)	7.8(1)	6.2(3)	Gassner et al. (2008)
L15^{u}	La	7.2(1)	12.9(1)	17.6(1)	5.7(2)	4.7(2)	Gassner et al. (2008)
	Eu	6.8(4)	14.7(4)	20.5(4)	7.9(8)	5.8(8)	Gassner et al. (2008)
	Lu	8.5(3)	15.5(4)	20.4(4)	7.0(7)	4.9(8)	Gassner et al. (2008)
L17^{a}	La	8.9(3)	16.8(8)	22.6(9)	7.9(4)	5.8(2)	Petoud et al. (1997a)
	Ce					6.0(1)	Petoud et al. (1997a)
	Pr					6.3(1)	Petoud et al. (1997a)
	Nd	8.7(2)	15.9(8)	22.4(8)	7.2(4)	6.5(2)	Petoud et al. (1997a)
	Sm					6.4(2)	Petoud et al. (1997a)
	Eu	9.0(2)	15.7(7)	22.6(6)	6.7(3)	6.9(4)	Petoud et al. (1997a)
	Gd	8.5(2)	15.2(8)	21.8(8)	6.7(4)	6.6(2)	Petoud et al. (1997a)
	Tb	9.3(3)	16.4(10)	22.5(10)	7.1(5)	6.1(1)	Petoud et al. (1997a)
	Dy					5.8(1)	Petoud et al. (1997a)
	Ho	8.9(3)	16.2(19)	21.5(10)	7.3(5)	5.3(1)	Petoud et al. (1997a)
	Er					4.7(2)	Petoud et al. (1997a)

(*continued*)

TABLE 1 (*continued*)

Ligand	*R*	$\log(\beta_{1,1}^{R,L})$	$\log(\beta_{1,2}^{R,L})$	$\log(\beta_{1,3}^{R,L})$	$\log(K_2^{R,L})$	$\log(K_3^{R,L})$	References
	Tm					3.9(1)	Petoud et al. (1997a)
	Yb	9.4(5)	16.5(14)	19.9(10)	7.1(6)	3.4(1)	Petoud et al. (1997a)
	Lu	9.0(4)	15.4(10)	18.1(10)	6.4(4)	2.7(1)	Petoud et al. (1997a)
L17[b]	Ca	4.4(1)	8.6(1)	11.8(3)			Canard et al. (2008)
	La	6.9(1)	13.0(1)	17.3(1)			Canard et al. (2008)
	Eu	9.2(5)	16.9(8)	21.8(8)			Canard et al. (2008)
	Lu	9.9(3)	17.7(5)	23.4(7)			Canard et al. (2008)
L17[e]	La				5.0(1)	2.2(2)	Petoud et al. (1997a)
	Ce				4.8(1)	2.9(3)	Petoud et al. (1997a)
	Pr				4.9(19	2.8(1)	Petoud et al. (1997a)
	Nd				4.9(1)	3.2(2)	Petoud et al. (1997a)
	Sm				5.5(1)	3.6(1)	Petoud et al. (1997a)
	Gd				4.8(1)	3.2(1)	Petoud et al. (1997a)
	Tb				4.9(1)	3.1(1)	Petoud et al. (1997a)
	Er				5.1(1)	3.0(1)	Petoud et al. (1997a)
	Lu				5.4(1)	2.9(1)	Petoud et al. (1997a)
L17[i]	La					4.8(2)	Petoud et al. (1997a)
	Pr					5.5(2)	Petoud et al. (1997a)
	Sm					6.0(1)	Petoud et al. (1997a)
	Gd					6.1(2)	Petoud et al. (1997a)
	Tb					5.9(1)	Petoud et al. (1997a)
	Dy					5.2(2)	Petoud et al. (1997a)
	Ho					4.8(2)	Petoud et al. (1997a)

	Tm					3.9(1)	Petoud et al. (1997a)
	Yb					3.1(1)	Petoud et al. (1997a)
L17[k]	La	8.1(1)			5.7(5)	1.2(2)	Muller et al. (2001a,b)
	Eu	8.2(2)			5.9(3)	0.9(1)	Muller et al. (2001a,b)
	Lu	6.9(1)			5.7(1)	<0.5	Muller et al. (2001a,b)
L17[l]	La	7.8(4)			6.0(5)	3.8(6)	Muller et al. (2002a,b)
	Eu	8.0(4)			6.4(4)	4.6(5)	Muller et al. (2002a,b)
	Lu	8.0(3)			6.4(4)	2.9(4)	Muller et al. (2002a,b)
L18[a]	La	7.4(3)	14.8(3)	21.0(3)			Renaud et al. (1997a)
	Ce	7.6(3)	14.3(4)	22.0(3)			Renaud et al. (1997a)
	Pr	7.6(3)	14.6(3)	22.2(3)			Renaud et al. (1997a)
	Nd	7.5(3)	13.8(4)	21.5(4)			Renaud et al. (1997a)
	Sm	7.3(3)	14.4(4)	22.0(4)			Renaud et al. (1997a)
	Eu	8.3(3)	15.3(3)	22.3(3)			Renaud et al. (1997a)
	Gd	7.9(3)	14.7(4)	22.6(4)			Renaud et al. (1997a)
	Tb	8.2(3)	14.5(4)	22.9(4)			Renaud et al. (1997a)
	Dy	7.5(3)	14.8(4)	22.5(4)			Renaud et al. (1997a)
	Ho	7.3(4)	14.8(4)	22.3(4)			Renaud et al. (1997a)
	Er	7.7(4)	14.4(4)	22.7(4)			Renaud et al. (1997a)
	Tm	8.5(3)	16.0(3)	22.1(4)			Renaud et al. (1997a)
	Yb	8.5(3)	15.6(3)	22.8(4)			Renaud et al. (1997a)
	Lu	8.1(3)	15.2(3)	22.9(3)			Renaud et al. (1997a)
	Y	7.6(3)	14.6(4)	22.4(4)			Renaud et al. (1997a)
L18[b]	La	7.4(4)	14.0(5)	19.0(5)			Muller et al. (2001a,b)
	Eu	8.2(4)	14.5(5)	19.8(5)			Muller et al. (2001a,b)

(*continued*)

TABLE 1 (*continued*)

Ligand	*R*	$\log(\beta_{1,1}^{R,L})$	$\log(\beta_{1,2}^{R,L})$	$\log(\beta_{1,3}^{R,L})$	$\log(K_2^{R,L})$	$\log(K_3^{R,L})$	References
	Lu	8.7(4)	15.3(5)	20.3(5)			Muller et al. (2001a,b)
L18[c]	La	7.4(4)	13.9(5)	19.0(5)			Muller et al. (2001a,b)
	Eu	8.2(4)	14.6(5)	19.7(5)			Muller et al. (2001a,b)
	Lu	8.7(4)	15.2(5)	20.5(5)			Muller et al. (2001a,b)
L18[d]	La	7.8(5)	14.0(7)	18.0(8)			Le Borgne et al. (2003)
	Ce	7.4(4)	13.0(6)	17.9(7)			Le Borgne et al. (2003)
	Pr	8.0(6)	13.8(8)	17.5(9)			Le Borgne et al. (2003)
	Nd	7.7(5)	13.5(7)	17.5(8)			Le Borgne et al. (2003)
	Sm	8.5(6)	12.9(7)	18.4(8)			Le Borgne et al. (2003)
	Eu	8.3(6)	13.9(6)	17.6(7)			Le Borgne et al. (2003)
	Gd	7.9(7)	13.7(9)	17.5(9)			Le Borgne et al. (2003)
	Tb	7.6(6)	13.8(7)	18.5(7)			Le Borgne et al. (2003)
	Dy	7.7(5)	14.4(6)	17.3(8)			Le Borgne et al. (2003)
	Ho	8.3(6)	14.2(7)	17.9(9)			Le Borgne et al. (2003)
	Er	8.3(5)	13.9(6)	17.5(8)			Le Borgne et al. (2003)
	Tm	7.9(6)	13.8(7)	17.8(9)			Le Borgne et al. (2003)
	Yb	7.7(4)	13.7(5)	16.7(6)			Le Borgne et al. (2003)
	Lu	7.6(4)	13.5(5)	17.3(6)			Le Borgne et al. (2003)
L18[e]	La	5.4(5)	11.1(6)				Le Borgne et al. (2003)
	Eu	4.9(5)	9.8(6)				Le Borgne et al. (2003)
	Lu	5.3(5)	9.7(6)				Le Borgne et al. (2003)

	Y	4.9(5)	9.4(6)		Le Borgne et al. (2004)
L19[a]	La	7.1(3)	11.6(4)	15.9(5)	Le Borgne et al. (2004)
	Pr	7.7(3)	13.7(5)	17.8(6)	Le Borgne et al. (2004)
	Gd	7.3(2)	12.3(3)	17.4(4)	Le Borgne et al. (2004)
	Dy	7.4(3)	12.5(4)	16.5(5)	Le Borgne et al. (2004)
	Er	8.0(4)	13.2(4)	17.9(5)	Le Borgne et al. (2004)
	Lu	7.2(2)	11.5(4)	17.3(4)	Le Borgne et al. (2004)
L19[b]	La	8.6(3)	15.1(4)	19.9(4)	Le Borgne et al. (2004)
	Eu	7.8(2)	13.5(2)	19.2(2)	Le Borgne et al. (2004)
	Lu	9.2(2)	16.8(4)	21.9(4)	Le Borgne et al. (2004)
L19[c]	La	6.7(2)	11.7(3)	17.1(4)	Le Borgne et al. (2004)
	Pr	7.6(4)	13.2(5)	17.6(7)	Le Borgne et al. (2004)
	Gd	7.0(2)	11.8(3)	17.0(5)	Le Borgne et al. (2004)
	Dy	7.7(3)	12.4(4)	16.9(5)	Le Borgne et al. (2004)
	Er	7.8(3)	12.7(3)	17.1(3)	Le Borgne et al. (2004)
	Lu	7.2(2)	12.7(3)	18.5(5)	Le Borgne et al. (2004)
L19[d]	La	7.3(3)	12.7(4)	17.0(5)	Le Borgne et al. (2004)
	Eu	7.6(4)	12.8(5)	18.0(7)	Le Borgne et al. (2004)
	Lu	7.0(8)	11.9(8)	17.5(7)	Le Borgne et al. (2004)

Values without uncertainties have been fixed in the fitting process.

Data characterizing the formation of the complexes $[R(\mathbf{Lk})_n]^{3+}$ ($k = 17$–19, $n = 1$–3) are also collected in Table 1. For unconstrained symmetrical ligands **L17** and **L18**, the free energy changes $\Delta G_{1,n}^{R,Lk}$ accompanying the formation of the complexes $[R(\mathbf{Lk})]^{3+}$ ($\Delta G_{1,1}^{R,Lk} = -42$ to -50 kJ mol^{-1}), $[R(\mathbf{Lk})_2]^{3+}$ ($\Delta G_{1,2}^{R,Lk} = -81$ to -93 kJ mol^{-1}) and $[R(\mathbf{Lk})_3]^{3+}$ ($\Delta G_{1,3}^{R,Lk} = -112$ to -123 kJ mol^{-1}) do not significantly depend on the nature of the donor atoms in the tridentate ligands (N_3 in **L17** and NO_2 in **L18**). This reflects the crucial role played by the entropic contribution in lanthanide complexation processes, which are mainly controlled by charge compensation effects (Choppin, 1989; Comuzzi et al., 2002; Di Bernardo et al., 2008; Piguet and Bünzli, 1999). This translates into a pronounced preference of the trivalent lanthanides for complexing negatively charged donor atoms, often oxygen atoms because of their large electronegativity. The latter trend is usually and erroneously assigned to some specific oxophilicity of R^{III}, but negatively charged nitrogen or carbon atoms are valuable alternatives (Anwander, 1999; Dehnicke and Greiner, 2003; Evans, 2007).

The complexation process involves a *trans–trans* → *cis–cis* conformational interconversion of the tridentate binding unit whose energetic costs is very sensitive to the size and bulkiness of the substituents bound to the N atoms of the benzimidazole rings in **L17**, or to the N atoms of the amide groups in **L18** (Figure 30). Consequently, $K_2^{R,L17}$ decreases by two orders of magnitude when the methyl groups in **L17^{a}** are replaced with bulky 3,5-dimethoxybenzyl groups in **L17^{e}**. Similarly, $\beta_{1,1}^{R,L18}$ (2–3 orders of magnitude) and $\beta_{1,2}^{R,L18}$ (4 orders of magnitude) are reduced when diethylamide groups in **L18^{a}** are replaced with dibenzyl groups in **L18^{e}** (Table 1). Intramolecular interligand interactions resulting from the tight wrapping of the three strands in $[R(\mathbf{Lk})_3]^{3+}$ may also tune the stability of the final triple-helical complexes as revealed by the decrease by two orders of magnitude of $\beta_{1,3}^{R,L18}$ values in going from **L18^{a}** ($R^2 = R^3 = C_2H_5$) to **L18^{d}** ($R^2 = R^3 = CH(CH_3)_2$), while $\beta_{1,2}^{R,L18}$ values are similar for both ligands (Table 1).

The unusual bowl-shaped curve found for $\log(\beta_{1,3}^{R,L17a})$ along the lanthanide series merits special comments since it represents a rare case of size-discriminating effect favoring the complexation of large lanthanides (Figure 31; Petoud et al., 1997a,b). Detailed structural data collected in the solid state (Piguet et al., 1993c) and in solution (Petoud et al., 1997a) for $[R(\mathbf{L17^{a}})_3]^{3+}$ firmly establish that the tight wrapping of the three helical ligand strands produces three efficient intramolecular interstrand interactions involving pairs of benzimidazole rings (Figure 26). Attractive π–π interactions are compatible with *R*-N bond lengths compatible with the coordination of large or midrange trivalent lanthanides, and they further contribute to stabilize the final triple-helical complexes (Table 1). The required contraction of the *R*–N bond

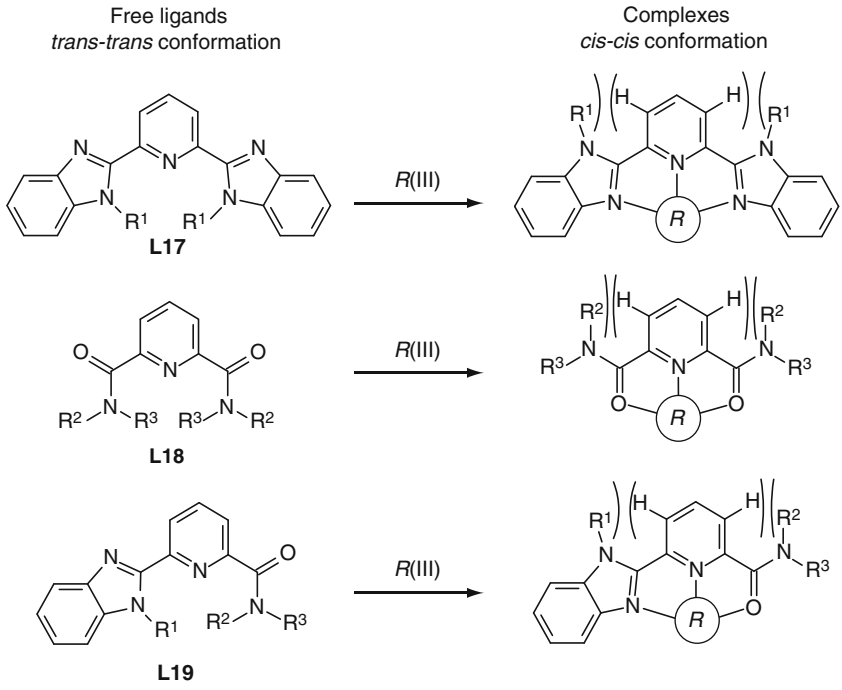

FIGURE 30 *Trans–trans* → *cis–cis* conformational change of the tridentate binding unit occurring upon complexation of **L17**–**L19** to trivalent lanthanides.

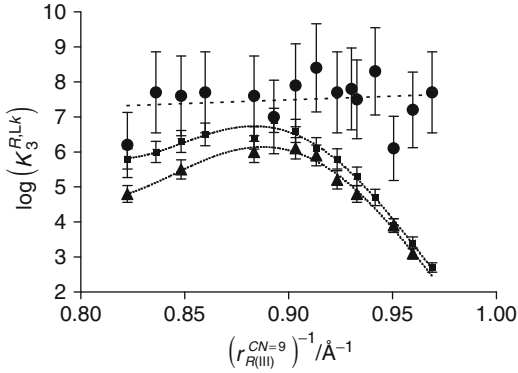

FIGURE 31 Third successive stability constants $\log(K_3^{R,Lk})$ measured in acetonitrile for the triple-helical complexes $[R(\mathbf{L17^a})_3]^{3+}$ (squares), $[R(\mathbf{L17^i})_3]^{3+}$ (triangles), and $[R(\mathbf{L18^a})_3]^{3+}$ (circles) versus the reciprocal of ionic radius for nine-coordinate R^{3+} (redrawn after Petoud et al., 1997a,b).

lengths along the second part of the lanthanide series in $[R(\mathbf{L17^a})_3]^{3+}$ is only possible at the cost of a closer packing of the pairs of benzimidazole rings, which induces repulsive van der Waals interactions and some slipping of the strands (Piguet et al., 1995b). Consequently, the third successive stability constants $\log(K_3^{R,\mathrm{L17a}})$ are significantly reduced for the smaller lanthanides, and a pronounced size-discriminating effect favoring the complexation of midrange R^{III} results (Figure 31; Table 1). Obviously, the latter effect is removed when at least one distal benzimidazole rings is replaced with a carboxamide group in $[R(\mathbf{L18^a})_3]^{3+}$ or $[R(\mathbf{L19^a})_3]^{3+}$, and the standard electrostatic trend is restored (Figure 31; Table 1; Piguet and Bünzli, 1999). Interestingly, the deleterious consequences on the thermodynamic constants produced by the introduction of bulky substituents in $[R(\mathbf{L17^e})_3]^{3+}$ can be overcome by the connection of a strong donor in the back of the central pyridine ring in $[R(\mathbf{L17^i})_3]^{3+}$ (Figure 31; Petoud et al., 1997a,b).

2.4 Isomerization and covalent tripods

When the tridentate binding unit does not possess a C_2-axis as in **L19**, two isomeric triple-helical complexes are formed upon reaction with R^{III} (Figure 28). Therefore, the associated macroscopic formation constant $\beta_{1,3}^{R,\mathrm{L19}}$ is made up of two microconstants, each characterizing the formation of the microspecies *mer*-$[R(\mathbf{L19})_3]^{3+}$ and *fac*-$[R(\mathbf{L19})_3]^{3+}$, Eq. (3), and whose ratio is given in Eq. (4).

$$\beta_{1,3}^{R,\mathrm{L19}} = \beta_{1,3,mer}^{R,\mathrm{L19}} + \beta_{1,3,fac}^{R,\mathrm{L19}} \tag{3}$$

$$fac-[R(\mathbf{L19})_3]^{3+} \rightleftharpoons mer-[R(\mathbf{L19})_3]^{3+} \quad K_{\mathrm{iso}}^{R,\mathrm{L19}} = \beta_{1,3,mer}^{R,\mathrm{L19}}/\beta_{1,3,fac}^{R,\mathrm{L19}} \tag{4}$$

Assuming a pure statistical entropic driving force for equilibrium (4) (i.e., $\Delta H_{\mathrm{iso}}^{R,\mathrm{L19}} = 0$), $K_{\mathrm{iso}}^{R,\mathrm{L19}}$ corresponds to the ratio of the external symmetry numbers of *fac*-$[R(\mathbf{L19})_3]^{3+}$ ($\sigma_{fac} = 3$, C_3-symmetrical) and *mer*-$[R(\mathbf{L19})_3]^{3+}$ ($\sigma_{mer} = 1$, C_1-symmetrical), which gives $K_{\mathrm{iso}}^{R,\mathrm{L19}} = \sigma_{fac}/\sigma_{mer} = 3$ (Ercolani et al., 2007), hence an entropic contribution of $\Delta S_{\mathrm{iso}}^{R,\mathrm{L19}} = R\ln(3) = 9.1\ \mathrm{J\,mol^{-1}\,K^{-1}}$ in favor of the meridional isomer. The detailed investigation of equilibrium (4) in acetonitrile for $\mathbf{L19^a}$, $\mathbf{L19^c}$, and $\mathbf{L19^d}$ shows that both experimental enthalpic, $\Delta H_{\mathrm{iso}}^{\mathrm{Lu,L19}}$, and entropic, $\Delta S_{\mathrm{iso}}^{\mathrm{Lu,L19}}$, contributions deviate from this simple statistical model (Table 2; Le Borgne et al., 2004).

For $[\mathrm{Lu}(\mathbf{L19^a})_3]^{3+}$ and $[\mathrm{Lu}(\mathbf{L19^d})_3]^{3+}$, the negative enthalpic contributions result from residual $\pi-\pi$ stacking interactions, which only operate

TABLE 2 Enthalpic ($\Delta H_{iso}^{Lu,L19}$ in kJ mol^{-1}) and entropic ($\Delta S_{iso}^{Lu,L19}$ in Jmol^{-1}K^{-1}) contributions to the *fac*-[Lu(**L19**)$_3$]$^{3+}$ ⇌ *mer*-[Lu(**L19**)$_3$]$^{3+}$ isomerization in acetonitrile at 293 K (see Eq. (4), Figure 22)

	[Lu(**L19**^{a})$_3$]$^{3+}$	[Lu(**L19**^{c})$_3$]$^{3+}$	[Lu(**L19**^{d})$_3$]$^{3+}$
$\Delta H_{iso}^{Lu,L19}$ (kJ mol^{-}1)	− 4.3(5)	21(2)	− 6.9(2.4)
$\Delta S_{iso}^{Lu,L19}$ (J mol^{-1} K^{-1})	5(5)	82(7)	− 10(10)
$-T\Delta S_{iso}^{Lu,L19}$ (kJ mol^{-}1)	− 1.5(1.5)	− 24(2)	3(3)

in the meridional isomer (Figure 28). The large, but opposite enthalpic contribution found in [Lu(**L19**^{c})$_3$]$^{3+}$ has the same origin because the bulky 3,5-dimethoxybenzyl groups prevent close packing of the strands in the meridional isomer. Although the deviations of the entropy changes from the statistical values of 9.1 J mol^{-1} K^{-1} are more difficult to rationalize, the global free energy changes at 293 K ($-4 < \Delta G_{iso}^{Lu,L19} < -2$ kJ mol^{-1}) systematically favor the meridional isomer, a severe drawback since the introduction of these unsymmetrical building blocks in polynuclear helicates requires the selective preparation of the facial C_3-symmetrical isomer (Le Borgne et al., 2004). To force facial coordination of the three strands about R^{III}, three unsymmetrical tridentate ONO (**L20**: Renaud et al., 1999; **L21**: Senegas et al., 2003; Figure 32), NNO (**L22**: Koeller et al., 2003a; **L23**: Koeller et al., 2003b; Figure 33), and NNN (**L24**: Canard et al., 2008; Figure 34) binding units have been connected to covalent tripods. Upon reaction with $R(ClO_4)_3$ or $R(CF_3SO_3)_3$, the expected C_3-symmetrical podates $[R(\mathbf{L20})]^{3+}$, $[R(\mathbf{L21}\text{-3H})]$, $[R(\mathbf{L22})]^{3+}$, $[R(\mathbf{L23})]^{3+}$, and $[R(\mathbf{L24})]^{3+}$ are formed in solution and in the solid state (Figures 32–34).

The pair of podands **L20** and [**L21**-3H]$^{3-}$ have been designed for exploring the effect of charge compensation on the energetics and structures of the final triple-helical podates $[R(\mathbf{L20})]^{3+}$ and $[R(\mathbf{L21}\text{-3H})]$. The formation constants reported for $[R(\mathbf{L20})]^{3+}$ in acetonitrile (Eq. (5)) and for $[R(\mathbf{L21}\text{-3H})]$ in water (Eq. (6)) are comparable (Table 3) and correspond to $\log(\beta_{1,1}^{R,Lk}) = 6.5$–$8.0$, which translates into $-45 < \Delta G_{1,1}^{R,Lk^{\circ}} < -36$ kJ mol^{-1}.

$$\mathbf{L}k + R^{3+} \rightleftharpoons [R(\mathbf{L}k)]^{3+} \quad \beta_{1,1}^{R,Lk} \tag{5}$$

$$[\mathbf{L21} - 3\mathrm{H}]^{3-} + R^{3+} \rightleftharpoons [R(\mathbf{L21} - 3\mathrm{H})]^{3+} \quad \beta_{1,1}^{R,Lk} \tag{6}$$

Since the solvation of R^{3+} is more energetic in water than in acetonitrile, the formation constants of $[R(\mathbf{L20})]^{3+}$ ($\log(\beta_{1,1}^{R,L20})$) decrease

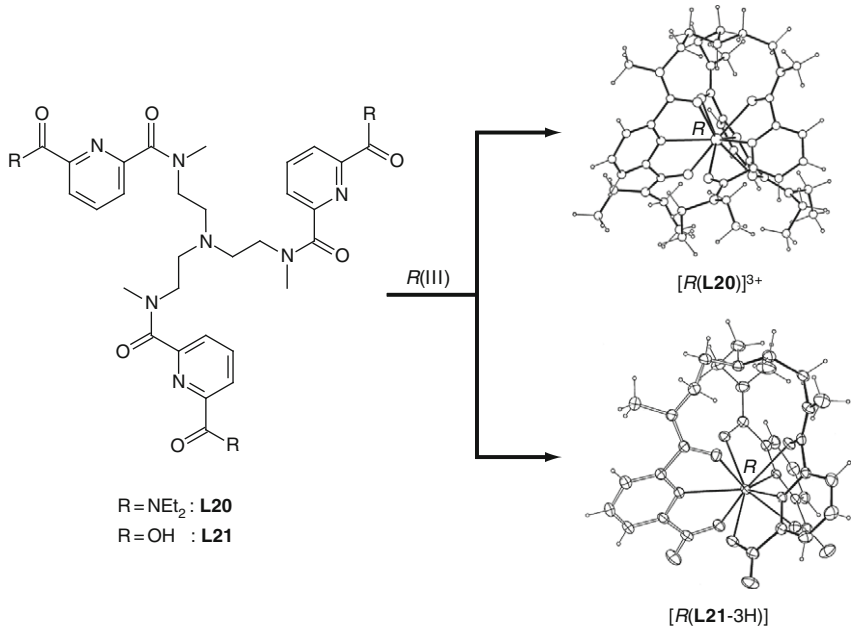

FIGURE 32 Schematic formation of the C_3-symmetrical N_3O_6 nine-coordinate triple-helical lanthanide podates with **L20** and **L21**. The representation of the complexes corresponds to the crystal structures of [Eu(**L20** + H)]$^{4+}$ and [Eu(**L21**-3H)] (redrawn after Renaud et al., 1999; Senegas et al., 2003).

by one order of magnitude in CH_3CN/H_2O (95:5) and $\beta_{1,1}^{R,L20} < 10$ is reached in pure water. However, the formation constants for [*R*(**L21**-3H)] in pure water still amount to $6.7 \leq \log(\beta_{1,1}^{R,L21}) \leq 7.0$, which unambiguously demonstrates the importance of the charge compensation process in the overall stability of the lanthanide complexes (Table 3). In this context, it is worth noting that Eu–O(carboxylate) bond lengths (average 2.45(1) Å) in the crystal structure of [Eu(**L21**-3H)] (Senegas et al., 2003) are similar to Eu–O(carboxamide) bond lengths (average 2.43(1) Å) found in [*R*(**L20** + H)]$^{4+}$ (Renaud et al., 1999). It can be concluded that the favorable charge compensation effect arises almost exclusively from an entropic contribution.

The next pair of podands **L22** and **L23** has been developed for exploring the effect of the conformation of the covalent tripod on the organization and binding efficiency of the tridentate binding units. Table 3 indeed shows that the methylation of the apical carbon atom in **L23** slightly increases the formation constant by approximately one order of magnitude, but the most striking difference concerns the formation of two endo conformers for [*R*(**L22**)]$^{3+}$ (ratio 7:3; Koeller et al., 2003a), while [*R*(**L23**)]$^{3+}$

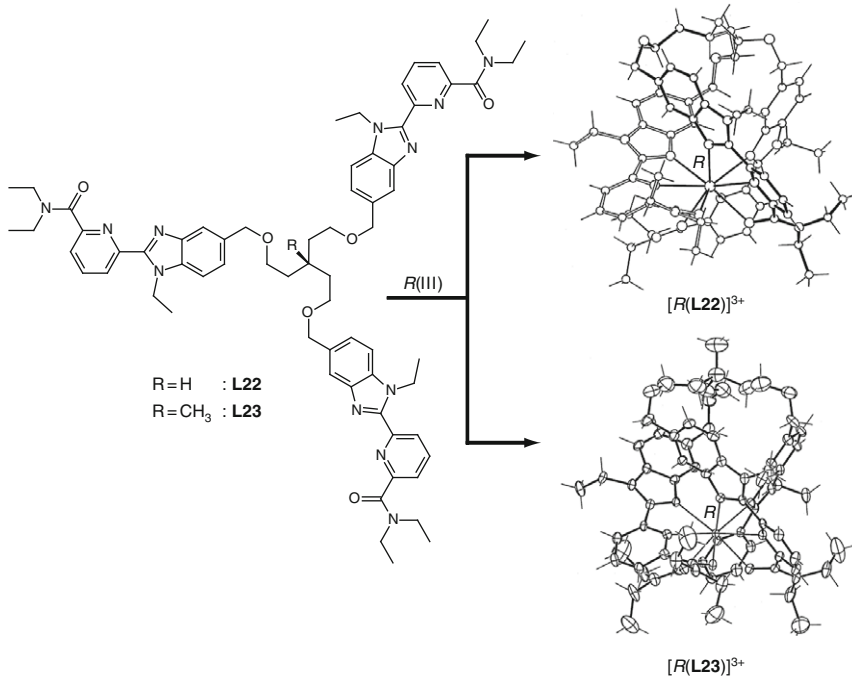

FIGURE 33 Schematic formation of the C_3-symmetrical N_6O_3 nine-coordinate triple-helical lanthanide podates with **L22** and **L23**. The representation of the complexes corresponds to the crystal structures of [La(**L22**)]$^{3+}$ and [Eu(**L23**)]$^{3+}$ (redrawn after Koeller et al., 2003a,b).

exists as a single exo-isomer, whereby the apical methyl group points out of the coordination cavity (Figure 33; Koeller et al., 2003b). Despite the latter structural change, the C_3-symmetrical organization of the three helically wrapped tridentate binding units are almost superimposable in the two podates, which explains the minor variations of the thermodynamic properties (Koeller et al., 2003b).

Taking the methylated exo-tripod of **L23** as a reference, podand **L24** was synthesized for combining the size-discriminating effect associated with 2,6-bis(benzimidazol-2-yl)pyridine ligand (Figure 31) with the preorganization of the covalent tripod (Figure 34; Canard et al., 2008). Surprisingly, the formation constants of [*R*(**L24**)]$^{3+}$ (three NNN donors) do not evidence measurable size-discriminating effect, and they correspond to a tiny domain of free energy $-48 < \Delta G_{1,1}^{R,L24} < -36$ kJ mol^{-1}, identical to those observed for [*R*(**L20**)]$^{3+}$ (three ONO donors), [*R*(**L22**)]$^{3+}$, and [*R*(**L23**)]$^{3+}$ (three NNO donors) in the same solvent (Table 3). However, the formation of nine *R*-ligand bonds in the latter

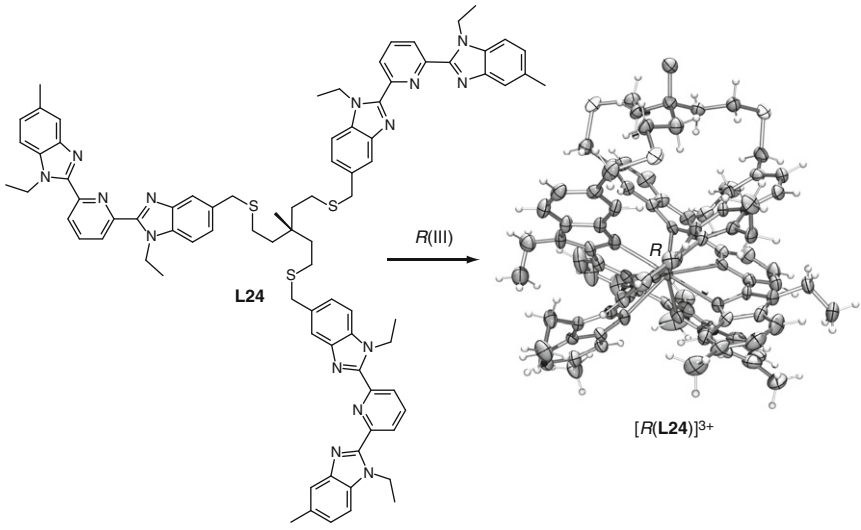

FIGURE 34 Schematic formation of the C_3-symmetrical N_9 nine-coordinate triple-helical lanthanide podates with **L24**. The representation of the complex corresponds to the crystal structure of [Eu(**L24**)]$^{3+}$ (redrawn after Canard et al., 2008).

podates is approximately three times less efficient that the same process observed for the native nonconnected tridentate binding units in [R(**L18**^{a})$_3$]$^{3+}$ (three ONO donors: $-128 < \Delta G^{R,L18a^\circ}_{1,3} < -117$ kJ mol^{-1}), [R(**L19**^{a})$_3$]$^{3+}$ (three NNO donors: $-100 < \Delta G^{R,L19a^\circ}_{1,1} < -89$ kJ mol^{-1}) and [R(**L17**^{a})$_3$]$^{3+}$ (three NNN donors: $-127 < \Delta G^{R,L17a^\circ}_{1,1} < -120$ kJ mol^{-1}; Table 1).

In going from the podates [R(**L***k*)]$^{3+}$ to the triple-helical complexes [R(**L***k*)$_3$]$^{3+}$ with the same set of donor atoms, the complexation processes only differ by the replacement of three intermolecular R-tridentate unit connections in [R(**L***k*)$_3$]$^{3+}$ with one intermolecular and two intramolecular connections in [R(**L***k*)]$^{3+}$ (Figure 35; Canard et al., 2008). It was thus concluded that the covalent tripod, instead of preorganizing the three tridentate units for their coordination to R^{III}, indeed dramatically disorganizes the binding units and prevents efficient connection processes. It is, however, worth noting that the pseudotricapped-trigonal prismatic coordination spheres in each pair [R(**L***k*)$_3$]$^{3+}$/[R(**L***k*)]$^{3+}$ are almost superimposable, which implies some drastic torsions and constraints in the covalent tripod. Consequently, minor changes in the structure of the tripod have considerable effects on the complexation process. For instance, insertion of one additional methylene unit in [R(**L25**)]$^{3+}$ changes the ratio of the two endo isomers from 7:3 in [R(**L22**)]$^{3+}$ to 13:1 in

TABLE 3 Overall stability constants, $\log(\beta_{1,1}^{R,Lk})$, reported at 293 K for the formation of the triple-helical podates $[R(\mathbf{L}k)]^{3+}$ ($k = 20$–24, see Figures 32–34)

Ligand	Salt	Solvent	$\log(\beta_{1,1}^{R,Lk})$	References
L20	$La(ClO_4)_3$	CH_3CN	8.3(2)	Renaud et al. (1999)
L20	$La(ClO_4)_3$	CH_3CN/H_2O (95:5)	5.0(1)	Renaud et al. (1999)
L20	$Ce(ClO_4)_3$	CH_3CN	8.5(7)	Renaud et al. (1999)
L20	$Pr(ClO_4)_3$	CH_3CN	8.0(7)	Renaud et al. (1999)
L20	$Nd(ClO_4)_3$	CH_3CN	8.1(5)	Renaud et al. (1999)
L20	$Sm(ClO_4)_3$	CH_3CN	7.0(4)	Renaud et al. (1999)
L20	$Sm(ClO_4)_3$	CH_3CN/H_2O (95:5)	6.3(3)	Renaud et al. (1999)
L20	$Gd(ClO_4)_3$	CH_3CN	7.6(4)	Renaud et al. (1999)
L20	$Dy(ClO_4)_3$	CH_3CN	7.4(3)	Renaud et al. (1999)
L20	$Tm(ClO_4)_3$	CH_3CN	7.2(6)	Renaud et al. (1999)
L20	$Lu(ClO_4)_3$	CH_3CN	8.0(6)	Renaud et al. (1999)
L20	$Lu(ClO_4)_3$	CH_3CN/H_2O (95:5)	7.5(3)	Renaud et al. (1999)
L20	$Y(ClO_4)_3$	CH_3CN	6.7(4)	Renaud et al. (1999)
L20	$Y(ClO_4)_3$	CH_3CN/H_2O (95:5)	6.8(1)	Renaud et al. (1999)
$[L21\text{-}3H]^{3-}$	$La(ClO_4)_3$	H_2O (pH 8.0)	6.8(1)	Senegas et al. (2003)
$[L21\text{-}3H]^{3-}$	$Nd(ClO_4)_3$	H_2O (pH 8.0)	6.7(2)	Senegas et al. (2003)
$[L21\text{-}3H]^{3-}$	$Sm(ClO_4)_3$	H_2O (pH 8.0)	6.9(2)	Senegas et al. (2003)
$[L21\text{-}3H]^{3-}$	$Gd(ClO_4)_3$	H_2O (pH 8.0)	6.7(2)	Senegas et al. (2003)
$[L21\text{-}3H]^{3-}$	$Dy(ClO_4)_3$	H_2O (pH 8.0)	6.8(2)	Senegas et al. (2003)
$[L21\text{-}3H]^{3-}$	$Ho(ClO_4)_3$	H_2O (pH 8.0)	7.0(2)	Senegas et al. (2003)
$[L21\text{-}3H]^{3-}$	$Er(ClO_4)_3$	H_2O (pH 8.0)	6.8(2)	Senegas et al. (2003)
$[L21\text{-}3H]^{3-}$	$Tm(ClO_4)_3$	H_2O (pH 8.0)	6.9(2)	Senegas et al. (2003)
$[L21\text{-}3H]^{3-}$	$Lu(ClO_4)_3$	H_2O (pH 8.0)	7.0(2)	Senegas et al. (2003)
L22	$La(CF_3SO_3)_3$	CH_3CN	7.0(2)	Koeller et al. (2003a)
L22	$Pr(CF_3SO_3)_3$	CH_3CN	7.3(4)	Koeller et al. (2003a)
L22	$Nd(CF_3SO_3)_3$	CH_3CN	6.5(3)	Koeller et al. (2003a)
L22	$Sm(CF_3SO_3)_3$	CH_3CN	6.8(3)	Koeller et al. (2003a)
L22	$Gd(CF_3SO_3)_3$	CH_3CN	7.6(3)	Koeller et al. (2003a)
L22	$Dy(CF_3SO_3)_3$	CH_3CN	7.2(2)	Koeller et al. (2003a)
L22	$Er(CF_3SO_3)_3$	CH_3CN	7.5(4)	Koeller et al. (2003a)
L22	$Lu(CF_3SO_3)_3$	CH_3CN	6.8(3)	Koeller et al. (2003a)
L23	$La(CF_3SO_3)_3$	CH_3CN	8.2(5)	Koeller et al. (2003b)
L23	$Pr(CF_3SO_3)_3$	CH_3CN	7.6(2)	Koeller et al. (2003b)
L23	$Eu(CF_3SO_3)_3$	CH_3CN	7.7(4)	Koeller et al. (2003b)

(*continued*)

TABLE 3 (*continued*)

Ligand	Salt	Solvent	$\log(\beta_{1,1}^{R,Lk})$	References
L23	$Dy(CF_3SO_3)_3$	CH_3CN	7.6(3)	Koeller et al. (2003b)
L23	$Er(CF_3SO_3)_3$	CH_3CN	7.2(2)	Koeller et al. (2003b)
L23	$Lu(CF_3SO_3)_3$	CH_3CN	7.9(3)	Koeller et al. (2003b)
L24	$Ca(CF_3SO_3)_2$	CH_3CN	8.6(8)	Canard et al. (2008)
L24	$La(CF_3SO_3)_3$	CH_3CN	7.6(2)	Canard et al. (2008)
L24	$Ce(CF_3SO_3)_3$	CH_3CN	7.2(2)	Canard et al. (2008)
L24	$Pr(CF_3SO_3)_3$	CH_3CN	7.3(2)	Canard et al. (2008)
L24	$Nd(CF_3SO_3)_3$	CH_3CN	7.6(2)	Canard et al. (2008)
L24	$Sm(CF_3SO_3)_3$	CH_3CN	7.8(2)	Canard et al. (2008)
L24	$Eu(CF_3SO_3)_3$	CH_3CN	7.2(1)	Canard et al. (2008)
L24	$Gd(CF_3SO_3)_3$	CH_3CN	7.5(2)	Canard et al. (2008)
L24	$Tb(CF_3SO_3)_3$	CH_3CN	7.8(2)	Canard et al. (2008)
L24	$Dy(CF_3SO_3)_3$	CH_3CN	7.4(2)	Canard et al. (2008)
L24	$Ho(CF_3SO_3)_3$	CH_3CN	7.9(1)	Canard et al. (2008)
L24	$Er(CF_3SO_3)_3$	CH_3CN	7.4(1)	Canard et al. (2008)
L24	$Tm(CF_3SO_3)_3$	CH_3CN	7.9(1)	Canard et al. (2008)
L24	$Yb(CF_3SO_3)_3$	CH_3CN	7.4(1)	Canard et al. (2008)
L24	$Lu(CF_3SO_3)_3$	CH_3CN	8.0(1)	Canard et al. (2008)
L24	$Y(CF_3SO_3)_3$	CH_3CN	7.3(2)	Canard et al. (2008)

$[R(\mathbf{L25})]^{3+}$ (Figure 36; Koeller et al., 2006), while the same homologation procedure transforming $[R(\mathbf{L20})]^{3+}$ in $[R(\mathbf{L26})]^{3+}$ eventually gives a podand with strongly reduced affinities for R^{III} in acetonitrile (Figure 36; Renaud et al., 2001).

2.5 Photophysical properties

2.5.1 General considerations: f–f transitions and luminescence sensitization

As a result of the poor expansion of the 4f-orbitals, the *R*-ligand bonds are mainly electrostatic and only some minute mixing of metal and ligand electronic wave functions contributes to covalency. It therefore often appears justified to consider separately ligand-centered and metal-centered excited states in lanthanide complexes, and *Jablonsky* diagrams (Figure 37) are adequate for attempting to rationalize photophysical properties (Bünzli and Piguet, 2002). Since the intrashell electric dipole $4f \rightarrow 4f$ electronic transitions are *Laporte*-forbidden (Bünzli, 1989), efficient light-harvesting is performed by the aromatic ($\pi \rightarrow \pi^*$) and/or

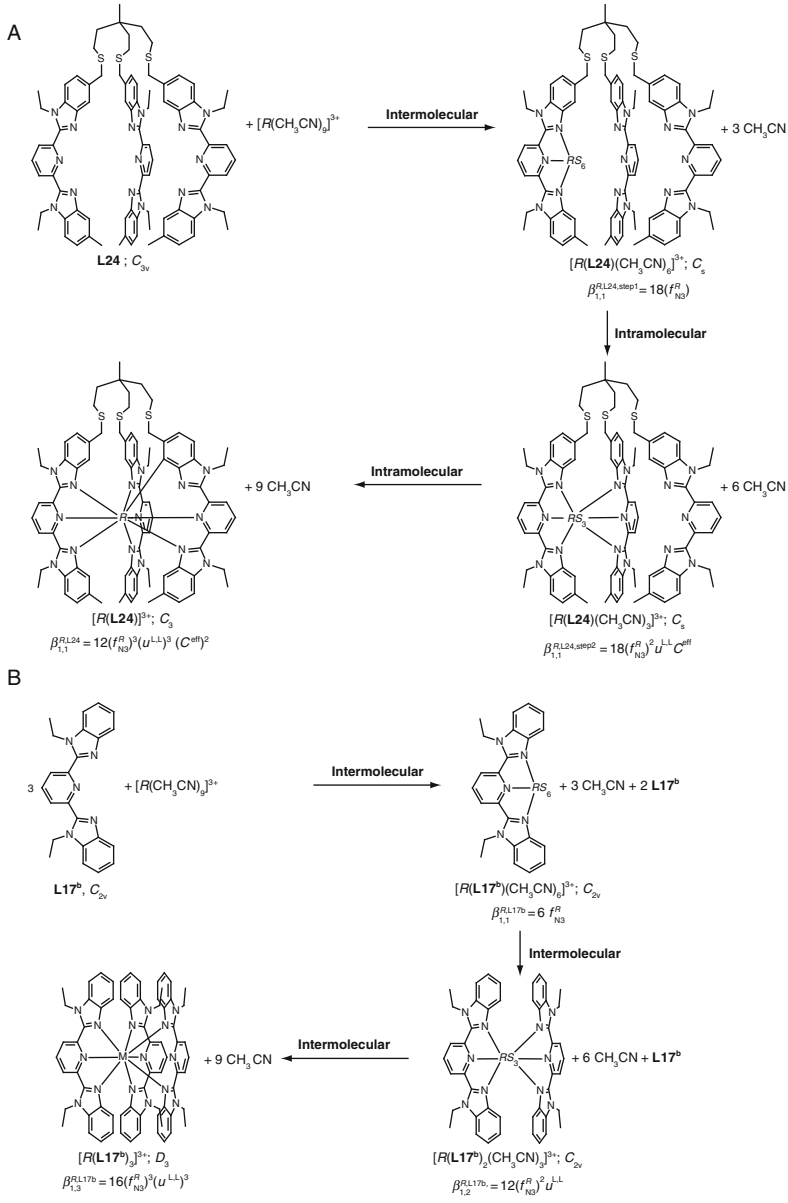

FIGURE 35 Successive complexation processes leading to (A) $[R(\mathbf{L24})]^{3+}$ and (B) $[R(\mathbf{L17^b})_3]^{3+}$. Symmetry point groups and stability constants obtained by the site-binding model are shown (redrawn after Canard et al., 2008).

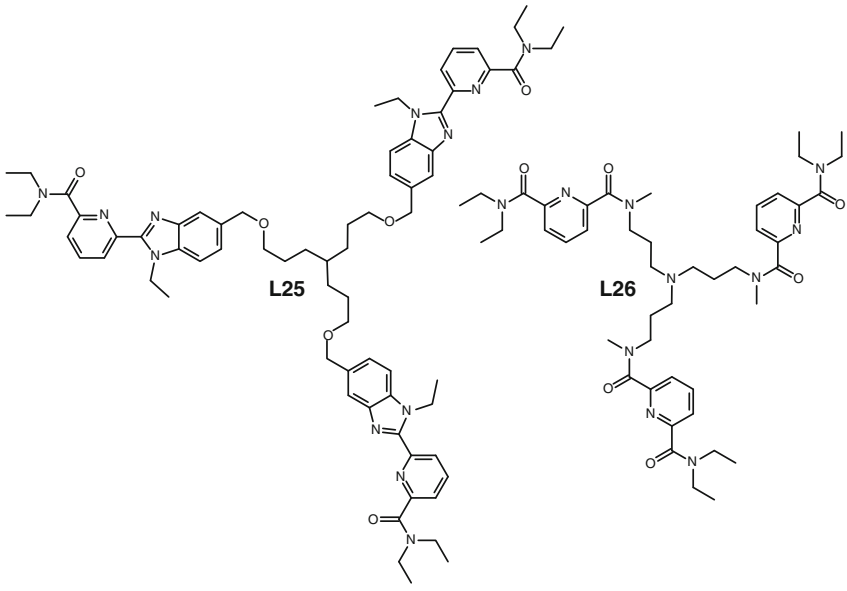

FIGURE 36 Chemical structures of podands **L25** and **L26**.

unsaturated ($n \rightarrow \pi^*$) transitions of ligands displaying large cross sections for one-photon absorption. Alternatively, intraligand charge-transfer states (ILCT, Ali et al., 2008; D'Aléo et al., 2008a,b; Puntus et al., 2007) or ligand-to-metal charge-transfer states (LMCT, Blasse, 1976; Loukova et al., 2007; Puntus et al., 2002) may also collect light. Subsequent intramolecular energy migrations obey *Fermi*'s golden rule modeling resonant energy transfer (Eq. (7)), whereby W_{DA} is the probability of energy transfer, Ω_{DA} is the spectral overlap integral between the absorption spectrum of the acceptor A and the emission spectrum of the donor D, H' is the perturbation operator in the matrix element $\langle DA^*|H'|D^*A\rangle$ (Hendersen and Imbusch, 1989). Depending on the electromagnetic nature of H', a double-electron exchange mechanism (Dexter, 1953) and an electrostatic multipolar (Förster, 1960) mechanism have been proposed and theoretically modeled. Their specific dependences on the distance d separating the donor D from the acceptor A, that is, $e^{-\beta d}$ for double-electron exchange and d^{-6} for dipole–dipolar processes, respectively, often limit *Dexter* mechanism to operate at short distance (typically 30–50 pm) at which orbital overlap is significant, while Förster mechanism may extend over much longer distances (up to 1000 pm). Interestingly, the dipole–quadrupolar mechanism may also be quite effective for short distances

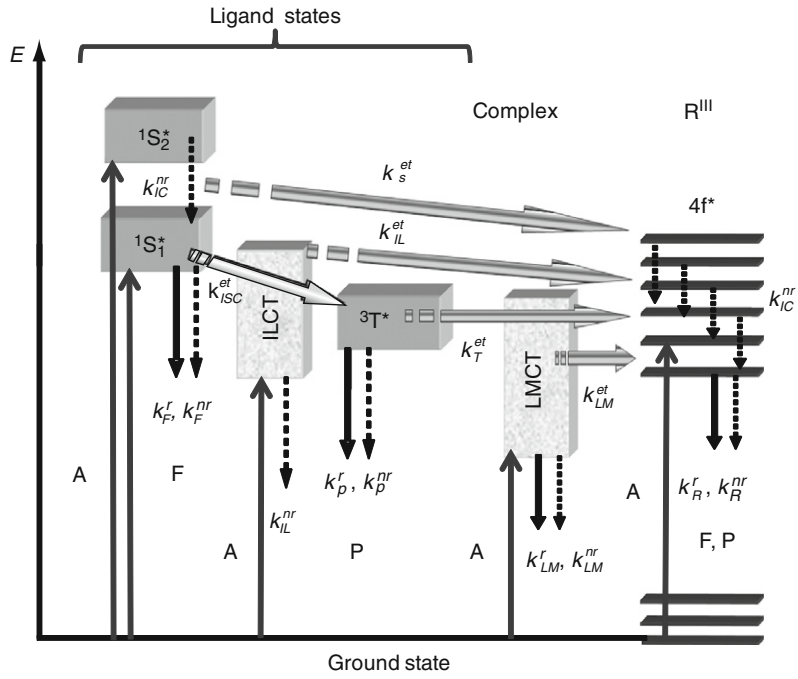

FIGURE 37 Schematic representation of energy absorption, emission, and dissipation (dotted arrows) processes in a lanthanide complex. ^{1}S* or S, singlet state; ^{3}T* or T, triplet state; A, absorption; F, fluorescence; P, phosphorescence; *k*, rate constant; *r*, radiative; *nr*, nonradiative; IC, internal conversion; ISC, intersystem crossing; ILCT (or IL), intraligand charge transfer; LMCT (or LM), ligand-to-metal charge transfer. Back transfer processes are not drawn for the sake of clarity.

(dependence in d^{-8}); in fact depending on Ω_{DA} it may be as efficient as the dipole–dipole mechanism up to distances as long as 300 pm (Malta, 1997).

$$W_{DA} = (2\pi/\hbar)|\langle DA^*|H'|D^*A\rangle|^2\Omega_{DA} \tag{7}$$

One of the main energy migration paths operating in lanthanide complexes implies spin-allowed and *Laporte*-allowed ligand-centered absorptions followed by intersystem crossing ($^1\pi\pi^* \rightarrow {}^3\pi\pi^*$, k_{ISC}) reaching the long-lived ligand-centered triplet state, from which ligand → metal energy transfer ($\pi\pi^* \rightarrow R^*$, k^{et}) eventually excites metal-centered states (Figure 37). Spontaneous metal-centered radiative emission (k_R^r) completes the light-conversion process. It is to be stressed that although important, this energy transfer path is by far not the only operative one. As early as 1969,

Kleinerman who studied over 600 lanthanide chelates pointed out that the excited ligand singlet state can contribute to the transfer and may even be the privileged donor state, depending on the rate constants of the various intervening processes (Kleinerman, 1969). In fact a workable model of the entire energy-converting mechanism has shown that as many as 20–30 rate constants (including those describing back transfers) may be implied (de Sá et al., 2000; Gonçalves e Silva et al., 2002). Efficient transfer from ILCT and LMCT states, as well as from ^{3}MLCT states localized on a transition-metal containing ligand (Chen et al., 2008) is also well documented. All these potential energy funnels render difficult the modeling of the energy transfer and, consequently, the a priori precise design of highly luminescent lanthanide-containing edifices.

Energy transfer from the ligand, evidenced for the first time in 1942 by Weissman (1942), is often referred to as the antenna effect (Sabbatini et al., 1996) or luminescence sensitization (Bünzli and Piguet, 2005). The overall quantum yield Q_L^R of the metal luminescence upon ligand excitation can be separated into three components characterizing successively: (1) the rate constant k_{pop}^D ($=k_{ISC}^{et}$ for triplet states) for the population of the donor state (^{3}T, ILCT, LMCT, ^{3}MLCT, possibly a 4f5d state; see Burdick and Reid, 2007 for instance), (2) the efficiency of the energy transfer (η_{et}) onto the R^{III} ion, and (3) the metal-centered emission characterized by the intrinsic quantum yield Q_R^R, that is, the quantum yield of the metal luminescence upon direct f–f excitation (Eq. (8); Beeby et al., 1999; Bünzli and Piguet, 2005; Parker et al., 2002; Werts et al., 2002). For specific lanthanides possessing low-lying charge-transfer excited states (e.g., Eu^{III}, $E^0(Eu^{III}/Eu^{II}) = -0.34$ V vs NHE; Cotton, 2006), or for complexes having low-lying ILCT states, the energy transfer process is further affected by additional nonradiative quenching arising from back energy transfer onto the ligand (not shown on Figure 37). Since in this case the accepting states are quite broad, minute differences in their energy may lead to large differences in the spectral overlap and therefore in the overall quantum yield (see Chauvin et al., 2007, 2008 for a discussion of this phenomenon with respect to Tb^{III} luminescence).

$$Q_L^R = \eta_{pop}^D \eta_{et} Q_R^R = \eta_{sens} Q_R^R \tag{8}$$

where η_{pop}^D is the efficiency with which the donor state is populated, η_{et} is the yield of the energy transfer to the lanthanide ion, and η_{sens} is the efficacy of the luminescence sensitization by the ligand.

$$\eta_{sens} = \frac{k_t}{k_D^r + k_D^{nr} + k_{CT}^R + k_t} \tag{9}$$

where k_D^r and k_D^{nr} are rate constants for the radiative and nonradiative deactivation of the donor state, k_{CT}^R rate constant for the quenching by the charge-transfer state, and k_t the rate constant of the energy transfer from the donor state D to the lanthanide ion R^{III}.

While the overall quantum yield is relatively easy to measure, Q_R^R, which is needed to evaluate η_{sens}, is quite difficult to determine experimentally in view of the weakness of the f–f transitions. One way to estimate it is by means of Eq. (10) where τ_{obs} is the actual lifetime of the emitting excited state and τ_{rad} is its natural radiative lifetime which obey *Einstein* relation for spontaneous emission probability between two states with quantum numbers J and J', $A(\Psi_J, \Psi_{J'})$ (Görller-Walrand and Binnemans, 1998):

$$Q_R^R = \frac{\tau_{obs}}{\tau_{rad}} \tag{10}$$

$$A(\Psi_J, \Psi'_{J'}) = \frac{1}{\tau_{rad}} = \frac{64\pi^4\tilde{\nu}^3}{3h(2J+1)}\left[\frac{n(n^2+2)^2}{9}D_{ED} + n^3 D_{MD}\right] \tag{11}$$

where $\tilde{\nu}$ is the average energy of the transition in cm^{-1}, h the Planck's constant, and $(2J+1)$ the degeneracy of the initial (emitting) state; the expressions involving the refractive index n are known as the Lorentz local field corrections and D_{ED} and D_{MD} are the electric and magnetic dipole oscillator strengths, respectively (in $esu^2\,cm^2$). The quantity D_{ED} is expressed by Eq. (11) within the frame of the Judd–Ofelt theory (Walsh, 2006):

$$D_{ED} = e^2 \sum_{\lambda=2,4,6} \Omega_\lambda |\langle \Psi || U^\lambda || \Psi' \rangle|^2 \tag{12}$$

in which Ω_λ ($\lambda = 2,4,6$) in cm^2 are phenomenological intensity parameters, e the electron electric charge in coulomb, and $\langle \Psi || U^\lambda || \Psi' \rangle$ are tabulated doubly reduced matrix elements (Nielson and Koster, 1963). The magnetic dipole strength is given by

$$D_{MD} = \left(\frac{eh}{4\pi m_e c}\right)^2 |\langle \Psi || \vec{L} + 2\vec{S} || \Psi' \rangle|^2 \tag{13}$$

where m_e is the electron mass and $\vec{L}$ and $\vec{S}$ are the orbital and spin angular momentum, respectively. The dipole strengths can be determined experimentally from the absorption spectrum (Walsh, 2006):

$$D(\exp) = \frac{1}{108.9cd\tilde{\nu}_{mean}} \int A(\tilde{\nu}) d\tilde{\nu} \tag{14a}$$

with

$$\tilde{\nu}_{\text{mean}} = \frac{\int \tilde{\nu} \cdot A(\tilde{\nu}) \mathrm{d}\tilde{\nu}}{\int A(\tilde{\nu}) \mathrm{d}\tilde{\nu}} \tag{14b}$$

In the case of Eu^{III} and in view of the special property of the purely magnetic dipole transition $^5D_0 \rightarrow {}^7F_1$, a simplified procedure is at hand whereby

$$A(\Psi_J, \Psi'_{J'}) = \frac{1}{\tau_{\text{rad}}} = A_{\text{MD},0} n^3 \left(\frac{I_{\text{tot}}}{I_{\text{MD}}} \right) \tag{15}$$

with $A_{\text{MD},0}$ being a constant equal to 14.65 s^{-1} and $(I_{\text{tot}}/I_{\text{MD}})$ the ratio of the total integrated emission from the Eu($^5D_0$) level to the integrated intensity of the MD transition $^5D_0 \rightarrow {}^7F_1$. In other cases, authors often rely on published values of τ_{rad} with the wrong hypothesis that the radiative lifetime is a constant for a given emitting level and does not depend on the metal ion surroundings (for a discussion see for instance Comby and Bünzli, 2007).

Since each of the nonradiative rate constants affecting the total quantum yield Q_L^R depend on the localization of the excited states and on the precise transfer mechanism, the correlation between this quantum yield and chemical and structural parameters at the molecular level is complicated and its rational programming is usually not available. On the other hand, Q_R^R depends on less parameters and is easier to rationalize because (i) the main contributions to k_R^{nr} arise from the interactions of the central lanthanide with surrounding high-frequency oscillators (Bünzli, 1989; Bünzli and Piguet, 2005) and (ii) the main contribution to k_R^{r} is usually dominated by forced electric dipole (hypersensitive) transitions, which result from the mixing of levels of opposite parity produced by the crystal field at noncentrosymmetric sites and from additional minute mixing of the ligand-centered and metal-centered wave functions in coordination complexes (Reisfeld and Jørgensen, 1977).

2.5.2 Mononuclear triple-helical precursors

For the triple-helical precursors $[Eu(\mathbf{L17})_3]^{3+}$, detailed photophysical studies show that the sensitization process is particularly inefficient (Table 4; Petoud et al., 1999; Piguet et al., 1993b, 1995b). This can be assigned to the formation of a pseudocentrosymmetric tricapped-trigonal prismatic arrangement of nine heterocyclic nitrogen donor atoms which limits k_R^{r} ($Q[Eu(\mathbf{L17^a})_3]^{3+}) = 0.3 \times Q([Eu(\mathbf{L17^a})(NO_3)_3]^{3+})$ by favoring the

TABLE 4 Photophysical properties of triple-helical complexes $[R(\mathbf{L}k)_3]^{3+}$ (R = Eu, Tb; k = 17–19, see Figures 26–28) in acetonitrile

Ligand	Metal	E($^1\pi\pi^*$) (cm^{-1})[a]	E($^3\pi\pi^*$) (cm^{-1})[b]	Q_L^R (%)	τ_{obs} (ms)[c]	E(Eu($^5D_0$)) (cm^{-1})	References
Terpyridine	Eu	26,670	21,230	32	2.31 (295 K)	–	Comby (2008)
Terpyridine	Tb	26,670	21,230	35	1.20 (295 K)	–	Comby (2008)
L17[a]	Eu	27,700	20,900	2×10^{-3} [d]	1.85 (77 K)	17,236 (77 K)	Piguet et al. (1993c)
L17[a]	Tb	27,700	20,900	–	1.46 (77 K)	–	Piguet et al. (1993c)
L17[b]	Eu	27,800	20,900	2×10^{-2} [d]	1.75 (77 K)	17,235 (77 K)	Piguet et al. (1995a,b,c,d,e)
L17[b]	Tb	27,700	20,900	–	1.95 (77 K)	–	Piguet et al. (1995a,b,c,d,e)
L17[c]	Eu	27,320	–	1.5×10^{-2} [d]		–	Piguet et al. (1995a,b,c,d,e)
L17[e]	Eu	27,700	–	7×10^{-2} [d]		–	Piguet et al. (1995a,b,c,d,e)
L17[f]	Eu	26,970	–	2×10^{-2} [d]		17,219 (77 K)	Piguet et al. (1995a,b,c,d,e)
L17[f]	Tb	26,970	20,900	–	1.14 (77 K)	–	Piguet et al. (1995a,b,c,d,e)
L17[l]	Eu	26,255	19,750	5×10^{-3}	0.85 (13 K)	17,258 (295 K)	Muller et al. (2002b)
L17[l]	Tb	27,175	21,050	–	0.38 (13 K)	–	Muller et al. (2002b)
L18[a]	Eu	35,840	23,600	0.2[d]	1.78 (10 K)	17,216 (10 K)	Renaud et al. (1997a)
L18[a]	Tb	35,830	23,600	26[d]	1.85 (295 K)	–	Renaud et al. (1997a)
L18[c]	Eu	35,850	23,200	0.2	1.45 (13 K)	17,211 (13 K)	Muller et al. (2001b)
L18[a]	Tb	35,630	23,200	1.2	0.92 (13 K)	–	Muller et al. (2001b)
L19[b]	Eu	29,410	20,660	5×10^{-2}	1.86 (77 K)	–	Le Borgne et al. (2004)
L19[b]	Tb	29,410	20,660	–	1.22 (77 K)	–	Le Borgne et al. (2004)

[a] Values obtained from absorption spectra in solution (293 K).
[b] Values obtained from emission spectra (0-phonon transition, 77 K).
[c] Metal-centered lifetime.
[d] Quantum yields have been recalculated by using the most recent values reported for the $[R(\text{terpyridine})_3]^{3+}$ internal references (Comby, 2008).

presence of a low-lying LMCT state (Petoud et al., 1999). Indeed, Eu(II) is stabilized by the heterocyclic nitrogen atoms, which puts the LMCT state close in energy to the **L17**-centered singlet state, thus allowing efficient $^1\pi\pi^* \rightarrow$ LMCT energy transfer (Eq. (7)) and maximizing k_{CT}^R (Eq. (9); Gonçalves e Silva et al., 2000; Petoud et al., 1999). For $[Tb(\mathbf{L17})_3]^{3+}$, the energy gap between the ligand-centered $^3\pi\pi^*$ feeding level (21,050 cm^{-1}) and the accepting metal-centered $Tb(^4D_4)$ level (20,490 cm^{-1}) is too small to ensure efficient and irreversible energy funneling (Steemers et al., 1995). Consequently, thermally activated $Tb(^4D_4) \rightarrow \mathbf{L17}(^3\pi\pi^*)$ back transfer becomes an efficient deexcitation pathway at room temperature, which drastically reduces Q_{Tb}. The replacement of the aromatic benzimidazole side arms in **L17** with carboxamide groups in **L18** significantly increases the energy of both ligand-centered $^1\pi\pi^3$ and $^3\pi\pi^*$ excited states in $[R(\mathbf{L18})_3]^{3+}$ (Table 4). Consequently, Tb^{III}-centered luminescence is detected at room temperature with an encouraging quantum yield of 26% for $[Tb(\mathbf{L18^a})_3]^{3+}$ in acetonitrile (Renaud et al., 1997a). Although the absolute values are less impressive for the related Eu^{III} complexes, the replacement of **L17** with **L18** produces triple-helical red emitters $[Eu(\mathbf{L18})_3]^{3+}$, the global quantum yields of which are larger by two to three orders of magnitude because the low-lying LMCT states have been pushed higher in energy (Table 4). Interestingly, all triple-helical complexes $[R(\mathbf{L17})_3]^{3+}$ and $[R(\mathbf{L18})_3]^{3+}$ (R = Eu, Tb) display metal-centered excited lifetimes characteristics of the absence of high-energy oscillators in the first coordination sphere, which demonstrates that the wrapping of the three ligand strands efficiently protects the metallic sites from external interactions (e.g., solvent molecules). As expected, the connection of three tridentate dicarboxamidopyridine tridentate units analogous to $\mathbf{L18^a}$, in podand **L20**, has minor effect on the quantum yields (Table 5; Renaud et al., 1999), but a slight improvement for the Eu-centered emission is evidenced when the terminal carboxamide groups are replaced with carboxylates in [Eu(**L21**-3H)] (Senegas et al., 2003). Finally, the facial organization of three 2-benzimidazole-6-carboxamidopyridine units (NNO donors) in $[R(\mathbf{L22})]^{3+}$ and $[R(\mathbf{L23})]^{3+}$ gives the best light converters of the series (R = Eu, Tb; Table 5).

Some thorough investigations of the energy migration processes according to Eq. (8) for [Eu(**L21**-3H)] in water shows that $Q_L^{Eu} = 4\%$ can be indeed separated into $Q_{Eu}^{Eu} = 31\%$ and $\eta_{sens} = 13\%$ (Senegas et al., 2003), which suggests that the moderate quantum yield originates from both limited intrinsic metal-centered quantum yield and sensitization processes. However, the same investigations performed in acetonitrile for $[Eu(\mathbf{L20} + H)]^{4+}$ ($Q_L^{Eu} = 0.4\%$, $Q_{Eu}^{Eu} = 55\%$, and $\eta_{sens} = 0.7\%$) and for $[Eu(\mathbf{L20})]^{3+}$ ($Q_L^{Eu} = 0.3\%$, $Q_{Eu}^{Eu} = 50\%$, and $\eta_{sens} = 0.6\%$) unambiguously establish that the sensitization process is by far the limiting factor for efficient light conversion in triple-helical complexes with N_3O_6

TABLE 5 Photophysical properties of triple-helical podates $[R(\mathbf{L}k)]^{3+}$ (R = Eu, Tb; k = 20–23, see Figures 32 and 33)

Ligand	Metal	Solvent	E($^1\pi\pi^*$) (cm^{-1})[a]	E($^3\pi\pi^*$) (cm^{-1})[b]	Q_L^R (%)	τ_{obs} (ms)[c]	E(Eu($^5D_0$)) (cm^{-1})	References
L20	Eu	CH_3CN	35,210	[d]	0.3[e]	1.41 (10 K)	17,213 (10 K)	Renaud et al. (1999)
L20	Tb	CH_3CN	35,210	[d]	4[e]	1.11 (295 K)	–	Renaud et al. (1999)
[L20 + H]$^+$	Eu	CH_3CN	35,090	[d]	0.4[e]	1.81 (10 K)	17,215 (10 K)	Renaud et al. (1999)
[L20 + H]$^+$	Tb	CH_3CN	35,090	[d]	25[e]	1.58 (295 K)	–	Renaud et al. (1999)
[L21-3H]$^{3-}$	Eu	H_2O	35,710	23,000	4[e]	1.45 (10 K)	17,209 (10 K)	Senegas et al. (2003)
[L21-3H]$^{3-}$	Tb	H_2O	35,710	23,000	7[e]	1.06 (10 K)	–	Senegas et al. (2003)
L22	Eu	CH_3CN	30,300	20,280	10[e]	2.58 (295 K)	–	Koeller et al. (2003a)
L22	Tb	CH_3CN	30,210	20,370	10[e]	0.02 (295 K)	–	Koeller et al. (2003a)
L23	Eu	CH_3CN	30,120	20,410	14[e]	2.87 (295 K)	–	Koeller et al. (2003b)
L23	Tb	CH_3CN	30,210	20,410	11[e]	0.02 (295 K)	–	Koeller et al. (2003b)

[a] Values obtained from absorption spectra in solution (293 K).
[b] Values obtained from emission spectra (0-phonon transition, 77 K).
[c] Lifetime of the metal excited state.
[d] Too weak to be detected in the emission spectra of the analogous Gd^{III} complexes.
[e] Quantum yields have been recalculated by using the most recent values reported for the $[R(terpyridine)_3]^{3+}$ internal references (Comby, 2008).

coordination spheres (Renaud et al., 1999). Although no intrinsic metal-centered quantum yields are available for the N_6O_3 coordination spheres in $[Eu(\mathbf{L22})]^{3+}$ and $[Eu(\mathbf{L23})]^{3+}$, we can reasonably assume that $Q_{Eu}^{Eu} \approx 50\%$, which translates into $\eta_{sens} \approx 20$–30%, thus making the organization of three helical NNO binding units around Eu^{III} the best candidate for producing luminescent triple-stranded helicates.

2.5.3 Water-soluble complexes derived from dipicolinic acid

Europium and terbium tris(dipicolinates) are known to be highly luminescent, with overall quantum yields of 24% and 22%, respectively, and lifetimes of 1.67 and 1.43 ms, respectively. This property is taken advantage of in simple luminescent methods for the determination of nanomolar concentrations of lanthanides (Barela and Sherry, 1976). In fact, both the quantum yield and lifetime heavily depend on the concentration of the chelates and the pH since the latter governs the speciation in solution (Figure 38). Three or six water molecules are coordinated onto the metal ion in the lower bis and monospecies, respectively. As a consequence, the corresponding quantum yields and lifetimes are drastically reduced with respect to the tris-species. For instance, a quantum yield of only 4.5% has been determined for $[Eu(dpa)_2]^-$ (Aebischer et al., 2009) while $\tau(^5D_0) = 0.35$ ms only for this complex (Chauvin et al., 2004).

The overall shape of the luminescence spectra of the Eu^{III} complex is compatible with a metal ion lying in a coordination site with a pseudo-tricapped-trigonal prismatic geometry. The magnetic dipole transition $^5D_0 \rightarrow {}^7F_1$ is split into two main components ($A_1 \rightarrow A_2$ and $A_1 \rightarrow E$ in trigonal symmetry), the $^5D_0 \rightarrow {}^7F_2$ transition is dominated by two strong components and at least five peaks are detected for the $^5D_0 \rightarrow {}^7F_4$ transition. This pattern is in agreement with a geometry derived from D_3-symmetry around the metal ion. Modulation of the photophysical properties can be achieved by adding a substituent X in the pyridine 4-position. For instance, Lamture et al. (1995) have shown that the relative efficiency for energy transfer (η_{sens}) in $[Tb(\mathbf{L15^{f-j}})_3]^{3-}$ species (see Figure 23) varies in the order $X = NH_2 > OH > NHCOCH_3 > Cl > H \approx Br$. That bromine substitution does not enhance the energy transfer efficiency through the heavy atom effect points to the singlet state playing a decisive role in the sensitization process.

These simple dipicolinates cannot, however, be coupled to biological molecules. Therefore derivatives in which the pyridine ring is decorated with substituted trioxyethylene pendants have been synthesized (Figure 24). In the resulting chelates, the metal-ion environment does not appear to undergo substantial changes, in that both the relative intensities of the $^5D_0 \rightarrow {}^7F_J$ transitions and the energies of the ligand-field sublevels determined for the $[Eu(\mathbf{L15^j})_3]^{3-}$ complexes are similar to those found for $[Eu(dpa)_3]^{3-}$. In addition, the lifetimes of the $Eu(^5D_0)$ level

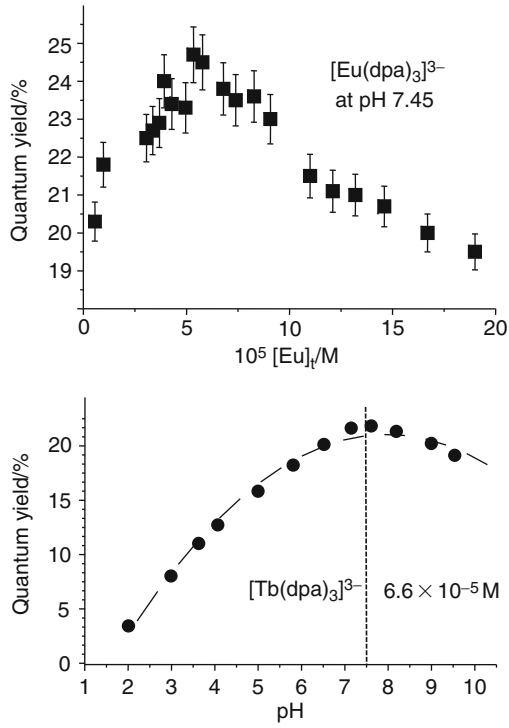

FIGURE 38 Top: variation of Q_{Eu}^{L} of the tris(dipicolinate) complex versus the metal ion concentration. Bottom: variation of Q_{Tb}^{L} versus pH (redrawn from Chauvin et al., 2004).

measured both in water and in deuterated water (Table 6) essentially translate into a hydration number $q = 0$ when known phenomenological equations are used to estimate it (Bünzli and Piguet, 2005). The overall quantum yields of all the solutions (Table 6) surprisingly show a marked dependence on the nature both of the pendant arm and of the metal ion: (i) the quantum yields of the Eu^{III} chelates range between 12% and 29% while those for Tb^{III} complexes are significantly smaller, ranging between 11% and 18%, and (ii) the sequence is different for both ions, Q_{L}^{Eu} decreasing in the series $[Eu(\mathbf{L}^{\mathbf{NH2}})_3]^{3-} > [Eu(\mathbf{L}^{\mathbf{OMe}})_3]^{3-} > [Eu(\mathbf{L}^{\mathbf{Phta}})_3]^{3-} > [Eu(\mathbf{L}^{\mathbf{OH}})_3]^{3-}$ while this series is $[Tb(\mathbf{L}^{\mathbf{OH}})_3]^{3-} > [Tb(\mathbf{L}^{\mathbf{NH2}})_3]^{3-} > [Tb(\mathbf{L}^{\mathbf{OMe}})_3]^{3-} > [Tb(\mathbf{L}^{\mathbf{Phta}})_3]^{3-}$ for Q_{L}^{Tb}. In fact, the intrinsic quantum yield Q_{Eu}^{Eu} is very similar for all chelates with the five dipicolinate ligands, within experimental errors, ranging between 36% and 42%, pointing to the substitution not affecting appreciably the deactivation processes within the triple-helical structures. Differences in the overall quantum yields, therefore, essentially arise from differences in the sensitization efficiency η_{sens} provided by the ligands. With respect

TABLE 6 Photophysical properties of triple-helical podates derived from dipicolinate, $[R(\mathbf{L15^x}\text{-}2H)_3]^{3-}$ (R = Eu, Tb; x = s–v, see Figures 23 and 24) in aqueous solution of Tris–HCl 0.1 M at 295 K (Gassner et al., 2008) compared to those of the parent chelates with **L15**[a]

Ligand	R	$E(^3\pi\pi^*)$ (cm^{-1})[a]	$\tau_{obs}(H_2O)$ (ms)[b]	τobs (D_2O) (ms)[b]	Q_L^R (%)[c]	Q_{Eu}^{Eu} (%)	η_{sens}
L15[a]	Eu	[d]	1.67(3)	3.0(1)	24	39	61
	Tb		1.41(1)	2.35(2)	22		
L15[s]	Eu	26,810	1.36(2)	2.23(1)	26.6	38	70
	Tb		1.25(2)	1.69(1)	12.7		
L15*t*	Eu	27,100	1.36(1)	2.15(1)	11.8	36	33
	Tb		0.99(1)	2.04(1)	17.8		
L15[u]	Eu	26,810	1.47(1)	1.95(2)	18.3	42	44
	Tb		1.08(2)	1.95(2)	10.8		
L15[v]	Eu	25,189	1.43(1)	2.20(1)	28.9	40	72
	Tb		1.58(2)	1.91(1)	15.3		

[a] From phosphorescence spectra of the La^{III} complex at 77 K, 0-phonon transition.
[b] Lifetime of the metal excited state.
[c] ±10%.
[d] Too weak to be detected in the emission spectra of the analogous Gd^{III} complexes.

to the parent dipicolinate (61%), **L15**[s] and **L15**[v] are slightly better sensitizers, with $\eta_{sens} \approx 70\%$, while the two other ligands transfer energy much less efficiently with $\eta_{sens} \approx 33$–45%. This points to a remarkable fine-tuning of the photophysical properties of the europium triple-helical chelates by the terminal functional group of the polyoxyethylene substituent, the most luminescent chelate being 2.4-fold as luminescent as the less emissive one. Para substitution with an ether group in the pyridine 4-position usually leads to a large decrease in Q_L^{Eu}, for example, from 24% for the tris(dipicolinate) to 16.1% for a simple OMe group (Gassner et al., 2008) or to 12% for the triple-helical complex with 4-(naphthalen-2-yloxy)-pyridine-2,6-dicarboxylate (Latva et al., 1997; the quantum yield has been recalculated with $Q([Ln(\mathbf{L15^a})_3]^{3-}) = 24\%$ instead of 13% as in the original paper). Therefore, the detrimental effect of ether substitution in the para position of the pyridine moiety is apparently compensated by the presence of a terminal substituent (X) on the polyoxyethylene arm, at least for X = OMe and NH_2 and, less efficiently, for X = Phta, while the alcohol group has no positive effect. On the other hand, the tuning for Tb^{III} chelates is less remarkable, the improvement factor between $[Tb(\mathbf{L15^u})_3]^{3-}$ and $[Tb(\mathbf{L15^t})_3]^{3-}$ being only 1.6-fold.

3. POLYNUCLEAR HOMOMETALLIC 4f HELICATES

The packing of triple-helical mononuclear precursors along the helical axis produces infinite columns, which are sometimes observed during the crystallization processes. For instance, $[Eu(\mathbf{L17^a})_3](ClO_4)_3$ crystallizes in the $R\bar{3}$ space group and forms polynuclear columns of closely packed triple-helical $[Eu(\mathbf{L17^a})_3]^{3+}$ cations (the Eu…Eu distances amount to 8.364(2) and 8.618(2) Å) possessing alternating helicities along the *c* direction (Figure 39; Piguet et al., 1993c).

However, such lucky and uncontrolled crystallization processes are rare, and the programming of polynuclear homometallic triple-stranded helicates normally relies on the connection of several tridentate segments by using adequate spacers (Figure 40). Homotopicity provides C_2-symmetrical segmental ligands, which eventually form D_3-symmetrical helicates upon reaction with R^{III} (Figure 40, left). The introduction of different binding units along the strand, that is, heterotopicity, results in the design of either axially symmetrical (twofold axis) or nonaxial ligands. Upon reaction with R^{III}, the latter axial ligand also gives D_3-symmetrical helicates, although different lanthanide triple-helical building blocks are packed along the helical axis (Figure 40, center). For nonaxial ligands, the complexation process leads to mixtures of HHH (C_3-symmetrical) and HHT (C_1-symmetrical) isomeric helicates (Figure 40, right).

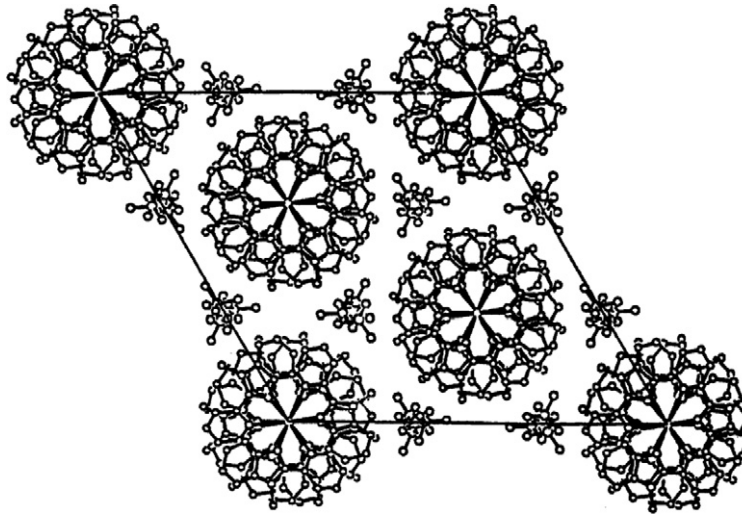

FIGURE 39 View of the unit cell along the *c*-axis in the crystal structure of $[Eu(\mathbf{L17^a})_3](ClO_4)_3$ (reproduced by permission from Piguet et al., 1993c, © American Chemical Society, 1993).

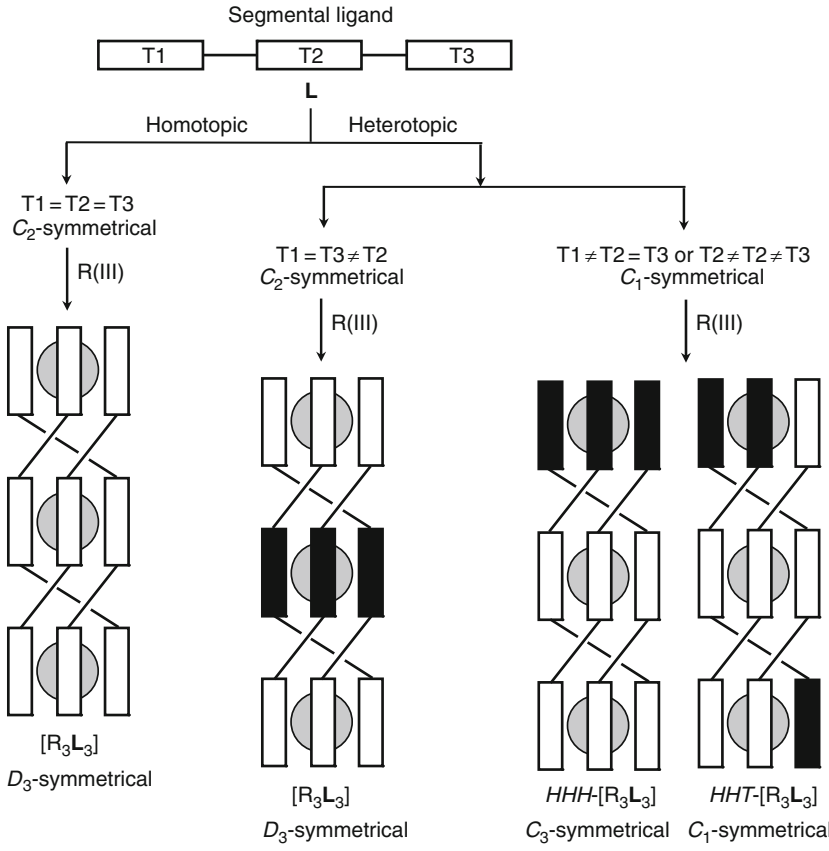

FIGURE 40 Correlations between the symmetry of the segmental multitridentate ligands and the nature of the final lanthanide helicates.

For generalization purpose, we do not consider the existence of symmetry elements of the second kind in the ligand (for instance a mirror plane), because they do not influence the issue of the self-assembly process.

3.1 Designing segmental ligands: Principles and synthetic routes

To minimize synthetic efforts, the design of both axial (i.e., $C_{2(v)}$-symmetrical) and nonaxial (i.e., C_1- or C_s-symmetrical) ligand strands relies on a common strategy, in which the spacer, *S*, plays a crucial role since it must be rigid enough to transmit the helical twist from one binding unit to the other, but flexible enough to allow helication with a minimum of structural constraints. Moreover, *S* must be compatible with its introduction

into homotopic and heterotopic receptors. When using d-block ions, the pronounced stereochemical preferences of these metals may compensate some weaknesses in the spacer design, and a plethora of connectors are then compatible with the formation of helicates (alkyl chains, polyether chains, disubstituted aromatic units; see Albrecht, 2001; Piguet et al., 1997a for extensive reviews), among which we find the diphenylmethane spacer (Hannon et al., 1997; Williams et al., 1991).

For f-block ions, the lack of directional bonding is more restrictive and the diphenylmethane spacer appears to be ideal because of (i) the steric repulsion between the two hydrogen atoms connected at the 2,2′ positions of the phenyl rings, which forces helication, (ii) its easy synthetic access from ortho-nitroamine arene precursors to give 3,3′,4,4′-tetrasubstituted synthon (Figure 41; Piguet et al., 1994), and (iii) its easy connection to tridentate binding units to give symmetrical (i.e., axial, Figures 41–43 and 49), or unsymmetrical (i.e., nonaxial, Figure 48) segmental multitridentate ligands. C_{2v}-symmetrical ligands incorporating NNO and NNN tridentate binding units in **L11** (homotopic: NNN-*S*-NNN), **L13** (homotopic: ONN-*S*-NNO, Figure 41), **L27** (heterotopic: NNN-*S*-NNN-*S*-NNN), **L28** (heterotopic: ONN-*S*-NNN-*S*-NNO, Figure 42), and **L29** (heterotopic: ONN-*S*-NNN-*S*-NNN-*S*-NNO, Figure 43) are obtained according to the standard amidation/reductive cyclization strategy previously developed for mononuclear triple-helical precursors (Figure 18B).

This synthetic path has been slightly modified to develop water-soluble homobimetallic helicates for bioanalyses which bear short polyoxyethylene substituents either on (*N*)1-position of the benzimidazole moiety or on the 4-position of the pyridine rings (Figure 44).

In the former case (Figure 45) the dinitro intermediate is first transformed into a tetra-amino intermediate before condensation with the dipicolinic acid derivative in presence of phosphoric acid at elevated temperature. The polyoxyethylene pendant is then grafted onto the ligand skeleton with the help of a Mitsunobu reaction. The methyl groups are then oxidized via an elaborate three-step route using hydrogen peroxide in acetic acid first, followed by treatment with acetic anhydride and finally conversion of the alcoholic functions by potassium permanganate (Chauvin et al., 2007). The synthesis of ligands derivatized in the 4-position of the pyridine is easier (Figure 46). Here the dinitro derivative is coupled with an asymmetrically derivatized dipicolinic acid bearing one carboxylic acid and one ethyl ester groups. The reaction then follows the same path as the one described in Figure 41, with reduction conducted with iron powder and followed by hydrolysis with sodium hydroxide. When ligands are derivatized both in the pyridine 4-position and in R^4, the synthetic path is accordingly more elaborate. In fact the trioxyethylene substituent is grafted on the dipicolinic acid synthon whereas the other substituent is grafted on the dinitro derivative (Figure 47).

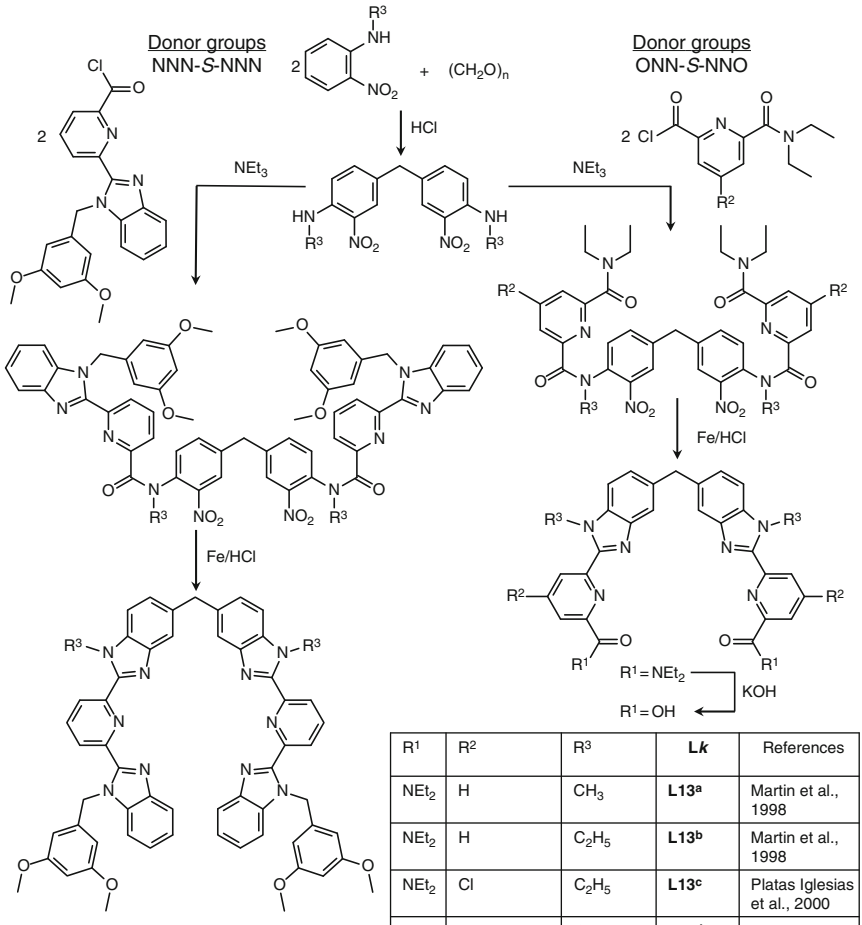

R^1	R^2	R^3	L*k*	References
NEt_2	H	CH_3	**L13[a]**	Martin et al., 1998
NEt_2	H	C_2H_5	**L13[b]**	Martin et al., 1998
NEt_2	Cl	C_2H_5	**L13[c]**	Platas Iglesias et al., 2000
NEt_2	Br	C_2H_5	**L13[d]**	Platas Iglesias et al., 2000
NEt_2	NCS–	C_2H_5	**L13[e]**	Tripier et al., 2002
HO	H	C_2H_5	**H_2L13[f]**	Elhabiri et al., 1999

FIGURE 41 Synthesis of 3,3′,4,4′-tetrasubstituted diphenylmethane spacers and its incorporation into homotopic C_2-symmetrical bis-tridentate segmental ligands (*S* = spacer).

The preparation of nonaxial C_s-symmetrical bis-tridentate ligands **L30** (heterotopic: NNN-*S*-NNO) and **L31** (heterotopic: ONN-*S*-NNO, Figure 48) relies on the disymmetrization of the diphenylmethane spacer as found in the multistep synthesis of tris-tridentate (Figure 42) and tetratridentate (Figure 43) axial receptors. Finally, two alternative homotopic bis-tridentate ligands possessing a central pyridine ring, but no

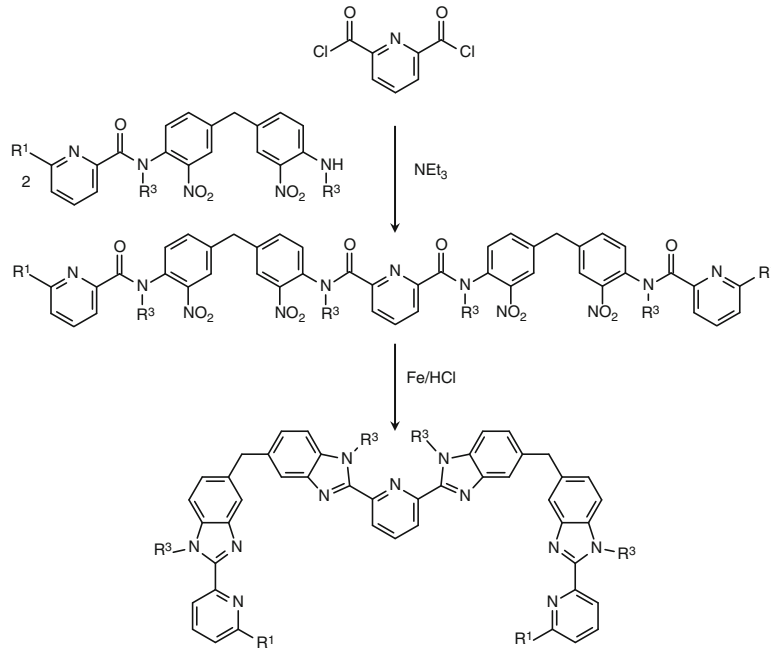

R^1	R^3	**L*k***	References
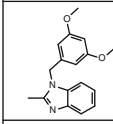	CH_3	**L27**	Piguet et al., 1994
$CONEt_2$	C_2H_5	**L28**	Floquet et al., 2003

FIGURE 42 Synthesis of heterotopic C_2-symmetrical tris-tridentate ligands.

adjacent benzimidazole group have been reported as potential receptors for the formation of binuclear triple-stranded helicates with trivalent lanthanides (ONO-*S*-ONO, **L32**, Lessmann and Horrocks, 2000, Figure 49A and ONN-*S*-NNO, **L33**, Ronson et al., 2007, Figure 49B).

3.2 Solid state and solution structure

Reaction of the homotopic C_{2v}-symmetrical bis-tridentate ligands **L11** or **L13^{a-e}** with $R(ClO_4)_3$ or $R(CF_3SO_3)_3$ gives the expected D_3-symmmetrical triple-stranded helicates $[R_2(\mathbf{L11})_3]^{6+}$ (Piguet et al., 1993a,b,c) and $[R_2(\mathbf{L13^{a-e}})_3]^{6+}$ (Martin et al., 1998; Platas-Iglesias et al., 2000; Tripier et al., 2002). The molecular structures of the cations in the solid state are characterized by a tight wrapping of the three strands about a helical axis

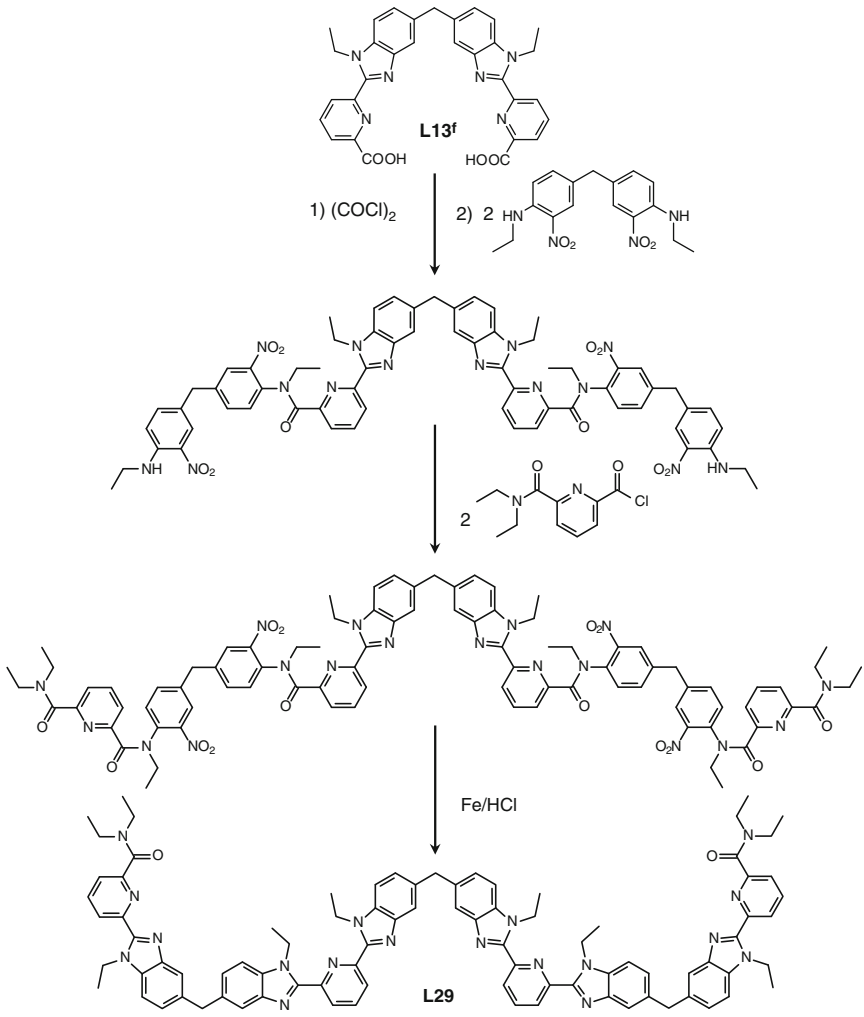

FIGURE 43 Synthesis of a heterotopic C_2-symmetrical tetratridentate ligand (Zeckert et al., 2005).

defined by the two metals, which are separated by ca. 9 Å (Figure 50). Interestingly, the intramolecular $R\ldots R$ separation in $[Eu_2(\mathbf{L11})_2]^{6+}$ (8.8876 Å) is similar to the intermolecular intermetallic distance between two precursors $[Eu(\mathbf{L17^a})_3]^{3+}$ in the packed column found in the crystal structure of the mononuclear complex (8.364(2) and 8.618(2) Å, Figure 39), which suggests, at first sight, that the diphenylmethane spacer ideally transmits helicity, and that the structure of the binuclear helicate can be derived from the packing of two mononuclear building blocks. This naïve view does not resist a more detailed structural analysis, which highlights

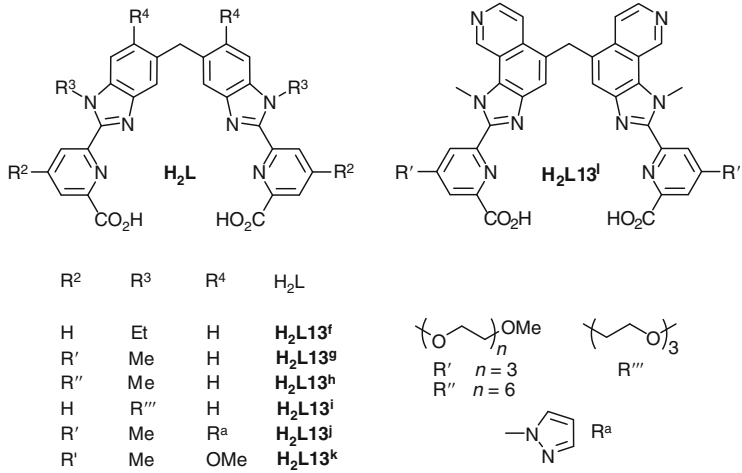

R^2	R^3	R^4	H_2L
H	Et	H	$\mathbf{H_2L13^f}$
R′	Me	H	$\mathbf{H_2L13^g}$
R″	Me	H	$\mathbf{H_2L13^h}$
H	R‴	H	$\mathbf{H_2L13^i}$
R′	Me	R^a	$\mathbf{H_2L13^j}$
R'	Me	OMe	$\mathbf{H_2L13^k}$

FIGURE 44 Ditopic bis-tridentate C_2-symmetrical ligands used for the self-assembly of bimetallic lanthanide luminescent probes.

two crucial differences. (1) The same screw direction of the helical twist is maintained around both metal ions in the binuclear helicate, thus leading to a discrete palindromic regular helix, while the screw direction systematically inverts along columns of packed mononuclear precursors, thus producing infinite palindromic amphiverse helices. (2) The helical pitch P = linear progression per complete turn of the helix in mononuclear complexes amounts to 9.28 Å for $[Eu(\mathbf{L17^a})_3]^{3+}$ (total rotation = 0.75 turn) and 9.12 Å for $[Eu(\mathbf{L18^a})_3]^{3+}$ (total rotation = 0.4 turn), which show much tighter wrapping of the strands compared to the average pitches in the binuclear helicates $[Eu_2(\mathbf{L11})_3]^{6+}$ (P = 13.9 Å, total rotation = 1.21 turn, Figure 50A) and $[Tb_2(\mathbf{L13^b})_3]^{6+}$ (P = 14.7 Å, total rotation = 0.81 turn, Figure 50B).

Calculation of local pitches for each helical portion along the threefold axis indeed points to P_{local} = 10.5 Å for the EuN_9 coordination spheres in $[Eu_2(\mathbf{L11})_3]^{6+}$ and P_{local} = 9.5 Å for the EuN_6O_3 coordination spheres in $[Tb_2(\mathbf{L13^b})_3]^{6+}$ in agreement with similar helical structures found in the mononuclear precursors. However, P_{local} = 17–18 Å observed within the spacer domain unambiguously demonstrates a severe relaxation of the helical wrapping in the latter intermetallic portion (Floquet et al., 2003). Closely related geometrical parameters are found in the extended D_3-symmetrical trinuclear $[R_3(\mathbf{L28})_3]^{9+}$ (Floquet et al., 2003) and tetranuclear $[R_4(\mathbf{L29})_3]^{12+}$ (Zeckert et al., 2005) triple-stranded helicates of nanometric dimensions (Figure 51).

Because of the very limited degrees of freedom in the rigid diphenylmethane spacers (i.e., rotations about the two single C_{arom}–C_{alkyl} bonds),

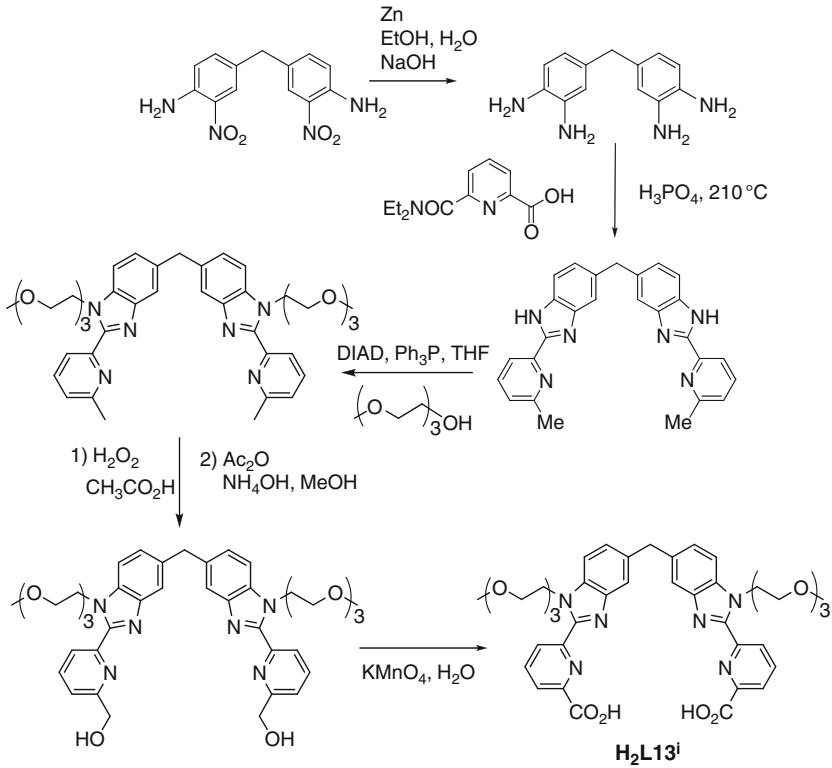

FIGURE 45 Synthesis of a dicarboxylic bis-tridentate receptor substituted in the (*N*)1-position of the benzimidazole moiety for the self-assembly of water-soluble helicates [Ln_2L_3] (redrawn after Chauvin et al., 2007).

the average intermetallic *R*. . .*R* distance of 9 Å combined with a pitch of 14 Å found in the initial series of D_3-symmetrical cationic polynuclear lanthanide helicates are maintained in the neutral analogues [R_2(**L13**$^{\mathbf{f-h}}$-2H)$_3$] (Elhabiri et al., 1999) and in the C_3-symmetrical complexes HHH-[R_2(**L30**$^{\mathbf{a,c,d}}$)$_3$]$^{6+}$ (André et al., 2004; Jensen et al., 2006, 2007, 2008) obtained with heterotopic bis-tridentate C_s-symmetrical ligands (Figure 52).

However, it is inadequate to believe that any mixture of bis-tridentate ligands with R^{III} will produce triple-stranded helicates. We already mentioned in the introduction how some competing counter-ions or solvent molecules may prevent the fixation of the third strand, thus leading to unsaturated complexes (Section 1.3, Figure 13B). A second illustrative example is shown in Figure 53, whereby the use of a 1–4-disubstituted phenyl spacer in **L33**$^{\mathbf{a}}$ makes the output of the assembly process extremely sensitive to the stoichiometric *R*:**L33**$^{\mathbf{a}}$ ratio (Ronson et al., 2007).

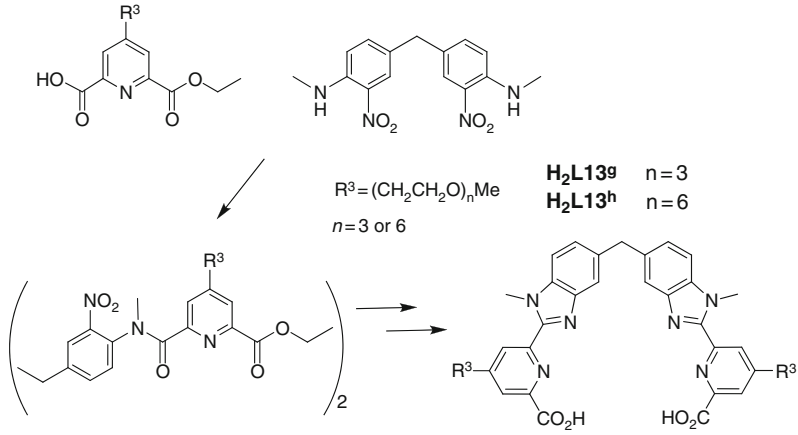

FIGURE 46 Synthesis of dicarboxylic bis-tridentate receptor substituted in R^2 (see Figure 44) for the self-assembly of water-soluble helicates $[Ln_2L_3]$ (Chauvin et al., 2008; Deiters et al., 2008).

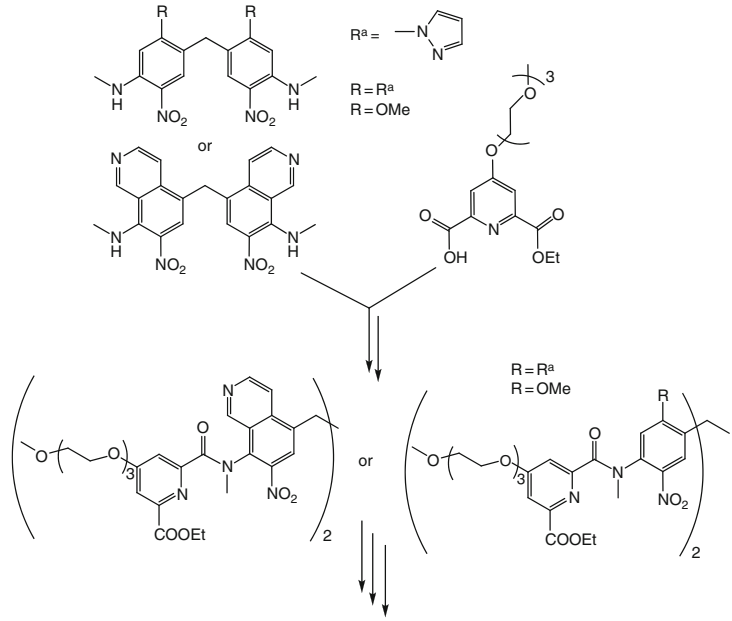

H_2L13^j, H_2L13^k, H_2L13^l

FIGURE 47 Synthesis of dicarboxylic bis-tridentate receptor substituted in R^2 and R^4 (see Figure 44) for the self-assembly of water-soluble helicates $[Ln_2L_3]$ (Deiters et al., 2009).

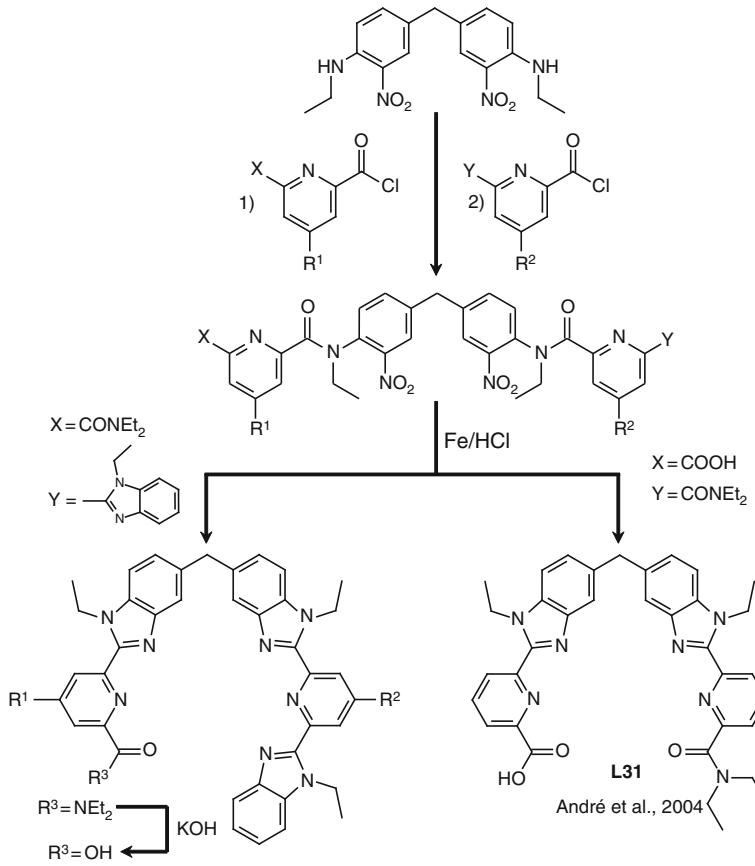

R1	R2	R3	L*k*	References
H	H	NEt_2	**L30**[a]	André et al., 2004
NEt_2	H	NEt_2	**L30**[b]	Jensen et al., 2006
Cl	H	NEt_2	**L30**[c]	Jensen et al., 2006
H	NEt_2	NEt_2	**L30**[d]	Jensen et al., 2008
H	Cl	NEt_2	**L30**[e]	Jensen et al., 2008
H	H	HO	**L30**[f]	André et al., 2004

FIGURE 48 Synthesis of heterotopic C_s-symmetrical bis-tridentate ligands.

Detailed solution structures have been obtained thanks to the analysis of the paramagnetic NMR lanthanide-induced relaxation and chemical shifts (Piguet and Geraldes, 2003, see Section 3.4) combined with high-resolution emission spectra recorded for the Eu^{III} helicates (Bünzli and Piguet, 2005; see Section 3.5). In all cases, the crystal structures represent

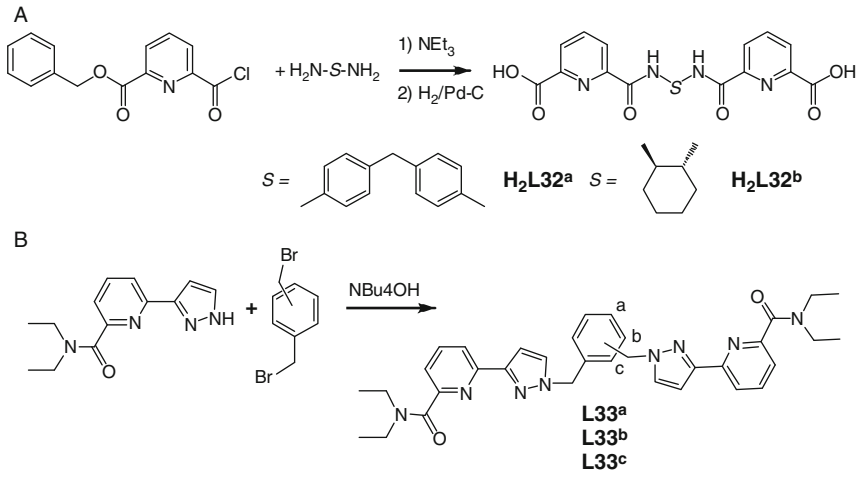

FIGURE 49 Synthesis of C_2-symmetrical bis-tridentate homotopic ligands with various spacers: (A) ONO-*S*-ONO donor groups (Lessmann and Horrocks, 2000) and (B) ONN-*S*-NNO donor groups (Ronson et al., 2007).

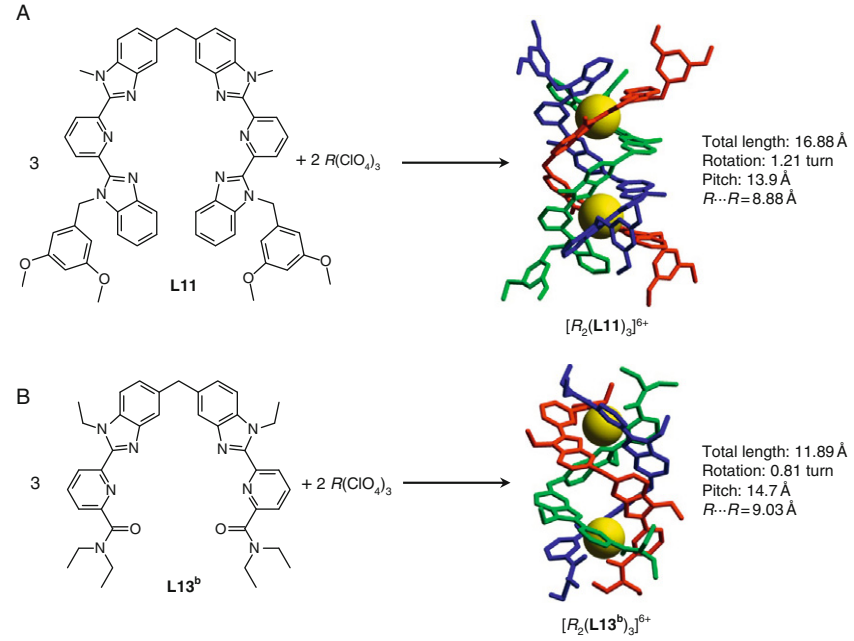

FIGURE 50 Formation of binuclear triple-stranded helicates with neutral bis-tridentate homotopic C_{2v}-symmetrical ligands: (A) NNN-*S*-NNN and (B) ONN-*S*-NNO. The structures of the complexes correspond to the crystal structures of $[Eu_2(\mathbf{L11})_3]^{6+}$ and $[Tb_2(\mathbf{L13^b})_3]^{6+}$ (redrawn after Martin et al., 1998; Piguet et al., 1993a,b,c.

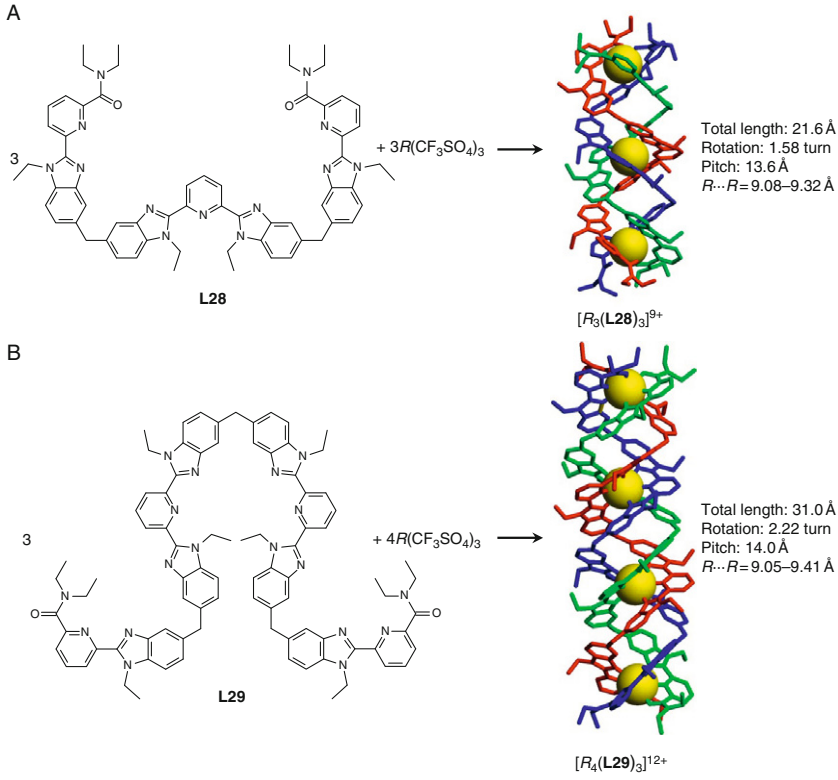

FIGURE 51 Formation of (A) trinuclear and (B) tetranuclear triple-stranded helicates with neutral heterotopic C_{2v}-symmetrical ligands. The structures of the complexes correspond to the crystal structures of $[Eu_3(\mathbf{L28})_3]^{9+}$ and $[Eu_4(\mathbf{L29})_3]^{12+}$ (redrawn after Floquet et al., 2003; Zeckert et al., 2005).

satisfying models for the solution structures. In several cases, such as $[R_2(\mathbf{L13^{c-e}})_3]^{6+}$ (Platas-Iglesias et al., 2000; Tripier et al., 2002), $[R_2(\mathbf{L13^{h}})_3]^{6+}$ (Chauvin et al., 2008), and $[R_2(\mathbf{L32})_3]^{6+}$ (Lessmann and Horrocks, 2000), no crystal structures are available, but the analysis of the UV-vis, NMR, ES-MS, and photophysical data are convincing enough to establish the solid-state and solution structures of these binuclear triple-stranded helicates.

On the contrary, dissolution of the C_3-symmetrical helicates HHH-$[R_2(\mathbf{L30})_3]^{6+}$ in acetonitrile gives mixtures of the HHH (C_3-symmetry) and HHT (C_1-symmetry) isomers (André et al., 2004; Figure 54). Systematic investigation of the enthalpic ($\Delta H_{iso}^{R,L30}$) and entropic ($\Delta S_{iso}^{R,L30}$) contributions to equilibrium (16) yields a scattered diagram, in which one can easily recognize enthalpy/entropy compensations for each studied C_s-symmetrical ligand (Jensen et al., 2007; Table 7; Figure 55).

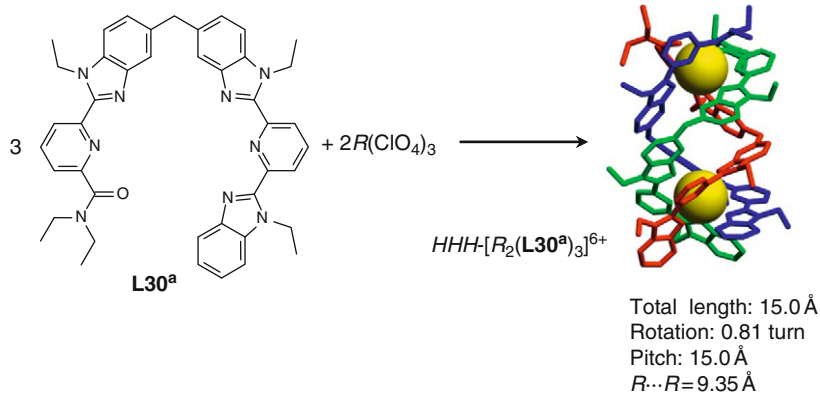

FIGURE 52 Formation of binuclear triple-stranded helicates with a neutral bis-tridentate heterotopic C_s-symmetrical ligand. The structure of the complex corresponds to the crystal structure of $[Eu_2(\mathbf{L30^a})_3]^{6+}$ (redrawn after André et al., 2004).

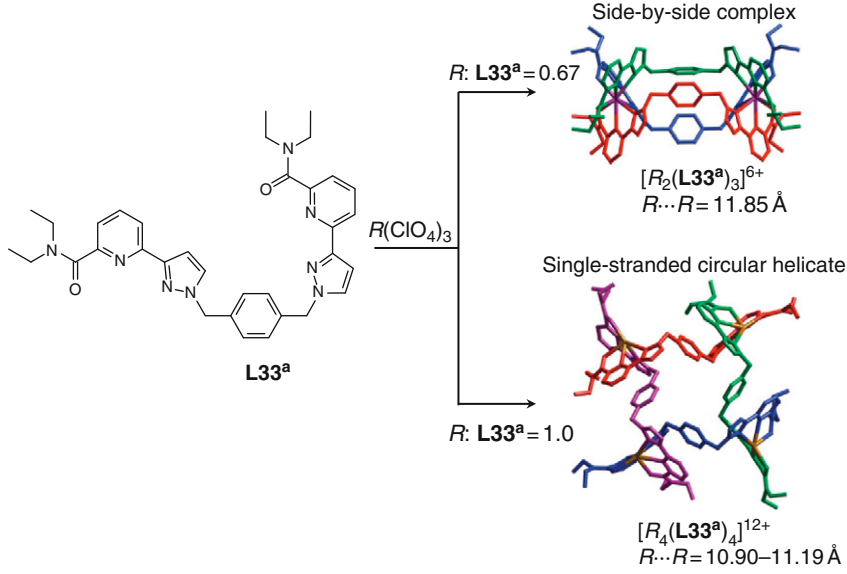

FIGURE 53 Formation of alternative polynuclear complexes with a homotopic C_{2v}-symmetrical bis-tridentate ligand. The structures of the complexes correspond to the crystal structures of $[Nd_2(\mathbf{L33^a})_3]^{6+}$ and $[Nd_4(\mathbf{L33^a})_4]^{12+}$ (redrawn after Ronson et al., 2007).

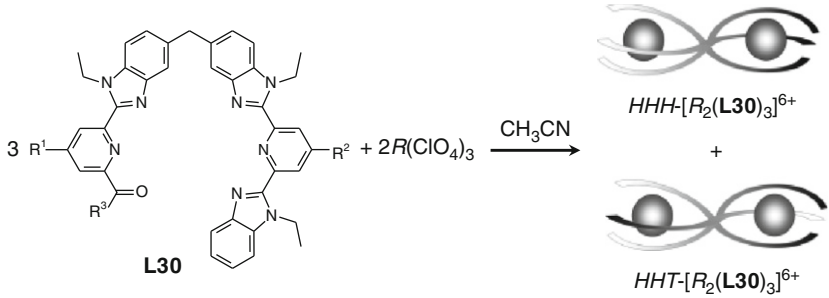

FIGURE 54 Solution structures of $[R_2(\mathbf{L30})_3]^{6+}$.

$$\mathrm{HHT}-[R_2(\mathbf{L30})_3]^{6+} \rightleftharpoons \mathrm{HHH}-[R_2(\mathbf{L30})_3]^{6+} \quad K_{\mathrm{iso}}^{R,\mathrm{L30}} = \beta_{2,3,\mathrm{HHH}}^{R,\mathrm{L30}}/\beta_{2,3,\mathrm{HHT}}^{R,\mathrm{L30}} \qquad (16)$$

Assuming that the metal–ligand, metal–metal and ligand–ligand interactions are identical in HHH-$[R_2(\mathbf{L30})_3]^{6+}$ and HHT-$[R_2(\mathbf{L30})_3]^{6+}$, we can easily deduce that the enthalpic contribution to equilibrium (16) is zero ($\Delta H_{\mathrm{iso,stat}}^{R,\mathrm{L30}} = 0$ kJ mol^{-1}), while the entropic contribution to the free energy change is given by $\Delta G_{\mathrm{iso,stat}}^{R,\mathrm{L30}} = -T\Delta S_{\mathrm{iso,stat}}^{R,\mathrm{L30}} = -RT\ln(K_{\mathrm{iso,stat}}^{R,\mathrm{L30}}) = 2.7$ kJ mol^{-1} because $K_{\mathrm{iso,stat}}^{R,\mathrm{L30}}$ is controlled by the ratio of the statistical factors of the self-assembly processes leading to the two microspecies (Eq. (17), Ercolani et al., 2007).

$$K_{\mathrm{iso,stat}}^{R,\mathrm{L30}} = \omega_{2,3,\mathrm{HHH}}^{R,\mathrm{L30}}/\omega_{2,3,\mathrm{HHT}}^{R,\mathrm{L30}} = 24/72 = 1/3 \qquad (17)$$

This translates into a statistical mixture of 25% HHH and 75% HHT isomers in solution, but we observe that none of the experimental data with ligands $\mathbf{L30}^{\mathbf{a-e}}$ follow this model (i.e., no experimental point at, or nearby, the crossing point of the two straight lines $\Delta H_{\mathrm{iso,stat}}^{R,\mathrm{L30}} = 0$ kJ mol^{-1} and $-T\Delta S_{\mathrm{iso,stat}}^{R,\mathrm{L30}} = 2.7$ kJ mol^{-1}, Figure 55). The most striking point concerns the quasi-systematic observation of $\Delta H_{\mathrm{iso}}^{R,\mathrm{L30}} < 0$ kJ mol^{-1} for all ligands, a trend which has been tentatively attributed to the existence of three intramolecular interaromatic π-stacking interactions involving the three wrapped NNN binding sites in the HHH isomer, while only one similar interaction remains in the HHT isomer (Jensen et al., 2007; see Figure 28 for a strict analogy of this phenomenon occurring in the mononuclear triple-helical precursors $[R(\mathbf{L19})_3]^{3+}$). Additional enthalpic contributions have been suggested to arise from some unknown cooperative processes favoring the formation of symmetrical homogeneous nine-coordinated binding sites in the final helicates, in other words the

TABLE 7 Thermodynamic parameters of equilibrium (16) for the triple-stranded binuclear helicates $[R_2(\mathbf{L30})_3]^{6+}$ in CD_3CN (see Figure 48)

	La	Ce	Pr	Sm	Eu	Lu	Y
L30[a]							
$\Delta H_{iso}^{R,L30}$ (kJ mol^{-1})	− 10.18	–	− 4.8(5)	− 1.5(2)	− 2.4(8)	1.9(2)	− 2.4(8)
$\Delta S_{iso}^{R,L30}$ (J mol^{-1} K^{-1})	− 26.1(3)	–	− 10(2)	0.1(7)	− 1(3)	12.6(8)	3.0(3)
% HHH (298 K)	73	–	67	65	69	68	63
L30[b]							
$\Delta H_{iso}^{R,L30}$ (kJ mol^{-1})	− 10.7(4)	− 2.9(5)	− 4(1)	0.60(9)	1(1)	1.1(4)	0.1(2)
$\Delta S_{iso}^{R,L30}$ (J mol^{-1} K^{-1})	− 47(1)	− 25(2)	− 31(5)	− 15.0(3)	− 18(4)	− 19(1)	− 20.4(6)
% HHH (298 K)	20	13	12	11	8	6	8
L30[c]							
$\Delta H_{iso}^{R,L30}$ (kJ mol^{-1})	− 3.3(3)	–	− 6.2(6)	− 6.6(3)	− 9.8(5)	− 12(2)	− 7.2(8)
$\Delta S_{iso}^{R,L30}$ (J mol^{-1} K^{-1})	0(1)	–	− 5(2)	− 8(1)	− 18(2)	25(7)	− 12(3)
% HHH (298 K)	79	–	87	85	85	86	82
L30[e]							
$\Delta H_{iso}^{R,L30}$ (kJ mol^{-1})	− 7.7(5)	− 5.7(3)	− 4.4(2)	− 4.1(2)	− 4.5(2)	− 3.4(3)	− 5.0(5)
$\Delta S_{iso}^{R,L30}$ (J mol^{-1} K^{-1})	− 23(2)	− 18(1)	− 13.8(8)	− 11.8(6)	− 13.9(8)	− 8(1)	− 13(2)
% HHH (298 K)	60	53	53	56	54	60	61

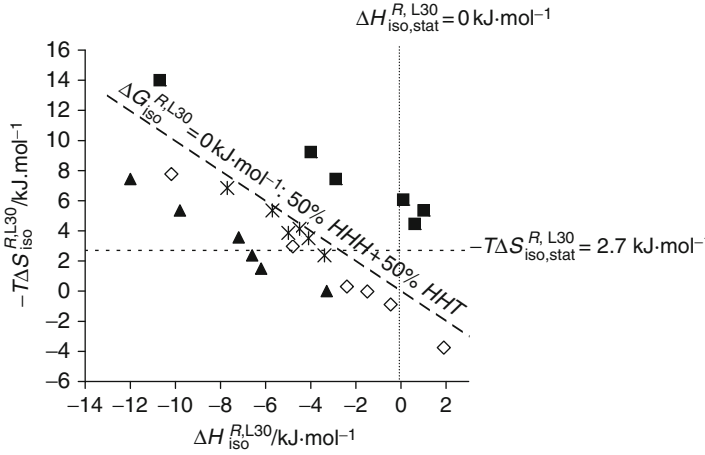

FIGURE 55 Entropic versus enthalpic contributions to the free energy of equilibrium (16); ◇, **L30[a]**; ■, **L30[b]**; ▲, **L30[c]**; *, **L30[e]**. The diagonal line indicates the domain, for which 50% of each isomer is formed in solution. Below this line, the HHH isomer is the major component of the mixture (redrawn from Jensen et al., 2007).

formation of the preorganized N_9-spacer-N_6O_3 binuclear receptor (HHH isomer) is preferred over the alternative N_8O-spacer-N_7O_2 binuclear receptor (HHT isomer, Jensen et al., 2007). In absence of a complete thermodynamic analysis of the self-assembly processes leading to HHH-$[R_2(\mathbf{L30})_3]^{6+}$ and HHT-$[R_2(\mathbf{L30})_3]^{6+}$, these interpretations remain elusive, but the empirical observations firmly establish the unusual formation of a large proportion (> 50%) of HHH isomer with ligands **L30[a]**, **L30[c]**, **L30[d]**, and **L30[e]**, while **L30[b]** is an exception (Figure 55).

3.3 Mechanisms of formation

Elucidation of the intricate mechanisms leading to the self-assembly of lanthanide helicates is indebted to the original kinetic investigations of the formation of binuclear double-stranded $[Cu_3(\mathbf{L1})_2]^{3+}$ (Fatin-Rouge et al., 2001; Figure 56), $[Cu_5(\mathbf{L6})_2]^{5+}$ (Marquis-Rigault et al., 1996), and triple-stranded $[Fe_2(\mathbf{L34})_3]^{4+}$ (Fatin-Rouge et al., 2000; Figure 57) helicates. As far as low charged Cu(I) is concerned, the limited electrostatic intermetallic repulsion can be easily balanced by solvation and polarization effects, and the successive fixation of several cations onto a single strand may offer a valuable route, which contrasts with the commonly invoked preorganization of several ligands prior to metal loading (Figure 56).

For the doubly charged cations Fe(II), the electrostatic metal–metal repulsion becomes strong enough so that the issue of the self-assembly

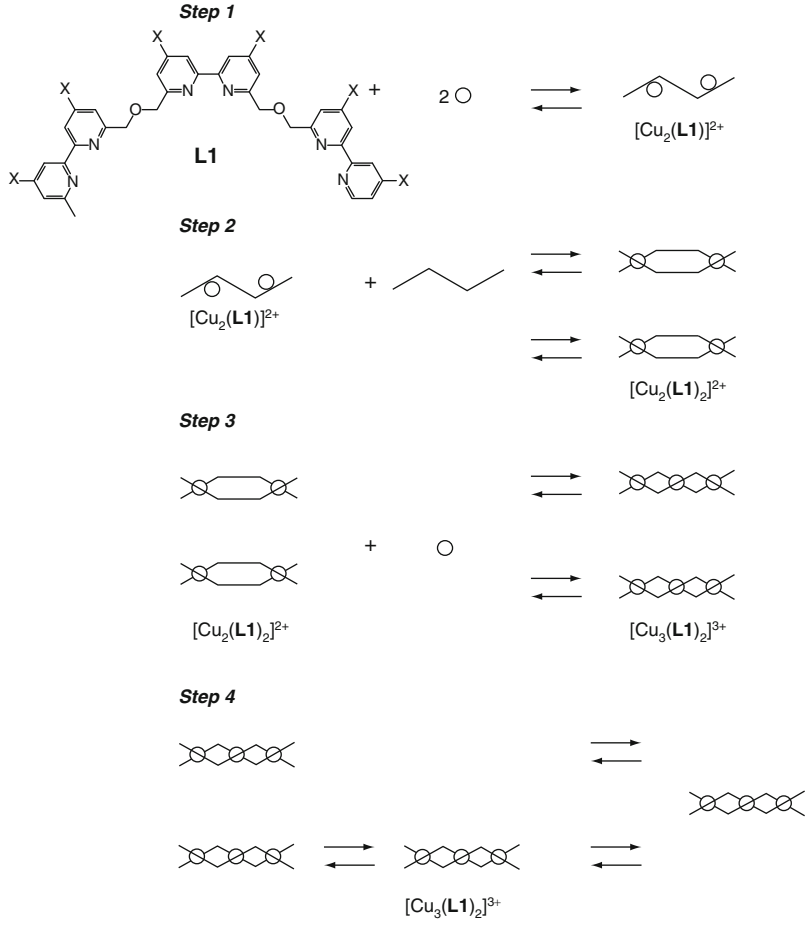

FIGURE 56 Mechanism of the self-assembly of the double-stranded helicate $[Cu_3(\mathbf{L1})_2]^{3+}$ (adapted from Fatin-Rouge et al., 2001).

process depends on the activity of the metal in solution (Figure 57). In excess of ligand, the connection of the third strand in $[Fe(\mathbf{L34})_3]^{2+}$ offers enough charge compensation by polarization for a second Fe(II) to enter into the complex in order to give $[Fe_2(\mathbf{L34})_3]^{4+}$. However, in excess of metal, only the hairpin arrangement of one ligand strand in $[Fe(\mathbf{L34})_2]^{2+}$ is able to reduce the effective charge of the coordinated metal to such an extent that the approach of a second Fe(II) is possible.

In the light of the latter observations, it is thus not so surprising that the mechanism of formation of the triple-stranded lanthanide helicates

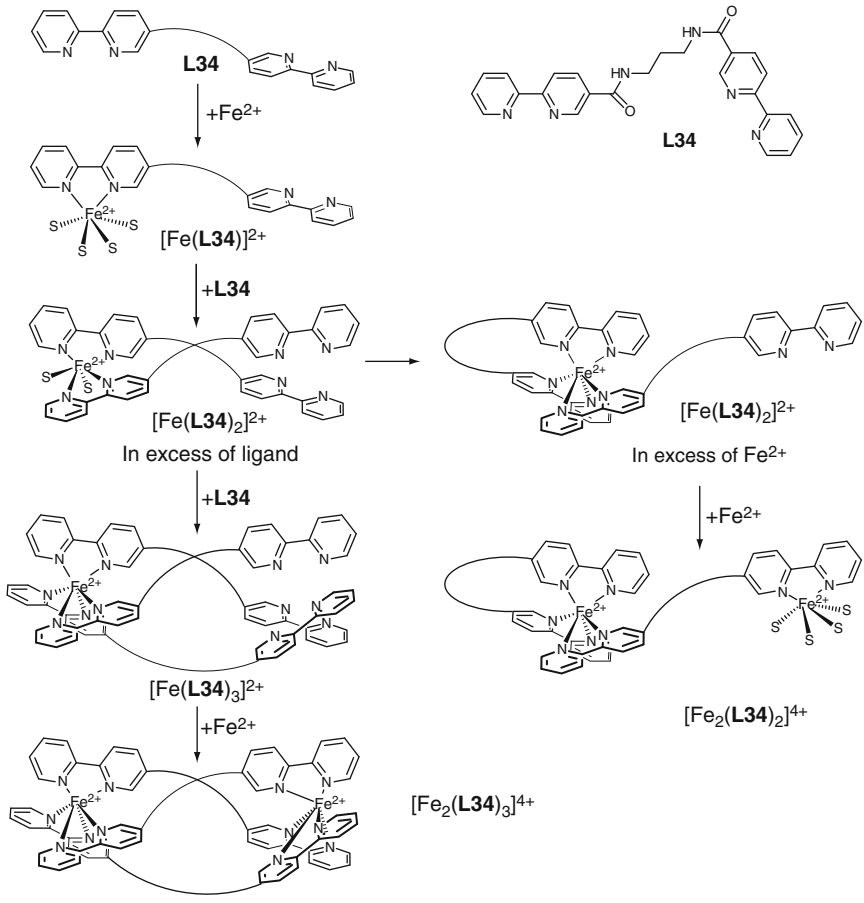

FIGURE 57 Mechanism of the self-assembly of the triple-stranded helicate $[Fe_2(\mathbf{L34})_3]^{4+}$ (adapted from Fatin-Rouge et al., 2000).

$[R_2(\mathbf{L11})_3]^{6+}$ avoids the connection of two triply charged cations in the early steps, but favors the successive fixation of ligand strands to a single metal (Hamacek et al., 2003; Figure 58A). Interestingly, the kinetics data indicate that the rate of the assembly of the different components strongly depends on the stoichiometric R:**L11** ratios. For R:**L11** = 2:3, the self-assembly process leads in a few minutes to the targeted $[R_2(\mathbf{L11})_3]^{6+}$ helicate, while several hours are required to reach thermodynamic equilibrium when R:**L11** = 10:1 (Hamacek et al., 2003).

The use of the hydrolyzed ligand $[\mathbf{L13^f}]^{2-}$ introduces charge neutralization as a novel parameter in helicate self-assembly. In these conditions, the coordination of a second metal to a single strand in $[R_2(\mathbf{L13^f})]^{3+}$ competes with the fixation of a second ligand in $[R(\mathbf{L13^f})_2]^{-}$ (Figure 58B;

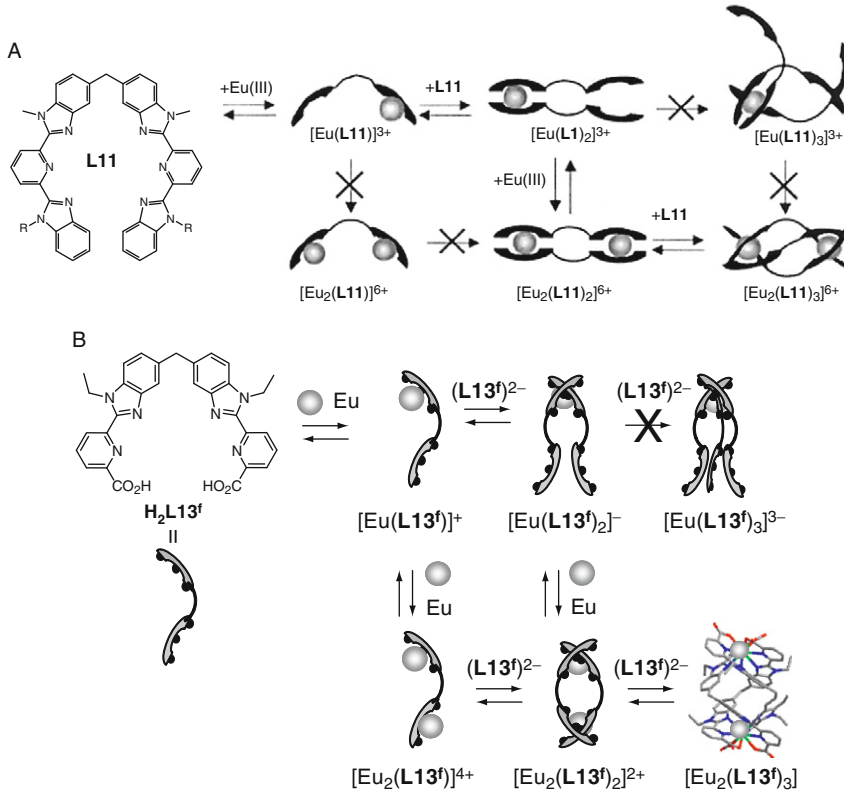

FIGURE 58 Mechanism of the self-assembly of the triple-stranded helicates: (A) $[Eu_2(\mathbf{L11})_3]^{6+}$ (redrawn from Hamacek et al., 2003) and (B) $[Eu_2(\mathbf{L13^f})_3]$ (redrawn from Elhabiri et al., 2004a).

Elhabiri et al., 2004a). The ultimate fixation of the third ligand in the neutral helicate $[R_2(\mathbf{L13^f})_3]$ induces a considerable entropic gain to the overall complexation process, which is responsible for both extreme thermodynamic stability (Elhabiri et al., 1999) and kinetic inertness (Elhabiri et al., 2004b, Figure 59), which make these helicates promising building blocks for the development of luminescent bioprobes (see Section 6).

3.4 Thermodynamics of the recognition processes

The majority of the formation constants $\beta_{m,n}^{R,Lk}$ (equilibrium (18)) characterizing the formation of triple-stranded lanthanide helicates in solution have been determined by direct spectrophotometric titrations in the UV-Vis range (Tables 8 and 9).

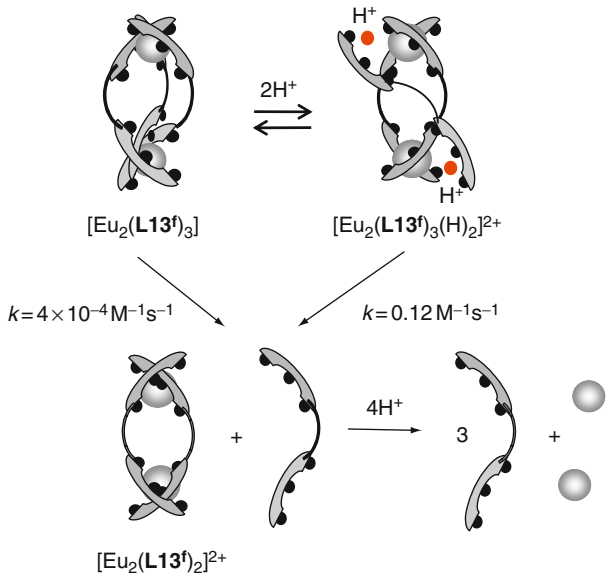

FIGURE 59 Dissociation mechanism of $[Eu_2(\mathbf{L13^f})_3]$ in water (redrawn from Elhabiri et al., 2004b).

$$n\mathbf{Lk}+mR^{3+} \rightleftharpoons [R_m(\mathbf{Lk})_n]^{3m+} \quad \beta_{m,n}^{R,Lk} \tag{18}$$

Since the allowed ligand-centered $n \rightarrow \pi^*$ and $\pi \rightarrow \pi^*$ transitions only display enough oscillator strength to monitor spectral changes accompanying the formation of the helicates in highly diluted solutions, the investigation of the complexation processes mainly relies on the *trans–trans* → *cis–cis* conformational change occurring upon complexation of the tridentate binding units (Figure 30). In other words, the recorded spectral changes are only sensitive to the on–off complexation of the tridentate binding units, whatever the nature and composition of the investigated complex. It is therefore difficult to detect the formation of poorly stable intermediates by spectrophotometry and only a partial set of stability constants are usually available for each ligand as shown in Tables 8 and 9.

The evolution of the formation constants of the binuclear triple-stranded helicates $[R_2(\mathbf{L11})_3]^{6+}$ (NNN-*S*-NNN donor sets) and $[R_2(\mathbf{L13^{a-d}})_3]^{6+}$ (ONN-*S*-NNO donor sets) along the lanthanide series mimics the size-discriminating effects previously established with the mononuclear precursors (Figure 31). When NNN donor sites are used in **L11**, the stability constants drops for the smaller R^{III}, a trend removed when the terminal benzimidazole rings are replaced with carboxamide units in $\mathbf{L13^{a-d}}$ (Table 8). The connection of electron-withdrawing halogenides (Cl in $\mathbf{L13^c}$, Br in $\mathbf{L13^d}$, Figure 41) at the 4-position of the central

TABLE 8 Cumulative $\log(\beta_{m,n}^{R,Lk})$ stability constants reported for the formation of binuclear helicates: (i) $[R_m(\mathbf{L}k)_n]^{3m+}$, $k = 11$ (Figure 12), 13[a–d] (Figure 41), and 30[a] (Figure 48); (ii) $[R_m(\mathbf{L}k\text{-H})_n]^{(3m-n)+}$, $k = 30$[f] and 31 (Figure 48); and (iii) $[R_m(\mathbf{L}k)_n]^{(3m-2n)+}$, $k = 13$[f–h] (Figures 46 and 47) and 32[a] (Figure 49)

(a) Homotopic binuclear helicates

Ligand	*R*	Solvent	$\log(\beta_{1,1}^{R,Lk})$	$\log(\beta_{1,2}^{R,Lk})$	$\log(\beta_{1,3}^{R,Lk})$	$\log(\beta_{2,1}^{R,Lk})$	$\log(\beta_{2,2}^{R,Lk})$	$\log(\beta_{2,3}^{R,Lk})$	References
L11	Eu	CH_3CN		11.6(3)			18.1(3)	24.3(4)	Hamacek et al. (2003)
	Lu							17.5(4)	Piguet et al. (1993b)
L13[a]	La	CH_3CN					20.4(8)	25.3(9)	Martin et al. (1998)
	Eu						19.9(10)	24.1(10)	Martin et al. (1998)
	La				17.0(4)		19.2(5)	25.1(2)	Zeckert et al. (2004)
	Ce				18.1(5)		18.9(1)	25.0(2)	Zeckert et al. (2004)
	Pr				16.7(4)		19.4(5)	25.3(2)	Zeckert et al. (2004)
	Nd				18.8(5)		19.3(4)	25.4(2)	Zeckert et al. (2004)
	Sm				17.5(4)		20.0(5)	25.9(2)	Zeckert et al. (2004)
	Eu				19.4(5)		19.6(2)	26.0(2)	Zeckert et al. (2004)
	Gd				18.8(5)		19.8(2)	26.0(2)	Zeckert et al. (2004)
	Tb				17.8(3)		20.0(5)	26.0(5)	Zeckert et al. (2004)
	Dy				17.2(4)		20.1(5)	25.0(5)	Zeckert et al. (2004)
	Ho				18.7(5)		19.6(2)	25.8(2)	Zeckert et al. (2004)
	Er				18.4(5)		19.4(3)	25.6(3)	Zeckert et al. (2004)
	Tm				18.7(5)		19.3(3)	25.6(3)	Zeckert et al. (2004)
	Yb				16.1(9)		19.2(5)	25.4(2)	Zeckert et al. (2004)
	Lu				17.1(5)		19.3(4)	25.4(5)	Zeckert et al. (2004)
	Y				17.2(4)		19.6(5)	25.8(2)	Zeckert et al. (2004)

(*continued*)

TABLE 8 (*continued*)

(a) Homotopic binuclear helicates

Ligand	*R*	Solvent	$\log(\beta_{1,1}^{R,Lk})$	$\log(\beta_{1,2}^{R,Lk})$	$\log(\beta_{1,3}^{R,Lk})$	$\log(\beta_{2,1}^{R,Lk})$	$\log(\beta_{2,2}^{R,Lk})$	$\log(\beta_{2,3}^{R,Lk})$	References
L13[c]	Eu	CH_3CN					18.3(15)	21.8(15)	Platas-Iglesias et al. (2000)
L13[d]	Eu	CH_3CN					19.9(15)	23.8(15)	Platas-Iglesias et al. (2000)
$(L13^f)^{2-}$	Eu	H_2O	4.3(1)			6.4(2)		50(2)	Elhabiri et al. (2004a)
H_2L13^f	La	H_2O						30(1)[a]	Elhabiri et al. (1999)
	Eu							26.1(4)[a]	Elhabiri et al. (1999)
	Lu							27.3(5)[a]	Elhabiri et al. (1999)
H_2L13^g	La	H_2O				10.9(1)[a]		22.7(2)[a]	Chauvin et al. (2007)
	Eu				16.8(1)[a]	11.4(1)[a]		23.4(1)[a]	Chauvin et al. (2007)
	Lu				17.0[a]	11.0(1)[a]		23.1(1)[a]	Chauvin et al. (2007)
H_2L13^h	La	H_2O			18.8(2)[a]	11.7(3)[a]		24.9(4)[a]	Chauvin et al. (2008)
	Eu				18.1(2)[a]	11.8(5)[a]		25.5(4)[a]	Chauvin et al. (2008)
	Lu				18.7(3)[a]	12.4(2)[a]		26.3(4)[a]	Chauvin et al. (2008)
H_2L13^i	La	H_2O		14.8(1)[a]		13.8(2)[a]		28.3(1)[a]	Deiters et al. (2008)
	Eu			14.7(1)[a]				28.0(1)[a]	Deiters et al. (2008)
	Lu			14.4(4)[a]				27.7(5)[a]	Deiters et al. (2008)
H_2L13	La	H_2O		14.2(3)[a]		13.6(3)[a]		28.1(4)[a]	Deiters et al. (2009)
	Eu			14.8(3)[a]		14.3(3)[a]		28.5(5)[a]	Deiters et al. (2009)
	Lu			13.6(1)[a]		14.3(1)[a]		26.3(2)[a]	Deiters et al. (2009)

H_2L13[k]	Eu	H_2O	14.0(1)[a]	15.4(1)[a]	27.9(1)[a]	Deiters et al. (2009)
H_2L13[l]	La	H_2O	14.0(1)[a]	15.9(1)[a]	27.4(3)[a]	Deiters et al. (2009)
	Eu		14.3(3)[a]	14.4(5)[a]	28.6(5)[a]	Deiters et al. (2009)
	Lu			16.0(3)[a]	28.8(3)[a]	Deiters et al. (2009)
H_2L32[a]	Eu	H_2O			31.6(2)[b]	Lessmann and Horrocks (2000)

(b) Heterotopic binuclear helicates

Ligand	Metal	Solvent	$\log(\beta_{1,1}^{R,Lk})$	$\log(\beta_{1,2}^{R,Lk})$	$\log(\beta_{1,3}^{R,Lk})$	$\log(\beta_{2,1}^{R,Lk})$	$\log(\beta_{2,2}^{R,Lk})$	$\log(\beta_{2,3}^{R,Lk})$	References
L30[a]	Eu	CH_3CN						23.9(5)	André et al. (2004)
[L30[f]**-H]**$^-$	La	CH_3OH	7.8(2)	13(1)	19.0(2)			25(1)	André et al. (2004)
	Eu			12.6(4)	17.9(5)			23.3(7)	André et al. (2004)
	Lu		7.2(2)	12.5(10)	17.3(1)			23.6(10)	André et al. (2004)
[L31-H]$^-$	Eu	CH_3OH		15.1(4)	20.8(4)		22.5(6)	29.7(6)	André et al. (2004)

All data are at 293 K.
[a] Conditional stability constants: pH 7.4, Tris–HCl 0.1 M.
[b] Conditional stability constants: pH 7.0, HEPES 0.05 M.

TABLE 9 Cumulative $\log(\beta_{m,n}^{R,Lk})$ stability constants reported for the formation of heterotopic tri- and tetranuclear helicates $[R_m(\mathbf{L}k)_n]^{3m+}$ ($k = 28$, 29) in acetonitrile at 293 K

Ligand	*R*	$\log(\beta_{2,3}^{R,Lk})$	$\log(\beta_{3,2}^{R,Lk})$	$\log(\beta_{3,3}^{R,Lk})$	$\log(\beta_{4,2}^{R,Lk})$	$\log(\beta_{4,3}^{R,Lk})$
L28[a]	La	25.0(11)	25.8(11)	34.3(12)		
	Nd	26.0(10)	26.4(10)	35.0(11)		
	Eu	25.9(14)	26.0(14)	34.8(16)		
	Tb	25.8(2)	27.2(1)	35.0(12)		
	Ho	26.0(10)	26.5(10)	35.0(12)		
	Tm	26.0(16)	26.9(9)	34.5(18)		
	Lu	25.5(11)	27.4(5)	33.9(3)		
L29[b]	La		25.2(15)	31.9(4)	30.4(15)	39.1(15)
	Nd			29.7(1.8)	29.6(18)	38.4(19)
	Sm			29.7(1.5)		35.7(15)
	Eu		28.9(14)	36.8(1.5)	32.8(14)	43.2(16)
	Ho		26.3(14)	34.5(15)	29.6(15)	40.6(16)
	Er			33.4(15)	28.9(13)	38.1(15)
	Yb		26.5(13)	32.5(15)		41.0(16)
	Lu		27.5(12)	34.5(13)	31.1(12)	40.8(13)

pyridine rings weakens the interactions with R^{III} by, respectively, three and two order of magnitudes in the $[Eu_2(\mathbf{L13})_3]^{6+}$ helicates, in line with decreasing electronegativity of these two substituents. As previously established with mononuclear precursors, the introduction of negatively charged carboxylate donor groups in $[\mathbf{L30^f}\text{-H}]^-$, $[\mathbf{L31}\text{-H}]^-$ or in $[\mathbf{L13^{f-l}}]^{2-}$ and $[\mathbf{L32}\text{-2H}]^{2-}$ drastically increases the stability of the final helicates, which can then easily survive in highly competing solvents such as methanol or water (Table 8). Finally, the combination of several neutral NNN and NNO tridentate binding units in the segmental ligands **L28** and **L29** gives trinuclear, respectively, tetranuclear triple-stranded helicates, whose cumulative formation constants are difficult to measure by direct titration because of the very minute decomplexation occurring at submillimolar concentrations (Table 8). In these conditions, any size-discriminating effect is probably masked by experimental uncertainties (Table 9).

3.5 Photophysical properties

Since the bidentate binding units in the segmental ligands are connected by saturated methylene units, which are poor electronic relays, we can expect that the photophysical properties of the helicates can be easily deduced from those found in the mononuclear triple-helical precursors.

A detailed comparison of Table 10 (dedicated to polynuclear helicates) with Table 4 (dedicated to mononuclear precursors) indeed supports this reasoning.

For the Eu^{III} complexes, the three wrapped tridentate NNN binding units produce poorly luminescent EuN_9 sites due to the quenching by LMCT states located close in energy to the ligand-centered $^1\pi\pi^*$ excited states in $[Eu_2(\mathbf{L11})_3]^{6+}$ (Piguet et al., 1993b) and as firmly established for its precursor $[Eu(\mathbf{L17^a})_3]^{3+}$ (Petoud et al., 1999). It is, however, worth noting that the global quantum yield increases by two orders of magnitude in going from $[Eu(\mathbf{L17^a})_3]^{3+}$ ($Q_L^{Eu} = 2 \times 10^{-3}\%$) to $[Eu_2(\mathbf{L11})_3]^{6+}$ ($Q_L^{Eu} = 0.2\%$), a phenomenon tentatively ascribed to some variation of the energy of the LMCT level in the constrained binuclear triple-stranded helicate. The replacement of the terminal benzimidazole rings with either carboxamide units in $[Eu_2(\mathbf{L13^{a-e}})_3]^{6+}$ or carboxylate groups in $[Eu_2(\mathbf{L13^{f-l}})_3]$ drastically improves quantum yields, as previously noticed in going from $[Eu(\mathbf{L17})_3]^{3+}$ to $[Eu(\mathbf{L18})_3]^{3+}$ or $[Eu(\mathbf{L19})_3]^{3+}$. In this context, $Q_L^{Eu} = 24\%$ measured for $[Eu_2(\mathbf{L13^f})_3]$ in water at pH 7.4 further confirms the high potential of this class of helicates as bioprobes and the detailed photophysical properties of the $[Eu_2(\mathbf{L13^{f-l}})_3]$ helicates will be discussed in Section 6. We also note that Q_L^{Ln} is extremely sensitive to the relative orientation of the tridentate binding units when C_s-symmetrical ligands are considered. Among the EuN_6O_3 coordination sites found in $[Eu(\mathbf{L19^b})_3]^{3+}$ ($Q_L^{Eu} = 0.05\%$ in CH_3CN), in $[Eu(\mathbf{L22})]^{3+}$ ($Q_L^{Eu} = 10\%$ in CH_3CN), in $[Eu(\mathbf{L23})]^{3+}$ ($Q_L^{Eu} = 14\%$ in CH_3CN), and in the binuclear helicate $[Eu_2(\mathbf{L13^b})_3]^{6+}$ ($Q_L^{Eu} = 9\%$ in CH_3CN), only the first one, with the very low quantum yield, exists as the meridional isomer in solution, while the other adopt pure facial organizations. With this empirical observation in mind, it is not so surprising that the heterotopic binuclear helicate $[Eu_2(\mathbf{L30^a})_3]^{6+}$, which mainly exist as the HHH isomer (69% HHH, Table 7), gives a relatively high quantum yield in acetonitrile ($Q_L^{Ln} = 15\%$, Table 10).

Both the ground state ($^7F_0$) and the most luminescent level ($^5D_0$) of Eu^{III} are nondegenerate so that the forbidden and therefore usually very weak $^5D_0 \rightarrow {}^7F_0$ (emission spectra) or $^5D_0 \leftarrow {}^7F_0$ (excitation spectra) transitions are unique whatever the symmetry of the metal-ion environment. As a consequence, Eu^{III} is widely used for monitoring the number of different metallic coordination sites existing in lanthanide complexes both in solution and in crystalline samples (Bünzli, 1989). Except for some broadening of this spectral line due to polycrystallinity, all mononuclear and binuclear triple-helical Eu^{III} complexes reported in Tables 4, 5, and 10 exhibit a single Eu($^7F_0 \rightarrow {}^5D_0$) transition, which is diagnostic for the existence of a single chemical environment around the metal ion. Moreover, the energy of this transition depends on the effective charge borne by Eu^{III} in the complexes (Bünzli, 1989), that is, on the

TABLE 10 Photophysical properties of triple-stranded helicates $[R_m(\mathbf{L}k)_3]^{6+}$ [$k = 11$ ($m = 2$), 13^{a-d} ($m = 2$), 28 ($m = 3$), 29 ($m = 4$), 30($m = 2$)] and $[R_2(\mathbf{L}k\text{-}2H)_3]$ ($k = 13^{f-h}$, 32)

Ligand	Ln	Solvent	E(*π ← π) (cm^{-1})[a]	E($^3\pi\pi^*$) (cm^{-1})[b]	Q_L^{Ln} (%)	τ_{obs} (ms)[c]	E(Eu($^5D_0$)) (cm^{-1})	References
L11	Eu	CH_3CN	25,640	19,880	0.2[d]	2.03[e]	17,227 (77 K)	Piguet et al. (1993b)
	Tb	CH_3CN	25,640	19,880	–	1.35[e]	–	Piguet et al. (1993b)
L13[b]	Eu	CH_3CN	29,760	20,930	9[d]	2.09[e]	17,229 (77 K)	Martin et al. (1998)
	Tb	CH_3CN	29,500	20,930	10[d]	1.96[e]	–	Martin et al. (1998)
L13[c]	Eu	CH_3CN	29,480	20,455	11[d]	2.28[e]	17,218 (10 K)	Platas-Iglesias et al. (2000)
L13[e]	Eu	CH_3CN	28,340	19,800	31[d]	2.02	17,222 (295 K)	Tripier et al. (2002)
$[\mathbf{L13}^f]^{2-}$	Sm	H_2O	30,120	20,660	0.14	0.042	–	Gonçalves e Silva et al. (2002)
	Eu	H_2O	30,120	20,660	24[d]	2.69[f]	17,232 (295 K)	Elhabiri et al. (1999)
	Tb	H_2O	30,120	20,660	1.2[d]	0.05	–	Bünzli et al. (2008) and Elhabiri et al. (1999)
	Yb	D_2O	30,120	20,660	1.8	0.04 (295 K)	–	Gonçalves e Silva et al. (2002)

$[\mathbf{L13^g}]^{2-}$	Nd	H_2O (pH 7.4)	31,250	–	0.031	2.1×10^{-4}	–	Chauvin et al. (2008)
	Sm	H_2O (pH 7.4)	31,150	–	0.38	0.03	–	Chauvin et al. (2008)
	Eu	H_2O (pH 7.4)	31,060	22,050	21	2.34	17,234 (295 K)	Chauvin et al. (2008)
	Tb	H_2O (pH 7.4)	30,960	22,050	11	0.65	–	Chauvin et al. (2008)
	Yb	H_2O (pH 7.4)	30,860	–	0.15	0.0044	–	Chauvin et al. (2008)
$[\mathbf{L13^h}]^{2-}$	Eu	H_2O (pH 7.4)	31,150	21,900	19	2.43	17,233 (295 K)	Deiters et al. (2008)
	Tb	H_2O (pH 7.4)	31,100	21,900	10	0.66		Deiters et al. (2008)
$[\mathbf{L13^i}]^{2-}$	Eu	H_2O (pH 7.4)	30,670	22,150	11	2.2	17,235 (295 K)	Chauvin et al. (2007)
	Tb	H_2O (pH 7.4)	30,670	22,100	0.34	0.39	–	Chauvin et al. (2007)
$[\mathbf{L13^j}]^{2-}$	Eu	H_2O (pH 7.4)	31,450	21,150	15	2.52	17,242 (10 K)	Deiters et al. (2009)
	Tb	H_2O (pH 7.4)	31,450	21,150	2.5	0.12	–	Deiters et al. (2009)

(*continued*)

TABLE 10 (*continued*)

Ligand	Ln	Solvent	E(*π ← π) (cm^{-1})[a]	E(^{3}ππ*) (cm^{-1})[b]	Q_L^{Ln} (%)	τ_{obs} (ms)[c]	E(Eu($^5D_0$)) (cm^{-1})	References
[L13^k]$^{2-}$	Eu	H_2O (pH 7.4)	29,500	19,550	0.35	0.54	17,237 (10 K)	Deiters et al. (2009)
	Tb	H_2O (pH 7.4)	29,500	19,550	–	0.01	–	Deiters et al. (2009)
	Yb	H_2O (pH 7.4)	29,500	19,550	0.15	0.0043	–	Deiters et al. (2009)
[L13l]$^{2-}$	Eu	H_2O (pH 7.4)	28,500	20,800	9	2.3	17,242 (10 K)	Deiters et al. (2009)
	Tb	H_2O (pH 7.4)	28,500	20,800	0.31	0.04	–	Deiters et al. (2009)
	Yb	H_2O (pH 7.4)	28,500	20,800	0.16	0.0043	–	
L32$_a$	Eu	H_2O	–	–	–	1.48	17,226 (295 K)	Lessmann and Horrocks (2000)
L32$_b$	Eu	H_2O	–	–	–	1.56	17,221 (295 K)	Lessmann and Horrocks (2000)
L30^a	Eu	CH_3CN	29,500	20,000	15[d]	2.26[e]	17,232 (295 K)	André et al. (2004)

L28	Eu	CH_3CN	30,390	20,260	0.3[d]	2.3[f] EuN_6O_3 site, 2.1[f] EuN_9 site	17,219 (10 K) EuN6O3 site 17,238 (10 K) EuN9 site	Floquet et al. (2003)
	Tb	CH_3CN	30,080	20,260	–	2.23[f]	–	Floquet et al. (2003)
L29	Eu	CH_3CN	30,580	20,040	–	2.0–2.2 (10 K)	17,221 (10 K) EuN_6O_3 sites, 17,235 (10 K) EuN_9 sites	Dalla Favera et al. (2008)

[a] Values obtained from absorption spectra in solution (293 K).
[b] Values obtained from emission spectra (0-phonon, 77 K).
[c] Metal-centered lifetime at 295 K if not otherwise stated.
[d] Quantum yields have been recalculated by using the most recent values reported for the $[R(\text{terpyridine})_3]^{3+}$ internal references (Comby, 2008).
[e] At 77 K.
[f] At 10 K.

nephelauxetic effect produced by the donor atoms bound to Eu^{III} (Choppin and Wang, 1997; Frey and Horrocks, 1995). Experimentally, the energy of the Eu($^5D_0 \leftarrow {}^7F_0$) transition is obtained from excitation spectra recorded at low temperature (<77 K) whereby vibrational contributions are minimized. Taking into account the accepted 1 cm^{-1}/24 K dependence of the energy of the Eu($^5D_0 \leftarrow {}^7F_0$) transition (Bünzli, 1989), we obtain $\tilde{\nu}^{obs} = 17{,}245$ cm^{-1} for the EuN_9 site in $[Eu_2(\mathbf{L17^a})_3]^{3+}$, $\tilde{\nu}^{obs} = 17{,}238$ cm^{-1} for the facial $Eu(N_{hetero})_6(O_{amide})_3$ site in $[Eu_2(\mathbf{L13^b})_3]^{6+}$, $\tilde{\nu}^{obs} = 17{,}232$ cm^{-1} for the facial $Eu(N_{hetero})_6(O_{acid})_3$ site in $[Eu_2(\mathbf{L13^f})_3]$, $\tilde{\nu}^{obs} = 17{,}227$ cm^{-1} for the $Eu(N_{hetero})_3(O_{amide})_6$ site in $[Eu(\mathbf{L18^a})_3]^{3+}$ and $\tilde{\nu}^{obs} = 17{,}221$ cm^{-1} for the facial $Eu(O_{acid})_3N_3(O_{amide})_3$ site in [Eu(**L21**-3H)] at 295 K (Tables 4, 5, and 10). These systematic, but small variations can be well reproduced by using the empirical linear Eq. (19), whereby $\tilde{\nu}_0 = 17{,}374$ cm^{-1} is the energy of the Eu($^7F_0 \rightarrow {}^5D_0$) transition in the free ion, C_{CN} is an empirical coefficient decreasing with the coordination numbers ($C_{CN=8} = 1.06$, $C_{CN=9} = 1.00$, $C_{CN=10} = 0.95$) and δ_i represents the nephelauxetic effect produced by an atom i bound to Eu^{III} (Frey and Horrocks, 1995).

$$\tilde{\nu}^{calcd} = \tilde{\nu}_0 + C_{CN}\sum_{i=1}^{CN} n_i\delta_i \tag{19}$$

The optimized values of δ_i adapted to $CN = 9$ amount to $\delta_{O\text{-carboxylate}} = -17.2$ $cm^{-1} < \delta_{O\text{-amide}} = -15.7$ $cm^{-1} < \delta_{N\text{-heterocycle}} = -15.3$ cm^{-1}, suggesting an improved delocalization of the electronic density in the order O-carboxylate > O-amide > N-heterocycle. In view of the large amount of data collected for the $Eu(N_{hetero})_9$ and $Eu(N_{hetero})_6(O_{amide})_3$ sites in triple-stranded helicates (ligands **L11**, **L13**, **L28**–**L30**) and in mononuclear precursors (ligands **L17** and **L19**), some further refinements have been proposed leading to the specific assignment $\delta_{N\text{-pyridine}} = -25.3$ cm^{-1} and $\delta_{N\text{-benzimidazole}} = -8.0$ cm^{-1} in 6-substituted-2-(2-benzimidazolyl)pyridine binding segments (Dalla Favera et al., 2008). With these parameters, Eq. (19) predicts $\tilde{\nu}^{calcd} = 17{,}227$ cm^{-1} for $Eu(N_{hetero})_6(O_{amide})_3$ and $\tilde{\nu}^{calcd} = 17{,}250$ cm^{-1} for $Eu(N_{hetero})_9$ at 295 K, in fair agreement with the experimental values found for the Eu ($^5D_0 \leftarrow {}^7F_0$) transition of these sites in $[Eu_3(\mathbf{L28})_3]^{9+}$ and in $[Eu_4(\mathbf{L29})_3]^{12+}$ (1 cm^{-1}/24 K dependence, Figure 60A; Table 10).

The use of powerful laser excitation beam at low temperature indeed allows the detection of two different sources of Eu-centered emission in the latter complexes (Figure 60A). Selective excitation of each site gives different emission spectra, which can be analyzed with crystal-field theory for estimating the strength of the different nonadentate donor sets and the degree of distortion from ideal tricapped-trigonal prismatic geometry (Görller-Walrand and Binnemans, 1996, 1998; Figure 60B). Since

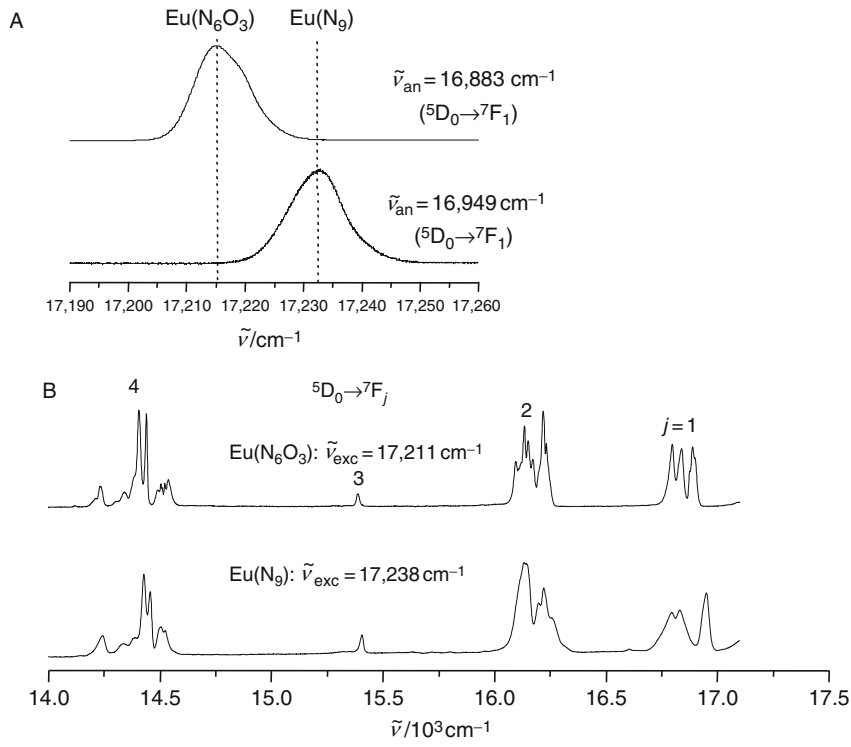

FIGURE 60 (A) Excitation profiles of the Eu($^5D_0 \leftarrow {}^7F_0$) transition for $[Eu_3(\mathbf{L28})_3]^{9+}$ at 10 K upon monitoring different components of the $^5D_0 \rightarrow {}^7F_1$ transition. (B) Emission spectra of $[Eu_3(\mathbf{L28})_3]^{9+}$ at 10 K recorded under selective excitation of the $Eu(N_6O_3)$ and $Eu(N_9)$ sites (adapted from Floquet et al., 2003).

$\tilde{\nu}^{\,obs}_{EuN_9} > \tilde{\nu}^{\,obs}_{EuN_6O_3}$, divergent intramolecular thermally activated energy migration processes from the central EuN_9 sites toward the EuN_6O_3 termini in $[Eu_3(\mathbf{L28})_3]^{9+}$ and $[Eu_4(\mathbf{L29})_3]^{12+}$ eventually produce pure emission of the terminal EuN_6O_3 sites at room temperature.

For Tb^{III} helicates with ligands **L11**, **L13**, and **L28–L32**, the ligand-centered $^3\pi\pi^*$ excited state is too close in energy to avoid thermally activated $Tb(^5D_4) \rightarrow {}^3\pi\pi^*$ energy transfers, which drastically reduces the intensity and lifetime of the Tb-centered luminescence upon increasing the temperature. Typically, $Tb(^5D_4)$ lifetimes vary from a few milliseconds at 10–77 K to reach a few tens of microseconds at room temperature in Tb^{III} triple-stranded helicates (Table 10). Interestingly, the stepwise approximate 1000–2000 cm^{-1} energy increase of the ligand-centered $^3\pi\pi^*$ excited state in going from $[Tb_2(\mathbf{L11})_3]^{6+}$ ($E(^3\pi\pi^*) = 19{,}880$ cm^{-1}, $Q_L^{Tb} < 0.01\%$, Table 10) to $[Tb_2(\mathbf{L13^b})_3]^{6+}$ ($E(^3\pi\pi^*) = 20{,}900$ cm^{-1},

$Q_L^{Tb} = 11\%$, Table 10) and $[Tb(\mathbf{L18^a})_3]^{3+}$ ($E(^3\pi\pi^*) = 23{,}600$ cm^{-1}, $Q_L^{Tb} = 26\%$, Table 4) supports this interpretation. Finally, a thorough theoretical modeling of the kinetic issues of the sensitization processes occurring in the triple-stranded helicates $[Sm_2(\mathbf{L13^f})_3]$ and $[Yb_2(\mathbf{L13^f})_3]$ suggests that the pivotal ligand($^3\pi\pi^*$) $\rightarrow R^{III}$ energy transfer is of the exchange type for Sm^{III} ($^3\pi\pi^* \rightarrow {}^5G_{5/2}{}^{(1)}$), but corresponds to an electron transfer mechanism for Yb^{III} (Gonçalves e Silva et al., 2002).

3.6 Paramagnetic properties

Because of the minute mixing of the metal 4f-orbitals with the ligand wave functions, the open-shell trivalent lanthanides can be used not only as luminescent sensors (Bünzli, 1989), but also as paramagnetic probes for elucidating molecular structures in solution. EPR spectroscopy is mainly limited to Gd^{III} complexes because an orbitally nondegenerated ground state ($^8S_{7/2}$ for Gd^{III}) is required for producing electronic relaxation times long enough to allow the detection of EPR signals with reasonable line width (Raitsimiring et al., 2007). Moreover, the structural information is mainly restricted to the first coordination sphere because of the very limited covalency of the Gd-donor bonds, hence producing negligible spin delocalization. On the other hand, the very fast electronic relaxation displayed by the other open-shell trivalent lanthanides possessing orbitally degenerate ground states is compatible with small perturbations of the nuclear relaxation processes and the recording of high-resolution NMR spectra (Bertini and Luchinat, 1996). A thorough review of the use of R^{III} as paramagnetic probes in triple-helical (C_3-symmetry) and quadruple helical (C_4-symmetry) complexes has been recently published (Piguet and Geraldes, 2003). However, the basic principles and concepts used for extracting solution structures of lanthanide complexes are briefly outlined here to discuss the main contribution brought by polynuclear lanthanide helicates in this field. Introduction of a paramagnetic trivalent lanthanide ion in a complex has two major effects on the spectra of the NMR-active atoms of the ligands (usually ^1H, ^{13}C, ^{31}P, and ^{15}N are commonly considered for these studies because of their 1/2 nuclear spin):

(1) The longitudinal ($1/T_{1i}$, Eq. (20)) and transversal ($1/T_{2i}$, Eq. (21)) nuclear relaxation rates of the nucleus i are enhanced by the combination of through-bond (contact *Fermi* interaction, Eqs. (22) and (23)) and through-space (dipolar-transient, Eqs. (24) and (25) and dipolar-Curie, Eqs. (26) and (27)) coupling of the nuclear and electronic magnetic moments.

$$\frac{1}{T_{1i}^{\mathrm{exp}}} = \frac{1}{T_{1i}^{\mathrm{dia}}} + \frac{1}{T_{1i}^{\mathrm{para}}} = \frac{1}{T_{1i}^{\mathrm{dia}}} + \frac{1}{T_{1i}^{\mathrm{para-contact}}} + \frac{1}{T_{1i}^{\mathrm{para-dip-transient}}} + \frac{1}{T_{1i}^{\mathrm{para-dip-Curie}}} \tag{20}$$

$$\frac{1}{T_{2i}^{\mathrm{exp}}} = \frac{1}{T_{2i}^{\mathrm{dia}}} + \frac{1}{T_{2i}^{\mathrm{para}}} = \frac{1}{T_{2i}^{\mathrm{dia}}} + \frac{1}{T_{2i}^{\mathrm{para-contact}}} + \frac{1}{T_{2i}^{\mathrm{para-dip-transient}}} + \frac{1}{T_{2i}^{\mathrm{para-dip-Curie}}} \tag{21}$$

$$\frac{1}{T_{1i}^{\mathrm{para-contact}}} = \frac{S(S+1)}{3}\left(\frac{A_i}{\hbar}\right)^2\left(\frac{2\tau_{\mathrm{e}}}{1+\omega_{\mathrm{S}}^2\tau_{\mathrm{e}}^2}\right) \tag{22}$$

$$\frac{1}{T_{2i}^{\mathrm{para-contact}}} = \frac{S(S+1)}{3}\left(\frac{A_i}{\hbar}\right)^2\left(\tau_e + \frac{\tau_e}{1+\omega_{\mathrm{S}}^2\tau_e^2}\right) \tag{23}$$

$$\frac{1}{T_{1i}^{\mathrm{para-dip-transient}}} = \frac{2}{15}\left(\frac{\mu_0}{4\pi}\right)^2 \frac{\gamma_I \mu_{\mathrm{eff}}^2 \mu_{\mathrm{B}}^2}{r_i^6}\left(\frac{3\tau_c}{1+\omega_{\mathrm{I}}^2\tau_c^2} + \frac{7\tau_c}{1+\omega_{\mathrm{S}}^2\tau_c^2}\right) \tag{24}$$

$$\frac{1}{T_{2i}^{\mathrm{para-dip-transient}}} = \frac{1}{15}\left(\frac{\mu_0}{4\pi}\right)^2 \frac{\gamma_I \mu_{\mathrm{eff}}^2 \mu_{\mathrm{B}}^2}{r_i^6}\left(4\tau_c + \frac{3\tau_c}{1+\omega_{\mathrm{I}}^2\tau_c^2} + \frac{13\tau_c}{1+\omega_{\mathrm{S}}^2\tau_c^2}\right) \tag{25}$$

$$\frac{1}{T_{1i}^{\mathrm{para-dip-Curie}}} = \frac{6}{5}\left(\frac{\mu_0}{4\pi}\right)^2 \frac{\gamma_I^2 \mu_{\mathrm{eff}}^4 \mu_{\mathrm{B}}^4 H_0^2}{r_i^6 (3kT)^2}\left(\frac{\tau_r}{1+\omega_{\mathrm{I}}^2\tau_r^2}\right) \tag{26}$$

$$\frac{1}{T_{2i}^{\mathrm{para-dip-Curie}}} = \frac{1}{5}\left(\frac{\mu_0}{4\pi}\right)^2 \frac{\gamma_I^2 \mu_{\mathrm{eff}}^4 \mu_{\mathrm{B}}^4 H_0^2}{r_i^6 (3kT)^2}\left(4\tau_r + \frac{3\tau_r}{1+\omega_{\mathrm{I}}^2\tau_r^2}\right) \tag{27}$$

The random modulation of the electron-nucleus magnetic coupling via electronic relaxation (characteristic time τ_{e}), molecular tumbling (characteristic time τ_{r}) and chemical exchange (ligand exchange reaction, characteristic time τ_{m} is assumed to be zero for saturated helicates in eqs (22 – 27)) can be combined in a global correlation time

$\tau_c^{-1} = \tau_e^{-1} + \tau_r^{-1} + \tau_m^{-1}$, which controls the extent to which the paramagnetic center affects the nuclear relaxation. When the electronic relaxation time is long as for example in Gd^{III} (typically $\tau_e \geq 1$ ns), the contribution of $1/T_{2i}^{para-contact}$ (Eq. (23)) is so large that NMR signals with reasonable line width cannot be recorded. For all the other paramagnetic lanthanides, τ_e falls in the picosecond range and well-resolved NMR spectra can be obtained. In these conditions, an acceptable approximation only considers the contribution of through-space dipolar interactions to the paramagnetic relaxation because the *Fermi* constants A_i are very small for lanthanide complexes ($1/T_{1i}^{para-contact}$ and $1/T_{2i}^{para-contact}$ are neglected). It is therefore a common practice to combine the transient and Curie contributions to the dipolar coupling in Eqs. (28) and (29), because both depend on r_i^{-6}, whereby r_i is the R^{III}-nucleus distance (Figure 61), E_{1j} and E_{2j} are magnetic constants depending on (i) the lanthanide j present in the complex, (ii) the temperature T, (iii) the external magnetic field of the spectrometer H_0, (iv) the effective electronic magnetic moment μ_{eff}, (v) the type of NMR-active nucleus under investigation, and (vi) the electronic and rotational correlation times. Within a given complex, all these parameters are fixed and once a reference R^{III}-nucleus distance r_{ref} is known for the complex in solution, E_{1j} and E_{2j} can be calibrated and all the others distances can be easily deduced from measurements of nuclear relaxation rates thanks to Eqs. (28) and (29).

$$\frac{1}{T_{1i}^{exp}} - \frac{1}{T_{1i}^{dia}} = \frac{1}{T_{1i}^{para}} = \frac{4}{3}\left(\frac{\mu_0}{4\pi}\right)^2 \frac{\gamma_I \mu_{eff}^2 \mu_B^2}{r_i^6} \tau_e + \frac{6}{5}\left(\frac{\mu_0}{4\pi}\right)^2 \frac{\gamma_I^2 \mu_{eff}^4 \mu_B^4 H_0^2}{r_i^6 (3kT)^2}\left(\frac{\tau_r}{1 + \omega_I^2 \tau_r^2}\right) = \frac{E_{1j}}{r_i^6} \quad (28)$$

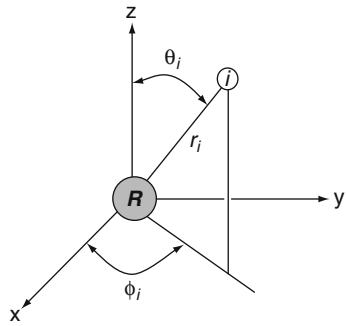

FIGURE 61 Spherical coordinates r_i, θ_i, and ϕ_i for a nucleus i in an arbitrary xyz reference frame with the metal ion R^{III} located at the origin.

$$\frac{1}{T_{2i}^{\mathrm{exp}}} - \frac{1}{T_{2i}^{\mathrm{dia}}} = \frac{1}{T_{2i}^{\mathrm{para}}} = \frac{4}{3}\left(\frac{\mu_0}{4\pi}\right)^2 \frac{\gamma_{\mathrm{I}}\mu_{\mathrm{eff}}^2\mu_{\mathrm{B}}^2}{r_i^6}\tau_{\mathrm{e}} + \frac{1}{5}\left(\frac{\mu_0}{4\pi}\right)^2 \frac{\gamma_{\mathrm{I}}^2\mu_{\mathrm{eff}}^4\mu_{\mathrm{B}}^4 H_0^2}{r_i^6(3kT)^2} \left(4\tau_r + \frac{3\tau_r}{1+\omega_{\mathrm{I}}^2\tau_r^2}\right) = \frac{E_{2j}}{r_i^6} \tag{29}$$

(2) The NMR chemical shift $\delta_{ij}^{\mathrm{exp}}$ of a nucleus i in a complex of a lanthanide ion j is also affected by the influence of the electronic magnetic moment on the local magnetic field felt by the nuclear spin under investigation (Eq. (30)). In this equation, the through-bond contribution δ_{ij}^{c} arises from partial delocalization of the electronic spin $\langle S_z\rangle_j$ via the contact *Fermi* mechanism and is expressed by Eq. (31). The through-space contribution $\delta_{ij}^{\mathrm{pc}}$ is a consequence of residual dipolar effects due to anisotropic electronic magnetic moments in the homogeneous medium and is often referred to as pseudocontact contribution (Eq. (32) in which Tr(χ) represents the trace of the magnetic susceptibility tensor).

$$\delta_{ij}^{\mathrm{exp}} = \delta_i^{\mathrm{dia}} + \delta_{ij}^{\mathrm{para-contact}} + \delta_{ij}^{\mathrm{para-pseudocontact}} = \delta_i^{\mathrm{dia}} + \delta_{ij}^{\mathrm{c}} + \delta_{ij}^{\mathrm{pc}} \tag{30}$$

$$\delta_{ij}^{c} = \frac{\Delta H^{\mathrm{c}}}{H_0} = \frac{A_i}{\hbar\gamma_I H_0}\langle S_z\rangle_j = F_i\langle S_z\rangle_j \tag{31}$$

$$\delta_i^{pc} = \frac{\Delta H^{\mathrm{pc}}}{H_0} = \frac{1}{2N_A r_i^3}\left[\left(\chi_{zz}^j - \frac{1}{3}\mathrm{Tr}(\chi)\right)(3\cos^2\theta_i - 1) + (\chi_{xx}^j - \chi_{yy}^j)(\sin^2\theta_i \cos 2\varphi_i)\right] \tag{32}$$

Both through-bond and pseudocontact contributions can be easily factorized into a series of products of two terms, each term depending either on the nucleus i (topologic and geometric location) or from the lanthanide j (electronic structure and crystal-field effects). For axial complexes, that is, possessing at least a three-fold axis as found in triple-stranded helicates, the molecular magnetic susceptibility tensor χ^j written in the principal magnetic axes system is symmetrical ($\chi_{xx}^j = \chi_{yy}^j$, z magnetic axis aligned along C_3). Equation (32) thus reduces to Eq. (33), whereby $G_i = (3\cos^2\theta_i - 1)/r_i^3$ is known as the geometrical factor.

$$\delta_i^{\mathrm{pc}} = \frac{1}{2N_{\mathrm{A}}r_i^3}\left[\left(\chi_{zz}^j - \frac{1}{3}\mathrm{Tr}(\chi)\right)\left(3\cos^2\theta_i - 1\right)\right] = \frac{1}{2N_A}\left(\chi_{zz}^j - \frac{1}{3}\mathrm{Tr}(\chi)\right)G_i \tag{33}$$

In a seminal contribution, *Bleaney* demonstrated that when the crystal-field splitting of the ground multiplet is smaller or comparable to kT, a situation often met with lanthanide complexes, the anisotropic part of the axial paramagnetic susceptibility tensor originates from second-order effects and can be simply estimated by the product of magnetic constants C_j, characteristics of the electronic configuration of each lanthanide (i.e., *Bleaney* factor), multiplied by the second-rank crystal-field parameter B_0^2 (Eq. (34), Bleaney, 1972).

$$\frac{1}{2N_A}\left(\chi_{zz}^{j} - \frac{1}{3}\mathrm{Tr}(\chi)\right) = B_0^2 C_j \tag{34}$$

Finally introducing Eqs. (31), (33), and (34) into Eq. (30) gives the simple linear Eq. (35), which is well adapted for testing isostructurality along the lanthanide series for complexes in solution since numerical values for $\langle S_z\rangle_j$ and C_j calculated at 300 K have been tabulated (Piguet and Geraldes, 2003).

$$\delta_{ij}^{\mathrm{exp}} - \delta_i^{\mathrm{dia}} = \delta_{ij}^{\mathrm{para}} = F_i\langle S_z\rangle_j + B_0^2 G_i C_j \tag{35}$$

However, B_0^2 is often very sensitive to the minor R^{III}-ligand bond contraction accompanying the loading of the 4f-orbitals along the lanthanide series. This often prevents a safe interpretation of deviations of Eq. (35) from linearity as arising from a structural change affecting the geometrical factor G_i (Ouali et al., 2002). The simultaneous consideration of two NMR-active nuclei i (Eq. (35)) and k (Eq. (36)) in the same complex provides two equations, which can be combined to give a novel linear equation (37), in which the influence of the crystal-field parameter has been removed (Platas et al., 1999).

$$\delta_{kj}^{\mathrm{exp}} - \delta_k^{\mathrm{dia}} = \delta_{kj}^{\mathrm{para}} = F_k\langle S_z\rangle_j + C_j B_0^2 G_k \tag{36}$$

$$\frac{\delta_{ij}^{\mathrm{para}}}{\langle S_z\rangle_j} = \left(F_i - F_k\frac{G_i}{G_k}\right) + \frac{G_i}{G_k}\cdot\frac{\delta_{kj}^{\mathrm{para}}}{\langle S_z\rangle_j} \tag{37}$$

Any variation of the slope for linear plots of $\delta_{ij}^{\mathrm{para}}/\langle S_z\rangle_j$ versus $\delta_{kj}^{\mathrm{para}}/\langle S_z\rangle_j$ along a series of lanthanide complexes j implies that the ratio of the geometrical factor G_i/G_k changes, hence the structure of the complex does too. The systematic application of nuclear relaxation measurements (Eqs. (28) and (29)) for obtaining R^{III}-nuclei distances, combined with the detailed analysis of NMR paramagnetic shifts with the help of the two nuclei method (Eq. (37), detection of isostructural series) as well

as the one nucleus analysis (Eq. (35), extraction of geometrical factors) provides an efficient tool for establishing the solution structures of mononuclear axial lanthanide complexes (see Section 2.2 for structural details on these complexes). For the homometallic polynuclear triple-stranded helicates $[R_m\mathbf{L}_3]^{3m+}$, the existence of m identical lanthanide ions packed along the C_3-symmetry axis requires some modifications of the basic equations derived for mononuclear systems (Figure 62).

Since the m identical trivalent lanthanides are not magnetically coupled in triple-stranded helicates (intermetallic separation ≈ 9 Å), the global effect of the electronic magnetic moments onto the nuclear relaxation in solution is given by a simple additive model, which transforms Eqs. (28) and (29) into Eqs. (38) and (39), and in which each specific distance r_i^l between the nucleus i and the lanthanide l is taken into account (Piguet and Geraldes, 2003, Figure 62).

$$\frac{1}{T_{1i}^{\text{exp}}} - \frac{1}{T_{1i}^{\text{dia}}} = \frac{1}{T_{1i}^{\text{para}}} = E_{1j}\sum_{l=1}^{m}\left(\frac{1}{(r_i^l)^6}\right) \tag{38}$$

$$\frac{1}{T_{2i}^{\text{exp}}} - \frac{1}{T_{2i}^{\text{dia}}} = \frac{1}{T_{2i}^{\text{para}}} = E_{2j}\sum_{l=1}^{m}\left(\frac{1}{(r_i^l)^6}\right) \tag{39}$$

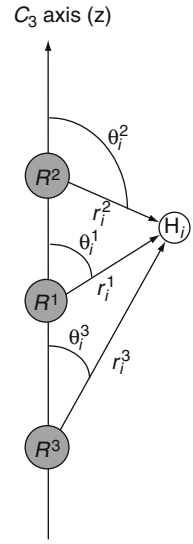

FIGURE 62 Example of axial coordinates in a trinuclear triple-stranded lanthanide helicate (adapted from Floquet et al., 2003).

Due to the dependence of $1/T_i^{para}$ on a set of different *R*-nucleus distances, these equations cannot be used for obtaining structural information in polynuclear helicates, but they are useful for confirming the assignment of paramagnetic NMR spectra, once a reasonable structure is at hand (Elhabiri et al., 1999; Ouali et al., 2003). The application of the additive model for the rationalization of the paramagnetic NMR shifts is more promising and Eq. (40) replaces Eq. (35) in a triple-stranded homopolynuclear helicate containing *m* magnetically noncoupled paramagnetic centers, each lanthanide *l* being located at the origin of its own reference frame (Figure 62).

$$\delta_{ij}^{exp} - \delta_i^{dia} = \delta_{ij}^{para} = (\sum_{l=1}^{m} F_i^l)\langle S_z\rangle_j + (\sum_{l=1}^{m} (B_0^2)^l G_i^l)C_j \qquad (40)$$

The case of the D_3-symmetrical binuclear helicate $[R_2(\mathbf{L13^f})_3]$ (Figure 41) is straightforward because $(B_0^2)^1 = (B_0^2)^2$ for symmetry reasons, and a simple factorization transforms Eq. (38) into the linear Eq. (41) (Elhabiri et al., 1999).

$$\delta_{ij}^{para} = (F_i^1 + F_i^2)\langle S_z\rangle_j + B_0^2(G_i^1 + G_i^2)C_j \qquad (41)$$

Consequently, the removal of the crystal-field parameter requires the same strategy as the one developed for the mononuclear complexes, thus eventually leading to the two nuclei crystal-field independent Eq. (42), which is mathematically analogous to Eq. (37).

$$\frac{\delta_{ij}^{para}}{\langle S_z\rangle_j} = \left((F_i^1 + F_i^2) - (F_k^1 + F_k^2)\left(\frac{G_i^1 + G_i^2}{G_k^1 + G_k^2}\right)\right) + \left(\frac{G_i^1 + G_i^2}{G_k^1 + G_k^2}\right)\cdot\frac{\delta_{kj}^{para}}{\langle S_z\rangle_j} \qquad (42)$$

Standard two-nuclei $\delta_{ij}^{para}/\langle S_z\rangle_j$ versus $\delta_{kj}^{para}/\langle S_z\rangle_j$ plots show straight lines (Eq. (37)) for $[R_2(\mathbf{L13^f})_3]$, except for some deviations for those nuclei, which are strongly affected by both paramagnetic centers (Rigault et al., 2000b). Globally, isostructurality was established along the complete lanthanide series in $[R_2(\mathbf{L13^f})_3]$ (Elhabiri et al., 1999), but with a smooth change in the crystal-field parameter occurring between *R* = Tb and *R* = Er (B_0^2(Ce − Tb)/B_0^2(Er − Yb) = 0.8, Piguet and Geraldes, 2003). A similar conclusion was reached for the series of helicates with the neutral ditopic ligand $\mathbf{L13^c}$ bearing chloride substituents in the para position of the pyridines, $[R_2(\mathbf{L13^c})_3]^{6+}$. The single nucleus method yields two straight lines (Pr–Dy and Ho–Yb) while the two-nucleus method points to a more intricate behavior: some proton pairs display a single straight line, while others produce two approximately parallel lines. A detailed analysis concluded that if the solution structure is essentially maintained in solution from Pr to Yb, changes in both the crystal-field parameter and

hyperfine coupling constants are responsible for the intricate behavior unraveled by these analyses (Platas-Iglesias et al., 2000). The case of the D_3-symmetrical trinuclear $[R_3(\mathbf{L28})_3]^{9+}$ helicate (Figure 51A) is more challenging because the crystal-field parameter of the central paramagnetic lanthanide $B_0^{2\text{central}} = (B_0^2)^1$ is different from those of the terminal paramagnetic centers $(B_0^2)^2 = (B_0^2)^3 = B_0^{2\text{terminal}}$ for symmetry reasons (Figure 62). In these conditions, factorization of Eq. (40) still gives a linear equation (Eq. (43), but with a second member containing a combination of crystal-field parameters and geometrical factors (Floquet et al., 2003).

$$\delta_{ij}^{\text{para}} = (F_i^1 + F_i^2 + F_i^3)\langle S_z\rangle_j + [B_0^{2\text{central}} G_i^1 + B_0^{2\text{terminal}}(G_i^2 + G_i^3)]C_j \quad (43)$$

The removal of the two different crystal-field parameters requires the simultaneous consideration of three different nuclei i, k, l in the same complex $[R_3(\mathbf{L28})_3]^{9+}$, thus leading to the multicenter Eq. (44), in which the factors B_{ikl}, C_{ikl}, and D_{ikl} are given in Eqs. (45)–(48) (Ouali et al., 2003).

$$\frac{\delta_{ij}^{\text{para}}}{\langle S_z\rangle_j} = B_{ikl} + C_{ikl}\frac{\delta_{kj}^{\text{para}}}{\langle S_z\rangle_j} + D_{ikl}\frac{\delta_{lj}^{\text{para}}}{\langle S_z\rangle_j} \quad (44)$$

$$B_{ikl} = F_i - F_k C_{ikl} - F_l D_{ikl} \quad (45)$$

$$C_{ikl} = R_{ik}\left(\frac{G_i^1 - G_l^1 R_{il}}{G_k^1 R_{ik} - G_l^1 R_{il}}\right) \quad (46)$$

$$D_{ikl} = -R_{il}\left(\frac{G_i^1 - G_k^1 R_{ik}}{G_k^1 R_{ik} - G_l^1 R_{il}}\right) \quad (47)$$

$$R_{xy} = \left(\frac{G_x^2 + G_x^3}{G_y^2 + G_y^3}\right) \quad (48)$$

Equation (44) corresponds to the equation of a plane perpendicular to the vector $(1, -C_{ikl}, -D_{ikl})$ and separated by a distance B_{ikl} from the origin in a homogeneous 3D space in which $\delta_{ij}^{\text{para}}/\langle S_z\rangle_j$, $\delta_{kj}^{\text{para}}/\langle S_z\rangle_j$, and $\delta_{lj}^{\text{para}}/\langle S_z\rangle_j$ define the orthogonal x, y, and z directions. The structural factors C_{ikl} and D_{ikl} are complicated nonlinear combinations of the geometrical factors

G_i^m, G_k^m, and G_l^m ($m = 1-3$), but any deviation of the triplets ($\delta_{ij}^{para}/\langle S_z\rangle_j$, $\delta_{kj}^{para}/\langle S_z\rangle_j$, $\delta_{lj}^{para}/\langle S_z\rangle_j$) from the plane along the lanthanide series affects C_{ikl} and D_{ikl} and implies a structural change occurring in the lanthanide helicates $[R_3(\mathbf{L28})_3]^{9+}$. Application of the three-nuclei Eq. (44) for any i,k,l proton triplets in $[R_3(\mathbf{L28})_3]^{9+}$ gives a single plane along the complete lanthanide series, in agreement with isostructurality (Figure 63). However, the one-nucleus linear Eq. (43) points to a pronounced break near the middle of the series ($R = Dy$), which implies some variations of the crystal-field parameters (Figure 64). A detailed analysis of these data confirms the expected slight decrease of the crystal-field strength with lanthanide contraction ($B_0^{2central}(Ce - Tb)/B_0^{2central}(Dy - Yb) = 1.4$ and $B_0^{2terminal}(Ce - Tb)/B_0^{2terminal}(Dy - Yb) = 1.1$), but $B_0^{2terminal}(Ce - Yb)/B_0^{2central}(Ce - Yb) = 2.0$ demonstrates that the terminal pseudotricapped-trigonal prismatic N_6O_3 sites produces stronger crystal-field splitting compared with the central N_9 site.

Interestingly, the mathematical treatment leading to Eq. (44) is very general and any paramagnetic system, for which Bleaney's approach requires two independent crystal-field parameters may benefit from its use for testing isostructurality, as demonstrated with the structural analyses of rhombic mononuclear (Terazzi et al., 2006) and polynuclear (Ouali et al., 2004) lanthanide complexes.

4. POLYNUCLEAR BIMETALLIC 4f HELICATES

The reaction of segmental ligand strands with two different trivalent lanthanides R^1(III) and R^2(III) enlarges the possible issues of the self-assembly processes. For axial C_2-symmetrical receptors, the threefold axis is maintained in the final triple-stranded polynuclear helicates $[(R^1)_x(R^2)_{m-x}(\mathbf{Lk})_3]^{3m+}$, but the three perpendicular twofold axes characterizing the homometallic complexes ($R^1 = R^2$) are present in the heterobimetallic systems ($R^1 \neq R^2$) only for some specific successions of metal ions (Dalla Favera et al., 2007). For nonaxial C_s-symmetrical ligands, the HHH ↔ HHT isomerization of the triple-stranded helicates already limits the final symmetry to C_3 (HHH) and C_1 (HHT) point groups for homometallic complexes, a situation which is further complicated by the consideration of R^1/R^2 pairs (Jensen et al., 2006). Therefore, the detection and the quantitative estimation of deviations from the statistical distribution of the different lanthanides R^1 and R^2 in the final helicates is a crucial theme for the rational design of selective complexation processes along the lanthanide series.

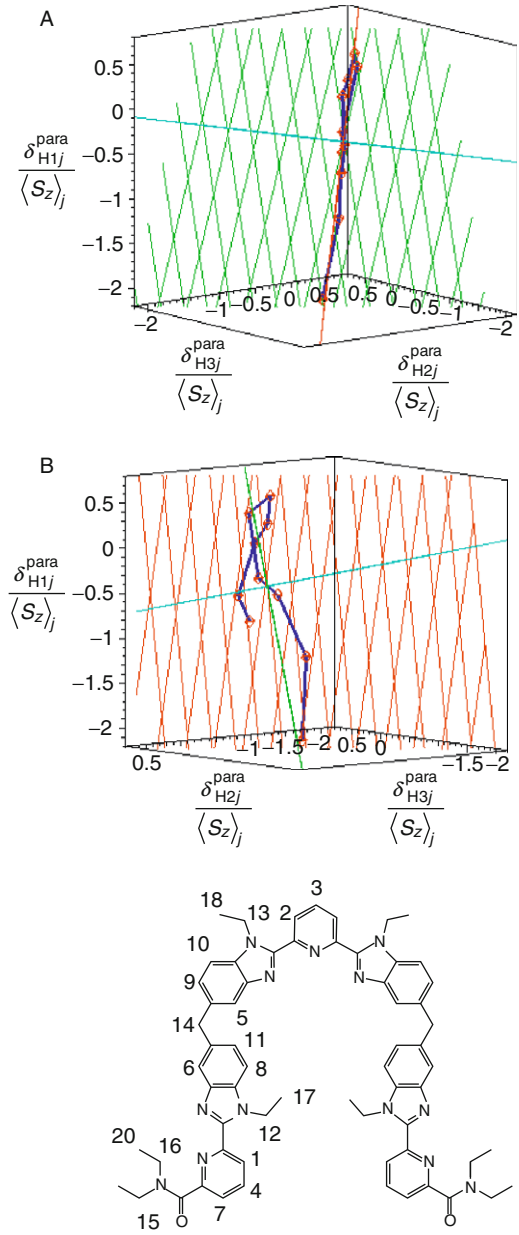

FIGURE 63 3D plots of $\delta^{para}_{ij}/\langle S_z\rangle_j$ versus $\delta^{para}_{kj}/\langle S_z\rangle_j$ and $\delta^{para}_{lj}/\langle S_z\rangle_j$ for H1, H2, H3 in $[R_3(\mathbf{L28})_3]^{9+}$ with numbering scheme of the ligand strand (CD_3CN, 298 K). (A) View of the best plane from profile showing the planar arrangement of the points (rhombs are used to highlight a plane orthogonal to the best plane). (B) View perpendicular to the best plane showing the location of the points within the plane (the lowest point is for R = Ce, the highest for R = Dy and the last point is for R = Yb, the line is only a guide for the eyes and rhombs are used to highlight the best plane) (adapted from Ouali et al., 2003).

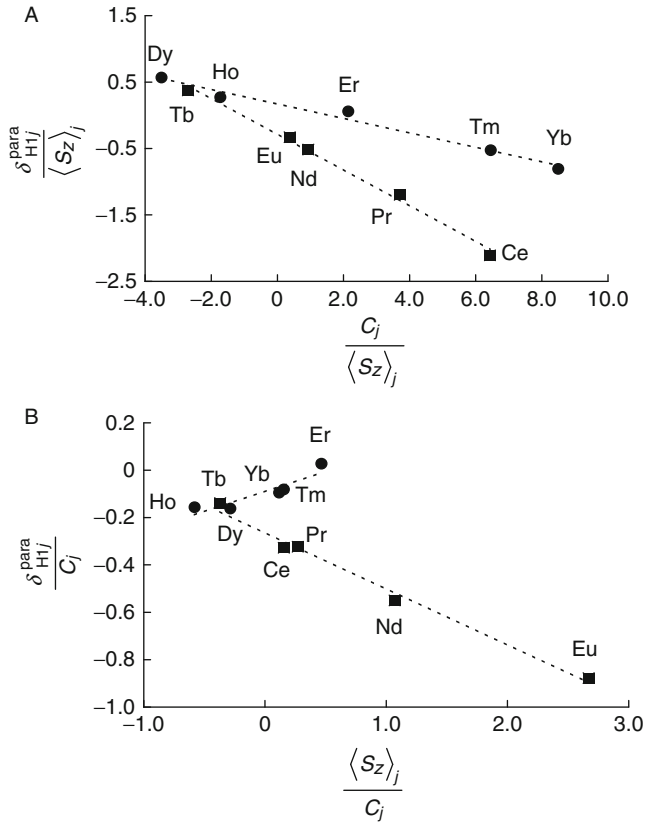

FIGURE 64 Plots of two linear forms of Eq. (43): (A) $\delta_{ij}^{para}/\langle S_z\rangle_j$ versus $C_j/\langle S_z\rangle_j$ and (B) δ_{ij}^{para}/C_j versus $\langle S_z\rangle_j/C_j$, for H1 in $[R_3(\mathbf{L28})_3]^{9+}$ (R = Ce–Yb, except Pm and Gd, CD_3CN, 298 K, numbering scheme in Figure 63) (adapted from Ouali et al., 2003).

4.1 Axial polytopic receptors: Statistical distributions and deviations

4.1.1 Binuclear helicates

Let us first consider the simple C_2-symmetrical bis-tridentate ligands **L11** or **L13**. Assuming that the principle of maximum site occupancy is obeyed (Hamacek et al., 2005b), the reaction of **L11** or **L13** with two different lanthanides gives three complexes $[(R^1)_2(\mathbf{Lk})_3]^{6+}$, $[(R^1)(R^2)(\mathbf{Lk})_3]^{6+}$, and $[(R^2)_2(\mathbf{Lk})_3]^{6+}$ whose intuitive statistical 1:2:1 distribution relies on the binomial distribution (Figure 65). At a lower level of modeling, the three wrapped ligand strands can be considered as a virtual preorganized molecular box of D_3-symmetry to which the zero level of the free energy of the self-assembly process is set (Figure 66, Piguet et al., 2005). The change in free energy accompanying the successive fixations of the

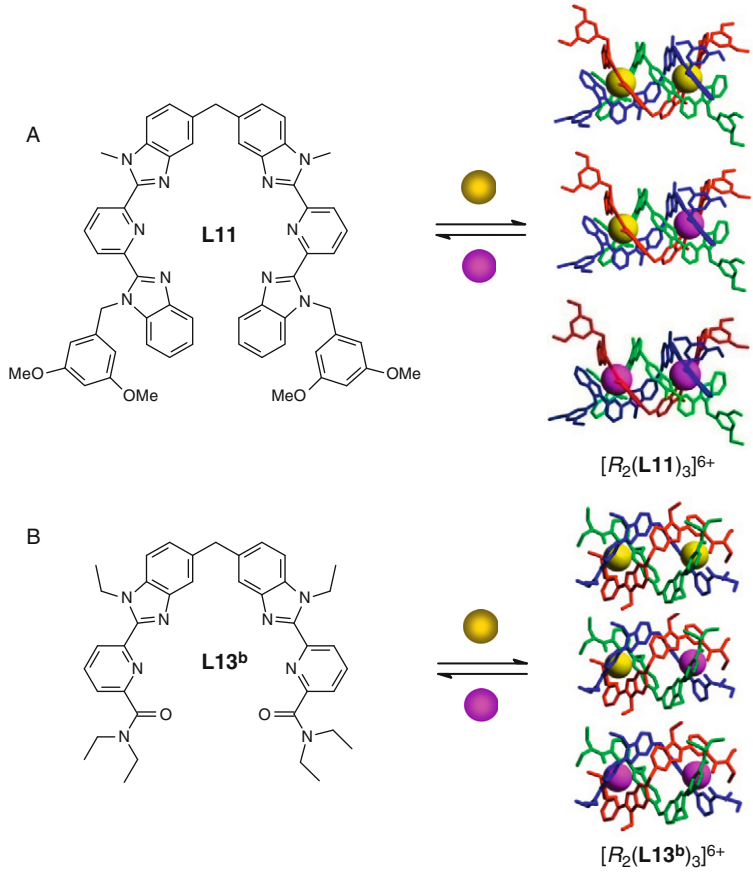

FIGURE 65 Self-assembly of the polynuclear triple-stranded helicates: (A) $[R_2(\mathbf{L11})_3]^{6+}$ (Piguet et al., 1993b) and (B) $[R_2(\mathbf{L13^b})_3]^{6+}$ (Zeckert et al., 2004) in acetonitrile. The final helicates correspond to the X-ray crystal structures of $[Eu_2(\mathbf{L11})_3]^{6+}$ (Piguet et al., 1993c) and $[Tb_2(\mathbf{L13^b})_3]^{6+}$ (Martin et al., 1998).

metal ions can then be easily described with the site-binding model (Koper and Borkovec, 2001), in which $\omega_{m,[L3]}^{R^i,R^j}$ is the statistical factor of the assembly (Ercolani et al., 2007), $f_k^{R^i}$ is the absolute intermolecular affinity (including solvation) of the lanthanide R^i for the k site of the preorganized box and $\Delta E_{1-2}^{R^i,R^j} = -RT\ \ln(u_{1-2}^{R^i,R^j})$ is the free energy of the intermetallic interaction operating between two nearest metallic neighbors (i.e., geminal) R^i and R^j in the final helicate (Eqs. (49)–(51), Figure 66).

The calculation of the statistical factors relies on the use of symmetry numbers $\sigma = \sigma^{ext}\sigma^{int}$ (Eq. (52), Ercolani et al., 2007), which are easy to obtain once the point groups of all partners contributing to the assembly process are at hand (Figure 66).

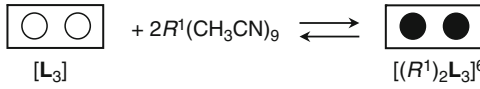

(49)

Point group: D_3	D_{3h}	D_3	C_{3v}
σ_{ext}: 6	6	6	3
σ_{int}: 1	3^9	1	1

$$\omega_{2,[L_3]}^{R^1,R^1} = \frac{6 \cdot 6^2 \cdot (3^9)^2}{6 \cdot 3^{18}} = 36 \Rightarrow \beta_{2,[L_3]}^{R^1,R^1} = 36 \cdot (f_k^{R^1})^2 \cdot u_{1-2}^{R^1,R^1}$$

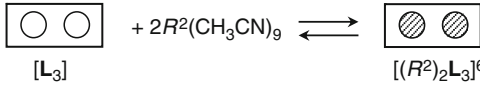

(50)

Point group: D_3	D_{3h}	D_3	C_{3v}
σ_{ext}: 6	6	6	3
σ_{int}: 1	3^9	1	1

$$\omega_{2,[L_3]}^{R^2,R^2} = \frac{6 \cdot 6^2 \cdot (3^9)^2}{6 \cdot 3^{18}} = 36 \Rightarrow \beta_{2,[L_3]}^{R^2,R^2} = 36 \cdot (f_k^{R^2})^2 \cdot u_{1-2}^{R^2,R^2}$$

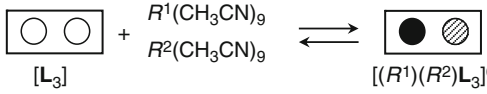

(51)

Point group: D_3	D_{3h}	C_3	C_{3v}
σ_{ext}: 6	6	3	1
σ_{int}: 1	3^9	1	1

$$\omega_{2,[L_3]}^{R^1,R^2} = \frac{6 \cdot 6^2 \cdot (3^9)^2}{3 \cdot 3^{18}} = 72 \Rightarrow \beta_{2,[L_3]}^{R^1,R^2} = 72 \cdot f_k^{R^1} \cdot f_k^{R^1} \cdot u_{1-2}^{R^1,R^2}$$

FIGURE 66 Thermodynamic modeling of the formation of binuclear triple-stranded helicates with ligands **L11** and **L13** in acetonitrile (Piguet et al., 2005). For the sake of simplicity, the unbound R^{III} cations are systematically considered as tricapped-trigonal prismatic nine-coordinate solvates.

$$\omega_{m,[L_3]}^{R^i,R^j} = \frac{\sigma_{[L_3]}\sigma_{R^i}\sigma_{R^i}}{\sigma_{[R^jR^jL_3]}(\sigma_{CH_3CN})^{18}} \tag{52}$$

From Eqs. (49)–(51), it is trivial to show that the thermodynamic constant characterizing the exchange process in equilibrium (53) only depends on the product of the ratio of statistical factors, which amounts to 4, and on the ratio of the Boltzmann factors referring to the various intermetallic interactions operating in the different complexes (Eq. (54), Piguet et al., 2005).

$$[(R^1)_2\mathbf{L}_3]^{6+} + [(R^2)_2\mathbf{L}_3]^{6+} \rightleftharpoons 2[(R^1)(R^2)\mathbf{L}_3]^{6+} \quad K_{\text{exch,bi}}^{R^1,R^2} \tag{53}$$

$$K_{\text{exch,bi}}^{R^1,R^2} = \frac{(\beta_{2,[\text{L}_3]}^{R^1,R^2})^2}{\beta_{2,[\text{L}_3]}^{R^1,R^1}\beta_{2,[\text{L}_3]}^{R^2,R^2}} = 4\cdot\frac{(u_{1-2}^{R^1,R^2})^2}{u_{1-2}^{R^1,R^1}u_{1-2}^{R^2,R^2}} = 4(u_{1-2}^{\text{mix}})^2 \tag{54}$$

In absence of heterometallic recognition, we have $\Delta E_{1-2}^{R^1,R^2} = 1/2(\Delta E_{1-2}^{R^1,R^1} + \Delta E_{1-2}^{R^2,R^2})$, and the mixing rule gives $\Delta E_{1-2}^{\text{mix}} = \Delta E_{1-2}^{R^1,R^2} - (\Delta E_{1-2}^{R^1,R^1} + \Delta E_{1-2}^{R^2,R^2})/2 = 0$ (Borkovec et al., 2004). Introducing $u_{1-2}^{\text{mix}} = \exp(-\Delta E_{1-2}^{\text{mix}}/RT)=1$ in Eq. (54) eventually confirms that $K_{\text{exch,bi}}^{R^1,R^2} = 4$ under pure statistical conditions, which translates into a 1:2:1 binomial distribution for the complexes $[(R^1)_2(\mathbf{L}k)_3]^{6+}$ (25%), $[(R^1)(R^2)(\mathbf{L}k)_3]^{6+}$ (50%), and $[(R^2)_2(\mathbf{L}k)_3]^{6+}$ (25%) at the stoichiometric ratio $[R^1]_{\text{tot}} : [R^2]_{\text{tot}} : [\text{L}]_{\text{tot}} = 1 : 1 : 3$. A thorough investigation of equilibrium (53) for 11 different R^1/R^2 lanthanide pairs with ligand **L13b** leading to two identical N_6O_3 nonadentate cavities in the virtual $(\mathbf{L13^b})_3$ molecule, indeed demonstrates that the mixing rule with $\Delta E_{1-2}^{\text{mix}} = 0$ is systematically obeyed ($K_{\text{exch,bi}}^{R^1,R^2} = 4.0(3)$, Zeckert et al., 2004), which implies no specific heterometallic recognition. The same trend is observed for ligand **L11** with the La^{III}/Eu^{III} pair, but $K_{\text{exch,L11}}^{\text{La,Lu}} = 1.2$ is found for the La^{III}/Lu^{III} pair, which indicates some deviations from statistical distribution with an approximate 1:1:1 speciation (i.e., $[(La_2(\mathbf{L11})_3]^{6+}$ (32.5%), $[\text{LaLu}(\mathbf{L11})_3]^{6+}$ (35%) and $[Lu_2(\mathbf{L11})_3]^{6+}$ (32.5%)) at the stoichiometric ratio $[R^1]_{\text{tot}} : [R^2]_{\text{tot}} : [\text{L}]_{\text{tot}} = 1 : 1 : 3$ (Piguet et al., 1993c). This trend has been tentatively assigned to a change in the affinity of the N_9 site for the smaller lanthanide due to unfavorable intramolecular interstrand packing, which specifically affects $f_{N_9}^{\text{Lu}}$ in $[\text{LaLu}(\mathbf{L11})_3]^{6+}$ ($f_{N_9}^{\text{Lu(La)}}$) and $[Lu_2(\mathbf{L11})_3]^{6+}$ ($f_{N_9}^{\text{Lu(Lu)}}$). In these conditions, $K_{\text{exch,bi}}^{\text{La,Lu}}$ depends on the specific affinities $f_{N_9}^{\text{Lu(La)}}$ and $f_{N_9}^{\text{Lu(Lu)}}$ (Eq. (55)), and no unambiguous assignment either to a change in local affinities, or to a change in intermetallic interaction can be proposed (Piguet et al., 1993c; Piguet et al., 2005).

$$K_{\text{exch,L11}}^{\text{La,Lu}} = \frac{(\beta_{2,[\text{L11}_3]}^{\text{La,Lu}})^2}{\beta_{2,[\text{L11}_3]}^{\text{La,La}}\beta_{2,[\text{L11}_3]}^{\text{Lu,Lu}}} = 4\left(\frac{f_{N_9}^{\text{Lu(La)}}}{f_{N_9}^{\text{Lu(Lu)}}}\right)^2\frac{(u_{1-2}^{\text{La,Lu}})^2}{u_{1-2}^{\text{La,La}}u_{1-2}^{\text{Lu,Lu}}} \tag{55}$$

Whatever the origin of this recognition effect is, it can be arbitrarily attributed to the sole effect of changes in intermetallic interactions. Introducing $K_{\text{exch,L11}}^{\text{La,Lu}} = 1.2$ in Eq. (54) gives $u_{1-2}^{\text{mix}} = 0.547$ and $\Delta E_{1-2}^{\text{mix}} = 1.5$ kJ mol^{-1}, a value much smaller than thermal energy $RT = 2.5$ kJ mol^{-1} at room temperature, which slightly disfavors the formation of the heterometallic $[\text{LaLu}(\mathbf{L11})_3]^{6+}$ helicate.

4.1.2 Polynuclear helicates

The extension of this approach to the heterobimetallic trinuclear helicates $[(R^1)_x(R^2)_{3-x}(\mathbf{L28})_3]^{9+}$ has to take into account the formation of a total of six microspecies contributing to four macrospecies (Eqs. (56)–(61) in Figure 67, Floquet et al., 2004).

The exchange process between these macrospecies (equilibrium (62)) can be modeled with Eq. (63).

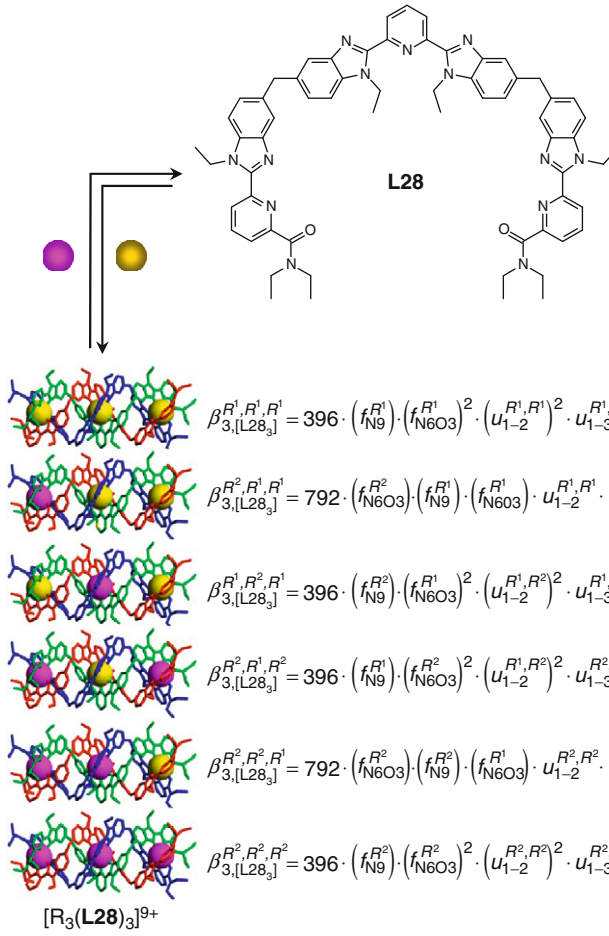

FIGURE 67 Self-assembly of the polynuclear triple-stranded helicates $[R_3(\mathbf{L28})_3]^{9+}$ in acetonitrile and associated site-binding model for their formation constants (Floquet et al., 2004); $f^R_{N_9}$ and $f^R_{N_6O_3}$ are the microscopic affinities of R^{III} for the N_9 and N_6O_3 sites, respectively, and $\Delta E^{R^i,R^j}_{1-2} = -RT\ln(u^{R^i,R^j}_{1-2})$ represents the intramolecular intermetallic interaction between two nearest neighbors, while $\Delta E^{R^i,R^j}_{1-3} = -RT\ln(u^{R^i,R^j}_{1-3})$ holds for related interaction between the terminal cations. The final helicates correspond to the X-ray crystal structure of $[Eu_3(\mathbf{L28})_3]^{9+}$ (Floquet et al., 2003).

$$[(R^1)_3(\mathbf{L28})_3]^{9+} + [(R^2)_3(\mathbf{L28})_3]^{9+} \rightleftharpoons [(R^1)_2(R^2)(\mathbf{L28})_3]^{9+} + [(R^1)(R^2)_2(\mathbf{L28})_3]^{9+} \quad K_{\text{exch,tri}}^{R^1,R^2} \tag{62}$$

$$K_{\text{exch,tri}}^{R^1,R^2} = \frac{\left(\beta_{3,[\text{L28}_3]}^{R^1,R^1,R^2} + \beta_{3,[\text{L28}_3]}^{R^1,R^2,R^1}\right)\left(\beta_{3,[\text{L28}_3]}^{R^2,R^1,R^2} + \beta_{3,[\text{L28}_3]}^{R^2,R^2,R^1}\right)}{\beta_{3,[\text{L28}_3]}^{R^1,R^1,R^1}\,\beta_{3,[\text{L28}_3]}^{R^2,R^2,R^2}} \tag{63}$$

The subsequent introduction of Eqs. (56)–(61) into Eq. (63) eventually gives an intricate mathematical expression because the additive contributions of the microspecies belonging to the same macrospecies prevent simplification. The equilibrium constant $K_{\text{exch,tri}}^{R^1,R^2}$ thus depends on all microscopic parameters used to model the formation of the microspecies. However, a statistical value of $K_{\text{exch,tri}}^{R^1,R^2} = 9$ can be obtained if (i) the absolute affinities of the N_9 and N_6O_3 sites do not vary along the lanthanide series ($f_{N_9}^{R^1} = f_{N_9}^{R^2}$ and $f_{N_6O_3}^{R^1} = f_{N_6O_3}^{R^2}$) and (ii) the intermetallic interactions also do not depend on the involved lanthanide pair ($\Delta E_{1-2}^{R^1,R^1} = \Delta E_{1-2}^{R^1,R^2} = \Delta E_{1-2}^{R^2,R^2}$ and $\Delta E_{1-3}^{R^1,R^1} = \Delta E_{1-3}^{R^1,R^2} = \Delta E_{1-3}^{R^2,R^2}$). In these conditions, reaction of lanthanide cations with the ligand **L28** in a $[R^1]_{\text{tot}} : [R^2]_{\text{tot}} : [\mathbf{L28}]_{\text{tot}} = 1:1:2$ stoichiometric ratio is expected to give the binomial distribution 1:3:3:1 for the macrospecies $[(R^1)_3(\mathbf{L28})_3]^{9+}$, $[(R^1)_2(R^2)(\mathbf{L28})_3]^{9+}$, $[(R^1)(R^2)_2(\mathbf{L28})_3]^{9+}$, and $[(R^1)_3(\mathbf{L28})_3]^{9+}$ (Floquet et al., 2004). Because of the latter demanding requirements, it is not so surprising that the experimental values $13 \leq K_{\text{exch,L28}}^{R^1,R^2} \leq 122$ found for nine different R^1/R^2 lanthanide pairs with **L28** in acetonitrile do not match the statistical distribution (Floquet et al., 2004). However, it is sufficient to consider that the absolute affinities vary along the lanthanide series ($f_{N_9}^{R^1} \neq f_{N_9}^{R^2}$ and $f_{N_6O_3}^{R^1} \neq f_{N_6O_3}^{R^2}$) to obtain a good agreement between theoretical (Eq. (63)) and experimental data, which indicates that $\Delta E_{1-2}^{\text{mix}} = 0$ kJ mol^{-1} and $\Delta E_{1-3}^{\text{mix}} = 0$ kJ mol^{-1}. In conclusion, the linear succession of N_6O_3 and N_9 sites in the triple-stranded helicates $[R_3(\mathbf{L28})_3]^{9+}$ does not evidence intermetallic recognition between pairs of lanthanides. The minute selectivity arises from minor difference in the absolute affinities of the N_6O_3 and N_9 sites along the lanthanide series (Floquet et al., 2004).

The tetranuclear homologue $[(R^1)_x(R^2)_{4-x}(\mathbf{L29})_3]^{12+}$ offers a tricky challenge since the reaction of **L29** with a R^1/R^2 pair of lanthanides produces 10 microspecies contributing to 5 macrospecies, and only the La/Lu pair has been investigated (Figure 68, Dalla Favera et al., 2007).

The adequate exchange process (equilibrium (64)), for which the site-binding model (Eq. (65)) predicts a statistical value of

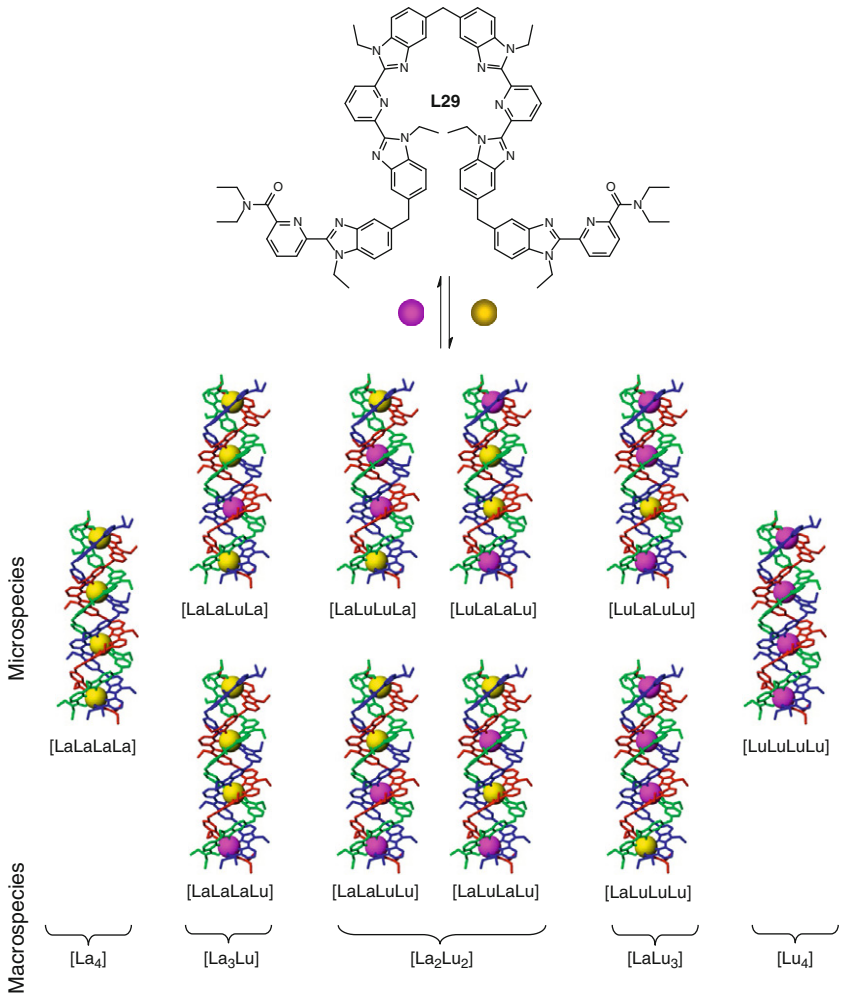

FIGURE 68 Self-assembly of the tetranuclear homo- and heterobimetallic triple-stranded helicates $[La_xLu_{4-x}(\mathbf{L29})_3]^{12+}$ showing the possible micro- and macrospecies (Dalla Favera et al., 2007).

$K^{La,Lu}_{exch,L29} = 9216 = \quad 10^{3.96}$ when $f^{La}_{N_9} = f^{Lu}_{N_9}$, $f^{La}_{N_6O_3} = f^{Lu}_{N_6O_3}$, $\Delta E^{La,La}_{1-2} = \Delta E^{La,Lu}_{1-2} = \Delta E^{Lu,Lu}_{1-2}$, $\Delta E^{La,La}_{1-3} = \Delta E^{La,Lu}_{1-3} = \Delta E^{Lu,Lu}_{1-3}$, and $\Delta E^{La,La}_{1-4} = \Delta E^{La,Lu}_{1-4} = \Delta E^{Lu,Lu}_{1-4}$, indeed shows a significant deviation with the experimental value of $K^{La,Lu}_{exch,L29} = 10^{8.5}$.

$$3[La_4(\mathbf{L29})_3]^{12+} + 3[Lu_4(\mathbf{L29})_3]^{12+} \rightleftharpoons 2[La_3Lu(\mathbf{L29})_3]^{12+} + 2[La_2Lu_2(\mathbf{L29})_3]^{12+} + 2[LaLu_3(\mathbf{L29})_3]^{12+} \; K^{La,Lu}_{exch,L29} \tag{64}$$

$$K^{\mathrm{La,Lu}}_{\mathrm{exch,L29}} = \frac{(\beta^{\mathrm{La,Lu,Lu,Lu}}_{4,[\mathrm{L29_3}]} + \beta^{\mathrm{Lu,La,Lu,Lu}}_{4,[\mathrm{L29_3}]})^2 (\beta^{\mathrm{La,La,Lu,Lu}}_{4,[\mathrm{L29_3}]} + \beta^{\mathrm{La,Lu,La,Lu}}_{4,[\mathrm{L29_3}]} + \beta^{\mathrm{La,Lu,Lu,La}}_{4,[\mathrm{L29_3}]} + \beta^{\mathrm{Lu,La,La,Lu}}_{4,[\mathrm{L29_3}]})^2}{(\beta^{\mathrm{La,La,La,La}}_{4,[\mathrm{L29_3}]})^3 (\beta^{\mathrm{Lu,Lu,Lu,Lu}}_{4,[\mathrm{L29_3}]})^3} \times \frac{(\beta^{\mathrm{La,La,La,Lu}}_{4,[\mathrm{L29_3}]} + \beta^{\mathrm{La,La,Lu,La}}_{4,[\mathrm{L29_3}]})^2}{1} \tag{65}$$

The minor variation of the absolute affinities of the two different sites for $R = \mathrm{La}$ and $R = \mathrm{Lu}$ ($f^{\mathrm{La}}_{\mathrm{N_9}} \neq f^{\mathrm{Lu}}_{\mathrm{N_9}}$ and $f^{\mathrm{La}}_{\mathrm{N_6O_3}} \neq f^{\mathrm{Lu}}_{\mathrm{N_6O_3}}$) is responsible for an increase in $K^{\mathrm{La,Lu}}_{\mathrm{exch,L29}}$ by a factor 2.8 from the statistics ($K^{\mathrm{La,Lu}}_{\mathrm{exch,L29}} = 10^{4.4}$), but the experimental values $K^{\mathrm{La,Lu}}_{\mathrm{exch,L29}} = 10^{8.5}$ can be only reproduced with the explicit consideration of intermetallic recognition $\Delta E^{\mathrm{mix}}_{1-2} = \Delta E^{\mathrm{La,Lu}}_{1-2} - (\Delta E^{\mathrm{La,La}}_{1-2} + \Delta E^{\mathrm{Lu,Lu}}_{1-2})/2 = -2.0$ kJ mol^{-1} favoring the formation of adjacent La/Lu pairs in the final helicates. It is difficult to assign an unambiguous origin to such small effects, but we notice that their existence relies on the connection of two adjacent polyaromatic N_9 sites in $[\mathrm{La}_x\mathrm{Lu}_{2-x}(\mathbf{L11})_3]^{6+}$ ($\Delta E^{\mathrm{mix}}_{1-2} = 1.5$ kJ mol^{-1}) and in $[\mathrm{La}_x\mathrm{Lu}_{4-x}(\mathbf{L29})_3]^{12+}$ ($\Delta E^{\mathrm{mix}}_{1-2} = -2$ kJ mol^{-1}) (Dalla Favera et al., 2007).

4.2 Nonaxial polytopic receptors: Statistical distributions and deviations

The heterobitopic C_s-symmetrical ligands **L30** and **L31** (Figure 48) have been designed for emphasizing the changes in absolute metal–ligand affinities *via* the formation of very different coordination sites in the binuclear heterometallic helicates HHH-$[(R^1)_x(R^2)_{2-x}(\mathbf{L30})_3]^{6+}$, HHT-$[(R^1)_x(R^2)_{2-x}(\mathbf{L30})_3]^{6+}$, HHH-$[(R^1)_x(R^2)_{2-x}(\mathbf{L31}\text{-H})_3]^{3+}$, and HHT-$[(R^1)_x(R^2)_{2-x}(\mathbf{L31}\text{-H})_3]^{3+}$ (André et al., 2002, 2004; Jensen et al., 2006, 2008). The existence of the facile HHH ↔ HHT isomerization process (Figure 69A) produces eight microspecies (Eqs. (66)–(73), Figure 69B)

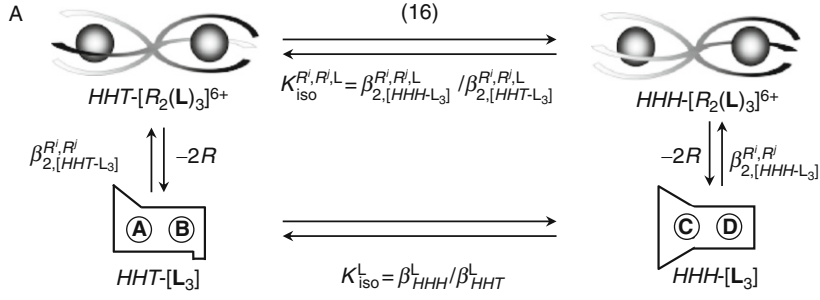

FIGURE 69 Continued

B

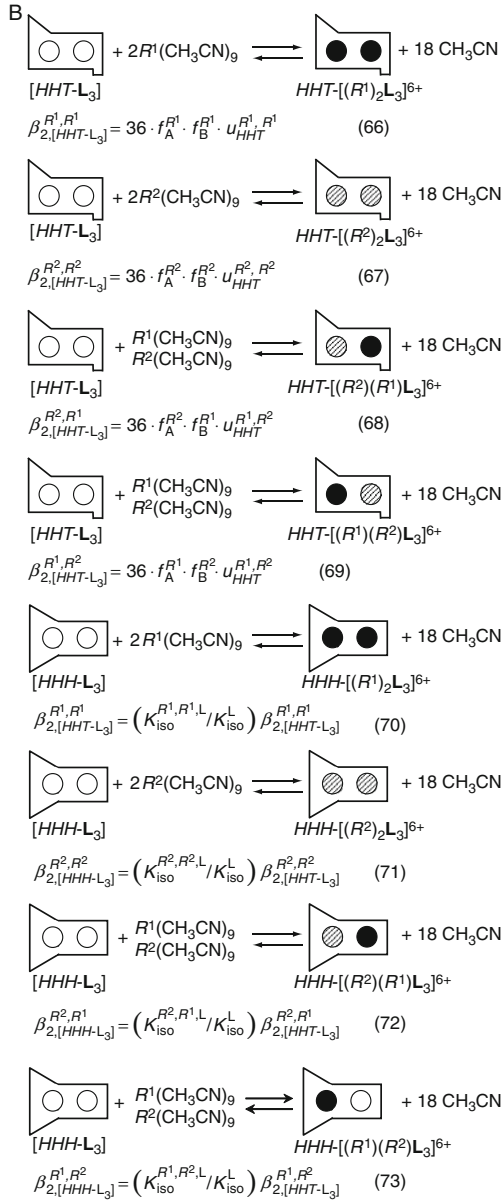

FIGURE 69 Thermodynamic modeling of the formation of the eight microspecies contributing to the binuclear triple-stranded helicates $[(R^1)_x(R^2)_{2-x}\mathbf{L}_3]^{6+}$ in acetonitrile (**L** is a nonaxial ligand). (A) HHT ↔ HHH isomerization process (Eq. (16)) and thermodynamic cycle and (B) complexation reactions. For the sake of simplicity, the unbound R^{III} cations are systematically considered as tricapped-trigonal prismatic nine-coordinate solvates.

contributing to the three macrospecies characterizing the exchange process of bimetallic binuclear helicates (equilibrium (53)).

The introduction of Eqs. (66)–(73) into Eq. (54) gives Eq. (74), which reduces to $K_{\mathrm{exch,bi}}^{R^1,R^2} = 4$ if the absolute affinities ($f_{\mathrm{A}}^{R^1} = f_{\mathrm{A}}^{R^2}, f_{\mathrm{B}}^{R^1} = f_{\mathrm{B}}^{R^2}$), intermetallic interactions ($u_{\mathrm{HHT}}^{R^1,R^1} = u_{\mathrm{HHT}}^{R^1,R^2} = u_{\mathrm{HHT}}^{R^2,R^2}$) and isomerization process ($K_{\mathrm{iso}}^{R^1,R^1,\mathrm{L}} = K_{\mathrm{iso}}^{R^2,R^2,\mathrm{L}} = K_{\mathrm{iso}}^{R^1,R^2,\mathrm{L}} = K_{\mathrm{iso}}^{R^2,R^1,\mathrm{L}}$) do not vary along the lanthanide series.

$$K_{\mathrm{exch,bi}}^{R^1,R^2} = \frac{(\beta_{2,[\mathrm{HHH-L_3}]}^{R^1,R^2} + \beta_{2,[\mathrm{HHH-L_3}]}^{R^2,R^1} + \beta_{2,[\mathrm{HHT-L_3}]}^{R^1,R^2} + \beta_{2,[\mathrm{HHT-L_3}]}^{R^2,R^1})^2}{(\beta_{2,[\mathrm{HHH-L_3}]}^{R^1,R^1} + \beta_{2,[\mathrm{HHT-L_3}]}^{R^1,R^1})(\beta_{2,[\mathrm{HHH-L_3}]}^{R^2,R^2} + \beta_{2,[\mathrm{HHT-L_3}]}^{R^2,R^2})} \qquad (74)$$

Although this complete derivation has not been previously published, it fully justifies the intuitive proposal of the formation of 50% of the bimetallic macrospecies $[(R^1)(R^2)\mathbf{L}_3]^{6+}$ for a stoichiometric ratio $[R^1]_{\mathrm{tot}} : [R^2]_{\mathrm{tot}} : [\mathrm{L}]_{\mathrm{tot}} = 1 : 1 : 3$ in absence of specific recognition of the metal ions (André et al., 2002). Interestingly, thorough studies of the distribution of the various macrospecies for different R^1/R^2 pairs with the ligands **L30**[a] (André et al., 2004), **L30**[b,c] (Jensen et al., 2006), and **L30**[d,e] (Jensen et al., 2008) show a systematic increase in the quantity of bimetallic complex upon increasing $\Delta r_{1,2}$, whereby $\Delta r_{1,2} = |r^{R^1} - r^{R^2}|$ is the difference in size between the two ionic radii of the lanthanides (Figure 70).

When we combine the latter trend with the observation of statistical distributions for all ligands, except **L30**[b], for $\Delta r_{1,2} \leq 2$ pm (Figure 70), we can tentatively assign a large part of the deviation from statistics to changes in the absolute affinities of the different sites along the lanthanide series. In the most favorable case, the bimetallic $[\mathrm{LaLu}(\mathbf{L30}^{\mathbf{a}})_3]^{6+}$ complex accounts for 90% of the distribution of the microspecies. Moreover, NMR data and X-ray crystal structures unambiguously establish that the macrospecies HHH-$[(R^1)(R^2)(\mathbf{L30})_3]^{6+}$ with the smallest lanthanide occupying the N_6O_3 site largely dominates the distribution of this bimetallic macrospecies. Since $K_{\mathrm{iso}}^{R^i,R^j,\mathrm{L}}$ also affects $K_{\mathrm{exch,bi}}^{R^1,R^2}$ (Eq. (74)), it is not so surprising that an experimental correlation has been evidenced between these two processes, which has been empirically expressed in Jensen et al. (2008) as the favored formation of bimetallic complexes ($K_{\mathrm{exch,bi}}^{R^1,R^2} > 4$) for ligands showing a preference for HHH isomer ($K_{\mathrm{iso}}^{R^i,R^j,\mathrm{L}} > 1$).

4.3 Solid state and solution structures

In view of the minute values of the mixing energies $|\Delta E_{1-2}^{\mathrm{mix}}| \leq 2.0$ kJ mol^{-1} associated with the recognition of the La/Lu pairs in triple-stranded helicates with the C_2-symmetrical ligands **L11**,

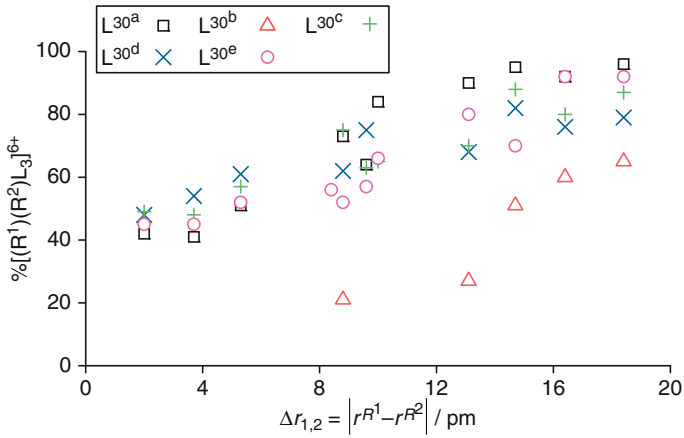

FIGURE 70 Percentage of bimetallic $[(R^1)(R^2)(\mathbf{L30})_3]^{6+}$ complexes in acetonitrile (adapted from Jensen et al., 2008).

L13, **L28**, and **L29**, the preparation of pure bimetallic complexes in solution almost entirely relies on the judicious tuning of the affinities of the various binding sites for given lanthanide ions, combined with entropic driving forces associated with the use of specific stoichiometric R^1:R^2:**L** ratios. The thermodynamic study of the formation of the homometallic trinuclear helicates with ligand **L28** indicates that the La/Eu pair is particularly favorable and 48% of the D_3-symmetrical $[EuLaEu(\mathbf{L28})_3]^{9+}$ microspecies is expected (shortly termed EuLaEu), and indeed observed in acetonitrile upon reaction of **L28** (10 mM) with La^{III} and Eu^{III} in a La:Eu:**L28** = 1:2:3 ratio (Floquet et al., 2004). EuEuEu (23%), LaLaEu (19%), LaEuEu (8%), and LaLaLa + LaEuLa (2%) complete the speciation in solution. Crystallization of this mixture produces X-ray quality crystals of empirical formulae $[La_{0.96}Eu_{2.04}(\mathbf{L28})_3](CF_3SO_3)_9$ and whose molecular structure of the cationic triple-stranded helicate is almost superimposable with that of $[Eu_3(\mathbf{L28})_3]^{9+}$, except for a significant expansion of the *R*–N bonds in the central N_9 coordination site (Figure 71, Floquet et al., 2004).

Refinements of the diffraction data with adjustable population parameters show that the terminal N_6O_3 sites contain 90% of Eu^{III} and 10% of La^{III}, while the central N_9 site accommodates 74% of La^{III} and 26% of Eu^{III}. Further high-resolution emission spectra using Eu^{III} as a probe (see next section) demonstrate that these global population parameters indeed correspond to the cocrystallization of EuLaEu (54%), LaLaEu (20%) and EuEuEu (26%), a distribution in the solid state which closely matches the speciation found in the original solution. Finally, paramagnetic ^1H NMR data collected for EuLaEu, YbLaYb, LuNdLu, and LuEuLu confirm the formation of D_3-symmetrical triple-stranded helicates in solution,

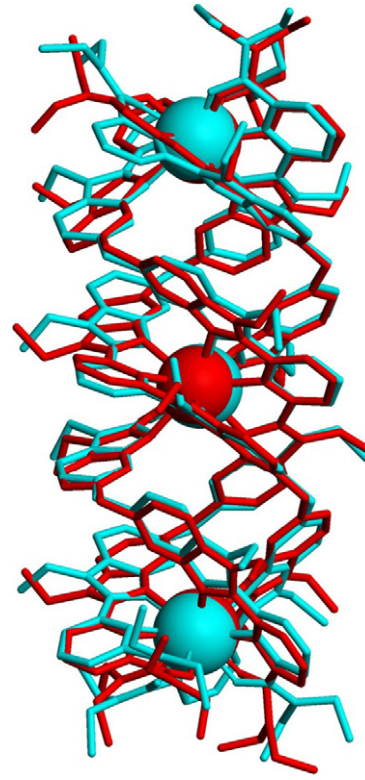

FIGURE 71 Optimized superimposition of the molecular structures of $[EuLaEu(\mathbf{L28})_3]^{9+}$ and $[Eu_3(\mathbf{L28})_3]^{9+}$ viewed perpendicular to the *pseudo*-C_3-axis (adapted from Floquet et al., 2004).

for which the crystal structure of $[Eu_3(\mathbf{L28})_3]^{9+}$ is a satisfying model. The same approach for the tetranuclear bimetallic helicates $[La_xLu_{4-x}(\mathbf{L29})_3]^{12+}$ (shortly termed La_xLu_{4-x}) leads to a more complicated speciation with considerable spectral overlap because of the coexistence of 10 microspecies possessing either C_3- or D_3-symmetry (Figure 68, Dalla Favera et al., 2007). The analysis of the intricate ^{1}H-NMR data requires multilinear least-squares techniques in order to assign clearly identified signals to each microspecies (Figure 72A), which eventually allows a direct access to experimental speciation in solution (Figure 72B).

A nonlinear least-squares fit of the experimental speciation eventually gives the micro- and macroscopic formation constants collected in Figure 73 (Dalla Favera et al., 2007).

The parallel global fit of binuclear (**L11**, **L13**), trinuclear (**L28**), and tetranuclear (**L29**) symmetrical helicates demonstrates that $f^{R^i}_{N_9} \approx f^{R^i}_{N_6O_3}$,

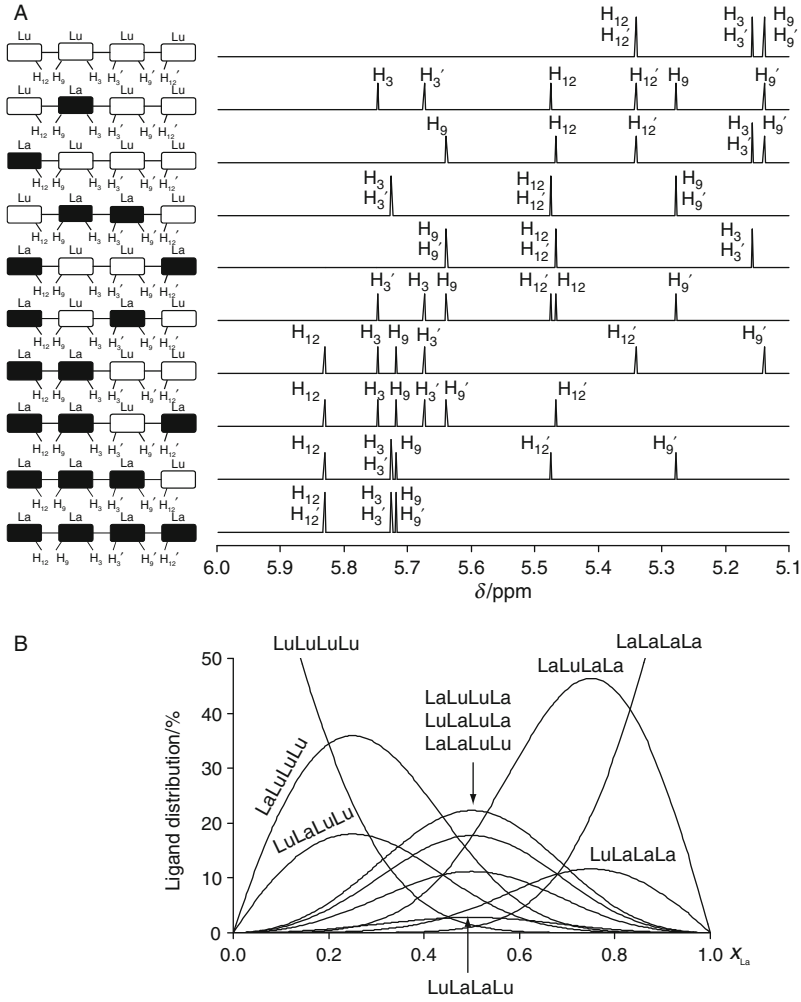

FIGURE 72 (A) Fitted individual ^{1}H NMR spectra of the 10 microspecies $[La_xLu_{4-x}(\mathbf{L29})_3]^{12+}$ in the 5–6 ppm range ($x = 0$–4) and (B) ligand distributions in the microspecies $[La_xLu_{4-x}(\mathbf{L29})_3]^{12+}$ observed during the titration of **L29** with La^{III} and Lu^{III} ($x = 0$–4, total ligand concentration $= 10^{-2}$ M, total metal concentration $= 1.33 \times 10^{-2}$ M, lanthanum mole fractions $x_{La} = [La]/([La]+[Lu]) = 0$–1 (adapted from Dalla Favera et al., 2007).

which limits deviation from statistics to $\Delta E_{1-2}^{mix} = -2$ kJ mol^{-1}. In these conditions, no attempt has been made to isolate pure bimetallic tetranuclear helicates because of insufficient selectivity. Surprisingly, basically the same adjacent N_9 and N_6O_3 coordination sites produced by the wrapping of three C_s-symmetrical ligand **L30** in HHH-$[R_2(\mathbf{L30})_3]^{6+}$

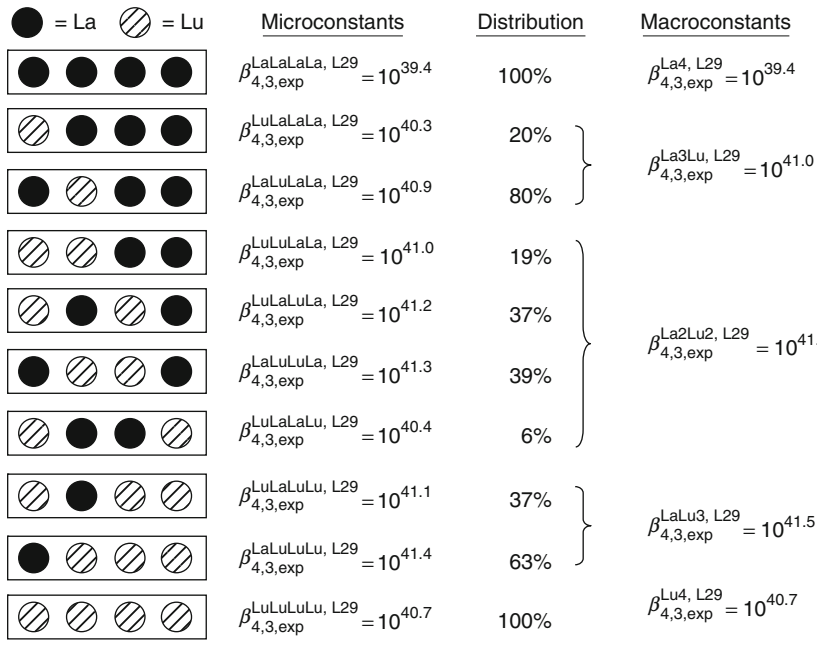

FIGURE 73 Thermodynamic macro- and microconstants characterizing the formation of the bimetallic complexes $[La_xLu_{4-x}(\mathbf{L29})_3]^{12+}$ (adapted from Dalla Favera et al., 2007).

produces more encouraging selectivity. According to ^{1}H-NMR data in acetonitrile solution, the bimetallic $[(R^1)(R^2)(\mathbf{L30^a})_3]^{6+}$ complexes exist mainly as the HHH-isomer with the smaller lanthanide located in the N_6O_3 site (André et al., 2004). X-ray diffraction measurements performed on crystals of $[(R^1)(R^2)(\mathbf{L30^a})_3]^{6+}$ (R^1R^2 = LaTb, LaEu, PrEr, PrLu; André et al., 2004) and $[(R^1)(R^2)(\mathbf{L30^c})_3]^{6+}$ (R^1R^2 = PrLu, NdLu; Jensen et al., 2006) isolated from thermodynamic mixtures indeed confirm the solution structures (Figure 74).

However, the limited quality of the refinement of the X-ray data suggests that some minor scrambling probably occurred, but its quantification within different microspecies is beyond the precision of the method (André et al., 2004). Though no complete thermodynamic analysis is available for helicates with nonaxial ligands, examination of the mathematical form of $K^{R^1,R^2}_{exch,bi}$ (Eq. (74)) implies that a strong selectivity for lanthanide pairs only results when $f^{R^i}_{N_9} \neq f^{R^i}_{N_6O_3}$, which also induces a strong dependency on $K^{R^i,R^j,L30}_{iso}$ (Eq. (16)). We are thus tempted to conclude that the absolute affinities of each adjacent N_9 and N_6O_3 site in C_3-symmetrical HHH-$[R_2(\mathbf{L30})_3]^{6+}$ display a more pronounced dependence on the lanthanide size than their similar counterpart in more symmetrical D_3-symmetrical helicates $[R_2(\mathbf{L11})_3]^{6+}$ or $[R_2(\mathbf{L13})_3]^{6+}$.

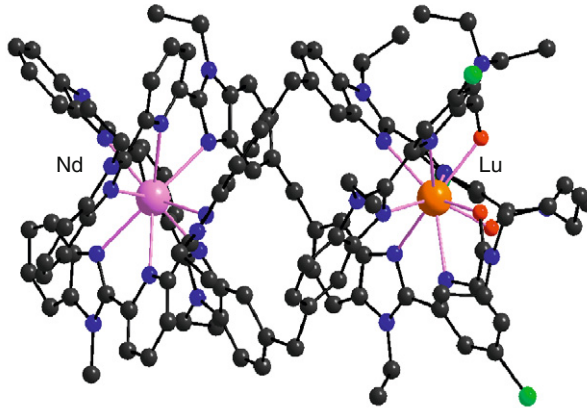

FIGURE 74 Molecular structure of $[NdLu(\mathbf{L30^c})_3]^{6+}$ (reproduced by permission from Jensen et al., 2006, © American Chemical Society, 2006).

4.4 Photophysical properties

The isolation of a heterometallic R^1/R^2 pair in a triple-stranded helicate brings novel photophysical properties, because $R^1 \rightarrow R^2$ energy transfers (or reverse $R^2 \rightarrow R^1$ depending on the relative energies of the donor and acceptor levels) may affect the energy migration processes in the complex and the final emission output (Figure 75).

Let us focus on the photophysical intermetallic communication $k^{et}_{R^1,R^2}$ resulting from intramolecular 4f → 4f energy transfer and whose global efficiency is given in Eq. (75).

$$\eta^{et}_{R^1,R^2} = \frac{k^{et}_{R^1,R^2}}{(k^{nr}_{R^1} + k^{r}_{R^1}) + k^{et}_{R^1,R^2}} \tag{75}$$

Assuming that (i) $k^{obs}_{R^1} = k^{nr}_{R^1} + k^{r}_{R^1} = (\tau^{obs}_{R^1,R^1})^{-1}$ is identical in the homometallic $[(R^1)_2\mathbf{L}_3]^{6+}$ and in the bimetallic $[(R^1)(R^2)\mathbf{L}_3]^{6+}$ complexes and (ii) the $R^1 \rightarrow R^2$ energy transfer is the only source of additional deactivation of the R^1 donor level, the rate transfer constant $k^{et}_{R^1,R^2}$ can be easily deduced from the measurement of the excited state lifetime $(\tau^{obs}_{R^1,R^2})^{-1} = k^{et}_{R^1,R^2} + k^{obs}_{R^1}$ of R^1 in the bimetallic complex $[(R^1)(R^2)\mathbf{L}_3]^{6+}$ (Eq. (76)).

$$k^{et}_{R^1,R^2} = (\tau^{obs}_{R^1,R^2})^{-1} - (\tau^{obs}_{R^1,R^1})^{-1} \tag{76}$$

Obviously, the intermetallic energy transfer rate $k^{et}_{R^1,R^2}$ obeys *Fermi*'s golden rule (Eq. (7)). The large intermetallic distances in bimetallic lanthanide helicates (≥9 Å) combined with the minute expansion of

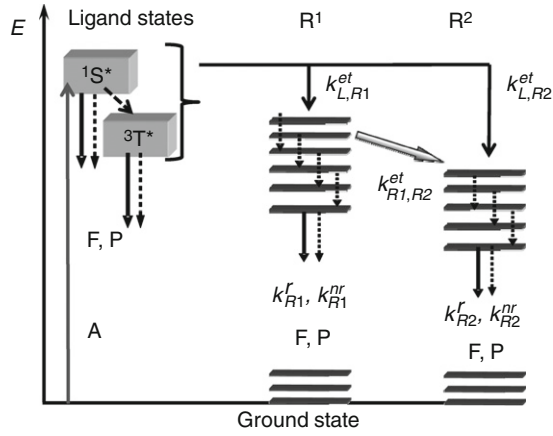

FIGURE 75 Schematic representation of energy absorption, emission, and dissipation processes in a bimetallic (R^1, R^2) lanthanide complex. F, fluorescence; P, phosphorescence; et, energy transfer; r, radiative; nr, nonradiative.

4f-orbitals justify the preponderance of an electrostatic multipolar mechanism limited to the dipole–dipolar interaction, namely *Förster's* mechanism described in Eq. (77), where R^{R^1,R^2} is the separation between the two oscillating dipoles, which is assumed to be the intermetallic distance for $4f \rightarrow 4f$ energy transfer, and $R_0^{R^1,R^2}$ is the contact distance for 50% energy transfer (Bünzli, 1989).

$$\eta^{et}_{R^1,R^2} = \frac{k^{et}_{R^1,R^2}}{(k^{nr}_{R^1} + k^{r}_{R^1}) + k^{et}_{R^1,R^2}} = 1 - \frac{\tau^{obs}_{R^1,R^2}}{\tau^{obs}_{R^1,R^1}} = \frac{1}{1 + (R^{R^1,R^2}/R_0^{R^1,R^2})^6} \qquad (77)$$

This approach has been applied to solid-state mixtures of $[Eu_2(\mathbf{L11})_3]^{6+}$, $[TbEu(\mathbf{L11})_3]^{6+}$, and $[Tb_2(\mathbf{L11})_3]^{6+}$ (Figure 12A), in which Tb^{III} acts as the donor ($R^{Tb,Eu} = 9$ Å, Piguet et al., 1993b). The Tb($^5D_4$) luminescence decay is indeed biexponential with one long lifetime corresponding to the emission of $[Tb_2(\mathbf{L11})_3]^{6+}$ ($\tau^{obs}_{Tb,Tb} = 0.66$ ms) and one short lifetime ($\tau^{obs}_{Tb,Eu} = 0.16$ ms) associated with $[TbEu(\mathbf{L11})_3]^{6+}$, in which $Tb \rightarrow Eu$ energy transfer occurs. Concomitantly, the intensity of the Tb emission decreases sharply while the photophysical properties of the Eu emission (spectrum and lifetime) are the same as in the homometallic Eu_2 helicate. Application of Eqs. (76) and (77) gives $k^{et}_{Tb\rightarrow Eu} = 4.7 \times 10^3\ s^{-1}$, $\eta^{et}_{Tb\rightarrow Eu} = 76\%$, and $R_0^{Tb,Eu} = 10.7$ Å at 77 K (Piguet et al., 1993b). Alternatively, the intermetallic distance R^{R^1,R^2} in a structurally noncharacterized helicate can be estimated from lifetime measurements and Eq. (77),

assuming that a theoretical value of $R_0^{R^1,R^2}$ can be obtained with Eq. (78) (Bünzli, 1989), in which κ^2 is an orientation factor having an isotropic limit of 2/3, Q_F is the quantum yield of the donor luminescence in absence of acceptor (i.e., the R^1 quantum yield measured in $[(R^1)_2\mathbf{L}_3]^{6+}$), n is the refractive index of the intermetallic medium and J is the overlap integral between the emission spectrum of the donor (R^1) and the absorption spectrum of the acceptor (R^2) in $cm^6\,mol^{-1}$.

$$(R_0^{R^1,R^2})^6 = 8.75 \times 10^{-25}\kappa^2 Q_F n^{-4} J \quad [cm^6] \tag{78}$$

Following this procedure, Lessmann and Horrocks (2000) computed $R_0^{Eu,Nd} = 9.9$ Å in [EuNd(**L32**)$_3$] which, combined with the determination of the Eu($^5D_0$) lifetimes, gave $R^{Eu,Nd} = 13.2$ Å and 7.4 Å in [EuNd(**L32^a**] and [EuNd(**L32^b**)$_3$], respectively (Figure 49).

When the triple-stranded helicate contains different adjacent sites as in $[R_2(\mathbf{L30})_3]^{6+}$ (Figure 48) or $[R_3(\mathbf{L28})_3]^{9+}$ (Figure 67), intermetallic energy transfers can be already detected in the homometallic complexes because the excited state of the same metal in different environments is slightly different. This is demonstrated in HHH-$[Eu_2(\mathbf{L30^a})_3]^{6+}$ (André et al., 2004) and $[Eu_3(\mathbf{L28})_3]^{9+}$ (Floquet et al., 2003), for which the only Eu^{III}-centered emission detected at room temperature arises from the EuN_6O_3 sites. At 10 K, a dual emission from both EuN_9 and EuN_6O_3 is observed because both the intramolecular intermetallic $EuN_9 \rightarrow EuN_6O_3$ energy migration and the temperature-assisted back transfer to the low-lying MLCT state become less efficient. Finally, the combination of Eu^{III} as a luminescent probe with closed-shell La^{III} and Lu^{III} has been exploited for structurally and electronically characterizing the different emission sites in [EuLa(**L30^a**)$_3$]$^{6+}$ (André et al., 2004) and in [EuLaEu(**L28**)$_3$]$^{9+}$ (Floquet et al., 2004). The latter is a nice example of the analytical power of the unsplit $^5D_0 \rightarrow {}^7F_0$ transition. The spectrum of the homotrimetallic EuEuEu helicate displays two components arising from the terminal and central sites (Figure 76); the central site has a smaller quantum yield due to the N_9 coordination environment. The proportion of the integrated emission intensity of the central site (obtained after decomposition of the band with Gaussian functions) is $F_c/(F_c + F_t) = 0.27$, from which the ratio of the quantum yields can be extracted, $Q_c/Q_t = 0.74$. Taking this value into consideration, as well as the experimental $F_c/(F_c + F_t)$ ratio of 0.094 for the heterotrimetallic species EuLaEu, and a suitable model inspired from NMR data which show that the LaLaEu species accounts for about 20% in solution, the following composition of the microcrystals can be extracted: EuLaEu (54%), LaLaEu (20%), and EuEuEu (26%), in excellent agreement with elemental analysis and X-ray data. That is the microcrystal composition reflects fairly closely the speciation obtained in solution.

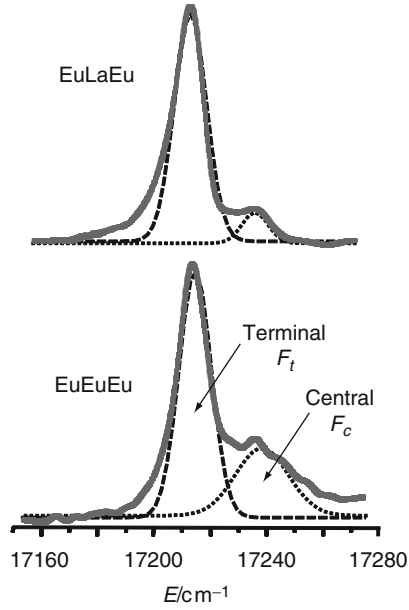

FIGURE 76 $^5D_0 \rightarrow {}^7F_0$ transitions of the hetero- (top) and homometallic (bottom) helicates with **L28** and their decomposition into Gaussian functions (redrawn after Floquet et al., 2004).

5. MODELING THE THERMODYNAMIC STABILITY OF HELICATES

In both living (Mammen et al., 1998) and inert (Huck et al., 2000; Thalladi et al., 2002) macroscopic systems, the multicomponent assembly of basic subunits plays a crucial role for the design of sophisticated organizations and functions. Replication of this approach at the molecular level is at the origin of supramolecular chemistry (Lehn, 1988), an aspect of chemistry which focuses on the combination of molecular building blocks (i.e., ligands and metal ions in coordination chemistry) to give complex nanoscopic architectures (Balzani et al., 2002, 2008; Lehn, 1995, 2007; Stoddart and Philp, 1996). The mechanical processes operating at the macroscopic level are controlled by enthalpic changes, which are much more intuitive than the cohesion of molecular units implying both enthalpic and entropic contributions. This statement can be illustrated if we consider a single macroscopic object that can be thrown from a distance and so be randomly distributed between two boxes, one twice the size of the other. The entropic contribution is simply given by Boltzmann relationship $\Delta S = k \ln (2/1) = 10^{-23}\,\mathrm{J\,K^{-1}}$, which translates into a negligible contribution to the total energy at room temperature ($\Delta E = -T\Delta S = -2.9 \times 10^{-21}\,\mathrm{J}$), which is

not necessary to take into account for further energetic calculations with this system. At the molecular level, the huge amount of particles contained in an acceptable macroscopic quantity such as one mole ($N_A = 6.02 \times 10^{23}$ molecules mol^{-1}) produces an entropic contribution of $\Delta S = k\ln(2^{N_{Av}}) = R\ln(2) = 5.8\ \ J\,K^{-1}$, which gives $\Delta E = -T\Delta S = -1.73\ kJ\ mol^{-1}$ at room temperature; a substantial and far from negligible contribution (Smith, 2004). Consequently, the rationalization of multicomponent helicate self-assembly requires an adequate modeling of the total free energy changes $\Delta G = \Delta H - T\Delta S$ occurring in solution. Since the number of independent components is only two for homometallic helicates (the metal M and the ligand L) or three for bimetallic helicates (two metals M^1, M^2, and a ligand L), these molecular edifices can serve as simple basic systems for the development of new thermodynamic tools in coordination and metallosupramolecular chemistry (Elhabiri and Albrecht-Gary, 2008; Elhabiri et al., 2004a; Fatin-Rouge et al., 2001; Hamacek et al., 2003, 2006; Pfeil and Lehn, 1992; Piguet et al., 2005).

5.1 Theoretical model for intermolecular connections: The site-binding model

The successive intermolecular connections of metal ions to a single multisite receptor represents the prototype of basic complexation processes. Its thermodynamic modeling is firmly established since the beginning of the twentieth century (Hill, 1910) and is often referred to as the protein–ligand model because of its widespread use in biology and biochemistry (Ben-Naim, 1998; Perlmutter-Hayman, 1986; van Holde, 1985). This additive free energy model has been recently formulated by introducing statistical mechanics in the site-binding model for the successive fixations of protons onto polyelectrolytes (Koper and Borkovec, 2001), and further extended for unraveling the fixation of metal ions onto a single ligand strand (Borkovec et al., 2004). Let us focus on the most simple case of the successive intermolecular connection of m trivalent lanthanide ions R to a preorganized receptor **L** possessing m binding sites (equilibrium (79), Figure 77).

$$\mathbf{L} + mR^{3+} \rightleftharpoons [R_m\mathbf{L}]^{3m+} \quad \beta_{m,1}^{R,L} \tag{79}$$

The total free energy change associated with equilibrium (79) is given by the sum of the individual free energies of connection of R to the different binding sites $\Delta G^0_{conn.,tot} = -RT\sum_{i=1}^{m}\ln(f_i^R)$ modulated by the sum of the intramolecular intermetallic interactions given by

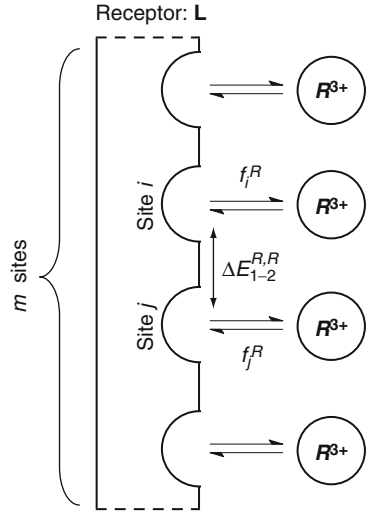

FIGURE 77 Thermodynamic protein–ligand model adapted for the successive intermolecular connections of metal ions to a one-dimensional multisite receptor (adapted from Piguet et al., 2005). f_i^R is the absolute affinity of site *i* for the entering lanthanide *R*, and $\Delta E_{1-2}^{R,R}$ is the intramolecular intermetallic interaction between two nearest neighbors.

$\Delta G_{\text{tot}}^{R,R} = \sum_{i<j} \Delta E_{1-2}^{R,R}$, if we restrict these interactions to the nearest neighbors (Eq. (80), Koper and Borkovec, 2001). Note that the notation of the last sum has been simplified; it should really be written as $\Delta G_{\text{tot}}^{R,R} = \sum_{i<j=2}^{i<j=m} \Delta E_{i-j}^{R_i,R_j}$; such simplified notation is used throughout in the following developments. However, depending on the symmetry of the reactants and products of the assembly process, several microspecies of the same energy contribute to the macrospecies, and this non-negligible entropic contribution is introduced as an additional statistical factor $\Delta G_{\text{stat}}^{R,\text{L}} = -RT\ln(\omega_{m,1}^{R,\text{L}})$ (Eq. (81), Benson, 1958, 1976).

$$\Delta G_{m,1}^{R,\text{L}} = -RT\ln(\beta_{m,1}^{R,\text{L}}) = -RT\ln(\omega_{m,1}^{R,\text{L}}) - RT\sum_{i=1}^{m} \ln(f_i^R) + \sum_{i<j} \Delta E_{1-2}^{R,R} \quad (80)$$

Since the formation constants are easily accessible in chemistry, the standard vant'Hoff isotherm transforms Eq. (80) into Eq. (81), whereby $u_{1-2}^{R,R} = \text{e}^{-\Delta E_{1-2}^{R,R}/RT}$ is often referred to as the Boltzmann factor of intermetallic interaction (Koper and Borkovec, 2001).

$$\beta_{m,1}^{R,L} = \omega_{m,1}^{R,L} \prod_{i=1}^{m} f_i^R \prod_{i<j} e^{-\Delta E_{1-2}^{R,R}/RT} = \omega_{m,1}^{R,L} \prod_{i=1}^{m} f_i^R \prod_{i<j} u_{1-2}^{R,R} \tag{81}$$

Surprisingly, one of the major difficulties encountered when applying this model in coordination chemistry is connected with the calculation of reliable statistical factors. Two parallel methods have been developed by using either the symmetry numbers of the molecules or the direct count of the microspecies formed in the reactants and products (Ercolani et al., 2007). Both techniques converge to the same result, but the symmetry number method, though less intuitive, is easier to handle and we will limit our discussion to this technique. According to Benson (1976), the symmetry number σ of a molecule affects its rotational entropy by a factor $-R\ln(\sigma)$. Consequently, the statistical contribution to the stability constant $\beta_{m,1}^{R,L}$ of equilibrium (79) is given by the ratio of the symmetry numbers of the reactants and products (Eq. (82)).

$$\omega_{m,1}^{R,L} = \frac{(\sigma^R)^m \cdot \sigma^L}{\sigma^{R_m L}} \tag{82}$$

Each factor σ is itself the product of the external (σ_{ext}) and internal (σ_{int}) symmetry numbers. The external symmetry number corresponds to the number of different but indistinguishable atomic arrangements that can be obtained by rotating a given molecule as a whole. It thus only considers symmetry operations of the first kind (that is not involving an inversion center or a symmetry plane) and it is found in practice by multiplying the order of the *independent* simple rotation axes of the point group to which the molecule belongs (axes of infinite orders are not considered because they do not generate different atomic arrangements). For instance, the tricapped-trigonal prismatic solvate $[R(CH_3CN)_9]^{3+}$ of D_{3h}-symmetry contains two types of *independent* rotational axes of the first kind: one twofold axis and one threefold axis, thus leading to $\sigma_{ext} = 2 \times 3 = 6$ (Table 11).

The internal symmetry number σ_{int} is similarly defined as the number of different but indistinguishable atomic arrangements that can be obtained by internal rotation about single bonds. The contribution of σ_{int} in a self-assembly process is nonzero only when internal rotations of the components are either blocked or released during the chemical transformation. The most straightforward application of the site-binding model (Eq. (81)) to lanthanide assembly concerns the successive fixation of Eu^{III} to $[\mathbf{L13^f}]^{2-}$ in water (equilibria (83) and (84), Piguet et al., 2005), the experimental stability constants of which have been obtained by a combination of thermodynamic and kinetic studies (Elhabiri et al., 2004a).

TABLE 11 External symmetry numbers for various point groups (Ercolani et al., 2007)

Point group	σ_{ext}
C_1, C_i, C_s, $C_{\infty v}$, R_3	1
$D_{\infty h}$	2
C_n, C_{nv}, C_{nh}	n
D_n, D_{nd}, D_{nh}	$2n$
S_n (n even)	$n/2$
T_d	12
O_h	24
I_h	60

$$[\mathbf{L13^f}]^{2-} + Eu^{3+} \rightleftharpoons [Eu(\mathbf{L13^f})]^{+} \quad \beta_{1,1}^{Eu,L13f} = 10^{4.28} \tag{83}$$

$$[\mathbf{L13^f}]^{2-} + 2Eu^{3+} \rightleftharpoons [Eu_2(\mathbf{L13^f})]^{4+} \quad \beta_{2,1}^{Eu,L13f} = 10^{6.36} \tag{84}$$

The modeling with Eq. (81) is trivial (Eqs. (85) and (86)) except for the calculation of the statistical factors. Originally, the trivalent europium atoms were considered as free cations with R_3 symmetry and $\omega_{1,1}^{Eu,L13f} = 2$ and $\omega_{2,1}^{Eu,L13f} = 1$ (Figure 78A). A fit of the model (Eqs. (85) and (86)) to the experimental data (Eqs. (83) and (84)) gave $\log(f_{N_2O}^{Eu}) = 3.98$ and $\Delta E_{1-2}^{Eu,Eu} = 9.1$ kJ mol^{-1} (Piguet et al., 2005).

$$\beta_{1,1}^{Eu,L13f} = \omega_{1,1}^{Eu,L13f} f_{N_2O}^{Eu} \tag{85}$$

$$\beta_{2,1}^{Eu,L13f} = \omega_{2,1}^{Eu,L13f} (f_{N_2O}^{Eu})^2 u_{1-2}^{Eu,Eu} \tag{86}$$

The first microscopic parameter $\Delta G_{connection}^{0} = -RT\ln(f_{N_2O}^{Eu}) = -22.7$ kJ mol^{-1} refers to the favorable free energy balance between the desolvation of the components and their binding in the complex to give one Eu-($\mathbf{L13^f}$) connection. $\Delta E_{1-2}^{Eu,Eu} > 0$ indicates a repulsive Eu. . .Eu interaction in $[Eu_2(\mathbf{L13^f})]^{4+}$ and thus the operation of an anticooperative process for the successive fixation of two Eu^{III} to $(\mathbf{L13^f})^{2-}$. Obviously, the explicit consideration of solvated cations $[Eu(H_2O)_9]^{3+}$ changes the statistical factors ($\omega_{1,1}^{Eu,L13f} = 12$ and $\omega_{2,1}^{Eu,L13f} = 36$, Figure 78B), which

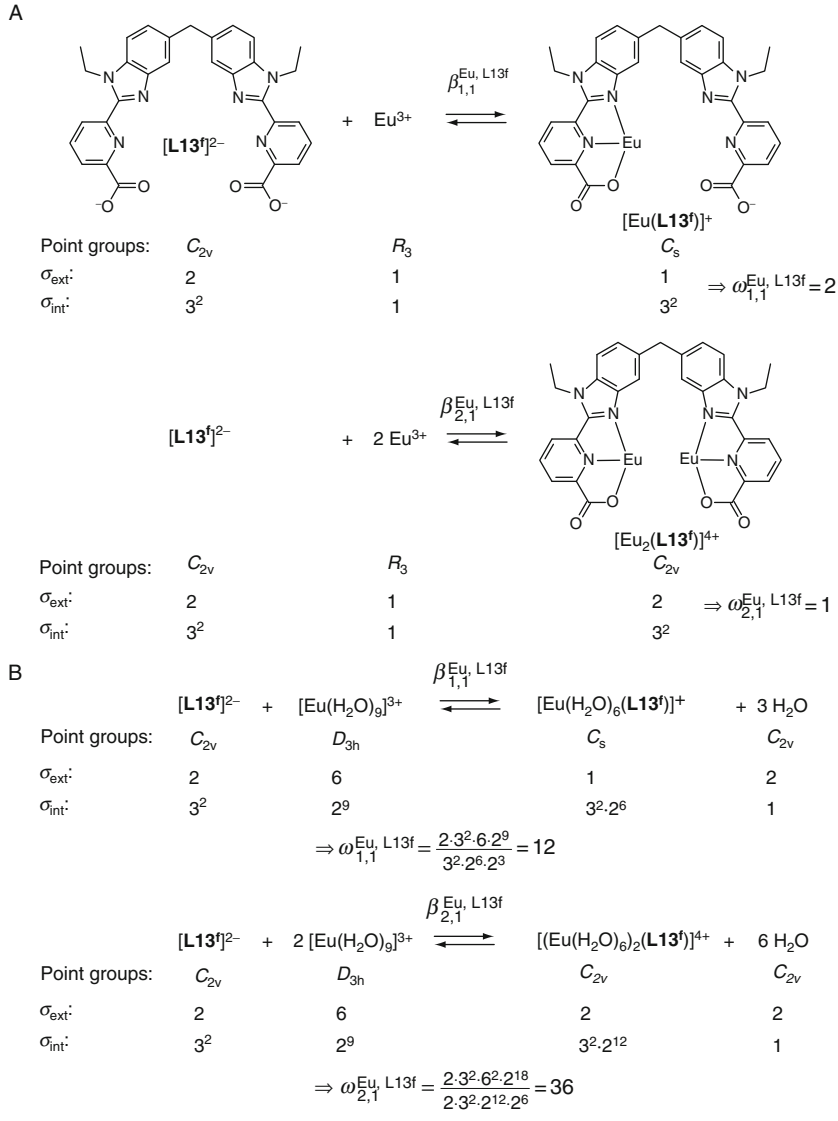

FIGURE 78 Calculation of statistical factors by using the method of the symmetry numbers for equilibrium (83) and (84). (A) The metal ions are considered as nonsolvated species and (B) the metal ions are considered as nine-coordinate tricapped-trigonal prismatic solvates.

consequently slightly affects the fitted R-ligand affinity $\log(f_{N_2O}^{Eu}) = 3.20$, but does not alter $\Delta E_{1-2}^{Eu,Eu} = 9.1$ kJ mol^{-1}.

To extend the use of the site-binding model for the assembly of lanthanide triple-stranded helicates, it is necessary to consider the three

wrapped strands as a virtual preorganized D_3-symmetrical molecular box, as exemplified for $[(\mathbf{L13^b})_3]$ in Figure 79. In these conditions, the global complexation process described by equilibrium (87) (path *i* in Figure 79A) can be partitioned into a first assembly process providing the virtual preorganized receptor $[(\mathbf{L13^b})_3]$ (equilibrium (88)) followed by purely intermolecular complexation of R^{III} (equilibrium (89), path *ii* in

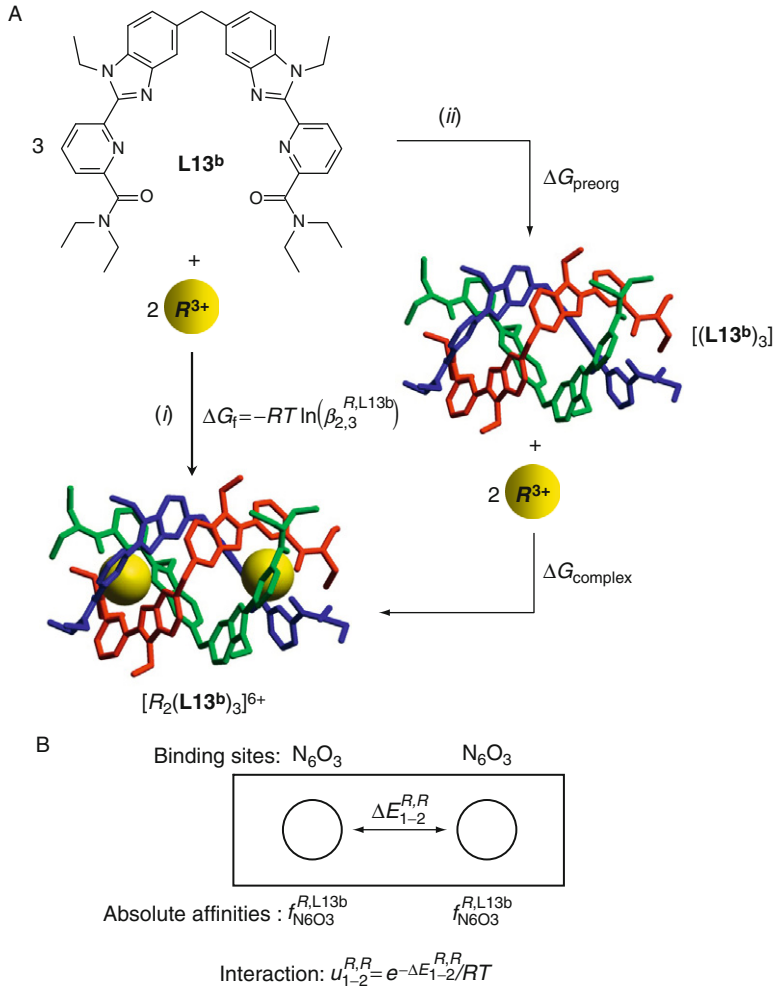

FIGURE 79 (A) Formation and solution structures of $[R_2(\mathbf{L13^b})_3]^{6+}$ showing the complete assembly process (ΔG_f, path *i*), and its partition into one virtual preorganization step (ΔG_{preorg}) followed by intermolecular complexation ($\Delta G_{complex}$, path *ii*). (B) Associated thermodynamic site-binding model.

Figure 79A), which can be easily modeled with the site-binding model (Eq. (81), Hamacek et al., 2006).

$$3\mathbf{L13^b} + 2R^{3+} \rightleftharpoons [R_2(\mathbf{L13^b})_3]^{6+} \quad \beta_{2,3}^{R,\mathrm{L13b}} \tag{87}$$

$$3\mathbf{L13^b} \rightleftharpoons (\mathbf{L13^b})_3 \quad e^{-\Delta G_{\mathrm{preog}}/RT} \tag{88}$$

.

$$[(\mathbf{L13^b})_3] + 2R^{3+} \rightleftharpoons [R_2(\mathbf{L13^b})_3]^{6+} \quad e^{-\Delta G_{\mathrm{complex}}/RT} \tag{89}$$

$\Delta G_{\mathrm{preorg}}$ is difficult to assess, but it similarly affects any complex of a given family derived from the same $[(\mathbf{L13^b})_3]$ box. In these conditions, $\Delta G_{\mathrm{preorg}}$ corresponds to a translation of the zero-level of the free energy of formation, and it can be arbitrarily set to $\Delta G_{\mathrm{preorg}} = 0$. Application of the site-binding model is then straightforward by using $[(\mathbf{L13^b})_3]$ as a pre-organized D_3-symmetrical receptor containing two N_6O_3 binding sites characterized by absolute affinities $f_{N_6O_3}^R$, $\Delta E_{1-2}^{R,R}$ being the usual intramolecular intermetallic interaction (Figure 79B). The two experimental stability constants respecting these conditions (equilibria (90) and (91)) have thus been fitted to the model (Eqs. (92) and (93)) along the lanthanide series (Table 8) to give $\log(f_{N_6O_3}^R)$ and $\Delta E_{1-2}^{R,R}$ collected in Figure 80 (R^{3+} were considered as nonsolvated cations of R_3 symmetry, Zeckert et al., 2004).

$$[(\mathbf{L13^b})_3] + R^{3+} \rightleftharpoons [R(\mathbf{L13^b})_3]^{3+} \quad \beta_{1,3}^{R,\mathrm{L13b}} \tag{90}$$

$$[(\mathbf{L13^b})_3] + 2R^{3+} \rightleftharpoons [R_2(\mathbf{L13^b})_3]^{6+} \quad \beta_{2,3}^{R,\mathrm{L13b}} \tag{91}$$

$$\beta_{1,3}^{R,\mathrm{L13b}} = 2f_{N_6O_3}^R \tag{92}$$

$$\beta_{2,3}^{R,\mathrm{L13b}} = (f_{N_6O_3}^R)^2 u_{1-2}^{R,R} \tag{93}$$

The scattered data and highly correlated parameters are mathematically reliable, but physically meaningless because two microscopic parameters $f_{N_6O_3}^R$ and $\Delta E_{1-2}^{R,R}$ are fitted to experimental data (i.e., including uncertainties) *via* exactly two equations (Eqs. (92) and (93)). To overcome this limitation, equilibria (90) and (91) have been simultaneously considered for a pair of lanthanide R^1/R^2, thus leading to four equations for four parameters ($f_{N_6O_3}^{R^1}$, $f_{N_6O_3}^{R^2}$, $\Delta E_{1-2}^{R^1,R^1}$, and $\Delta E_{1-2}^{R^2,R^2}$), together with one additional equilibrium (94) corresponding to the formation of the bimetallic helicate modeled with Eq. (95).

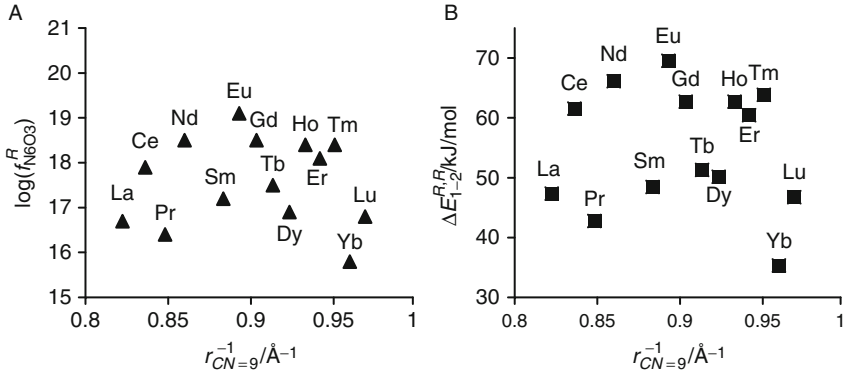

FIGURE 80 (A) Computed absolute affinities for the terminal sites ($\log(f^R_{N_6O_3})$) and (B) intermetallic interaction parameters ($\Delta E^{R,R}_{1-2}$) in the triple-stranded bimetallic helicates $[R_2(\mathbf{L13^b})_3]^{6+}$ as a function of the inverse of nine-coordinate ionic radii (fit of Eqs. (92) and (93)) (adapted from Zeckert et al., 2004).

$$[(\mathbf{L13^b})_3] + (R^1)^{3+} + (R^2)^{3+} \rightleftharpoons [(R^1)(R^2)(\mathbf{L13^b})_3]^{6+} \quad \beta^{R^1,R^2,\mathrm{L13b}}_{2,3} \tag{94}$$

$$\beta^{R^1,R^2,\mathrm{L13b}}_{2,3} = 2 f^{R^1}_{N_6O_3} f^{R^2}_{N_6O_3} u^{R^1,R^2}_{1-2} \tag{95}$$

The demonstration that no intermetallic recognition occurs and that the mixing rule $\Delta E^{R^1,R^2}_{1-2} = 1/2(\Delta E^{R^1,R^1}_{1-2} + \Delta E^{R^2,R^2}_{1-2})$ is obeyed ($K^{R^1,R^2,\mathrm{L13b}}_{\mathrm{exch,bi}} = 4.0(3)$, Eq. (54), Section 4) for 11 R^1/R^2 pairs obtained from R = La, Nd, Sm, Eu, Yb, Lu, and Y limits the number of microscopic parameters to four for a total of five experimentally accessible stability constants. Absolute affinities and intermetallic interactions can be then obtained with large, but physically meaningful uncertainties (Figure 81, Zeckert et al., 2004). The arbitrary value of $\Delta G_{\mathrm{preorg}} = 0$, which fixes the zero-point energy, prevents a physical interpretation of the absolute values of $\Delta G^0_{\mathrm{connection}} = -RT\ln(f^R_{N_6O_3})$ and $\Delta E^{R,R}_{1-2}$, but the relative trends along the series can be analyzed. According to Figure 81, we deduce that the N_6O_3 binding site is optimum for midrange R^{III} and that the intermetallic interaction is systematically repulsive (i.e., anticooperative) and roughly constant along the complete series (Zeckert et al., 2004). The same approach has been applied for the virtual preorganized receptor $[(\mathbf{L28})_3]$ in the self-assembly of the trinuclear helicates $[R_3(\mathbf{L28})_3]^{9+}$, which possess two different nine-coordinate N_9 and N_6O_3 binding sites (Figure 82, Floquet et al., 2003, 2004; Zeckert et al., 2004). Since two stability constants $\beta^{R,\mathrm{L28}}_{2,3}$ and $\beta^{R,\mathrm{L28}}_{3,3}$ for homometallic complexes, together with two macroscopic constants for the bimetallic macrospecies

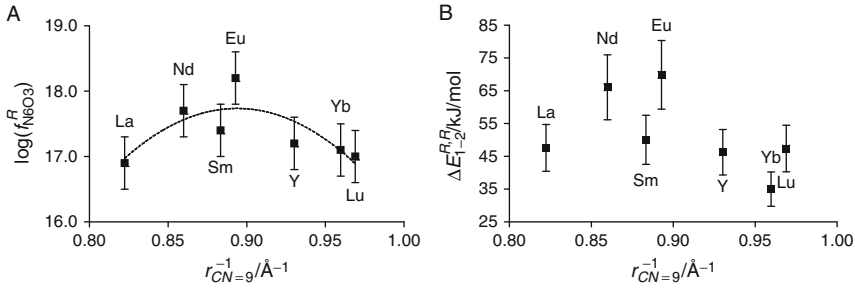

FIGURE 81 (A) Computed absolute affinities for the terminal sites ($\log(f^R_{N_6O_3})$) and (B) intermetallic interaction parameters ($\Delta E^{R,R}_{1-2}$) in the triple-stranded bimetallic helicates $[R_2(\mathbf{L13^b})_3]^{6+}$ as a function of the inverse of nine-coordinate ionic radii (fit of Eqs. (92), (93), and (95) for 11 R^1/R^2 pairs) (adapted from Zeckert et al., 2004).

$[(R^1)_2(R^2)(\mathbf{L28})_3]^{9+}$ and $[(R^1)(R^2)_2(\mathbf{L28})_3]^{9+}$ meet the conditions of their formation from the preorganized $[(\mathbf{L28})_3]$ box (Table 9), any R^1/R^2 pair provides six stability constants. This is, however, not sufficient for fitting a minimal set of six parameters ($f^{R^1}_{N_6O_3}$, $f^{R^2}_{N_6O_3}$, $f^{R^1}_{N_9}$, $f^{R^2}_{N_9}$, $\Delta E^{R^1,R^1}_{1-2}$, and $\Delta E^{R^2,R^2}_{1-2}$) even if we assume that (i) long-range intermetallic interactions are neglected ($\Delta E^{R,R}_{1-3}=0$) and (ii) the mixing rule is obeyed ($\Delta E^{mix}_{1-2}=0$, Eq. (63), Section 4). An attempt to overcome this limitation considers that (i) $\Delta G^{L13b}_{preorg}=\Delta G^{L28}_{preorg}=0$ and (ii) the six adjustable microscopic parameters are identical for the two $[(\mathbf{L13^b})_3]$ and $[(\mathbf{L28})_3]$ preorganized boxes. Under these debatable hypotheses (particularly point i, Hamacek et al., 2006), a total of 11 experimental stability constants (5 for the binuclear and 6 for the trinuclear helicates) are then available for fitting the six parameters shown in Figure 82 (Zeckert et al., 2004).

Interestingly, the absolute affinities of the N_6O_3 and N_9 sites are comparable in magnitude, but with a slightly different trend along the lanthanide series (Figure 83). The short-range intermetallic interactions remain repulsive and roughly constant along the series. Whatever the quality of the hypotheses leading to this result, it is clear that the site-binding model has reached its limits for describing the assembly of polynuclear helicates and more fundamental thermodynamic concepts are required for avoiding the need of a virtual preorganized receptor, to which metal ions are attached through ''intermolecular'' bonds. It is, however, worth noting that the simple site-binding model is well-adapted for the rationalization of metal exchange processes occurring in heterometallic triple-stranded helicates (equilibria (53), (62), and (64)), because only saturated complexes participate to the equilibria, which automatically agrees with the consideration of pure intermolecular binding processes (see Section 4).

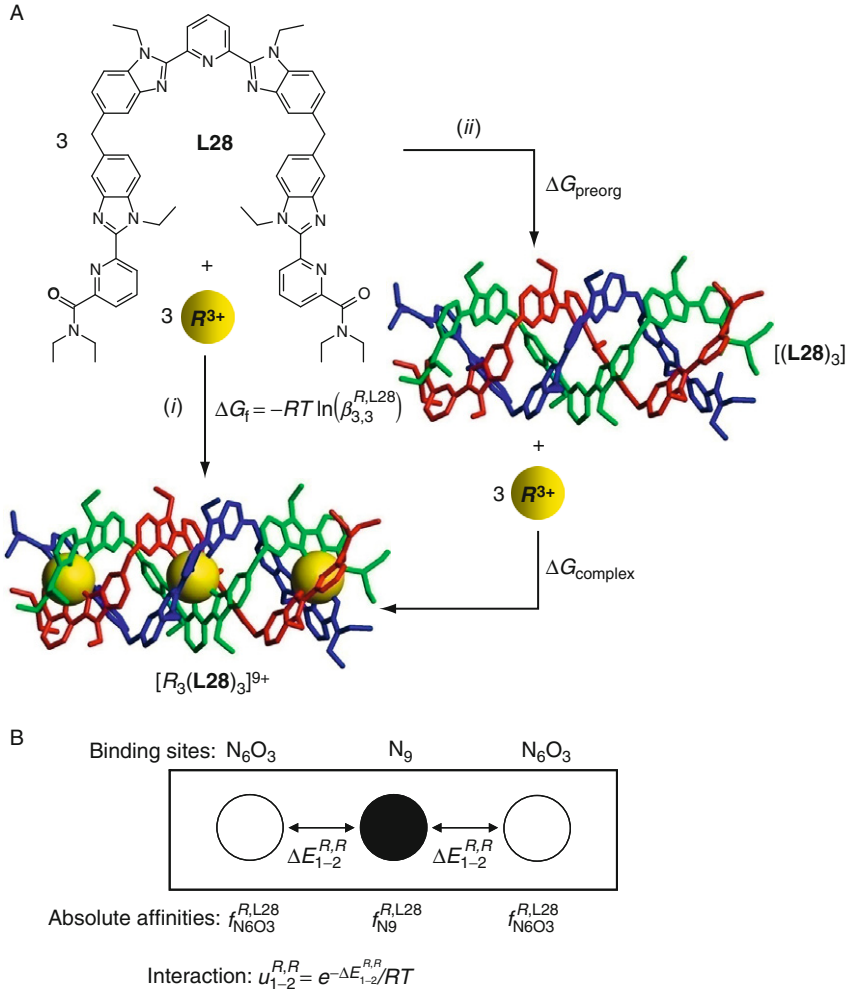

FIGURE 82 (A) Formation and solution structures of $[R_3(\mathbf{L28})_3]^{9+}$ showing the complete assembly process (ΔG_f, path *i*), and its partition into one virtual preorganization step (ΔG_{preorg}) followed by intermolecular complexation ($\Delta G_{complex}$, path *ii*). (B) Associated thermodynamic site-binding model.

5.2 Mixing intra- and intermolecular connections: The extended site-binding model

Let us consider the fixation of a bidentate ligand to a single metal as depicted in Figure 84. The first step simply corresponds to a standard intermolecular binding process modeled by a statistical factor and an absolute intermolecular affinity f_{site}^{M} according to the site-binding model

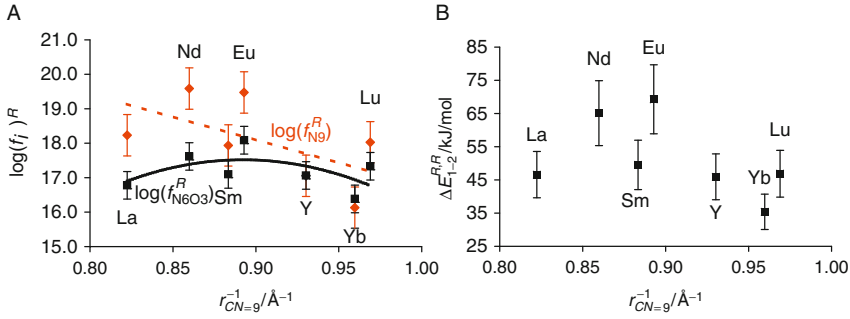

FIGURE 83 (A) Computed absolute affinities for the binding sites ($\log(f^R_{N_6O_3})$ in black and $\log(f^R_{N_9})$ in red) and (B) intermetallic interaction parameters ($\Delta E^{R,R}_{1-2}$) in the triple-stranded helicates $[R_2(\mathbf{L13^b})_3]^{6+}$ and $[R_3(\mathbf{L28})_3]^{9+}$ as a function of the inverse of nine-coordinate ionic radii (adapted from Zeckert et al., 2004).

(Eq. (81)). However, the second step is slightly different because the entering donor atom on the ligand is mechanically coupled to the first binding site, already bound to the metal ion. Both enthalpic and entropic contributions to the free energy of connection of the second site are modified and a global correction term, often referred to as the effective concentration c^{eff}, is used for correlating inter- and intramolecular processes (Eq. (96), Ercolani, 2006; Flory et al., 1976; Fyles and Tong, 2007; Gargano et al., 2001; Jacobson and Stockmayer, 1950; Jencks, 1981; Kuhn, 1934; Winnik, 1981; Figure 84).

$$-RT\ln(c^{\text{eff}}) = \Delta G^{\text{M,intra}}_{\text{connection}} - \Delta G^{\text{M,inter}}_{\text{connection}} = -RT\,\ln(f^{\text{M,intra}}_{\text{site}}) + RT\ln(f^{\text{M,inter}}_{\text{site}}) \tag{96}$$

Even if we consider that the chain of atoms connecting the two binding site of the ligand is long and flexible enough to produce no additional strain during the intramolecular connection ($\Delta H^{\text{M,intra}}_{\text{connection}} = \Delta H^{\text{M,inter}}_{\text{connection}}$), the entropic contribution of the two processes will be different because the degrees of freedoms of the second binding site of the ligand to reach an available coordination site on the metal is different from that of an independent ligand molecule. A theoretical approach based on the systematic Gaussian exploration of the available space by the free end of a flexible polymeric chain is available (Ercolani, 2006; Gargano et al., 2001; Kuhn, 1934). It indeed predicts that $c^{\text{eff}} \propto d^{-3/2}$, whereby d is the average length of the chain of atoms connecting the two binding sites of the ligand. We are now in a position to extend the site-binding model, which is limited to the assembly of $[R_m\mathbf{L}]^{3m+}$ edifices (Eq. (79)) possessing m

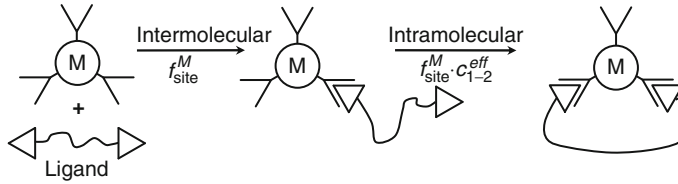

FIGURE 84 Intermolecular and intramolecular connection processes operating during complexation.

intermolecular bonds, toward the rationalization of the formation of $[R_m\mathbf{L}_n]^{3m+}$ complexes (Eq. (97)), in which the mn R-ligand bonds are partitioned between $m+n-1$ intermolecular and mn-$(m+n-1)$ intramolecular connections (Ercolani, 2003).

$$n\mathbf{L} + mR^{3+} \rightleftharpoons [R_m\mathbf{L}_n]^{3m+} \quad \beta^{R,\mathrm{L}}_{m,n} \tag{97}$$

The total free energy is given in Eq. (98) if we assume that metal–metal and ligand–ligand interactions do not contribute to the stability of the final helicate.

$$\begin{aligned}\Delta G^{R,\mathrm{L}}_{m,n} &= -RT\ln(\beta^{R,\mathrm{L}}_{m,n}) \\ &= -RT\ln(\omega^{R,\mathrm{L}}_{m,n}) - RT\sum_{i=1}^{m+n-1}\ln(f_i^R) - RT\sum_{i=1}^{mn-m-n+1}\ln(f_i^R c_i^{\mathrm{eff}})\end{aligned} \tag{98}$$

Regrouping the absolute intermolecular affinities followed by application of the standard vant'Hoff isotherm eventually leads to Eq. (99), which is known as Ercolani's model (Ercolani, 2003; Hamacek et al., 2006).

$$\beta^{R,\mathrm{L}}_{m,n} = \omega^{R,\mathrm{L}}_{m,n}\prod_{i=1}^{mn}(f_i^R)\prod_{i=1}^{mn-m-n+1}(c_i^{\mathrm{eff}}) \tag{99}$$

When both f_i^R and c_i^{eff} are constant for all inter- and intramolecular connections in $[R_m\mathbf{L}_n]^{3m+}$, the self-assembly is said to be statistical or noncooperative (Ercolani, 2003). The initial application of Eq. (99) for rationalizing the formation of Lehn's famous helicate $[Cu_3(\mathbf{L1})_2]^{3+}$ (Figure 3), indeed evidenced the occurrence of a noncooperative process (Ercolani, 2003), despite previous claims for positive cooperativity based on the erroneous neglect of the separation of intra- and intermolecular

binding processes (Fatin-Rouge et al., 2001; Garrett et al., 1992; Pfeil and Lehn, 1992). Any variation of c^{eff} is assigned to changes in preorganization occurring during the self-assembly process, while change of f_i^R refers to cooperativity, which can be either positive (f_i^R increases during the assembly process) or negative (f_i^R decreases during the assembly process). The ''sign'' (i.e., positive or negative) of cooperativity for pure intermolecular assemblies can be easily deduced from the construction of Langmuir isotherms (Hamacek et al., 2006) or from the more popular Scatchard or Hill plots (Perlmutter-Hayman, 1986), while a quantitative assessment of cooperativity requires the estimation of the homocomponent interactions $\Delta E^{R,R}$ ($n=1$ in $[R_m\mathbf{L}]^{3m+}$) or $\Delta E^{\mathrm{L,L}}$ ($m=1$ in $[R\mathbf{L}_n]^{3+}$) by using the site-binding model (Eq. (81)). When both inter- and intramolecular connections occur in $[R_m\mathbf{L}_n]^{3m+}$, partial Langmuir isotherms are required to graphically detect cooperativity in Hamacek plots (Hamacek and Piguet, 2006). A quantitative assessment now requires the simultaneous estimation of intermetallic and interligand interactions expressed as Boltzmann factors in Eq. (100), an equation referred to as the extended site-binding model (Hamacek et al., 2005a,b, 2006).

$$\begin{aligned}\beta_{m,n}^{R,\mathrm{L}} &= \omega_{m,n}^{R,\mathrm{L}}\prod_{i=1}^{mn} f_i^R \prod_{i=1}^{mn-m-n+1} c_i^{\text{eff}} \prod_{i<j} \mathrm{e}^{-\Delta E_{1-2}^{R,R}/RT} \prod_{k<l} \mathrm{e}^{-\Delta E_{1-2}^{L,L}/RT} \\ &= \omega_{m,n}^{R,\mathrm{L}}\prod_{i=1}^{mn} f_i^R \prod_{i=1}^{mn-m-n+1} c_i^{\text{eff}} \prod_{i<j} u_{1-2}^{R,R} \prod_{k<l} u_{1-2}^{L,L}\end{aligned} \tag{100}$$

Application of Eq. (100) to Lehn's helicate $[Cu_3(\mathbf{L1})_2]^{3+}$ and some of its analogues indeed demonstrates a modest negative cooperativity, which disfavors the successive fixation of ligands ($\Delta E_{1-2}^{\mathrm{L1,L1}} = 4(2)$ kJ mol^{-1}) and of metals ($\Delta E_{1-2}^{\mathrm{Cu,Cu}} = 5(3)$ kJ mol^{-1}) in solution (Hamacek et al., 2005b). However, these minute values fully agree with the prior conclusion of noncooperativity deduced from the use of Eq. (99) for a partial set of experimental data.

5.3 Modeling lanthanide helicate self-assembly in solution

Since the application of Eq. (100) may become complicated and tedious for assembly processes involving a considerable amount of microspecies (Dalla Favera et al., 2008), we first focus on the self-assembly of the well-studied binuclear helicate $[Eu_2(\mathbf{L13^f})_3]$, in which each macrospecies contains a single microspecies (Figure 58B, Elhabiri et al., 1999, 2004a). Figure 85 shows the complete set of five thermodynamic equilibria with

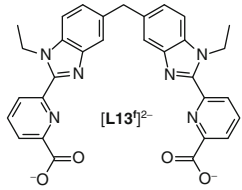

$[\mathbf{L13^f}]^{2-} + [Eu(H_2O)_9]^{3+} \overset{\beta_{1,1}^{Eu,L13f} = 10^{4.3}}{\rightleftharpoons} [Eu(H_2O)_6(\mathbf{L13^f})]^{+} + 3\,H_2O$ (83)

Point groups:	C_{2v}	D_{3h}	C_s	C_{2v}
σ_{ext} :	2	6	1	2
σ_{int} :	3^2	2^9	$3^2 \cdot 2^6$	1

$$\omega_{1,1}^{Eu,L13f} = 12 \Rightarrow \beta_{1,1}^{Eu,L13f} = 12 \cdot f_{N2O}^{Eu}$$

$2\,[\mathbf{L13^f}]^{2-} + [Eu(H_2O)_9]^{3+} \overset{\beta_{2,1}^{Eu,L13f} = 10^{6.4}}{\rightleftharpoons} [Eu(H_2O)_6)_2(\mathbf{L13^f})]^{4+} + 6\,H_2O$ (84)

Point groups:	C_{2v}	D_{3h}	C_{2v}	C_{2v}
σ_{ext} :	2	6	2	2
σ_{int} :	3^2	2^9	$3^2 \cdot 2^{12}$	1

$$\omega_{2,1}^{Eu,L13f} = 36 \Rightarrow \beta_{2,1}^{Eu,L13f} = 36 \cdot (f_{N2O}^{Eu})^2 \cdot u_{1-2}^{Eu,Eu}$$

$2\,[\mathbf{L13^f}]^{2-} + [Eu(H_2O)_9]^{3+} \overset{\beta_{1,2}^{Eu,L13f} = 10^{9.3}}{\rightleftharpoons} [Eu(H_2O)_3(\mathbf{L13^f})_2]^{-} + 6\,H_2O$ (101)

Point groups:	C_{2v}	D_{3h}	C_{2v}	C_{2v}
σ_{ext} :	2	6	2	2
σ_{int} :	3^2	2^9	$3^4 \cdot 2^3$	1

$$\omega_{1,2}^{Eu,L13f} = 12 \Rightarrow \beta_{1,2}^{Eu,L13f} = 12 \cdot (f_{N2O}^{Eu})^2 \cdot u_{1-2}^{L,L}$$

$2\,[\mathbf{L13^f}]^{2-} + 2\,[Eu(H_2O)_9]^{3+} \overset{\beta_{2,2}^{Eu,L13f} = 10^{16.0}}{\rightleftharpoons} [Eu(H_2O)_3)_2(\mathbf{L13^f})_2]^{2+} + 12\,H_2O$ (102)

Point groups:	C_{2v}	D_{3h}	C_{2h}	C_{2v}
σ_{ext} :	2	6	2	2
σ_{int} :	3^2	2^9	$3^4 \cdot 2^6$	1

$$\omega_{2,2}^{Eu,L13f} = 72 \Rightarrow \beta_{2,2}^{Eu,L13f} = 72 \cdot \left(f_{N2O}^{Eu}\right)^4 \cdot c_{1-2}^{eff} \cdot \left(u_{1-2}^{L,L}\right)^2 \cdot u_{1-2}^{Eu,Eu}$$

$3\,[\mathbf{L13^f}]^{2-} + 2\,[Eu(H_2O)_9]^{3+} \overset{\beta_{2,3}^{Eu,L13f} = 10^{26.1}}{\rightleftharpoons} [Eu_2(\mathbf{L13^f})_3] + 18\,H_2O$ (103)

Point groups:	C_{2v}	D_{3h}	D_3	C_{2v}
σ_{ext} :	2	6	6/2	2
σ_{int} :	3^2	2^9	3^6	1

$$\omega_{2,3}^{Eu,L13f} = 96 \Rightarrow \beta_{2,3}^{Eu,L13f} = 96 \cdot \left(f_{N2O}^{Eu}\right)^6 \cdot \left(c_{1-2}^{eff}\right)^2 \cdot \left(u_{1-2}^{L,L}\right)^6 \cdot u_{1-2}^{Eu,Eu}$$

FIGURE 85 Available thermodynamic data characterizing the self-assembly of $[Eu_2(\mathbf{L13^f})_3]$ in water (Elhabiri et al., 1999, 2004a). Each tridentate N_2O binding site is considered as a single point connector.

associated stability constants, statistical factors and extended site-binding equations, required for satisfying the multilinear least-squares fit of the four pertinent microscopic parameters collected in Table 12. The two initial complexation steps leading to $[Eu(\mathbf{L13^f})]^{+}$ (Eq. (83)) and $[Eu_2(\mathbf{L13^f})]^{4+}$ (Eq. (84)) strictly involve intermolecular connection processes and the extended site-binding model reduces here to the original site-binding model. The formation of $[Eu(\mathbf{L13^f})_2]^{-}$ (Eq. (101)) still corresponds to a pure intermolecular mechanism, but it introduces the interligand parameter $\Delta E^{L,L}_{1-2}$, which is assumed to operate when two binding units are coordinated to the same metal. The next complex $[Eu_2(\mathbf{L13^f})_2]^{2+}$ (Eq. (102)) involves the formation of the first metallomacrocycle resulting from an intramolecular binding event.

Finally the fixation of the third ligand to give $[Eu_2(\mathbf{L13^f})_3]$ further involves an intramolecular connection leading to a macrobicyclic complex (Eq. (103)). It is worth noting that $[Eu_2(\mathbf{L13^f})_3]$ is a chiral molecule (D_3 point group), which exists at equilibrium as a racemic mixture. Its symmetry number must be divided by two to account for the entropy of mixing of the two enantiomers (Figure 85, Ercolani et al., 2007).

Despite the large uncertainties induced by (i) the very limited number of available stability constants (five constants for fitting four microscopic parameters) and (ii) the use of kinetic data for estimating some thermodynamic constants, we conclude that the assembly of $[Eu_m(\mathbf{L13^f})_n]^{(3m-2n)+}$ complexes is characterized by a favorable connection of Eu^{III} to the N_2O site (including desolvation), a negligible preorganization, which does not significantly favor intramolecular connection processes, and two opposite contributions to the global cooperativity. The successive binding of ligands to the same metal ion is favorable ($\Delta E^{L,L}_{1-2} < 0$), while the successive filling of two adjacent N_2O sites with Eu^{III} is unfavorable ($\Delta E^{Eu,Eu}_{1-2} > 0$). To improve the quality and reliability of the fitting process, a larger number of experimental thermodynamic constants is required, while limiting the number of microscopic thermodynamic descriptors. This can be obtained with the combination of the thermodynamic data collected for the assemblies of a series of closely related helicates such as

TABLE 12 Fitted thermodynamic parameters for the formation of $[Eu_m(\mathbf{L13^f})_n]^{(3m-2n)+}$ complexes in water at 298 K and pH 6.15 (Hamacek et al., 2005b)

Parameters			Free energies	kJ mol^{-1}
$\log(f^{Eu}_{N_2O})$	3.7(4)	$\Rightarrow$	$\Delta G^{Eu,L13f}_{connection}$	−21(2)
$\log(c^{eff}_{1-2})$	0.3(1.5)	$\Rightarrow$	$\Delta G^{intra}_{correction}$	−2(8)
$\log(u^{L,L}_{1-2})$	0.7(7)	$\Rightarrow$	$\Delta E^{L,L}_{1-2}$	−4(3)
$\log(u^{Eu,Eu}_{1-2})$	−2.4(1.0)	$\Rightarrow$	$\Delta E^{Eu,Eu}_{1-2}$	14(6)

$[Eu_m(\mathbf{L11})_n]^{3m+}$, $[Eu_m(\mathbf{L13^b})_n]^{3m+}$, $[Eu_m(\mathbf{L28})_n]^{3m+}$, and $[Eu_m(\mathbf{L29})_n]^{3m+}$ (Tables 8 and 9). Assuming the following reasonable simplifications:

(1) $f^R_{N_2O}$, $f^R_{N_3}$, $u^{L,L}_{1-2}$, and $u^{R,R}_{1-2}$ are identical in all microspecies.
(2) $\Delta E^{R,R}_{1-n} \propto d^{-1}$ in agreement with Coulomb's law, which allows the estimation of long-range intermetallic interactions $\Delta E^{R,R}_{1-3} = \Delta E^{R,R}_{1-2}/2$ and $\Delta E^{R,R}_{1-4} = \Delta E^{R,R}_{1-2}/3$ in linear helicates (d is the intermetallic distance).
(3) $c^{eff}_{1-n} \propto d^{-3/2}$ in agreement with Kuhn's theory for nonconstrained polymers (Kuhn, 1934), which allows the estimation of long-range macrocyclization processes $c^{eff}_{1-3} = c^{eff}_{1-2}/2^{3/2}$ and $c^{eff}_{1-4} = c^{eff}_{1-2}/3^{3/2}$.

we obtain 13 available macroconstants by using the extended site-binding model (Eqs. (104)–(116)) corresponding to 13 macrospecies. The 17 contributing microspecies (with adapted statistical factors) are shown in Figure 86 (binuclear helicates), Figure 87 (trinuclear helicates), and Figure 88 (tetranuclear helicates).

$$\beta^{R,L11}_{1,2} = 48(f^R_{N_3})^2(u^{L,L}_{1-2}) \tag{104}$$

$$\beta^{R,L11}_{2,2} = 144(f^R_{N_3})^4(u^{L,L}_{1-2})^2(u^{R,R}_{1-2})(c^{eff}_{1-2}) \tag{105}$$

$$\beta^{R,L11}_{2,3} = 96(f^R_{N_3})^6(u^{L,L}_{1-2})^6(u^{R,R}_{1-2})(c^{eff}_{1-2})^2 \tag{106}$$

$$\beta^{R,L13b}_{2,2} = 144(f^R_{N_2O})^4(u^{L,L}_{1-2})^2(u^{R,R}_{1-2})(c^{eff}_{1-2}) \tag{107}$$

$$\beta^{R,L13b}_{1,3} = 32(f^R_{N_2O})^3(u^{L,L}_{1-2})^3 \tag{108}$$

$$\beta^{R,L13b}_{2,3} = 96(f^R_{N_2O})^6(u^{L,L}_{1-2})^6(u^{R,R}_{1-2})(c^{eff}_{1-2})^2 \tag{109}$$

$$\begin{aligned}\beta^{R,L28}_{2,3} &= \beta^{R,L28}_{2,3}(tt) + \beta^{R,L28}_{2,3}(ct) + \beta^{R,L28}_{2,3}(cctctt)\\ &= 96(f^R_{N_2O})^6(u^{L,L}_{1-2})^6(u^{R,R}_{1-2})^{0.5}(c^{eff}_{1-2}/2^{3/2})^2\\ &\quad + 768(f^R_{N_2O})^3(f^R_{N_3})^3(u^{L,L}_{1-2})^6(u^{R,R}_{1-2})(c^{eff}_{1-2})^2\end{aligned} \tag{110}$$

$$\beta^{R,L28}_{3,2} = 864(f^R_{N_2O})^4(f^R_{N_3})^2(u^{L,L}_{1-2})^3(u^{EuEu}_{1-2})^{2.5}(c^{eff}_{1-2})^2 \tag{111}$$

$$\beta^{R,L28}_{3,3} = 576(f^R_{N_2O})^6(f^R_{N_3})^3(u^{L,L}_{1-2})^9(u^{EuEu}_{1-2})^{2.5}(c^{eff}_{1-2})^4 \tag{112}$$

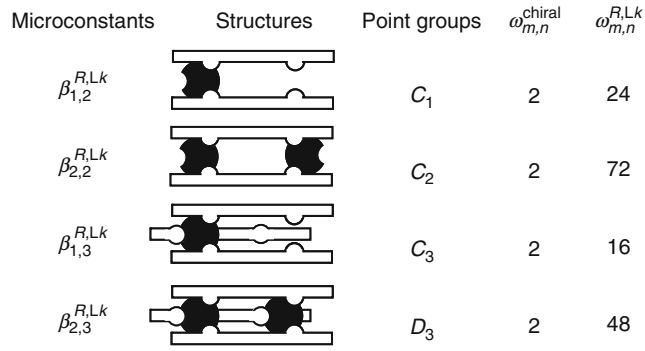

FIGURE 86 Schematic structures, symmetries, and statistical factors for $[R_m(\mathbf{Lk})_n]^{3m+}$ ($k = 11$, 13b) microspecies.

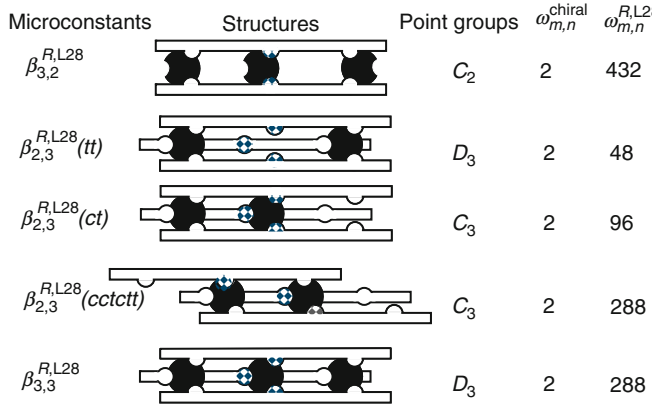

FIGURE 87 Schematic structures, symmetries, and statistical factors for $[R_m(\mathbf{L28})_n]^{3m+}$ microspecies.

$$\begin{aligned}\beta_{3,2}^{R,\mathrm{L29}} &= \beta_{3,2}^{R,\mathrm{L29}}(tcc) + \beta_{3,2}^{R,\mathrm{L29}}(ttc) + \beta_{3,2}^{R,\mathrm{L29}}(tcc-s)\\ &= 1728(f_{\mathrm{N_2O}}^{R})^2(f_{\mathrm{N_3}}^{R})^4(c_{1-2}^{\mathrm{eff}})^2(u_{1-2}^{R,R})^{2.5}(u_{1-2}^{\mathrm{L,L}})^3\\ &\quad + 864(f_{\mathrm{N_2O}}^{R})^4(f_{\mathrm{N_3}}^{R})^2(c_{1-2}^{\mathrm{eff}})^2/2^{3/2}(u_{1-2}^{R,R})^{1.83}(u_{1-2}^{\mathrm{L,L}})^3\end{aligned} \tag{113}$$

$$\begin{aligned}\beta_{3,3}^{R,\mathrm{L29}} &= \beta_{3,3}^{R,\mathrm{L29}}(tcc) + \beta_{3,3}^{R,\mathrm{L29}}(ttc) + \beta_{3,3}^{R,\mathrm{L29}}(tcc-s)\\ &= 4608(f_{\mathrm{N_2O}}^{R})^3(f_{\mathrm{N_3}}^{R})^6(c_{1-2}^{\mathrm{eff}})^4(u_{1-2}^{R,R})^{2.5}(u_{1-2}^{\mathrm{L,L}})^9\\ &\quad + 1152(f_{\mathrm{N_2O}}^{R})^6(f_{\mathrm{N_3}}^{R})^3(c_{1-2}^{\mathrm{eff}})^4/2^3(u_{1-2}^{R,R})^{1.83}(u_{1-2}^{\mathrm{L,L}})^9\end{aligned} \tag{114}$$

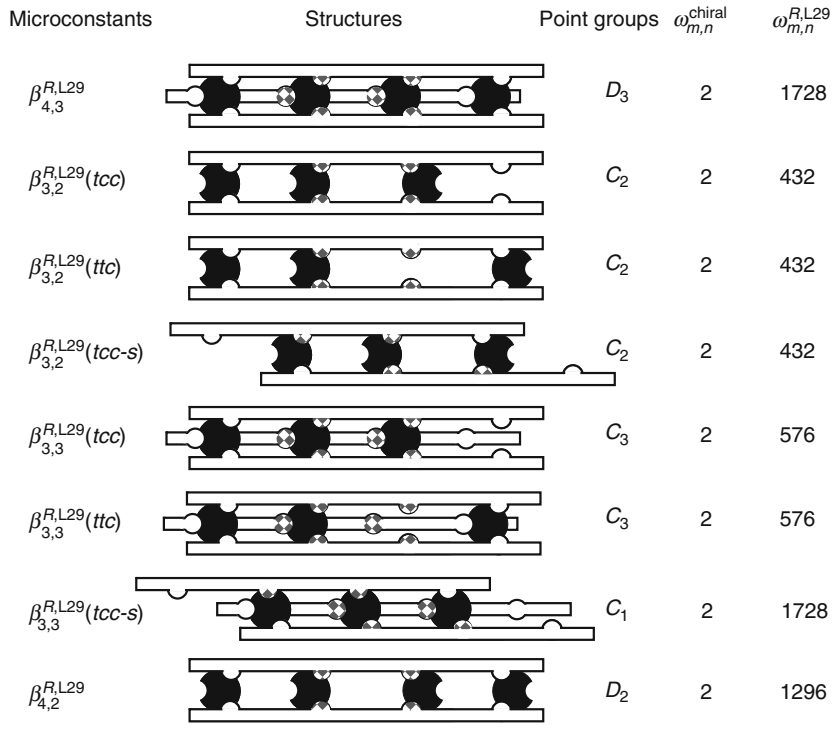

FIGURE 88 Schematic structures, symmetries, and statistical factors for $[R_m(\mathbf{L29})_n]^{3m+}$ microspecies.

$$\beta_{4,2}^{R,L29} = 2592(f_{N_2O}^{R})^4(f_{N_3}^{R})^4(c_{1-2}^{eff})^3(u_{1-2}^{R,R})^{4.33}(u_{1-2}^{L,L})^4 \quad (115)$$

$$\beta_{4,3}^{R,L29} = 3456(f_{N_2O}^{R})^6(f_{N_3}^{R})^6(c_{1-2}^{eff})^6(u_{1-2}^{R,R})^{4.33}(u_{1-2}^{L,L})^{12} \quad (116)$$

A nonlinear least-squares fit of these 13 equations with five microscopic parameters $f_{N_2O}^{R}$, $f_{N_3}^{R}$, $u_{1-2}^{L,L}$, $u_{1-2}^{R,R}$, and c_{1-2}^{eff} ($R = Eu$, Table 13) provides a satisfying model for the reproduction of the experimental stability constants, as shown on Figure 89, Dalla Favera et al., 2008).

The absolute affinities of Eu^{III} for the neutral N_2O and N_3 sites are very similar ($f_{N_2O}^{Eu} \approx f_{N_3}^{Eu}$, Table 13), which confirms that the so-called oxophilicity of trivalent lanthanides is limited to negatively charged donor atoms as found in carboxylates or in phosphonates (Senegas et al., 2003). Obviously, comparison of the absolute affinity of the neutral N_2O site for Eu^{III} in $\mathbf{L13^b}$ (-33 kJ mol^{-1}, Table 13) with that of the negatively charged N_2O site in $(\mathbf{L13^f})^{2-}$ (-21 kJ mol^{-1}, Table 12) is precluded by the use of water as solvent in the second case. The small magnitude of

TABLE 13 Fitted thermodynamic parameters for the formation of $[Eu_m(\mathbf{L}k)_n]^{3m+}$ complexes ($k = 11$, 13[b], 28, 29) in acetonitrile at 298 K (from Dalla Favera et al., 2008)

Parameters			Free energies	kJ mol^{-1}
$\log(f_{N_3}^{Eu})$	5.4(2)	$\Rightarrow$	$\Delta G_{connection}^{Eu,N_3}$	$-31(1)$
$\log(f_{N_2O}^{Eu})$	5.6(2)	$\Rightarrow$	$\Delta G_{connection}^{Eu,N_2O}$	$-33(1)$
$\log(c_{1-2}^{eff})$	$-1.0(9)$	$\Rightarrow$	$\Delta G_{correction}^{intra}$	6(5)
$\log(u_{1-2}^{L,L})$	$-1.0(3)$	$\Rightarrow$	$\Delta E_{1-2}^{L,L}$	6(2)
$\log(u_{1-2}^{Eu,Eu})$	$-1.8(7)$	$\Rightarrow$	$\Delta E_{1-2}^{Eu,Eu}$	10(4)

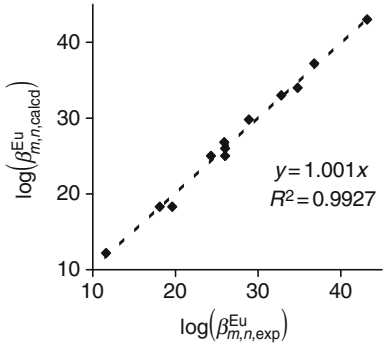

FIGURE 89 Comparison between experimental ($\log(\beta_{m,n,exp}^{Eu})$) and calculated ($\log(\beta_{m,n,calcd}^{Eu})$) stability constants for the 13 macroscopic equilibria described in Eqs. (104)–(116) (Dalla Favera et al., 2008).

$c_{1-2}^{eff} = 0.1$ M indicates a moderate preorganization of the ligand strands for macrocyclization. It is in line with the theoretically predicted value of $c^{eff} = 0.25$ M for two binding sites separated by 10 Å and connected by a bidentate ligand with optimum flexibility (Gargano et al., 2001). Finally, both homocomponent interactions are repulsive ($\Delta E_{1-2}^{L,L} > 0$, $\Delta E_{1-2}^{R,R} > 0$), which implies that any intermediate or triple-stranded helicate in this family of complexes is driven to complexion with negative cooperativity.

5.4 The origin of the unusual stability of highly charged lanthanide helicates in solution

The considerable stability of trinuclear $[R_3(\mathbf{L28})_3]^{9+}$ and tetranuclear $[R_4(\mathbf{L29})_3]^{12+}$ helicates, which indeed correspond to more than 90% of the ligand speciation at millimolar concentration, can be assigned to the nontrivial apparent minute repulsive intramolecular intermetallic interaction $\Delta E_{1-2}^{R,R} \approx 10$ kJ mol^{-1} operating between two R^{3+} held at a distance of ≈9Å in these complexes. The straightforward application of Coulomb's

Eq. (117) ($N_A = 6.023 \times 10^{23}\,\text{mol}^{-1}$ is Avogadro's number, z_i are the atomic charges of the interacting particles in electrostatic units, $e = 1.602 \times 10^{-19}\,\text{C}$ is the elemental charge, $\varepsilon_0 = 8.859 \times 10^{-12}\,\text{CN}^{-1}\,\text{m}^{-2}$ is the permittivity constant of the vacuum, ε_r is the relative permittivity constant of the medium, $d = 9.0$ Å is the intermetallic separation in the complex) predicts $39\ \text{kJ mol}^{-1}$ ($\varepsilon_r = 36.1$) $\leq \Delta E^{R,R}_{1-2,\text{calcd}} \leq 1389\ \text{kJ mol}^{-1}$ ($\varepsilon_r = 1.0$) for two R^{3+} in these helicates considered as dielectric continuums with limiting relative permittivities of $\varepsilon_r = 36.1$ (pure acetonitrile) or $\varepsilon_r = 1.0$ (vacuum). Assuming that the major contribution to the electrostatic work arises for distances close to equilibrium whereby $\varepsilon_r \to 1.0$, we can safely conclude that $\Delta E^{R,R}_{1-2,\text{calcd}}$ is approximately two orders of magnitude larger than its apparent value in acetonitrile (Canard and Piguet, 2007).

$$\Delta E^{R,R}_{1-2,\text{calcd}} = W_{\text{elec}} = -\frac{N_{\text{Av}} z_1 z_2 e^2}{4\pi\varepsilon_0} \int_{\infty}^{d=9\,\text{Å}} \frac{dr}{\varepsilon_r r^2} \tag{117}$$

The use of thermodynamic Born–Haber cycles modeling the successive coordination of the second and third Eu^{III} in $[Eu(\mathbf{L28})_3]^{3+}$ to give $[Eu_2(\mathbf{L28})_3]^{6+}$ (Figure 90A) and $[Eu_3(\mathbf{L28})_3]^{9+}$ (Figure 90B) provides some rationalizations for this surprising dichotomy (Canard and Piguet, 2007).

Let us first apply the extended site-binding model (Eq. (100)) to the four complexation processes shown in Figure 90 (Eqs. (118)–(121)).

$$\beta_{K2,\text{gas}} = e^{-\Delta G^0_{K2,\text{gas}}/RT} = 1(f^{\text{Eu}}_{N_3,g})^3 (u^{\text{L,L}}_{1-2,g})^3 u^{\text{Eu,Eu}}_{1-2,g} (c^{\text{eff}}_{1-2,g})^2 \tag{118}$$

$$\beta_{K3,\text{gas}} = e^{-\Delta G^0_{K3,\text{gas}}/RT} = \frac{1}{2}(f^{\text{Eu}}_{N_3,g})^3 (u^{\text{L,L}}_{1-2,g})^3 u^{\text{Eu,Eu}}_{1-2,g} u^{\text{Eu,Eu}}_{1-3,g} (c^{\text{eff}}_{1-2,g})^2 \tag{119}$$

$$\beta_{K2,\text{sol}} = e^{-\Delta G^0_{K2,\text{sol}}/RT} = 6(f^{\text{Eu}}_{N_3,s})^3 (u^{\text{L,L}}_{1-2,s})^3 u^{\text{Eu,Eu}}_{1-2,s} (c^{\text{eff}}_{1-2,s})^2 \tag{120}$$

$$\beta_{K3,\text{sol}} = e^{-\Delta G^0_{K3,\text{sol}}/RT} = 3(f^{\text{Eu}}_{N_3,s})^3 (u^{\text{L,L}}_{1-2,s})^3 u^{\text{Eu,Eu}}_{1-2,s} u^{\text{Eu,Eu}}_{1-3,s} (c^{\text{eff}}_{1-2,s})^2 \tag{121}$$

From the Born–Haber cycles, we can write

$$\Delta G^0_{K2,\text{gas}} = \Delta G^0_{K2,\text{sol}} + \Delta_{\text{solv}} G^0\left(\text{Eu}(\mathbf{L28})_3\right) + \Delta_{\text{solv}} G^0(\text{Eu}) - \Delta_{\text{solv}} G^0\left(\text{Eu}_2(\mathbf{L28})_3\right) \tag{122}$$

$$\Delta G^0_{K3,\text{gas}} = \Delta G^0_{K3,\text{sol}} + \Delta_{\text{solv}} G^0\left(\text{Eu}_2(\mathbf{L28})_3\right) + \Delta_{\text{solv}} G^0(\text{Eu}) - \Delta_{\text{solv}} G^0\left(\text{Eu}_3(\mathbf{L28})_3\right) \tag{123}$$

which can be combined in Eq. (124).

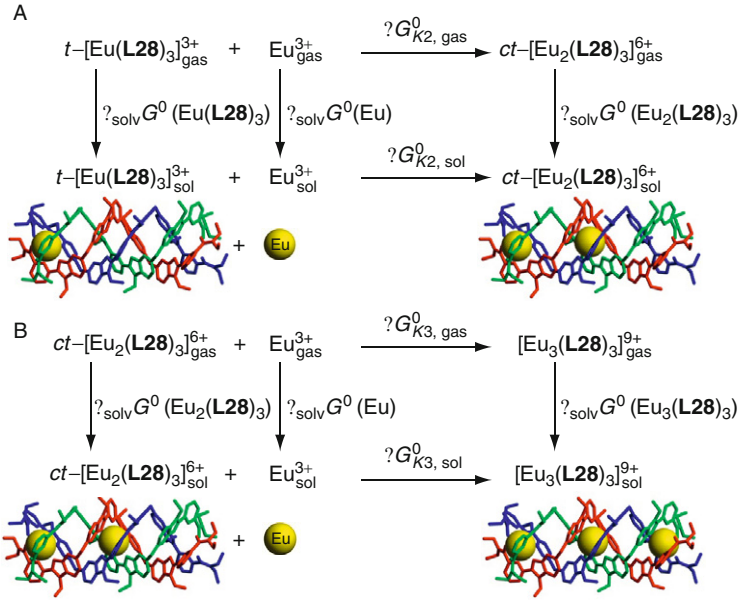

FIGURE 90 Thermodynamic Born–Haber cycles for the successive complexation of Eu^{III} to (A) *t*-$[Eu(\mathbf{L28})_3]^{3+}$ to give *ct*-$[Eu_2(\mathbf{L28})_3]^{6+}$ and (B) *ct*-$[Eu_2(\mathbf{L28})_3]^{6+}$ to give $[Eu_3(\mathbf{L28})_3]^{9+}$. Letters *c* and *t* denote the central and terminal sites, respectively.

$$\Delta G^0_{K3,\mathrm{sol}} - \Delta G^0_{K2,\mathrm{sol}} = \Delta G^0_{K3,\mathrm{gas}} - \Delta G^0_{K2,\mathrm{gas}} + \Delta_{\mathrm{solv}}G^0\left(\mathrm{Eu}(\mathbf{L28})_3\right) + \Delta_{\mathrm{solv}}G^0\left(\mathrm{Eu_3}(\mathbf{L28})_3\right) - 2\Delta_{\mathrm{solv}}G^0\left(\mathrm{Eu_2}(\mathbf{L28})_3\right) \tag{124}$$

The introduction of Eqs. (118)–(121) into Eq. (124) eventually gives

$$\Delta E^{\mathrm{Eu,Eu}}_{1-3,\mathrm{sol}} - 3RT\ln\left(\frac{f^{\mathrm{Eu}}_{\mathrm{N_3,s}}}{f^{\mathrm{Eu}}_{\mathrm{N_2O,s}}}\right) = \Delta E^{\mathrm{Eu,Eu}}_{1-3,\mathrm{gas}} - 3RT\ln\left(\frac{f^{\mathrm{Eu}}_{\mathrm{N_3,g}}}{f^{\mathrm{Eu}}_{\mathrm{N_2O,g}}}\right) + \Delta_{\mathrm{solv}}G^0\left(\mathrm{Eu}(\mathbf{L28})_3\right) + \Delta_{\mathrm{solv}}G^0\left(\mathrm{Eu_3}(\mathbf{L28})_3\right) - 2\Delta_{\mathrm{solv}}G^0\left(\mathrm{Eu_2}(\mathbf{L28})_3\right) \tag{125}$$

Assuming that (i) the ratio of the absolute affinities of the N_3 and N_2O sites for Eu^{III} are similar in the gas phase and in solution ($f^{\mathrm{Eu}}_{\mathrm{N_3,g}}/f^{\mathrm{Eu}}_{\mathrm{N_2O,g}} = f^{\mathrm{Eu}}_{\mathrm{N_3,s}}/f^{\mathrm{Eu}}_{\mathrm{N_2O,s}}$) and (ii) $\Delta E^{\mathrm{Eu,Eu}}_{1-3,\mathrm{gas}}$ is reasonably approximated by Coulomb's Eq. (117) with $\varepsilon_r = 1.0$, we can deduce that the deviation of the intermetallic interaction in solution from classical electrostatic trends

can be ascribed to the contribution of the solvation energies of the different complexes (Eq. (126), Canard and Piguet, 2007).

$$\Delta E^{\mathrm{Eu,Eu}}_{1-3,\mathrm{sol}} = \frac{9N_{\mathrm{Av}}e^2}{4\pi\varepsilon_0 2d} + \Delta_{\mathrm{solv}}G^0\left(\mathrm{Eu}(\mathbf{L28})_3\right) + \Delta_{\mathrm{solv}}G^0\left(\mathrm{Eu}_3(\mathbf{L28})_3\right) - 2\Delta_{\mathrm{solv}}G^0\left(\mathrm{Eu}_2(\mathbf{L28})_3\right) \tag{126}$$

Estimating $\Delta_{\mathrm{solv}}G^0\left(\mathrm{Eu}_m(\mathbf{L28})_3\right)$ with Born Eq. (127) for these large molecular ions in acetonitrile with $\varepsilon_r = 36.1$ and gas-phase radii $r(\mathrm{Eu}(\mathbf{L28})_3) = 10$ Å, $r(\mathrm{Eu}_2(\mathbf{L28})_3) = 11$ Å and $r(\mathrm{Eu}_3(\mathbf{L28})_3) = 12$ Å gives $\Delta_{\mathrm{solv}}G^0\left(\mathrm{Eu(L28)}_3\right) = -607$ kJ mol^{-1}, $\Delta_{\mathrm{solv}}G^0\left(\mathrm{Eu}_2\mathrm{(L28)}_3\right) = -2208$ kJ mol^{-1} and $\Delta_{\mathrm{solv}}G^0\left(\mathrm{Eu}_3\mathrm{(L28)}_3\right) = -4554$ kJ mol^{-1} (Canard and Piguet, 2007).

$$\Delta_{\mathrm{solv}}G^0\left(\mathrm{Eu}_m(\mathbf{L28})_3\right) = -\frac{N_{\mathrm{Av}}(3m)^2e^2}{8\pi\varepsilon_0 r}\left(1-\frac{1}{\varepsilon_r}\right) \tag{127}$$

The introduction of these values into Eq. (126) shows that the solvation correction and the Coulombic repulsion are of the same magnitude, but of opposite trend, which explains the minute apparent intermetallic interaction detected in solution when using the extended site-binding model (Eq. (128)).

$$\Delta E^{\mathrm{Eu,Eu}}_{1-3,\mathrm{sol,\ exp}} = +694 - 745 = -51\,\mathrm{kJ/mol} \tag{128}$$

Interestingly, a refined treatment of the experimental data which does not impose a Coulombic correlation between $\Delta E^{\mathrm{Eu,Eu}}_{1-2,\mathrm{sol}}$ and $\Delta E^{\mathrm{Eu,Eu}}_{1-3,\mathrm{sol}}$, eventually concludes that $\Delta E^{\mathrm{Eu,Eu}}_{1-3,\mathrm{sol,\ exp}} = -7(3)$ kJ mol^{-1}, in good agreement with the rough attractive interaction predicted in Eq. (128) (Riis-Johannessen et al., 2009). The same thermodynamic approach applies for unraveling $\Delta E^{\mathrm{Eu,Eu}}_{1-4,\mathrm{sol}}$ in $[\mathrm{Eu}_m(\mathbf{L29})_3]^{3m+}$, while some modifications are required for $\Delta E^{\mathrm{Eu,Eu}}_{1-2,\mathrm{sol}}$ (Riis-Johannessen et al., 2009). Altogether, the conclusions are similar with the observation of unusually small intermetallic interactions resulting from the competition between electrostatic repulsion, which prevents the formation of small and highly charged polynuclear helicates, and opposite favorable solvation effects, which are maximum for small ions with high charge density. For linear (i.e., one-dimensional) complexes such as helicates, the coordination of an additional trivalent lanthanide involves a single short-range intermetallic repulsion $\Delta E^{\mathrm{Eu,Eu}}_{1-2}$, while the total charge of the supramolecular edifice is increased by three unit and its size by a concomitant increase of ca. 10% (Canard and

Piguet, 2007). The balance of these effects for the intermetallic interaction operating in solution is close to zero (see Eq. (128) for $\Delta E^{Eu,Eu}_{1-3,sol}$), which explains the considerable stability of lanthanide helicates in solution.

5.5 Predictive approaches

Although not explicitly considered to date in the literature, the balance between intermetallic repulsion and solvation energies as a major contribution to the stability (or instability) of the final polynuclear lanthanide complexes is not limited to one-dimensional lanthanide helicates, but obviously extends to two-dimensional (2D, Chapon et al., 2001, 2002; Chen et al., 2007; Lama et al., 2007; Mamula et al., 2005; Ronson et al., 2007; Senegas et al., 2005; Xu and Raymond, 2000) and three-dimensional (3D) lanthanide complexes (Hamacek et al., 2008; He et al., 2008; Mamula et al., 2006) in solution. One can thus easily realize that 2D and 3D organizations involve a large amount of short-range intermetallic interactions affected by strong electrostatic repulsion, which requires very compact structures avoiding large increase in size for maintaining large and favorable solvation effects. In this context, it is worth noting that the vast majority of stable 2D and 3D polynuclear lanthanide complexes in solution incorporate negatively charged binding units, for which the absolute affinities f^R are maximum and can overcome unfavorable intermetallic interactions. This understanding of the parameters controlling the stability of lanthanide complexes paves the way for evolving from the usual deductive approach toward some inductive counterpart. The prediction of the formation constants and ligand distributions in the heterobimetallic trinuclear complexes $[La_xEu_{3-x}(\mathbf{L28})_3]^{9+}$ represents a first attempt in this direction (Floquet et al., 2004). Taking into account the absolute affinities $f^{Eu}_{N_2O}$, $f^{Eu}_{N_3}$, $f^{La}_{N_2O}$, $f^{La}_{N_3}$, and the intermetallic interactions $u^{La,La}_{1-2}$, $u^{Eu,Eu}_{1-2}$, and $u^{La,Eu}_{1-2}$ obeying the mixing rule, it was possible to predict that the target microspecies $[EuLaEu(\mathbf{L28})_3]^{9+}$ accounts for 48% of the thermodynamic mixture (La:Eu:**L28** = 1:2:3, total ligand concentration = 10 mM). Detailed ^{1}H-NMR investigations confirmed these predictions, which allowed to unravel the effect of the crystallization process on the distribution of La^{III} and Eu^{III} in solid-state materials (Floquet et al., 2004). A second success arose with the prediction that $[Eu_4(\mathbf{L29})_3]^{12+}$ would be the major component (>90%) for a Eu:**L29** ratio = 4:3 in acetonitrile with a global stability constant $\log(\beta^{Eu,L29}_{4,3,calcd}) = 42.5$ (Zeckert et al., 2005). After 11 synthetic steps leading to **L29** (Figure 43), subsequent spectrophotometric titration in acetonitrile with $Eu(CF_3SO_3)_3$ indeed confirmed these predictions with $\log(\beta^{Eu,L29}_{4,3,exp}) = 43.2(1.9)$, in very good agreement with the calculated value (Dalla Favera et al., 2008).

6. HELICATES AS LUMINESCENT BIOPROBES

6.1 Lanthanide luminescent bioprobes

Luminescence and time-resolved luminescence have grown during the past 20 years into major methodologies in biochemistry, biophysics, biotechnology, and medicine. They are indispensable research tools in noninvasive medical diagnostics, flow cytometry, analysis of polymerase chain reaction (PCR) products, gene analysis, DNA sequencing, luminescence microscopy, and cellular imaging, only to name a few. The reason is very simple. Light travels almost instantaneously through a sample (about 30 cm ns^{-1}) and can reach regions of complex molecular edifices not accessible to other molecular probes, such as magnetic resonance probes. Furthermore, light is easily detected by highly sensitive devices (e.g., charge-coupled device cameras) and techniques, including single-photon detection, so that analyses based on luminescence are the most sensitive available, while being environmentally clean, as opposed to methods using radiolabels.

Luminescence is defined as emission of light from an electronically excited state. Depending on the spin of the initial (emitting) and final (often ground) states, two categories of emission are distinguished: *fluorescence* for transitions without spin change ($\Delta S = 0$) and *phosphorescence* for transitions with spin change ($\Delta S > 0$). In the case of organic luminophores, which usually bear aromatic residues, absorption of light leads to a singlet excited state and the return to the ground state is allowed, so that the emission rate is fast, in the range $k_F = 10^7$–$10^9\ s^{-1}$, corresponding to a lifetime of the excited state $\tau_F = 100$–1 ns. Due to this short timescale, time-resolved detection (TRD) of fluorescence necessitates sophisticated optics and detection systems. On the other hand, spectral discrimination is often impossible to achieve because the Stokes' shifts of the organic chromophores are small. Quinine sulfate (blue), fluorescein (green), acridine orange (AO, yellow), rhodamine (orange), and pyridine-1 (red) are common fluorescent analytical probes covering the entire visible range while cyanine (CY), Alexa Fluor®, and BODIPY® dyes are examples of more recently proposed luminescent tags (Lakowicz, 2006). In some cases, the excited organic luminophore relaxes to a triplet state and since transitions from this state to the singlet ground state are forbidden by the spin selection rule, the emission of light is slow with rates in the range $k_P = 1$–$10^3\ s^{-1}$, corresponding to lifetimes τ_P of 1 s to 1 ms. Time-resolved experiments are consequently easy to conduct, but the fraction of molecules reaching the triplet state is usually small, at least at room temperature, and due to their long lifetime, triplet states often give rise to photochemical reactions which destroy the luminophore, a phenomenon known as photobleaching. The need for time or spectral discrimination, or

both, is considerable in bioanalyses because the samples contain a large variety of aromatic substances and when illuminated with UV or blue light, they generate a highly undesirable and intense luminescence background (autofluorescence).

Given these limitations, lanthanide ions emerge more and more as alternatives to organic bioprobes for time-resolved bioanalyses. Indeed, the $4f^n$ electronic configurations of R^{III} ions are protected from outside interactions by the more external $5s^25p^6$ subshells of the xenon core. Since the 4f wave functions are fairly pure, the plentiful electronic transitions (the $4f^6$ configuration of Eu^{III} generates 3003 electronic levels for instance) are narrow and easily recognizable, their energy being fairly insensitive to the chemical environment. Additionally, most of the ions are luminescent and their emissions extend over a broad spectral range (Figure 91), from UV (Gd^{III}) to visible (e.g., Sm^{III}, Eu^{III}, Tb^{III}, Dy^{III}, Tm^{III}) and near infrared (NIR, e.g., Nd^{III}, Ho^{III}, Er^{III}, Yb^{III}). Some ions are fluorescent, others are phosphorescent, and some are both. Electric-dipole intraconfigurational 4f–4f transitions are forbidden by Laporte's rule so that the lifetimes of the excited states are long (μs ms) allowing easy TRD experiments with rugged and cheap instrumentation. The inherent drawback of these ions, namely the very weak oscillator strengths of the f–f transitions, can be circumvented by exciting the *R*-containing chromophores into their surroundings through a process termed ''luminescence sensitization'' and discussed in Section 2.5.1 (Figure 37). A lanthanide luminescent bioprobe (LLB) usually consists in a lanthanide chelate the luminescence of which is modulated by interaction with the biological material.

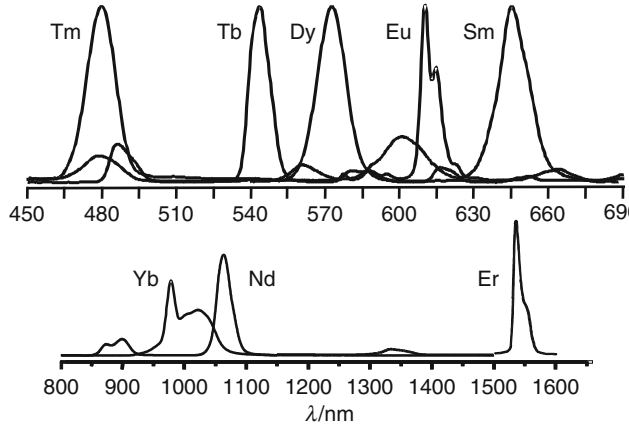

FIGURE 91 Luminescence of lanthanide β-diketonates (redrawn from Eliseeva et al., 2006).

An LLB may be used in a variety of different techniques. Initial applications include (i) simple substitution of Ca^{II} or Zn^{II} by luminescent R^{III} ions in proteins to obtain information on the composition of metal-binding sites, for instance the number of coordinated water molecules, or metal-to-metal and metal-to-chromophore distances by energy transfer experiments, or (ii) titration of a biocompound with salts of luminescent R^{III} ions to determine the number of metal-binding sites (Bünzli, 1989). Starting in the early 1980s, more subtle applications have been proposed, primarily for the design of luminescent time-resolved immunoassays (Siitari et al., 1983). The luminescent lanthanide ion is embedded into a suitable coordinating cavity and the resulting chelate is either used directly as an analytical responsive probe without specific targeting, or conjugated to a protein or to an antibody which specifically couples with a targeted biomolecule (Bünzli, 2009).

Requirements for an efficient LLB are numerous and challenging: (i) water solubility, (ii) large thermodynamic stability, (iii) kinetic inertness, (iv) intense absorption at least above 330 nm and if possible in the visible or NIR ranges, (v) efficient sensitization of the lanthanide ion luminescence, (vi) protection of the emitting ion by inserting it into a rigid and protective cavity minimizing nonradiative deactivation processes, (vii) long excited state lifetime, and (viii) when relevant, ability to couple to bioactive molecules while simultaneously retaining the sought for photophysical properties and leaving the bioaffinity of the host unchanged. Hundreds of chelates have been synthesized and tested during the past 30 years so that the design of LLBs is becoming well understood at least from the chemical and biochemical points of view, since *in silico* predictions are still far from being feasible. An LLB can be used directly, its luminescence being detected (usually in TRD mode) after a suitable and specific reaction with the analyte, or indirectly by transferring the excitation energy onto an organic acceptor by a process called Förster resonance energy transfer (FRET). An example of direct measurement is depicted in Figure 92 for an assay in which the luminescent lanthanide

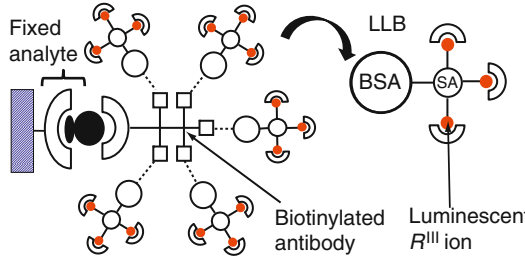

FIGURE 92 Direct use of an LLB conjugated to a biotinylated antibody (redrawn after Bünzli, 2009).

chelate is coupled firstly to streptavidin (SA) itself linked to bovine serum albumin (BSA); BSA can be easily conjugated to almost any biotinylated antibody. The latter reacts specifically with the (antigen) analyte and luminescence is detected after removal of the reactants in excess.

On the other hand, FRET occurs when the donor (D) and the acceptor (A) lie at distances $R_{DA} > 40$ pm, the corresponding mechanism being dipole–dipolar (through space), as opposed to through-bond (Dexter) mechanism which operates at shorter distances (Selvin, 2000). The yield of the FRET transfer is given by an equation similar to Eq. (77), Section 4.4, with R_0 defined by Eq. (78):

$$\eta_{FRET} = 1 - \frac{\tau_{obs}}{\tau_0} = \frac{1}{1 + \left(\frac{R_{DA}}{R_0}\right)^6} = \frac{R_0^6}{R_0^6 + R_{DA}^6} \tag{129}$$

This efficiency can therefore be easily estimated from lifetime measurements. Alternatively, it can be extracted from the absorption and emission spectra (Charbonnière and Hildebrandt, 2008):

$$\eta_{FRET} = \frac{A_A(\lambda_D)}{A_D(\lambda_D)}\left[\frac{E_{AD}(\lambda_D)}{E_A(\lambda_D)} - 1\right] \tag{130}$$

where λ_D is the excitation wavelength of the (donor) LLB, A_D and A_A are the absorbances of the donor and acceptor at this wavelength while E_A and E_{AD} are the integrated emission intensities of the acceptor in absence and in presence of the donor, respectively. The corresponding bioanalysis is sketched on Figure 93. The LLB is bioconjugated to a biotinylated antibody while a cyanine dye is linked to another such antibody. Both antibodies are specific for the (antigen) analyte. The advantage of this technique is that no washing is required since the transfer only occurs when the two antibodies are connected to the analyte simultaneously. In addition the excited state of the organic acceptor dye is populated with a lifetime equal to the one of the excited R^{III} ion so that TRD discriminates between this emission and the emission of the dye upon direct excitation. Finally, emission from the LLB upon direct excitation is discriminated spectrally; that is, the dye is chosen so that its emission range is distinct from the R^{III} emission bands.

Covalent coupling of a lanthanide luminescent chelate to bioactive molecules such as peptides, proteins, or nucleic acids makes use of the chemically reactive groups of these molecules. The most common ones are aliphatic α- or ε-amines. A typical example of ε-amine is lysine, the pK_a of which is 9.2 so that it reacts cleanly above pH 8 to yield stable

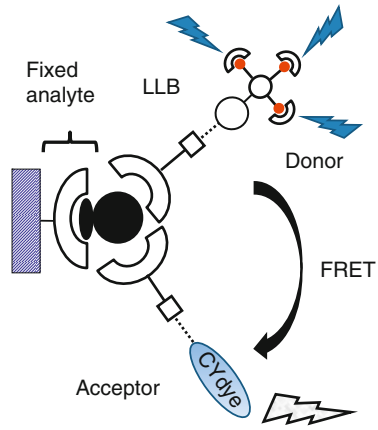

FIGURE 93 Förster resonant energy transfer between an LLB bioconjugated to a biotinylated antibody and a cyanine dye coupled to another biotinylated antibody.

covalent binding. There are usually several lysine groups per protein, compare streptavidin which bears 36 of them, so that several luminescent lanthanide chelates may be conjugated simultaneously. The α-amino group is more acidic with pK_a around 7 and every protein bears at least one such group per subunit or peptide chain. Thiol residues are other common reactive groups. The free thiol group (e.g., in cysteine) is more nucleophilic than amines and generally is the more reactive group in proteins, even at neutral pH. Phenol (e.g., in tyrosine) or carboxylic acids (e.g., in aspartic and glutamic acids) are other potential candidates. The lanthanide chelate must be activated before coupling with these functional groups. In immunoassays and many other bioanalyses, coupling between proteinic amines and LLBs fitted with isothiocyanato, chlorosulfonyl (particularly arenesulfonyl), or 2,4-dichloro-1,3,5-triazinyl groups have proved to be the most successful (Nishioka et al., 2007). Another very convenient coupling group is *N*-hydroxysuccinimide (NHS, or its sulfo derivative, sulfo-NHS) which can be easily generated by direct reaction of a carboxylic acid with *N*-hydroxysuccinimide in presence of the dehydrating agent (1-ethyl-3-(3-dimethylaminopropyl) carbodiimide hydrochloride (EDC or EDAC). Since proteins bear many coupling functions, the number of attached LLBs may be large, up to 46 as reported to date, especially if the bioconjugate is further attached to a protein such as BSA which smoothly reacts with biotinylated biomolecules, as shown in Figures 92 and 93, and this results in more sensitive analyses.

6.2 Dipicolinic acid derivatives as LLBs

The intense luminescence displayed by lanthanide dipicolinates (Table 6) as well as their easy synthesis have prompted their use in various analytical and imaging applications and some of them are briefly reviewed in this section.

6.2.1 Simple analyses

Bacterial spores are the most resistant microbial structures toward extreme conditions. As a consequence, they find applications in the evaluation of the efficiency of sterilization processes. They are also present in the ominous *Bacillus anthracis* spores which have been the biological vectors in anthrax attacks. Dipicolinic acid is a remarkable constituent of these spores so that they may be detected through complexation with Tb^{III}. In the proposed procedure, Cable et al. (2007) start from a macrocyclic complex, $[Tb(DO2A)]^{+}$ where DO2A is 1,4,7,10-tetraazacyclododecane-1,7-diacetate, to saturate the lanthanide inner coordination sphere in $[Tb(DO2A)(\mathbf{L15^a})]^{-}$ for maintaining excellent photophysical properties. Detection limits are as low as 2.1×10^4 spores per ml.

The lanthanide tris(dipicolinates) usually exist as racemic mixtures of Δ and Λ isomers. However, the luminescent complexes may be used for chirality recognition by perturbing the racemic equilibrium with enantiomerically resolved nonluminescent acceptor molecules or complexes (see Aspinall, 2002 for a review). Along these lines, Metcalf et al. (1992) have proposed a method based on time-resolved chiroptical luminescence spectroscopy for investigating enantioselective excited-state quenching processes in solutions containing the racemic LLB and a small concentration of dissymmetric quencher molecules. The latter are six-coordinate $[Co^{III}(NH_3)_4(L)]$ complexes with diphosphate or triphosphate nucleotides (adenosine, guanosine, inosine, cytidine, uridine, and deoxythymidine). The quenching rate constants display significant variations among the different systems. More interestingly, all of the Co^{III} complexes exhibit differential quenching of *Λ*-*R** compared to Δ-*R** enantiomers of the europium and terbium tris(dipicolinates) which can be related to structural differences between the nucleoside base moieties.

6.2.2 Immunoreactive conjugates of proteins

The 4-iodo(acetoamido) derivative of dipicolinic acid ($\mathbf{Na_2L15^i}$, Figure 23) readily alkylates proteins. However, the stability of its R^{III} chelates is not very large and since three ligands are needed to saturate the lanthanide inner coordination sphere, some crosslinking by the R^{III} ions occurs. To circumvent these problems, Lamture and Wensel (1995) have proposed to couple $(\mathbf{L15^i})^{2-}$ onto a polylysine framework, simultaneously to succinate, to produce a

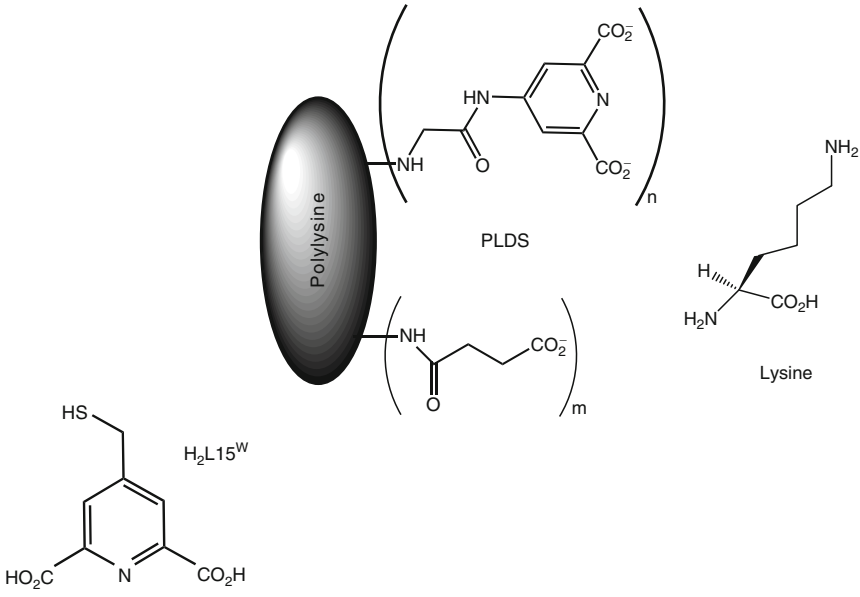

FIGURE 94 Top: polylysine derivatized with dipicolinate and succinate (PLDS) (redrawn from Lamture and Wensel, 1995). Bottom: chelating unit for paramagnetic tags used for exploring the magnetic susceptibility anisotropy sensors of proteins (Su et al., 2008a).

polylysine dicarboxylate succinate polymer (PLDS) bearing 50–100 4-substituted dipicolinate moieties per molecule while the remaining lysyl chains are succinylated (Figure 94). The binding affinity of PLDS for Tb^{III} is larger than the affinity of EDTA (ethylenediamine tetraacetate) and carbodiimide-mediated coupling reactions to proteins result in highly luminescent protein-PLDS-Tb conjugates. These conjugates retain sufficient immunoreactivity to design luminescent assays of proteins immobilized on nitrocellulose, such as BSA, protein A and ovalbumin. When simultaneously probed with a rabbit antiovalbumin and the protein-PLDS-Tb conjugate, a quantity as small as 10 ng of ovalbumin can be detected by the naked eye.

Lanthanide ions with anisotropic molecular magnetic susceptibility tensor $\Delta\chi$, for example, Er^{III}, Tm^{III}, or Yb^{III}, allow valuable structural information to be extracted from pseudocontact shifts (PCS, see also Section 3.6) and residual dipolar couplings (RDCs) arising from the partial alignment of the R^{III}-labeled biomolecules in the induced magnetic field (Su et al., 2008b):

$$\Delta\delta^{PCS} = \frac{1}{12\pi r^3}\left[\Delta\chi_{ax}(3\cos^2\theta - 1) + 1.5\Delta\chi_{rh}\sin^2\theta\cos 2\varphi\right] \qquad (131)$$

where r, θ, and φ are the polar coordinates of the nucleus spin with respect to the principal axes of the $\Delta\chi$ tensor; $\Delta\chi_{ax}$ and $\Delta\chi_{rh}$ are the axial and rhombic components of the susceptibility anisotropy tensor, respectively. The RDC between spins i and j, D_{ij}, is given by a similar equation:

$$D_{ij} = -\frac{S\gamma_i\gamma_j\mu_0\hbar}{8\pi^2 r_{ij}^3}[A_{ax}(3\cos^2\partial - 1) + 1.5A_{rh}\sin^2\partial\cos 2\varphi] \quad (132)$$

in which ∂ and φ characterize the orientation of the internuclear vector with respect to the principal axes of the alignment tensor, A_{ax} and A_{rh} are the axial and rhombic components of this tensor, S is the order parameter, γ_i and γ_j are the magnetogyric ratios for nuclei i and j separated by a distance r_{ij}, and $\hbar$ is Planck's constant divided by 2π. When a rigid molecule is partially aligned in the magnetic field as a result of its paramagnetism, the alignment tensor A is directly proportional to the susceptibility tensor (B_0 is the magnetic induction field strength, k is Boltzmann's constant, and T the temperature):

$$A_{ax,rh} = \frac{B_0^2}{15\mu_0 kT}\Delta\chi_{ax,rh} \quad (133)$$

Therefore, PCS and D_{ij} data bear orientation information useful for structure analysis and study of protein mobility, particularly when data are collected for several orientations. Alternatively, PCS induced by several different R^{III} ions provide similar information. For the latter investigations, the lanthanide paramagnetic tag is attached at different positions of the protein or lanthanide tags with different $\Delta\chi$ tensors are used.

In a recent study, Su et al. (2008b) have designed a protein-specific lanthanide tag based on the derivatized dipicolinic acid $\mathbf{H_2L15^w}$ (Figure 94, bottom). The 4-mercaptomethyl-dipicolinate unit coordinates to lanthanide ions with nanomolar affinity and builds a disulfide bond with proteins. In this way, the lanthanide dipicolinate is close to the protein domain to be investigated, resulting in an accurate determination of the $\Delta\chi$ tensor and in a rigid attachment of the tag to the protein, limiting variation in PCS and D_{ij} when the lanthanide tag reorientates with respect to the protein. The *N*-terminal DNA-binding domain of an *E. coli* Arginine repressor was derivatized with $\mathbf{H_2L15^w}$ and heteronuclear single quantum coherence (HSQC) ^{15}N-NMR spectra were recorded. In presence of R^{III} ions, a single crosspeak was observed for each backbone amide; Yb^{III} induced shifts up to 2 ppm. The geometric parameters of the $\Delta\chi$ tensor were determined in the simultaneous presence of Tb^{III}, Tm^{III}, and Yb^{III}. Although the $\Delta\chi$ tensor is only half as large as the ones reported for proteins and peptides, the new tags present decisive advantages, such as their straightforward synthesis, their nonchirality (reduction of the number of NMR signals by a factor 2), and a reduced probability of unwanted interferences.

6.2.3 Two-photon luminescence microscopy

One difficulty encountered when working with LLBs is the relatively short excitation wavelength they require, typically 270–360 nm, very few of them, particularly those containing Eu^{III} or Tb^{III}, being amenable to excitation wavelength above 400 nm. In addition to having a comparatively short penetration depth, UV and blue lights are detrimental to living systems, so that alternate ligands are being developed for which either longer wavelength excitation or higher-order excitation is feasible. In the case of dipicolinic acid derivatives, longer excitation wavelengths have been achieved by tuning the energy of the charge-transfer states in push–pull type ligands (Figure 95).

For instance, $[Eu(\mathbf{L15^{Wi}})_3]^{3-}$ ($i = 2$, 3, and 4) have absorption maxima around 320 nm instead of 280 for the parent dipicolinate and their quantum yield in CH_2Cl_2 are sizeable, between 0.15 and 0.43. However, extending one-photon excitation of the ligand into the visible range often proves to be problematic because the lowering of the ligand excited levels facilitates back transfer processes. When the excitation wavelength is shifted to 427 nm in $[Eu(\mathbf{L13^{W5}})_3]^{3-}$, no emission from Eu^{III} is detected at room temperature (D'Aléo et al., 2008b). As a consequence scientists are now turning to multiphoton excitation, especially that presently two-photon excitation is commercially available in confocal microscopy, following the pioneering work of Denk et al. (1990) and the commercialization of femtosecond laser sources. This allows noninvasive 3D imaging of biological tissue without creating collateral damage. Two-photon (or biphotonic, TPA) absorption is related to nonlinear optical (NLO) properties of the chromophore under consideration. It turns out that lanthanide tris(dipicolinates) possess NLO properties as demonstrated by their second-order hyperpolarizability coefficient $\langle\beta\rangle$ which was measured by the harmonic light scattering method (Tancrez et al., 2005). In this experiment, the intensity of the scattered light $I^{2\lambda}$ is plotted versus the square of the intensity of the incident light, I^{λ}, according to

$$I^{2\lambda} = G(N_S\langle\beta_S\rangle + N\langle\beta\rangle)(I^{\lambda})^2 \tag{134}$$

where indices S denote the solvent and N is the number of molecules per cm^3. Data plotted on Figure 96 clearly point to a contribution of the 4f-orbitals to this parameter in that the second-order hyperpolarizability increases with the number of 4f electrons and, moreover, it is the same for Y^{III} and La^{III}, within experimental errors. When excited with a laser line at 532 nm, an aqueous solution of $Na_3[Eu(\mathbf{L15^a})_3]$, which possesses two absorption bands at 270 and 278 nm, exhibits the characteristic Eu ($^5D_0$) emission. However, the plot of the emitted intensity versus the excitation power is linear, indicating that excitation is a single-photon absorption by the weak $^5D_1 \leftarrow {}^7F_1$ transition centered at

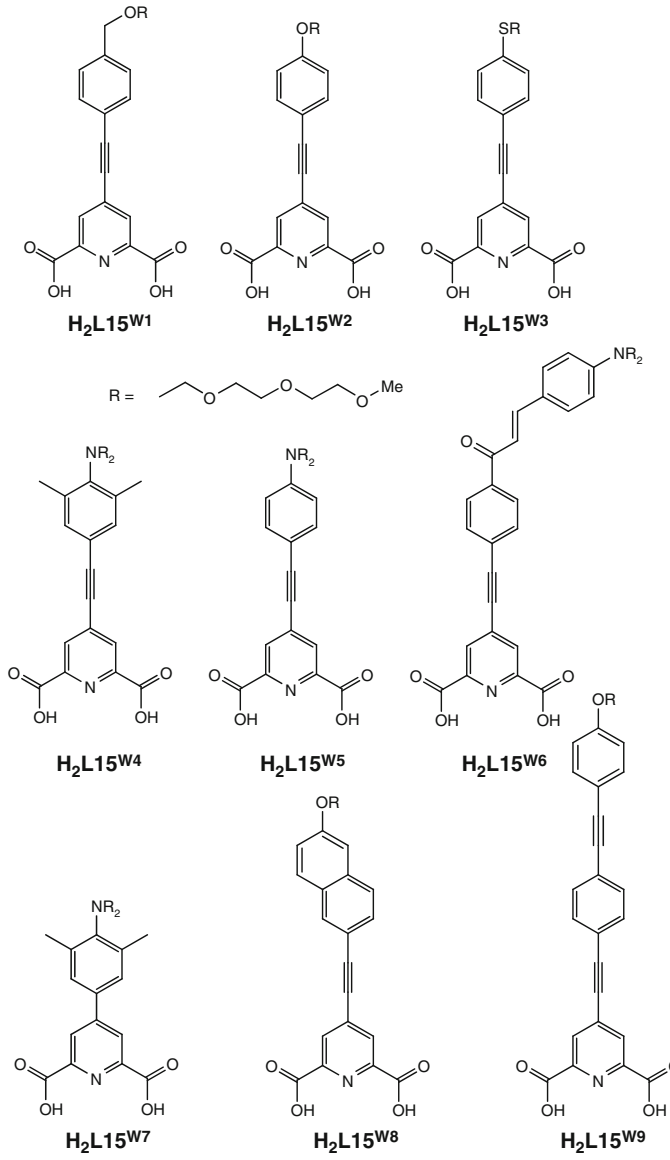

FIGURE 95 Push–pull derivatives of dipicolinic acid leading to longer excitation wavelengths for the $[Ln(\mathbf{L15})_3]^{3-}$ complexes (top two rows: D'Aléo et al., 2008b; bottom row: D'Aléo et al., 2008a).

536 nm. This transition has an estimated molar absorption coefficient of only 0.015 $M^{-1}cm^{-1}$ at 532 nm (also partly due to the fact that the fractional population of the $^7F_1$ sublevel at room temperature is only

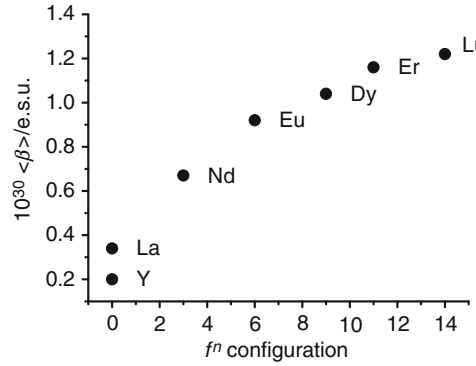

FIGURE 96 Second-order hyperpolarizability constant of lanthanide tris(dipicolinates) [*R*(**L15^{a}**)$_3$] 0.1 M in water (redrawn after Tancrez et al., 2005).

0.33) but the large laser power (0.1–1.7 mW) compensates for this weak oscillator strength. On the other hand, the same plot for Na_3[Tb(**L15^{a}**)$_3$] reveals a quadratic variation of the Tb($^5D_4$) emission intensity with excitation power (between 0.5 and 3 mW, experimental exponent: 1.95), indicating that the luminescence originates from TPA absorption in the organic ligand. Similarly, crystals of the guanidinium salt of [Tb(**L15^{a}**)$_3$]$^{3-}$ could be observed under biphotonic excitation at 532 nm (D'Aléo et al., 2007).

In addition to the octupolar D_3-symmetry found in lanthanide tris (dipicolinates), favorable to NLO effects, the bulk of the NLO properties of a complex depend on the electronic properties of the ligands. With this in mind, Picot et al. (2007) have developed new push–pull chromophores based on the pyridine-carboxamide framework (**L15^{k-p}**, see Figure 24). The best chromophore is ligand **L15^{l}** in which the hexyloxy donor on the phenylacetylene para position pushes the charge-transfer state to a sufficiently high energy to avoid quenching of the Eu^{III} luminescence. The corresponding tris(complex), [Eu(**L15^{l}**)$_3$]$^{3+}$, has a relatively modest quantum yield (5.6% in acetonitrile), but it displays two-photon excitation luminescence, contrary to the parent compound discussed above. This is demonstrated in Figure 97 in which the TPA excitation spectrum is superimposed to the absorption spectrum of the complex. The calculated two-photon absorption cross section amounts to 96 GM at 720 nm (1 Göppert-Mayer unit (GM) = 10^{-50} cm^4 s photon^{-1}), a value somewhat lower compared to the best dipolar lanthanide β-diketonate complexes, for example, [Eu(tta)$_3$(dpbt)], where tta stands for thenoyltrifluoroacetylacetonate and dpbt for 2-(*N*,*N*-diethylanilin-4-yl)-4,6-bis(3,5-dimethylpyrazol-1-yl)-1,3,5-triazine (157 GM at 810 nm), or [Eu(fod)$_3$(Mk)] where fod is 6,6,7,7,8,8,8-heptafluoro-2,2-dimethyl-3,5-octanedionate and Mk Mischler's ketone (253 GM at 810 nm).

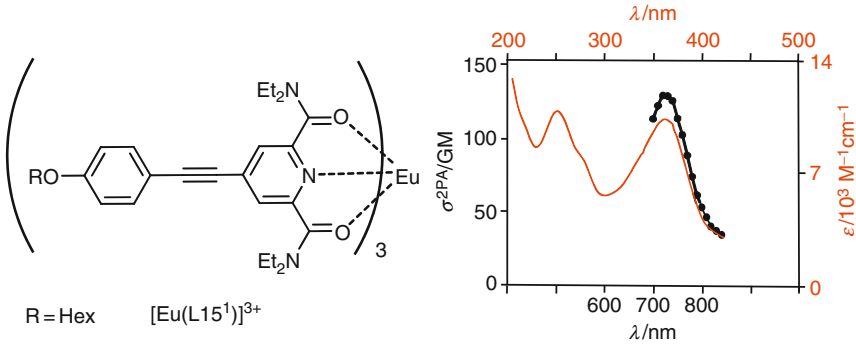

FIGURE 97 Left: formula of the Eu^{III} complex displaying a large TPA cross section. Right: absorption spectrum (top and right scales) and biphotonic excitation spectrum (bottom and left scales) of $[Eu(\mathbf{L15^{I}})_3]^{3+}$ in acetonitrile solution (redrawn from Picot et al., 2007).

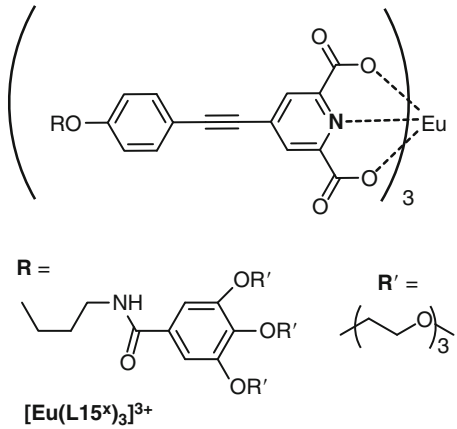

FIGURE 98 Structure of the $[Eu(\mathbf{L15^{x}})_3]^{3-}$ complex used for two-photon luminescence microscopy (Picot et al., 2008a).

Ligand $\mathbf{L15^{I}}$ was further modified to ensure water solubility through triethyleneglycol moieties, better stability by substitution of the amide groups with carboxylate units, as well as improved photophysical properties of the resulting Eu^{III} chelate (Figure 98, Picot et al., 2008a). The quantum yield of the tris-complex $Na_3[Eu(\mathbf{L15^{x}})_3]$ amounts to 15.6% in water and can be excited by a TPA process at 720 nm, the corresponding excitation spectrum again matching the absorption spectrum. The biphotonic absorption cross section remains modest, but is comparable to the one of the previous complex, 92 GM. T24 cancer cells were incubated in a solution of this complex 20 μM in phosphate buffer solution and fixed

with ethanol. Images taken with a biphotonic femtosecond laser scanning microscope with excitation wavelength at 760 nm ($\sigma^{TPA} = 19$ GM at this wavelength) indicates that the complex localizes in the perinuclear region of the cells, possibly in the endoplasmatic reticulum. This demonstrates the feasibility of two-photon LLBs for this type of analysis.

After publication of this work, the same authors have shown that $[Eu(\mathbf{L15^{Wi}})_3]^{3-}$ complexes with $i = 5$–9 (Figure 95) have much larger TPA cross sections, ranging from 110 ($i = 8$) to 173 ($i = 6$), 193 ($i = 7$), 218 ($i = 9$), and to the record 775 ($i = 5$) GM (D'Aléo et al., 2008a).

6.3 Homobinuclear helicates as LLBs for cell imaging and sensing

Despite the known advantages of lanthanide luminescent probes for bioanalyses (see Section 6.1), there has been few attempts to use them for cell imaging and sensing and some are summarized below. To our knowledge, the first experiments were carried out by Scaff et al. (1969) who treated bacterial smears from *E. coli* cell walls with a millimolar solution of europium thenoyl-trifluoroacetonate, $[Eu(tta)_3(H_2O)_2]$ in 50% ethanol before examining them under a luminescence microscope illuminated by a continuous mercury lamp: the intense emission from the $Eu(^5D_0)$ level brightly stained the cells especially when the pH was around 7. Later, Canada (1983) investigated the calcium-binding site of GH3/B6 pituitary tumor cells by binding Tb^{III} to these cells; in this way two sites were evidenced, one of which being specific for calcium. Furthermore, the luminescent properties of the Tb–GH3/B6 complex are sensitive to the presence of various analytes, such a adriamycin, or drugs, such as cisplatin, which allows their quantification (Canada, 1988). The same authors have also examined the binding sites of cisplatin to cisplatin-resistant human breast and ovarian cancer cells thanks to the Tb^{III} luminescence detected in TRD mode (Canada and Paltoo, 1998). The Eu^{III} ion has also been often used as luminescent bioprobe, for instance for characterizing the binding sites on the cell walls of *Datura Innoxia* (Ke et al., 1992). A thermal imaging method based on a Eu^{III} β-diketonate succeeded in mapping receptor-activated heat waves in Chinese hamster ovaries (Zohar et al., 1998) while the usefulness of LLBs for eliminating the autofluorescence background of biological samples by TRD was further demonstrated by Phimphivong and Saavedra (1998): a lipid-conjugated Tb^{III} diethylenetrinitrilotetraacetate complex proved to be an efficient membrane-staining agent for morphological studies of Swiss albino mouse 3T3 cultured cells. The first long-lasting efforts toward developing LLBs for imaging stemmed from the group of D. J. Bornhop who advocated a highly luminescent terbium macrocyclic complex for the *in vitro* and *in vivo* imaging of anomalous tissues as well as

for specific targeting of cancerous tissues (Bornhop et al., 1999, 2003; Manning et al., 2006). More recently, Parker and coworkers have designed macrocyclic Eu^{III} complexes staining either the nucleoli or the cytoplasm of several live cell lines such as NIH 3T3, HeLa, and HDF (Frias et al., 2003; Poole et al., 2007; Yu et al., 2006).

Taking into account the luminescent chelates developed for bioanalyses (mainly immunoassays), most of the presently available LLBs fall into the following classes: (i) polyaminocarboxylates (Latva et al., 1997; Takalo et al., 1997), (ii) bipyridine-based cryptates (Guillaumont et al., 2007), (iii) cyclen derivatives (Pandya et al., 2006), (iv) aza macrocycles incorporating a pyridine, bipyridine, or terpyridine unit (Bornhop et al., 1999; Nasso et al., 2005), (v) β-diketonates (Nishioka et al., 2007), or (vi) chelates bearing 2-hydroxyisophthalamide chromophores (Samuel et al., 2008a). With few exceptions, all of the above-mentioned LLBs are mononuclear species. However, associating two luminescent stains emitting different colors or one luminescent and one magnetic stains into a single-probe system is an attractive way of integrating the advantages of multiplex analyses. This has been achieved by attaching an organic chromophore to a Gd^{III} contrast agent for instance (Manning et al., 2004) or by developing receptors able to bind Gd^{III} and luminescent R^{III} ions while preserving the specific physicochemical properties of each metal ion (Picard et al., 2006). Finally, Imperiali has recently advocated ''double-lanthanide-binding tags'' (Dlbt) consisting in homobinuclear Tb^{III} species in which the metal ion is bound by encoded amino acids (Martin et al., 2007); in this case the presence of the two metal ions simply reinforce the luminescent and/or X-ray diffracting properties of the conjugates.

For testing the utility of binuclear LLBs, Bünzli and coworker have developed a library of water-soluble hexadentate ditopic ligands with benzimidazole-pyridine cores, $\mathbf{H_2L13^{f-1}}$ (see Figure 44), which self-assemble in water, at room temperature, and physiological pH 7.4 to give the corresponding homobinuclear helicates in large yield (usually $>95\%$ at millimolar total ligand concentration). This molecular framework possesses two additional properties: (i) rendering the two tridentate binding units slightly different allows the formation of heterobinuclear helicates, for the time being only in organic solvents though (see Section 4.2) and (ii) the helical edifices are potentially chiral which opens interesting perspectives for chiral recognition.

6.3.1 Thermodynamic, photophysical, and kinetic properties of the neutral, water-soluble $[R_2(\mathbf{L13})_3]$ helicates

The cumulative stability constants for the formation of the homobinuclear helicates with the seven ligands $\mathbf{H_2L13^{f-1}}$ are reported in Table 8 and a typical distribution diagram is represented on Figure 99 for ligand

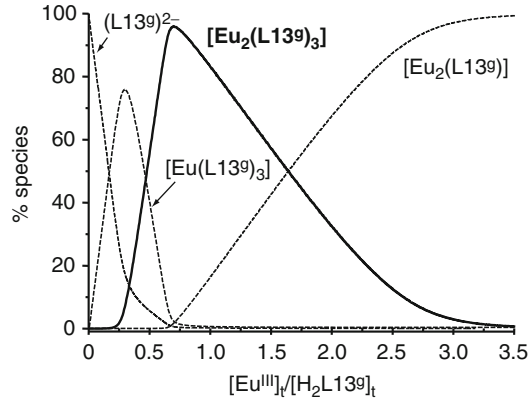

FIGURE 99 Distribution diagram for the system Eu^{III}/**H_2L13^g** at pH 7.4 (Tris–HCl buffer) and for $[\mathbf{H_2L13^g}]_t = 10^{-4}$ M (redrawn from Chauvin et al., 2008).

H_2L13^g. With respect to the parent ''unsubstituted'' helicates $[Ln_2(\mathbf{L13^f})_3]$ the grafting of the polyoxyethylene pendant has relatively little effect on the stability constant of the main 2:3 species, given the fact that the spectrophotometrically determined constants have been calculated from heavily correlated spectra. Indeed, if the log $\beta_{23}(Eu^{III})$ values span a range from 23.4 (**H_2L13^g**) to 28.6 (**H_2L13^k**) the speciation of the homobinuclear helicate at stoichiometric ratio 2:3 and total ligand concentration of 4.5×10^{-4} M (Table 14) varies between relatively narrow limits: from 88.7% (**H_2L13^l**) to 99.5% (**H_2L13^f**).

Moreover, the next more abundant species (1:2 or 1:3, R^{III}:L) accounts for most of the remaining speciation; that is, the stoichiometric 2:3 solutions contain only minute concentrations of uncomplexed R^{III}, an important feature when it comes to put them into contact with living materials. Another finding is that the stability does not vary much along the lanthanide series, so that one lanthanide ion may be replaced by another one with different photophysical properties without affecting much the speciation, another useful feature for multiplex experiments.

Biological media contain a wealth of substances potentially able to interfere with the LLB, either chemically by ligand exchange or transmetallation, or photophysically by quenching of the metal-centered luminescence by endogenous antioxidants. To both ascertain the stability data gathered by spectrophotometric titration and to test the action of potential interfering substances, several experiments were conducted on $[Eu_2(\mathbf{L13^g})_3]$ to which were added 10–100 equivalents of EDTA, DTPA, citrate, L-ascorbate or zinc. The luminescence of the resulting solutions did not decrease substantially (0–10%) 24 h after the addition (Table 15) meaning that the binuclear LLB is well suited for bioanalyses which are

TABLE 14 Percentage of the main complexed species in stoichiometric 2:3 solutions of Eu^{III} and $\mathbf{H_2L13^{f-l}}$ in aqueous solutions at pH 7.4 (Tris–HCl 0.1 M), as recalculated from published conditional stability constants for a total ligand concentration of 4.5×10^{-4} M

Ligand	2:3 species (%)	1:2 species (%)	References
$\mathbf{H_2L13^f}$	99.5	NA	Elhabiri et al. (1999)
$\mathbf{H_2L13^g}$	97.1	2.1[a]	Chauvin et al. (2008)
$\mathbf{H_2L13^h}$	92.9	7.1	Deiters et al. (2008)
$\mathbf{H_2L13^i}$	89.2	7.9[a]	Chauvin et al. (2007)
$\mathbf{H_2L13^j}$	92.5	5.9	Deiters et al. (2009)
$\mathbf{H_2L13^k}$	94.6	4.5	Deiters et al. (2009)
$\mathbf{H_2L13^l}$	88.7	9.1	Deiters et al. (2009)

[a] 1:3 species.

TABLE 15 Stability of the $[Eu_2(\mathbf{L13^g})_3]$ helicate versus pH, several complexing agents, and Zn^{II}, as monitored by luminescence, at room temperature and pH 7.4 (Tris–HCl) (from Bünzli et al., 2008)

Parameter/chemical species	Eqs added	Time (h)	Loss in luminescence intensity (%)
pH	(pH 3)	24	No
	(pH 10)	24	No
EDTA	100	48	No
DTPA	100	24	10
Citrate	100	96	No
L-Ascorbate	100	96	10
Zn^{II}	10	24	10
	100		15

usually carried out in far less than 24 h. The ditopic ligand $\mathbf{H_2L13^g}$ has also been added to solutions of [Eu(EDTA)] and [Eu(DTPA)] and formation of the helicate was almost complete (92.5%) after 21 days in the first case, but partial in the second case. This shows that the helicate is more stable than the EDTA chelate and has stability comparable to that of the DTPA complex. Moreover, no ligand exchange occurs and transmetallation with zinc starts only to be problematic when 100 equivalents are added, a concentration far more important than the largest one found in biosystems.

Since no single crystal suitable for X-ray diffraction analysis could be obtained for the helicates with $\mathbf{H_2L13^{g-l}}$, Eu^{III} was chosen as a structural

luminescent tag to probe the chemical environment of the metal ions in the homobinuclear helicates. As shown in Table 10, the $^5D_0 \rightarrow {}^7F_0$ transition of all of the $[Eu_2(\mathbf{L13^{g-l}})_3]$ helicates is unique, as for $[Eu_2(\mathbf{L13^f})_3]$, pointing to the equivalence of the two metal ion sites. Moreover, its energy is predicted to be 17,231 cm^{-1}, taking into account the nephelauxetic effect described by Eq. (19) (see Section 3.5) for a N_6O_3 environment. The experimental values for the seven investigated helicates deviate by at most 4 cm^{-1} from this expected energy. The emission spectra recorded at low temperature (10 K) to remove the broadening due to vibronic contributions can be interpreted as arising from a species with idealized D_3-symmetry (Figure 100). In addition to the unique and very weak $^5D_0 \rightarrow {}^7F_0$ transition (forbidden in this symmetry), the $^5D_0 \rightarrow {}^7F_1$ transition displays a sharp component corresponding to the transition to the A_1 ligand-field sublevel and a second band corresponding to a transition terminating onto the split E sublevel. The A_1-E separation reflects the strength of the B_0^2 crystal-field parameter, which can be estimated to be around -600 cm^{-1} for $\Delta E(A_1\text{-}E) \approx 160$ cm^{-1} (Binnemans and Görller-Walrand, 1995), while the splitting of the E component, ΔE(E-E), is indicative of the distortion from the idealized D_3-symmetry. Data reported in Table 16 point to these two parameters being very similar for the seven studied helicates, meaning that the inner coordination sphere of the Eu^{III} ions is little affected by the various substituents grafted on the bis(benzimidazole)pyridine core. The luminescence decays confirm this finding in that they are usually single

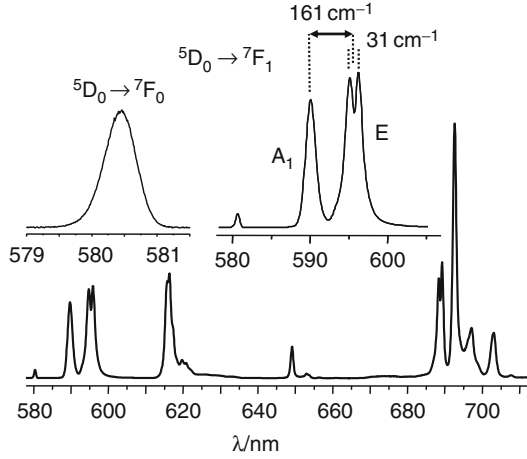

FIGURE 100 High-resolution emission spectrum of $[Eu_2(\mathbf{L13^g})_3]$ 10^{-4} M in water/glycerol 9/1, v/v at 10 K, under ligand excitation. Top: details of the $^5D_0 \rightarrow {}^7F_J$ ($J = 0, 1$) transitions (redrawn from Bünzli et al., 2008).

TABLE 16 Photophysical properties of solutions of the helicates $[Eu_2(\mathbf{L13})_3]$ in aqueous solution (Tris–HCl 0.1 M) at pH 7.4 and 295 K (references: see Table 14)

		$^5D_0 \rightarrow {}^7F_1$[a]			Q^L_{Eu}	τ_{rad} (ms)	Q^{Eu}_{Eu}	η_{sens}
Ligand	$^5D_0 \rightarrow {}^7F_0$ E_{exp} (cm^{-1})	ΔE(A–E) (cm^{-1})	ΔE(E–E) (cm^{-1})	q[b]	±15%	±0.3[c]	±15%[d]	±15%[e]
$\mathbf{H_2L13}$[f]	17,232	156	28	0.2	0.24	6.9	0.37	0.67
$\mathbf{H_2L13}$[g]	17,234	161	31	−0.1	0.21	6.9	0.36	0.58
$\mathbf{H_2L13}$[h]	17,233	146	31	−0.1	0.19	6.3	0.37	0.52
$\mathbf{H_2L13}$[i]	17,235	162	38	0.0	0.11	6.2	0.36	0.30
$\mathbf{H_2L13}$[j]	17,235	168	26	−0.1	0.15	6.4	0.40	0.38
$\mathbf{H_2L13}$[k]	17,235	160	34	−0.1	0.9	6.7	0.34	0.26
$\mathbf{H_2L13}$[l]	17,227	145	31	0.1	0.035	6.8	0.08	0.044

[a] At 10 K in water/glycerol 9/1, v/v; see text.
[b] Hydration number calculated from the phenomenological equation of Supkowski and de Horrocks (2002); estimated error: ±0.3.
[c] Eu($^5D_0$) radiative lifetime calculated from Eq. (15).
[d] Intrinsic quantum yield estimated from Eq. (10).
[e] Ligand sensitization efficiency obtained from Eq. (8).

exponential functions associated with a long Eu($^5D_0$) lifetime (2.3–2.4 ms), except in the case of $\mathbf{H_2L13^l}$. The latter ligand has too low a triplet state, so that back transfer occurs in the helicate, reducing both the lifetime and the quantum yield. In the case of $\mathbf{H_2L13^i}$ the decay measured under high-resolution conditions is biexponential, from which two lifetimes can be extracted, a longer one (2.2 ms) and a shorter one (0.53 ms) assigned to a hydrated species with a population of about 10%, reflecting the speciation reported in Table 14. A similar situation is met for $\mathbf{H_2L13^h}$, the shorter lifetime (0.89 ms) corresponding to a population of about 6%, again in line with the speciation for this system. Finally, an estimate of the hydration number by means of the phenomenological equation of Supkowski and de Horrocks (2002) taking into account lifetimes determined in water (τ_{H_2O}) and deuterated water (τ_{D_2O}) and correcting for second sphere effects, leads to a value which is essentially equal to zero.

$$q = 1.11 \times \left(\frac{1}{\tau_{H_2O}} - \frac{1}{\tau_{D_2O}} - 0.31 \right) \tag{135}$$

Insight into the energy transfer processes operating in the Eu^{III} helicates can be gained by analyzing the emission spectra and lifetimes in terms of Eqs. (8), (10), and (15) (Section 2.5). The relevant data are also listed in Table 16. Surprisingly, the radiative lifetime (6.2–6.9 ms) and intrinsic quantum yields (0.34–0.37, except for $\mathbf{H_2L13^l}$, 0.08) are the same for all the chelates, within experimental errors. This is again in line with an almost identical and fairly rigid nine-coordinate environment for the metal ions featuring very similar deactivation processes. Therefore, the differences observed in the overall quantum yields Q^L_{Eu}, which are among the largest reported for this ion in water, almost exclusively arise from differences in the ligand-to-metal energy transfers, as indicated by the sensitization efficiency η_{sens} which decreases about two-fold from 0.67 in [$Eu_2(\mathbf{L13^f})_3$] to 0.26–0.38 in [$Eu_2(\mathbf{L13^{i-k}})_3$], and to only 0.08 in [$Eu_2(\mathbf{L13^l})_3$], while it is much less affected in the remaining two helicates [$Eu_2(\mathbf{L13^{g,h}})_3$]. Comparing [$Eu_2(\mathbf{L13^g})_3$] and [$Eu_2(\mathbf{L13^h})_3$] shows that the lengthening of the polyoxyethylene pendant does not affect the photophysical properties. On the other hand, its grafting on the benzimidazole core in $\mathbf{H_2L13^i}$ is detrimental to both the thermodynamic stability (Table 14) and the photophysical properties of the helicates (Table 16). Finally, when the energy of the triplet state is lowered in $\mathbf{H_2L13^k}$ and $\mathbf{H_2L13^l}$, back transfer starts to be operative, henceforth the decrease in the quantum yield and sensitization efficiency, a phenomenon particularly acute for the latter ligand. It is common to discuss sensitization efficiency with respect to the energy gap between the emitting level and the 0-phonon energy of the triplet state and some phenomenological correlations have been found. For

instance, the quantum yield of Eu^{III} appears to be maximum when ΔE ($^3\pi\pi^*$–$^5D_0$) is around 2700 cm^{-1} in β-diketonates (Sato and Wada, 1970), between 2500 and 5000 cm^{-1} in polyaminocarboxylates (Latva et al., 1997), and only a few hundred cm^{-1} in Schiff base derivatives (Archer et al., 1998). For Tb^{III}, substantial quantum yields are obtained when ΔE ($^3\pi\pi^*$–$^5D_4$) > 1500 cm^{-1} for polyaminocarboxylates (Latva et al., 1997) or for complexes of *p*-substituted 2-hydroxyisophthalamides (Samuel et al., 2008b). On the other hand, the correlation between η_{sens} and $\Delta E(^3\pi\pi^*$–$^5D_0)$ for binuclear helicates is not obvious, especially when considering $\mathbf{H_2L13^f}$ and $\mathbf{H_2L13^i}$ (Figure 101, top).

In the case of Tb^{III}, the quantum yield is indeed very low when the ΔE ($^3\pi\pi^*$–$^5D_4$) gap is <1500 cm^{-1}. Vibration-assisted back energy transfer is operating, which results in very short lifetimes at room temperature (Table 10). The corresponding activation energy is around 1600–1800 cm^{-1} for $[Tb_2(\mathbf{L13^g})_3]$, roughly corresponding to the energy of CO and CC vibrations (Chauvin et al., 2008). As a consequence, hydration

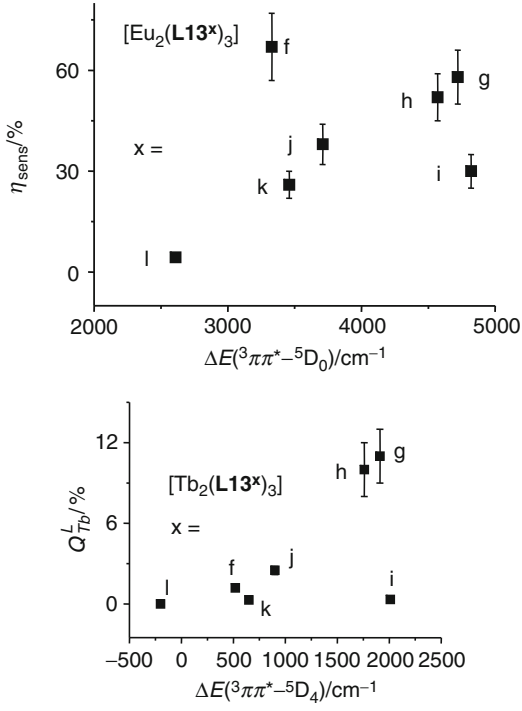

FIGURE 101 Top: sensitization efficiency of the $(\mathbf{L13^x})^{2-}$ ($x = j - l$) ligands for Eu^{III} luminescence versus the energy gap. Bottom: overall quantum yield of the $[Tb_2(\mathbf{L13^x})_3]$ helicates versus the energy gap (redrawn after Deiters et al., 2009).

numbers cannot be estimated with Eq. (135) because nonradiative deactivation by O–H vibrators is not the main quenching process in the helicates. Only two of the seven ligands $\mathbf{H_2L13^{f-l}}$ sensitize the Tb^{III} luminescence reasonably well, $\mathbf{H_2L13^{g}}$ and $\mathbf{H_2L13^{h}}$ (Figure 101, bottom) although quantum yields (11% and 9%, respectively) are not up to those reported in the literature for other chelates, ≈60% for water-soluble podates featuring 2-hydroxyisophthalamide antennae for instance (Petoud et al., 2003; Samuel et al., 2008a,b). The best ditopic ligand for both Eu^{III} and Tb^{III} is therefore $\mathbf{H_2L13^{g}}$ and it also sensitizes the luminescence of other ions such as Nd^{III}, Sm^{III} ($Q^{L}_{Sm} = 0.38\%$), and Yb^{III} ($Q^{L}_{Yb} = 0.15\%$).

6.3.2 Biocompatibility of the neutral water-soluble $[Ln_2(\mathbf{L13})_3]$ helicates

Absence of or small cytotoxicity is an important prerequisite for LLBs intended for the sensing and imaging of live biomaterials. Bünzli et al. (2008) have conducted WST-1 cell viability and proliferation tests on various cancerous cell lines, 5D10 (mouse hybridoma), Jurkat (human T leukemia), MCF-7 (human breast carcinoma), HeLa (human cervical adenocarcinoma), as well as on a noncancerous line, HaCat (human keratinocyte). Typically, cells are grown in RPMI-1640 supplemented cell culture medium containing various concentrations of the helicate, at 37 °C in an atmosphere containing 5% CO_2. The viability test is performed at several time intervals between 0.5 and 24 h and selected results are reported in Table 17 while a typical example of the influence of $[Eu_2(\mathbf{L13^{i}})_3]$ on cell proliferation is shown on Figure 102. These data clearly demonstrate that the cytotoxicity of all the tested helicates is very small, with half-maximal inhibitory concentration $IC_{50} > 500$ μM. Some of these results were also confirmed by the lactase dehydrogenase (LDH) test which allows an assessment of damages caused to the cell membrane by determining the LDH leakage out of the cell; in the case of $[Eu_2(\mathbf{L13^{i}})_3]$, this leakage was found to be less than 4% for the three tested cell lines, Jurkat, 5D10, and MCF-7 (Chauvin et al., 2007). Not only cell viability and proliferation are not affected by the presence of the binuclear LLBs in the cell culture medium but, also, their morphology remains unchanged. No swollen nuclei or visible granules developed upon incubation of HeLa cells during 7 h with $[Eu_2(\mathbf{L13^{g}})_3]$ 100 μM for instance. As a comparison, a popular nucleic acid intercalating dye, acridine orange (AO), induces swollen nuclei after the same incubation time, and necrotic cells are seen after 24 h (Figure 103). These results point to the lanthanide helicates being indeed biocompatible luminescent tags (Song et al., 2008c).

TABLE 17 Selected cell viability values (%) as determined from the WST-1 test after incubation for 24 h at 37 °C in RPMI-1640 containing various concentrations of $[Eu_2(\mathbf{L13})_3]$ helicates

Ligand	c (μM)	Jurkat	$^5D_{10}$	MCF-7	HeLa	References
None	0	100	100	100	100	
$\mathbf{H_2L13}^{f}$	125	NA	NA	NA	111 ± 3	Bünzli et al. (2008)
$\mathbf{H_2L13}^{g}$	125	92 ± 16	93 ± 1.1	92 ± 13	88 ± 3	Chauvin et al. (2008) and Vandevyver et al. (2007)
	250	101 ± 4	99 ± 1	102 ± 7	101 ± 1	Chauvin et al. (2008) and Vandevyver et al. (2007)
	500	107 ± 4	89 ± 4	101 ± 1	108 ± 2	Chauvin et al. (2008) and Vandevyver et al. (2007)
$\mathbf{H_2L13}^{h}$	500	NA	NA	NA	101 ± 1	Deiters et al. (2008)
$\mathbf{H_2L13}^{i}$	125	90 ± 1	88 ± 1	89 ± 1	119 ± 2	Chauvin et al. (2007)
	250	89 ± 1	87 ± 2	87 ± 1	105 ± 6	Chauvin et al. (2007)
	500	89 ± 1	90 ± 6	89 ± 1	110 ± 3	Chauvin et al. (2007)
$\mathbf{H_2L13}^{k}$	500	NA	NA	NA	101 ± 1	Deiters et al. (2009)

Data are averages of 3–4 independent determinations.

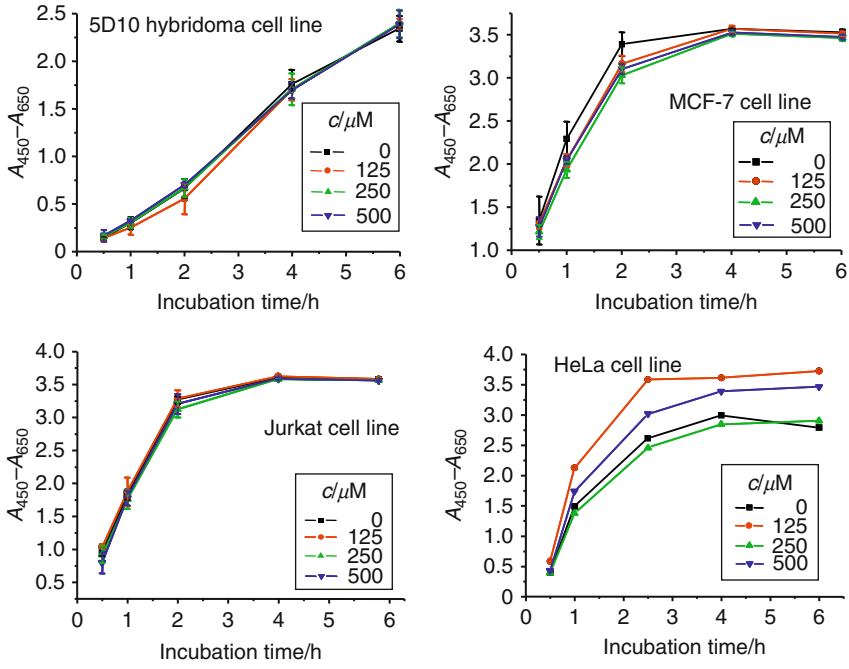

FIGURE 102 Cell proliferation of various cancerous cell lines when incubated with $[Eu_2(\mathbf{L13^i})_3]$ (redrawn from Chauvin et al., 2007).

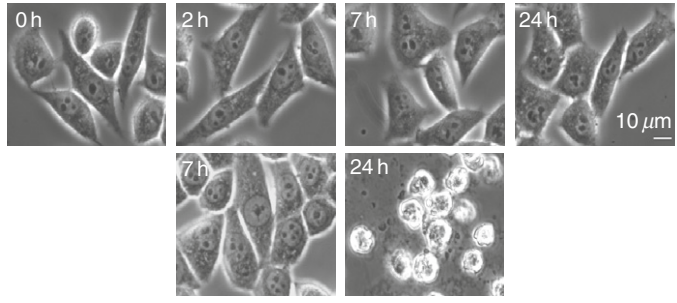

FIGURE 103 Phase contrast microscopy of HeLa cells exposed to 100 μM $[Eu_2(\mathbf{L13^g})_3]$ (top row) or 3.2 μM acridine orange (bottom row) at 37 °C for the indicated time interval (reproduced by permission from Song et al., 2008a, © The Royal Society of Chemistry, 2008).

6.3.3 Uptake of the neutral water-soluble $[Ln_2(\mathbf{L13})_3]$ helicates in living cells

Most of the work published to date with lanthanide helicates as LLBs has been performed on the easy-to-grow HeLa cell line (Bünzli et al., 2008). When incubated with the $[Ln_2(\mathbf{L13})_3]$ helicates, live HeLa cells uptake the LLBs in a concentration-dependent way (Chauvin et al., 2007, 2008; Deiters et al., 2008, 2009; Song et al., 2008c; Vandevyver et al., 2007). There are essentially two mechanisms by which an exogenous substance can penetrate membrane cells. The first one is ''tunneling'' through the hydrophobic cell membrane through channels having usually some specificity; this occurs when the molecular weight of the penetrating molecule is not too large (typically < 800 Da). Otherwise, a process known as endocytosis is operating. In this process the cell membrane engulfs the incoming molecule to form a pocket which escapes into the cell to produce a vesicle filled with extracellular fluid, including the exogenous substance. The vesicle moves into the cytosol and then merges with endosomes and liposomes. As the $[Ln_2(\mathbf{L13})_3]$ helicates have molecular weight around 2600–3100 Da, this mechanism is likely to occur. An easy way to prove it is to conduct the uptake experiments at 4 °C because endocytosis is not occurring at low temperature. As depicted on Figure 104, the total emitted light by HeLa cells grown under the usual conditions in absence or in presence of an helicate is the same at low temperature. On the other hand, if the background noise remains the same at 37 °C in absence of helicate in the culture medium, the intensity increases considerably when the cells are loaded with the helicate. Additional proofs for this receptor-mediated uptake mechanism come from the use of endocytosis inhibitors. When the same HeLa cells are incubated with the Eu^{III} helicate in a hypertonic medium containing 0.45 M of sucrose, a 92% decrease in the uptake of the LLB is observed because hypertonicity prevents the association

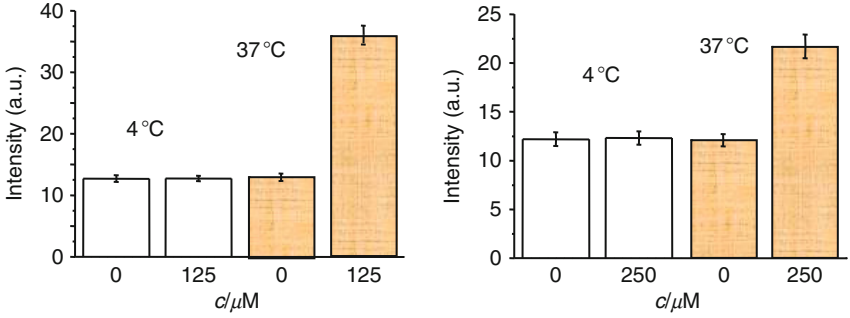

FIGURE 104 Integrated emitted light by HeLa cells grown in absence and presence of $[Eu_2(\mathbf{L13^g})_3]$ 125 μM (left) or $[Eu_2(\mathbf{L13^i})_3]$ 250 μM (right) at 4 and 37 °C (redrawn from Chauvin et al., 2007, 2008).

between the receptor-LLB complex and the clathrin lattice to form the coated pit; it also blocks the receptor clustering necessary to the formation of the endosomes. Similarly, potassium depletion blocks the receptor clustering and indeed, low concentration of this ion in the culture medium results in a decrease of 83% of the LLB uptake in the cells (Song et al., 2008c).

Initial experiments with a conventional luminescence microscope equipped with the relevant filters point to the $[Ln_2(\mathbf{L13})_3]$ helicates penetrating into HeLa cells in a concentration- and time-depending manner. In Figure 105 (top), the Eu^{III} luminescence is plotted versus the concentration of the $[Eu_2(\mathbf{L13})_3]$ helicates in the culture medium after an incubation time of 7 h at 37 °C. The luminescence emitted by the $[Eu_2(\mathbf{L13^i})_3]$ chelate at all concentrations is understandably smaller than the light emitted by the two other helicates, in view of it smaller quantum

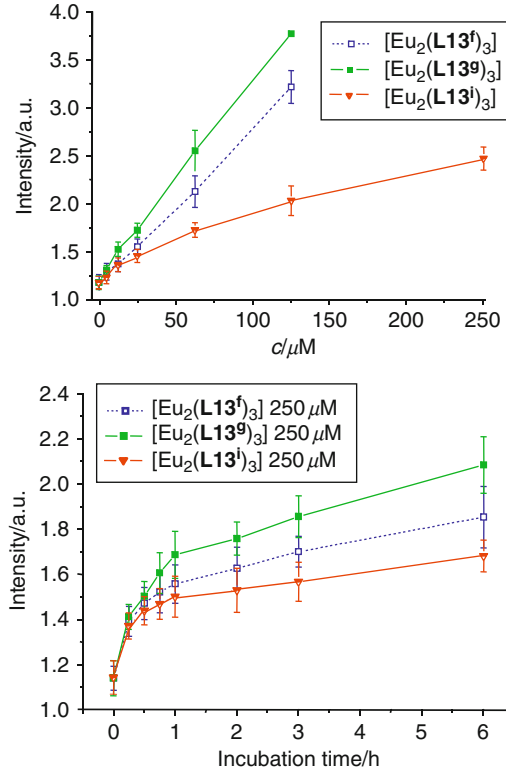

FIGURE 105 Integrated luminescence intensity from $[Eu_2(\mathbf{L13})_3]$ helicates internalized in HeLa cells versus (top) the concentration of the LLB in the culture medium and (bottom) the incubation time (redrawn from Bünzli et al., 2008).

yield, 11% versus 21% and 24%, for $[Eu_2(\mathbf{L13^g})_3]$ and $[Eu_2(\mathbf{L13^f})_3]$, respectively (Table 10). On the other hand, $[Eu_2(\mathbf{L13^g})_3]$ appears to be the best cell-staining agent despite its somewhat reduced quantum yield compared to $[Eu_2(\mathbf{L13^f})_3]$. It is noteworthy that readable images can be obtained for a helicate concentration in the culture medium as low as 10 μM (Deiters et al., 2008). With a time-resolved luminescence microscope (TRLM, Connally and Piper, 2008), this limit is still lower, elimination of the background auto-fluorescence of the cells improving the signal-to-noise ratio considerably (Figure 106). The time-course experiments depicted on the bottom of Figure 105 confirm that $[Eu_2(\mathbf{L13^g})_3]$ is the best cell-staining helicate since for a given time, its intracellular luminescence is always brighter compared to the two other stains (Bünzli et al., 2008).

An important information is to find out where the luminescent helicates are located within the cytosol of the live cells. Several experiments have been conducted, including colocalization experiments in which the cells were incubated successively with the helicate and with organic stains known to localize in specific compartments of the HeLa cells, such as acridine orange (AO) which stains the cell nuclei. Part of these experiments are shown on Figure 107. In the top part, the helicate is shown, after a short incubation time, to be entrapped into isolated vesicles which diffuse into the cytoplasm and the size of which is usually around 0.5–1.5 μm, with shapes ranging from flecks, spheres to ellipsoids.

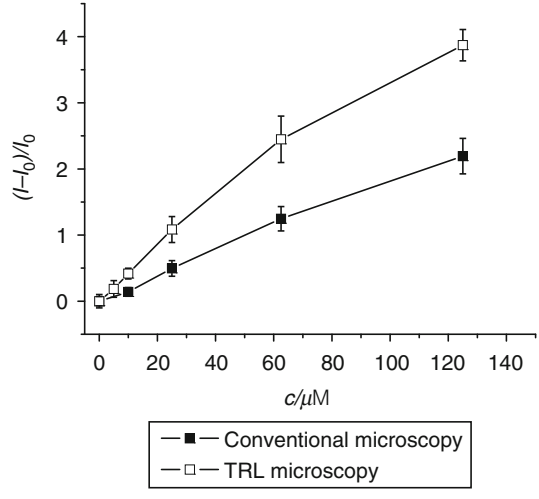

FIGURE 106 Plot of the luminescence intensity ratio $(I - I_0)/I_0$, where I_0 is the intensity of the background noise for HeLa cells incubated during 6 h at 37 °C with various concentrations of $[Eu_2(\mathbf{L13^g})_3]$ (redrawn from Song et al., 2008a).

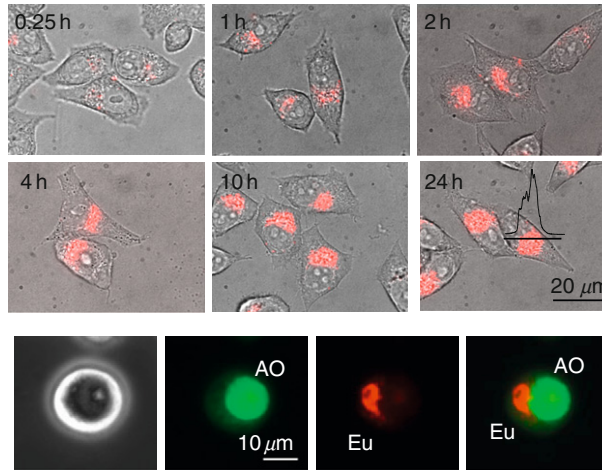

FIGURE 107 Top: successive TRLM images showing the penetration of the LLB into HeLa cells incubated at 37 °C in presence of $[Eu_2(\mathbf{L13^g})_3]$ 100 μM (redrawn from Song et al., 2008a). Bottom: colocalization experiment with AO, pointing to the helicate remaining out of the cell nucleus (redrawn from Chauvin et al., 2008).

After 1 h of incubation, vesicles have concentrated around the nucleus, as ascertained by the counter-staining experiment with AO (Figure 107, bottom). In fact, other counter-staining experiments with the Lyso-Tracker blue (localizing in the lysosomes), Golgi-Tracker (Golgi apparatus), and ER-Tracker (endoplasmatic reticulum) demonstrate a localization in the endoplasmatic reticulum (Song et al., 2008a).

All the helicates with ligands $\mathbf{H_2L13}$ behave similarly: lengthening of the polyoxyethylene chain (Deiters et al., 2008) or adding various substituents in an effort to shift the excitation wavelength toward the visible (Deiters et al., 2009) does not affect their cell-staining properties. The best luminescent tag with respect to lengthening the excitation wavelength is $[Eu_2(\mathbf{L13^l})_3]$ with absorption maxima at 350 and 365 nm and an ability to be excited at 405 nm by a confocal microscope (Deiters et al., 2009).

Egress of the LLBs from the cells is slow and both the emission spectra recorded in cellulo and the excited state lifetimes for Eu^{III} or Tb^{III} helicates, as well analysis of the Eu($^5D_0 \leftarrow {}^7F_0$) transition, prove that the LLBs are essentially undissociated in the intracellular medium. The intracellular concentration of the helicates was determined after incubation of HeLa cells 12 h with 25 μM of LLB by measuring the lanthanide concentration with the time-resolved Delfia© method. It was found to be surprisingly high: under the loading conditions used, there is, on average, 8.8×10^{-16} mol $[Eu_2(\mathbf{L13^h})_3]$ per cell, which, taking into account an estimated cell volume between 2600 and 4200 μm^3, translates into 0.21–0.34 mM

(Deiters et al., 2008). Similar concentrations were found for the helicates with $\mathbf{H_2L13^f}$, $\mathbf{H_2L13^g}$, $\mathbf{H_2L13^i}$ (Bünzli et al., 2008), and $\mathbf{H_2L13^l}$ (Deiters et al., 2009), as well as for complexes with cyclen derivatives (Yu et al., 2006).[1]

Other cell lines can be stained (MCF-7, HaCat, for instance) and multi-staining with Sm^{III}, Eu^{III}, Tb^{III}, and even Yb^{III} is possible. In the latter case, no image was obtained, but an emission spectrum could be measured *in cellulo* (Chauvin et al., 2008; Deiters et al., 2009). The next step will be to bioconjugate the helicates with specific peptides and proteins in order to perform targeting experiments. The polyoxyethylene pendants of ligand $\mathbf{H_2L13^g}$ have been derivatized with carboxylic acid, amine, and pthalimide groups for this purpose.

6.3.4 The $[Eu_2(L13^g)_3]$ helicate as luminescent sensor for DNA and PCR products

Many biological and diagnostic applications require accurate quantification of nucleic acids extracted from various sources (e.g., blood, cells, bones). In addition to spectrophotometry, several fluorometric DNA assays have been proposed based on intercalating fluorescent reagents which display enhanced fluorescence upon interaction with DNA. Many of these dyes have high autofluorescence, which limits the accuracy of the assay or its sensitivity, and some are quite specific with respect to the nature of the sample. Given the photophysical properties of $[Eu_2(\mathbf{L13^g})_3]$, Song et al. (2008b) have proposed a rugged and versatile assay applicable to several different types of DNA (single-stranded, ssDNA; double-stranded, dsDNA; circular, cDNA) and to small PCR products, that is, having less than 500 base pairs (bp). The principle of the method takes advantage of the quenching of the Eu^{III} luminescence induced by acridine orange (AO). This quenching is purely dynamic, with a bimolecular rate constant of $k_q = 2.7 \times 10^8\,M^{-1}s^{-1}$ and a quenching constant $K_D = 6.7 \times 10^5\,M^{-1}$ (see Eq. (136), where I and I_0 are the luminescence intensities in absence and in presence of the quencher and τ_0 is the observed lifetime in absence of quencher). This is the reason why AO has been preferred to ethidium bromide (EB) which induces simultaneous dynamic and static quenching processes.

$$\frac{I_0}{I} = 1 + K_D[AO] = 1 + k_q\tau_0[AO] \tag{136}$$

When DNA is added to a solution containing $[Eu_2(\mathbf{L13^g})_3]$ and AO, the latter intercalates into the nucleic acid and Eu^{III} luminescence is restored (Figure 108). In TRD mode, detection limits are in the range

[1] This high concentration is so surprising that both the Durham and Lausanne groups have mentioned concentrations in the micromolar range in their respective papers; however, careful recalculation from the number of complex molecules found per cell indeed yields figures in the mM range.

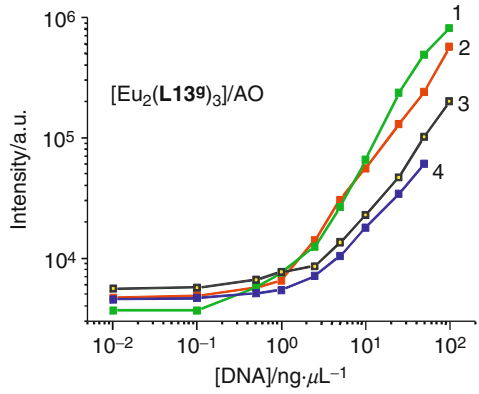

FIGURE 108 Luminescence intensity in TRD mode upon addition of DNA to [Eu$_2$(**L13^8**)$_3$] 0.1 μM + AO 33.1 μM in 0.1 M Tris–HCl buffer; 1: plasmid DNA; 2: actin sens-2 DNA; 3: salmon sperm DNA; 4: λDNA/*Hind*III (redrawn after Song et al., 2008b).

TABLE 18 Influence of potentially interfering analytes on the luminescence intensity of the DNA analytical system based on the [Eu$_2$(**L13^8**)$_3$]–AO mix[a] (from Song et al., 2008b)

Compound	*c* (mM)	Δ*I* (%)	Compound	*c* (mM)	Δ*I* (%)
BSA	10[b]	+6.2	Cu^{II}	0.1	−32.9
Glucose	0.1	+3.2	Fe^{II}	0.1	+0.021
SDS	0.2[c]	+9.2	Fe^{III}	0.1	−3.2
Na_2HPO_4	0.1	−0.03	Co^{II}	0.1	−14.9
EDTA	1	+1.1	Mn^{II}	0.1	−9.4
Ca^{II}	0.1	+0.34	Citrate	0.1	+3.6
Mg^{II}	0.1	+0.89	Ascorbate	0.1	−6.5
Zn^{II}	0.1	−1.5	Urate	0.1	+4.6

[a] [Eu$_2$(**L13^8**)$_3$] 0.1 μM, 10 μg ml^{-1} AO, and 100 ng μl^{-1} sheared salmon sperm DNA in 0.1 M Tris–HCl buffer, pH 7.4.
[b] In ng μl^{-1}.
[c] In mass %.

0.2–0.7 ng μl^{-1} for the four investigated DNAs. Reinstatement of luminescence can also be monitored by measuring the Eu($^5D_0$) lifetime which increases when DNA is added, but the sensitivity is about ten-fold less. The method is quite rugged, being insensitive to pH in the range 3–10 and to the presence of many potentially interfering species added in 100- to 1000-fold excess (see Table 18). Only Cu^{II} and Co^{II} have a detrimental influence, probably because they induce transmetallation of the helicate.

Finally, smaller dsDNA fragments, such as PCR products are also detected by this method, which compares very well with existing

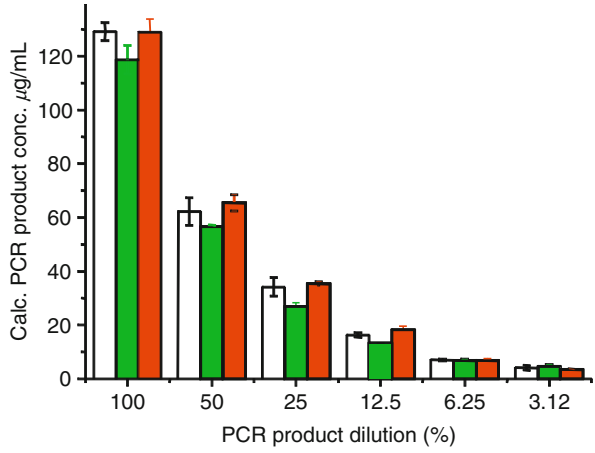

FIGURE 109 Comparison between three DNA quantification methods used in the assay of a PCR product (347 bp fragment of the actin gene); from left to right: UV absorption, PicoGreen® -dye method, and [Eu(**L13^{8}**)$_3$]/AO method (redrawn after Song et al., 2008b).

procedures (Figure 109). An additional advantage of the proposed protocol is the measurement of Eu^{III} luminescence with a cheap, easy-to-use, and commercially available time-resolved spectrometer.

7. BIMETALLIC POLYNUCLEAR nd–4f HELICATES

7.1 Choosing the d-transition partner

Metal ions from the d-transition series display rich spectroscopic and magnetic properties which are extremely sensitive to the metal-ion environment, contrary to f-transition ions, in view of the outer nature of d-orbitals allowing easy mixing with ligand orbitals. In addition, these ions have usually strong stereochemical requirements which may prove useful in preorganizing ligand strands and subsequently facilitating complexation of 4f ions. Combining the unique properties of both series of ions into a single molecular edifice is therefore appealing. For instance, despite its programmed weakness resulting from the lack of expansion of the 4f-orbitals, the magnetic coupling between d and 4f ions has been and is still the focus of much attention (Barta et al., 2008; Benelli, 2002), especially when it comes to searching for single molecule magnets (Costes et al., 2006; Novitchi et al., 2008). On the other hand, a wealth of efforts have been devoted by the authors of the present chapter for designing adequate ligands able to simultaneously recognize an isolated d–f ion pair while leading to triple-helical molecular assemblies with programmed magnetic and/or photophysical functionalities (Bünzli

and Piguet, 2002, 2005; Bünzli et al., 1997; Piguet, 1996; Piguet and Bünzli, 1996, 1998, 1999; Piguet et al., 2000). Most of this work relies on the exciting possibility to tune the properties of one ion by intramolecular communication with the other metal along the C_3-axis of the binuclear helicate.

There are three main mechanisms through which two metal ions may interact and exchange information. (i) Through-bond interaction requiring large orbital overlap, which compels the two protagonists to be located close enough from each other for their valence orbitals to interact; this distance should be smaller than 40 pm for instance for noticeable magnetic interactions to operate between nd and 4f ions or between two 4f ions; as an example, the coupling parameter J for antiferromagnetic coupling of two R^{III} ions is usually on the order of -0.1 cm^{-1} when the intermetallic distance is in the range 35–40 pm and drops sharply with increasing distance. (ii) Through-space interaction arising via multipolar energy transfers; one common mechanism for this is Förster's dipole–dipolar model with a $1/r^6$ dependence (see Section 4.4, Eqs. (77) and (78)); such transfers have been detected over very large distances, up to 10 nm when the donor is a lanthanide ion. (iii) Mechanical coupling of the two metal ions, that is, modification of the inner coordination sphere of one ion, the coordination of the other metal ion inducing some deformation of the ditopic ligand linking the two centers; this is well documented in solid state networks, particularly with respect to thermal magnetic hysteresis.

In the case of the 4f–4f polynuclear helicates, the polytopic ligands described in Sections 3–6 position the two lanthanide ions at a distance of about 90 pm in the final supramolecular assemblies. In addition, the various tridentate coordination moieties are separated by methylene bridges which prevent electronic density from flowing between these units. As a result, the lanthanide ions are isolated and can only communicate by a through-space mechanism, as seen in Section 4.4. If the bis (tridentate) ligands are modified into tridentate-bidentate guests to match the often observed octahedral coordination of nd transition metal ions, it is foreseen that the intermetallic distance will not be much affected. Therefore in this case again, only the last two types of intermetallic communications can be programmed in the self-assembled molecular edifices. The extensive work performed on nd–4f helicates since 1995 by the authors has pursued the following main objectives:

(1) Inducing a preorganization of the ligand strands to provide a less energetic pathway facilitating lanthanide coordination during the self-assembly process. Initially, a spectroscopically silent, nonmagnetic ion, Zn^{II}, was chosen for this purpose (Piguet et al., 1995c) since, in addition, R^{III} ions are often used as replacement probes for this cation when studying the properties of Zn^{II} sites in proteins and

other biological molecules. In this way, it was expected that the facial ZnL_3 tripod will serve as a dedicated receptor for the selective complexation of R^{III} ions. This strategy was then expanded to include more transition metal ions in the *fac*-ML_3 noncovalent tripods which self-assemble with R^{III} ions to yield the HHH-[$RM^{II/III}L_3$] supramolecular triple-helical edifices (M = Cr, Fe, Co, Ru, and Os).

(2) Isolation of enantiomerically pure helicates. One disadvantage of Zn^{II} is its relatively large lability with respect to transmetallation, so that successful attempts have been made to replace it with Cr^{III} which, in addition to be optically active (see point 4 below), is kinetically inert, opening the way to designing chiral helical luminescent probes (Cantuel et al., 2004). Another possibility to produce inert 3d–4f helicates is to insert Co^{II} ions into the self-assembled edifices, followed by a mild and selective oxidation into the low-spin diamagnetic, and kinetically inert Co^{III} ion (Rigault et al., 1998).

(3) Modification of Fe^{II} spin-crossover parameters through mechanical coupling with $R^{III}L_3$ moieties containing different lanthanide ions. Indeed, minute distortions of the octahedral, or pseudo-octahedral, coordination environment of the d^6 transition metal ion leads to sizeable changes in these parameters and/or in the thermal hysteresis loop (Kahn and Kodjovi, 1999). This study is coupled with the investigation of the electrochemical behavior of the MLn helicates (Fe^{II}/Fe^{III}, Co^{II}/Co^{III}, Ru^{II}/Ru^{III}, and Os^{II}/Os^{III}).

(4) Tuning the photophysical properties of one ion by means of energy transfer from the other ion. The energy transfer may take place in either direction, depending on the effect sought for. A first candidate is Cr^{III} the $3d^3$ electronic structure of which is such that its first electronic excited state (^2E_g in octahedral symmetry) is fairly insensitive to ligand-field effects and has a spin multiplicity different from the ground state ($^4A_{2g}$) leading to a bright red, and long-lived phosphorescence. Excitation can be achieved through the spin-allowed $^4T_{2g} \leftarrow {}^4A_{2g}$ transition which is very sensitive to the ligand-field strength and can therefore easily be tuned. Partial overlap of the Cr^{III} levels with those of several lanthanide ions has prompted the introduction of Cr^{III} as sensitizer for near-infrared emissive R^{III} ions such as Nd^{III} (e.g., in neodymium YAG lasers), Er^{III}, and Tm^{III}. Feeding the excited state of a NIR-emissive R^{III} ion through the long-lived ^2E_g level of Cr^{III} will artificially increase its lifetime, providing an original handle to control this parameter. Other luminescent d-transition metal ions such as Ru^{II} and Os^{II} possess long-lived metal-to-ligand charge-transfer states (^{3}MLCT) which also overlap with R^{III} electronic levels facilitating energy transfer from these states via either conjugated bridging ligands (Herrera et al., 2006b; Lazarides et al., 2008) or through-space (Förster-like) energy transfer.

7.2 Tailoring adequate pentadentate ligands

The design of adequate ligands for the self-assembly of nd–4f isolated pairs into triple-stranded helical molecular edifices is straightforward in that it only requires modification of one of the tridentate coordination units of the bis(tridentate) receptors presented earlier, all the other modulation possibilities described for the assembly of 4f–4f helicates remaining open. One tridentate unit is simply trimmed to a bidentate chelating one featuring an α,α'-diimine group and allowing pseudo-octahedral coordination of a d-transition metal ion (Figure 110). Such pentadentate ligands are programmed for the simultaneous recognition of a nd–4f pair of ions by strict self-assembly under stoichiometric conditions, the three ligand strands being designed so that they will adopt a ''natural'' HHH orientation in the final binuclear edifices, with the three bidentate chelating units bound to the nd transition metal ion. They appear to be optimally designed for this purpose since a maximum of ion–dipole bonds will be produced upon self-assembly of three ligand strands with a

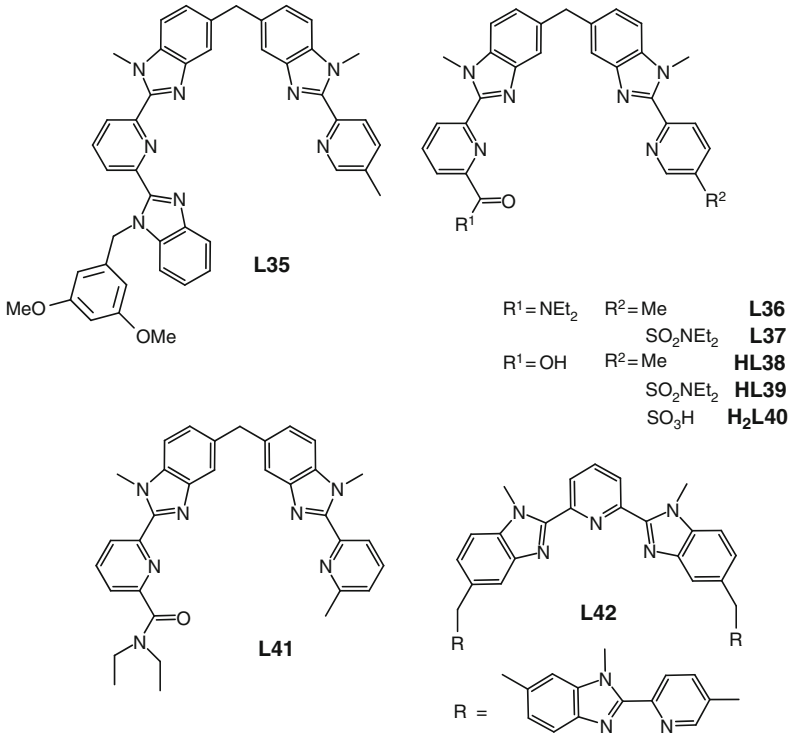

FIGURE 110 Segmental ligands for nd–4f triple-stranded heterometallic helicates.

stoichiometric mix of nd and 4f ions. Indeed, the receptor ligands obey the maximum occupancy rule (Lehn and Eliseev, 2001), henceforth maximizing the favorable part of the enthalpic contribution to the overall free energy change during the recognition process, especially if this process is conducted in a weakly coordinating solvent such as acetonitrile. The entropic contribution is also maximized through a large chelate effect. Finally, the stereochemical preferences of both nd and 4f metal ions are met by the ligand design with the methylene bridge inducing the right helical twist when the ligand strands wrap around the metal ions. Programming higher nuclearity for the self-assembled edifices translates into increasing the number of coordinating units, either bidentate or tridentate, along the ligand strand so that incoming metal ions can ''read'' the information specific to their coordination requirements.

The polydentate ligands investigated so far are schematized on Figure 110. Ligand **L35** with N_3 and N_2 chelating units is the pendent of the bis(tridentate) receptor **L11** (Section 3.1, Figure 41). The 3,5-dimethoxy-benzyl group has been introduced both for increasing solubility and for its easy recognition in mass spectra when it is cleaved from the ligand backbone. Ligands **L36–L41** with N_2O and N_2 chelating units correspond to the hexadentate ligand **L13^b**, while the N_2-N_3-N_2 heptadentate host **L42**, tailored for trinuclear M*R*M recognition, is derived from ligands **L27–L28** (Section 3.1, Figure 42).

As for the hexadentate ligands, the synthesis of the bidentate-tridentate receptors relies on the modified Phillips coupling reaction. The starting point in the synthesis of **L35** is the production of the nonsymmetrical **Int-1** intermediate by monoacylation of symmetrical 4,4′-methylene-2,2′-dinitrobis(benzamide) with 6-methylpyridine-2-carbonyl chloride obtained from the parent carboxylic acid (Figure 111). A second acylation with the adequately derivatized picolinic acid leads to the key intermediate *N*-(2-nitroaryl)arenecarboxamide. *In situ* reduction of the latter with metallic iron followed by cyclization under mild acidic conditions represents the key step of the synthetic path for the formation of aromatic 1H-benzimidazole rings (Piguet et al., 1994). Similar reactions are used for **L36** (Piguet et al., 1996) and **L42** (Piguet et al., 1994), see Figure 112. Ligand **HL38** is obtained by hydrolysis of **L36** with potassium hydroxide (Edder et al., 1997).

A slightly different starting dinitro compound (**Int-2**) is used for the synthesis of ligands **L37**, **HL39**, and **H2L40** but the overall procedure is the same, with **HL39** obtained by hydrolysis of **L37** with KOH and **H_2L40** by hydrolysis of **HL39** with concentrated sulfuric acid. Introduction of sulfonate groups is generally achieved by regioselective sulfonation occurring during the final step of the synthetic scheme because the purification of sulfonated compounds is time-consuming. However in the case of ligands **L37-H_2L40**, the lack of strong electronic effects favoring

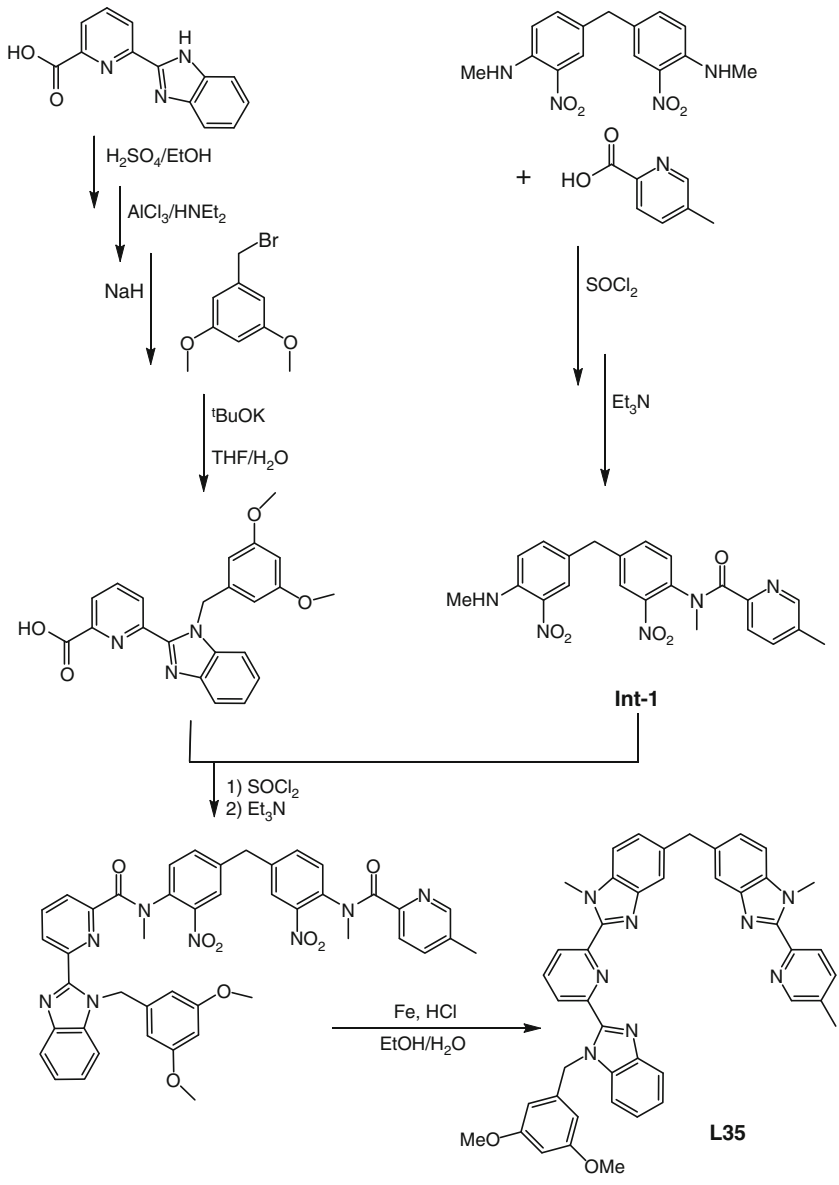

FIGURE 111 Synthetic scheme for ligand **L35** (redrawn after Piguet et al., 1994).

one particular carbon for the electrophilic attack in the targeted pentadentate ditopic ligands and the considerable number of aromatic carbon atoms suitable for sulfonation required a different approach in which 2-methyl-5-pyridinesulfonic acid (obtained by reacting 2-picoline with

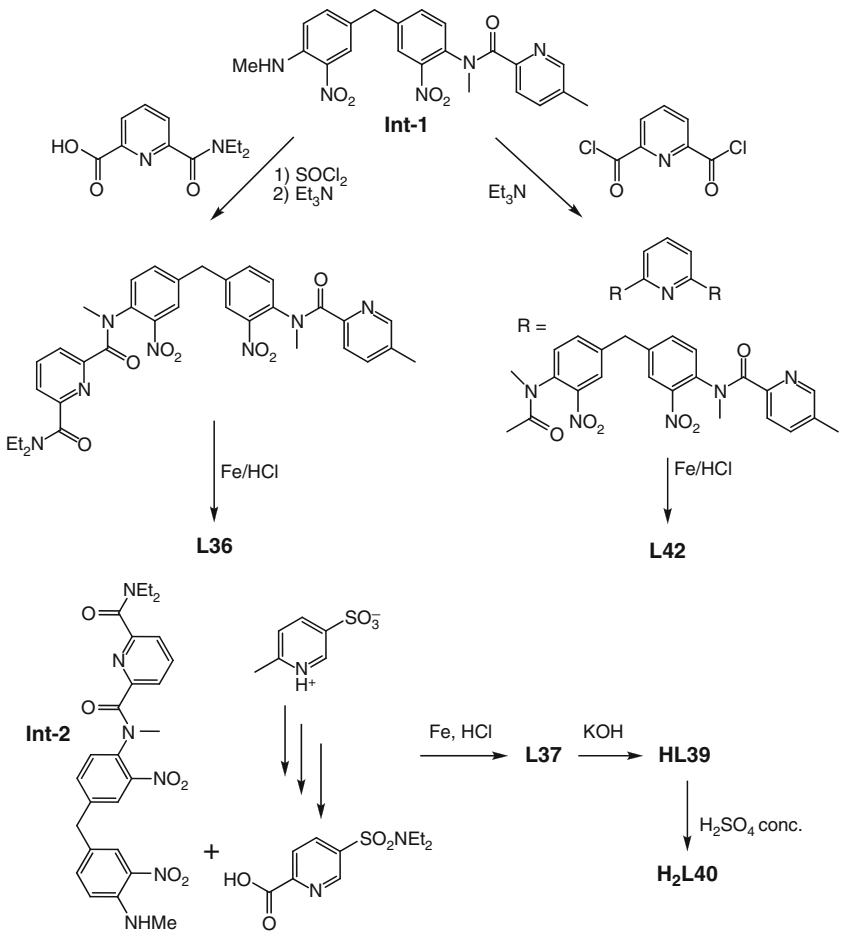

FIGURE 112 Top: synthetic scheme for ligands **L36** (Piguet et al., 1996) and **L42** (Piguet et al., 1994); for the synthesis of the starting dinitro compound **Int-1**, see Figure 111. Bottom: synthetic route to ligands **L37**, **HL39**, and **H_2L40** (Edder et al., 2000).

oleum followed by extensive separation/purification) was coupled to **Int-2** (Edder et al., 2000).

7.3 Preparation of the nd–4f helicates in acetonitrile and corresponding speciation

The self-assembly of helicates is a relatively complex process (see Section 3.3), even for homometallic binuclear 4f–4f species. Introducing dissymmetry both in the receptor ligand and in the nature of the metal

ions renders the process yet more intricate. Experimental techniques such as NMR and ES-MS are ideally suited for characterizing the species formed in solution, an essential step before quantifying the stability of the binuclear helicates and other species with UV-vis titrations. NMR spectra will be discussed in the following section, together with solution structures so that we concentrate here on ES-MS data. The binuclear helicates are easy to recognize in the ES-MS spectra because the molecular peak is often accompanied by adduct ions with perchlorates (Hopfgartner et al., 1994) or triflates, and can be further characterized by their isotopic distributions. The species evidenced during the titration of ligands **L35**–**L37**, **HL38**, and **L41** 10^{-4} M in acetonitrile by metal perchlorates or triflates are reported in Table 19. When $R^{III}/M^{II/III}$ mixtures are used, the preponderant species is always by far the RML_3 helicate, at stoichiometric ratio, whatever the lanthanide and the d-transition metal ions are; this is particularly well illustrated for **L36** for which lanthanide helicates with Zn^{II}, Cr^{III}, Fe^{II}, Co^{II}, Ru^{II}, and Os^{II} have been investigated. Similarly to the 4f–4f helicates, stability constants have been determined by electronic absorption spectroscopy, with the same limitations, for example, the difficulty of detecting poorly stable intermediates or complexes due to correlated spectra.

Titration of the ditopic pentadentate ligands with either a kinetically labile d-transition metal ($M = Fe^{II}$, Co^{II}, Zn^{II}) or a lanthanide ion often leads to the observation of several different species in equilibrium. On the other hand, the RML_3 helicate is always the most abundant species when the titrant is a stoichiometric R^{III}/M^{II} mixture, when the total ligand concentrations is $>10^{-3}$ M, and in presence of poorly coordinating anions; the other complexes are often not detected in NMR spectra under these conditions. The spectrophotometric data have been fitted to the following set of equations (A stands for nd (M) or for 4f (R) ion, charges are omitted for clarity):

$$\mathrm{A} + n\mathbf{L}\boldsymbol{k} \rightleftarrows [\mathsf{A}(\mathbf{L}\boldsymbol{k})_n] \quad \beta_{1,n}^{\mathrm{A,L}k} \tag{137}$$

$$2\mathrm{A} + n\mathbf{L}\boldsymbol{k} \rightleftarrows [\mathsf{A}_2(\mathbf{L}\boldsymbol{k})_n] \quad \beta_{2,n}^{\mathrm{A,L}k} \tag{138}$$

$$3A + 2\mathbf{L}\boldsymbol{k} \rightleftarrows [\mathsf{A}_3(\mathbf{L}\boldsymbol{k})_2] \quad \beta_{2,3}^{\mathrm{A,L}k} \tag{139}$$

$$R + \mathrm{M} + 3\mathbf{L}\boldsymbol{k} \rightleftarrows [R\mathrm{M}(\mathbf{L}\boldsymbol{k})_3] \quad \beta_{1,1,3}^{R,\mathrm{M,L}k} \tag{140}$$

Alternatively, thermodynamic data for inert d-transition metal ions Cr^{III}, Co^{III}, Ru^{II}, and Os^{II} cannot be obtained easily because the formation

TABLE 19 Metal-containing species observed by ES-MS from solutions in acetonitrile during the titration of the pentadentate ligands **L35–L41** (Figure 110) with transition metal (3d, 4f) perchlorates

Ligand	Metal ions	Species	References
L35	M^{II} (M = Zn, Fe)	$[M(\mathbf{L35})_n]^{2+}$, $n = 2, 3$	Piguet et al. (1995d)
		$[M_2(\mathbf{L35})_2]^{4+}$	Piguet et al. (1995e)
	R^{III} (R = La, Eu)	$[R_2(\mathbf{L35})_2(ClO_4)_x]^{(6-x)+}$, $x = 1$–3	
	R^{III}/Zn^{II} (R = Y, La, Nd, Tb, Lu)	$[RZn(\mathbf{L35})_3(ClO_4)_x]^{(5-x)+}$, $x = 0$–3	
		$[Zn(\mathbf{L35})_2]^{2+}$	
	R^{III}/Fe^{II} (R = La, Nd, Eu)	$[RFe(\mathbf{L35})_3(ClO_4)_x]^{(5-x)+}$, $x = 0$–3	
		$[Fe(\mathbf{L35})_2]^{2+}$	
	Eu^{III}/Fe^{II}	$[EuFe(\mathbf{L35})_3(ClO_4)_x]^{(5-x)+}$, $x = 0$–4	Hopfgartner et al. (1994)
L36	Zn^{II}	$[Zn(\mathbf{L36})_n(ClO_4)_x]^{(2-x)+}$, $n = 2, 3$; $x = 0, 1$	Piguet et al. (1996)
		$[Zn_2(\mathbf{L36})_n(ClO_4)_x]^{(4-x)+}$, $n = 2, 3$; $x = 0, 2$	
	R^{III}/Zn^{II} (R = La, Eu, Gd, Tb)	$[RZn(\mathbf{L36})_3(ClO_4)_x]^{(5-x)+}$, $x = 0$–3	
	Fe^{II}	$[Fe(\mathbf{L36})_n(ClO_4)_x]^{(2-x)+}$, $n = 1$–3; $x = 0, 1$	Piguet et al. (1997b)
		$[Fe_2(\mathbf{L36})_n(ClO_4)_x]^{(4-x)+}$, $n = 2, 3$; $x = 0, 2$	
	R^{III}/Fe^{II} (R = La, Eu, Gd, Tb, Lu)	$[RFe(\mathbf{L36})_3(ClO_4)_x]^{(5-x)+}$, $x = 0$–3	
		$[Fe(\mathbf{L36})_2]^{2+}$	
	R^{III}/Co^{II} (R = La, Eu, Lu)	$[RCo(\mathbf{L36})_3]^{5+}$	Rigault et al. (1998)
		$[Co(\mathbf{L36})_2]^{2+}$ (traces)	
	R^{III}/Cr^{III} (R = La, Eu, Gd, Tb, Tm, Lu)	$[RCr(\mathbf{L36})_3(CF_3SO_3)_x]^{(6-x)+}$, $x = 0$–4	Cantuel et al. (2002)
		$[Cr(\mathbf{L36})_3(CF_3SO_3)_x]^{(3-x)+}$, $x = 0$–1 (R = La, Gd)	
	Lu^{III}/Ru^{II}	$[LuRu(\mathbf{L36})_3(CF_3SO_3)]^{4+}$	Torelli et al. (2004)
	Lu^{III}/Os^{II}	$[LuRu(\mathbf{L36})_3(CF_3SO_3)_x]^{(5-x)+}$, $x = 1$–3	Riis-Johannessen et al. (2008)

L37	M^{II} (M = Zn, Fe)	$[M(\mathbf{L37})_n]^{2+}$, $n = 2, 3$ $[M_2(\mathbf{L37})_2(ClO_4)_x]^{(4-x)+}$, x = 0–2 (Zn), 0–1 (Fe)	Edder et al. (2000)
	La^{III}	$[La(\mathbf{L37})_n(ClO_4)_x]^{(3-x)+}$, $n = 2, 3$; $x = 0, 1$ $[La(\mathbf{L37})_n]^{3+}$, $n = 4, 5$	
	La^{III}/M^{II} (M = Zn, Fe)	$[LaM(\mathbf{L37})_3(ClO_4)_x]^{(5-x)+}$, x = 0–2 $[M(\mathbf{L37})_n]^{2+}$, $n = 2, 3$ $[Zn_2(\mathbf{L37})_2(ClO_4)_x]^{(4-x)+}$, x = 0–3 $[Zn_2(\mathbf{L37})_3]^{4+}$	
HL38	R^{III}/Zn^{II} (R = La, Eu)	$[RZn(\mathbf{L38})_3]^{2+}$	Edder et al. (1997)
L41	La^{III}/M^{II} (M = Zn, Fe)	$[LaM(\mathbf{L41})_3(ClO_4)_x]^{(5-x)+}$, x = 0–3 $[M(\mathbf{L41})_n]^{2+}$, $n = 2, 3$ $[M_2(\mathbf{L41})_2(ClO_4)_x]^{(4-x)+}$, x = 0–2 (Zn); $x = 0$ (Fe)	Edder et al. (2001)

of $[RM(\mathbf{L}k)_3]^{m+}$ by reacting stoichiometric mixtures of R, M and $\mathbf{L}k$ proved to be not feasible in that this invariably led to intricate mixtures of species with varying stoichiometry and symmetry (HHH, HHT, HH, HT isomers). Therefore, thermodynamic data for heterometallic binuclear species including inert d-block ions are limited to the formation of the final helicate from its preorganized tripodal receptor (Eq. (141)):

$$[M(\mathbf{L}k)_3]^{z+} + R^{3+} \rightleftarrows [RM(\mathbf{L}k)_3]^{(z+3)+} \quad \beta_{1,1}^{R,M(Lk)3} \tag{141}$$

Due to these difficulties, only a limited number of stability constants could be determined and are listed in Table 20. For a given d-transition metal ion, the evolution of the data along the lanthanide series seems to parallel the tendency observed with the mononuclear precursors: the N_3 chelating unit in **L35** induces less stable complexes with heavier lanthanides, contrary to the N_2O donor site in **L36**. The difference, however, remains small and close to the experimental uncertainties. On the other hand, the 3d-transition metal ion has a much larger influence, compare for instance $\beta_{1,1,3}^{La,M,L36}$ values for the LaM complexes with **L36**: the $M = Zn^{II}$ complex is 6 orders of magnitude more stable than the $M = Fe^{II}$ edifice, itself one order of magnitude more stable than the $M = Co^{II}$ helicate. Finally the expected stabilization of the pseudotricapped-trigonal prismatic coordination to lanthanides in going from a N_9 (**L35**) to a N_6O_3 (**L36**) environment is only seen with the Zn^{II} helicates, $\beta_{1,1,3}^{R,Zn,Lk}$ increasing by three orders of magnitude, while the Fe^{II} helicates have a tendency to be somewhat less stable with **L36** compared to **L35**.

The most striking feature of these thermodynamic data is the selectivity of the recognition process for a R^{III}/M^{II} pair, which is schematized for **L37** on Figure 113. When this ligand is reacted with either M^{II} (M = Zn, Fe) or R^{III}, it generates a mixture of several species with different stoichiometries and conformations; this is referred to as a dynamical combinatorial library of species (Lehn and Eliseev, 2001). On the other hand, when an equimolar mixture of R^{III} and M^{II} is mixed with **L37**, only one major species forms with stability far larger than the stability of any of the other mono- and binuclear species. To substantiate this further, the dissociation constant of the RML_3 helicate can be recalculated from available stability data for the other species (Eq. (142)). In the case of **L35** for instance:

$$4[RFe(\mathbf{L35})_3]^{5+} \rightleftarrows 2[R_2(\mathbf{L35}_3)]^{6+} + [Fe_2(\mathbf{L35}_2)]^{4+} + 2[Fe(\mathbf{L35}_2)]^{2+} \quad log(K) \tag{142}$$

$\log(K) = -8$ and -2 for $R = La$ and Eu, respectively.

TABLE 20 Cumulative stability constants reported for the formation of mononuclear and homometallic binuclear complexes in acetonitrile solution (spectrophotometric titration of **L***k* or $[M(\mathbf{L}k)_3]^{m+}$ 10^{-4} M)

Ligand	M	*y*:*n*	$\log(\beta_{y,n}^{M,Lk})$	*R*	*y*:*n*	$\log(\beta_{y,n}^{R,Lk})$	M/*R*	$\log(\beta_{1,1,3}^{R,M,Lk})$ or $\log(\beta_{1,1}^{R,ML3})$	Reference
L35	Zn^{II}	1:2	15.4(8)	La	2:3	22.3(3)	La/Zn	26.2(3)	Piguet et al. (1995d)
		2:2	22(1)	Eu	2:3	23.5(8)	Eu/Zn	25.3(4)	
	Fe^{II}	1:2	14.1(4)				La/Fe	25.2(5)	Piguet et al. (1995e)
		2:2	20.0(8)				Eu/Fe	24.3(8)	
L36	Zn^{II}	1:3	22(1)	La	1:3	19.6(5)	La/Zn	29.0(4)	Piguet et al. (1996)
		2:2	28.4(8)		2:3	27.5(9)	Eu/Zn	28.6(6)	
		2:3	21.5(9)		2:2	22.3(9)			
	Fe^{II}	1:2	13.0(8)		3:2	29.0(9)	La/Fe	23.0(8)	Piguet et al. (1997b)
		2:2	18.0(9)				Eu/Fe	24.6(9)	
							Lu/Fe	23.6(7)	
	Co^{II}	1:2	14.4(6)				La/Co	21.7(6)	Rigault et al. (1998)
							Eu/Co	23.2(9)	
							Lu/Co	23.9(6)	
	Cr^{III}						La/Cr	5.9(3)[a]	Cantuel et al. (2004)
							Lu/Cr	5.3(3)[a]	
	Ru^{II}						La/Ru	5.4(2)[a]	Canard and Piguet (2007)
							Lu/Ru	5.2(2)[a]	
L37	Zn^{II}	1:2	14.4(2)	La	1:3	15.1(4)	La/Zn	30(2)	Edder et al. (2000)
		1:3	18.8(3)		2:3	20.1(4)			
		2:2	21.9(3)						
		2:3	28.5(3)						

(*continued*)

TABLE 20 (*continued*)

Ligand	M	*y*:*n*	$\log(\beta_{y,n}^{M,Lk})$	*R*	*y*:*n*	$\log(\beta_{y,n}^{R,Lk})$	M/*R*	$\log(\beta_{1,1,3}^{R,M,Lk})$ or $\log(\beta_{1,1}^{R,ML3})$	Reference
	Fe^{II}	1:2	14.8(6)				La/Fe	26(2)	
		1:3	20.4(8)						
		2:2	21.2(7)						
		2:3	27.6(8)						
L41	Zn^{II}	1:2	12.2(5)	La	1:3	17.7(3)	La/Zn	[b]	Edder et al. (2001)
		2:2	17.3(5)		2:3	22.9(3)	Eu/Zn	[b]	

[a] $\log(\beta_{1,1}^{R,ML3})$, Eq. (141).
[b] Spectra are too correlated for allowing the extraction of the stability constants; however, ^{1}H-NMR data point to the "quantitative" formation of the 1:1:3 species.

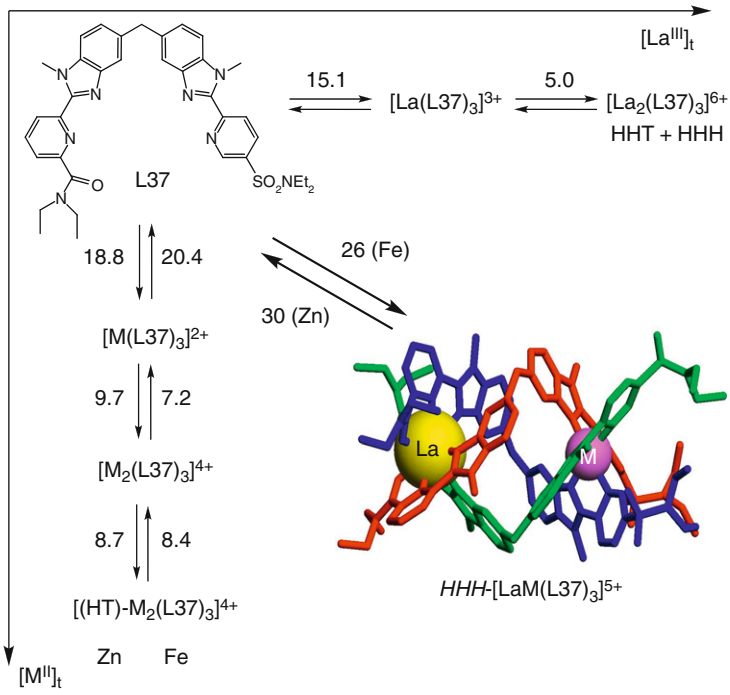

FIGURE 113 Selective formation of the heterometallic binuclear helicate $[LaM(\mathbf{L37})_3]^{5+}$ (M = Fe, Zn) in acetonitrile from a dynamic library of species. The numbers correspond to logarithmic values of the thermodynamic constants (redrawn after Edder et al., 2000).

Origin of the thermodynamic stability of the $[RM(\mathbf{L36})_3]^{m+}$ helicates ($M = Cr^{III}$, Ru^{II})

As discussed for polynuclear f–f helicates (Section 5.4), the surprising stability of highly charged d–f helicates in solution results from a balance between the unfavorable intramolecular electrostatic intermetallic repulsion and the favorable increase in solvation energy accompanying the successive fixation of charged cations within the complex. Interestingly, an intermetallic separation of 90 pm, as found in the triple-stranded helicates with ligands **L11**, **L13**, **L28**–**L31** (f–f helicates), or **L35**–**L42** (d–f helicates), leads to an almost exact compensation of these two opposite contributions produced by the fixation of a trivalent lanthanide. This is illustrated by the negligible variation of the formation constants $\log(\beta_{1,1}^{R,M(Lk)3})$ (Eq. (141)) in going from HHH-$[Ru(\mathbf{L36})_3]^{2+}$ ($5.4 \geq \log(\beta_{1,1}^{R,Ru(Lk)3}) \geq 5.2$ which translates into $-31 \geq \Delta G^{\circ}_{c,sol}(RRu) \geq -30$ kJ mol^{-1}) to HHH-$[Cr(\mathbf{L36})_3]^{3+}$ ($5.9 \geq \log(\beta_{1,1}^{R,Cr(Lk)3}) \geq 5.3$ which

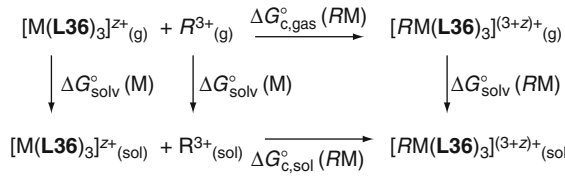

FIGURE 114 Born–Haber cycle for the formation of $[RM(\mathbf{L36})_3]^{(3+z)+}$ helicates.

translates into $-34 \geq \Delta G^{\circ}_{c,sol}(RCr) \geq -30\ kJ\ mol^{-1}$); this can be summarized with $\Delta G^{\circ}_{c,sol}(RRu) - \Delta G^{\circ}_{c,sol}(RCr) \approx 0$ despite the obvious increase of the d–f electrostatic repulsion in going from the Ru^{II}-R^{III} to the Cr^{III}- R^{III} helicates (Canard and Piguet, 2007; Figure 114).

The introduction of the solvation free energies estimated by using Born's Eq. (127) for $[Ru(\mathbf{L36})_3]^{2+}$ ($-342\ kJ\ mol^{-1}$), $[Cr(\mathbf{L36})_3]^{3+}$ ($-771\ kJ\ mol^{-1}$), $[LuRu(\mathbf{L36})_3]^{5+}$ ($-2091\ kJ\ mol^{-1}$), and $[LuCr(\mathbf{L36})_3]^{6+}$ ($-3012\ kJ\ mol^{-1}$) into the adequate thermodynamic Born–Haber cycles (Figure 114) allows the calculation of the difference in free energies for these two complexation processes in the gas phase $\Delta G^{\circ}_{c,gas}(LuCr) - \Delta G^{\circ}_{c,gas}(LuRu) = 492\ kJ\ mol^{-1}$ (Eq. (143), Canard and Piguet, 2007).

$$\begin{aligned}\Delta G^{\circ}_{c,gas}(LuCr) - \Delta G^{\circ}_{c,gas}(LuRu) = {} & \Delta G^{\circ}_{c,sol}(LuCr) - \Delta G^{\circ}_{c,sol}(LuRu) \\ & + \Delta G^{\circ}_{solv}(Cr) - \Delta G^{\circ}_{solv}(Ru) \\ & + \Delta G^{\circ}_{solv}(LuRu) - \Delta G^{\circ}_{solv}(LuCr)\end{aligned} \tag{143}$$

Assuming that the *R*-ligand-binding energies (including the reorganization of the $[M(\mathbf{L36})_3]^{z+}$ tripod) are identical for M = Ru or M = Cr, the calculated difference of the free energies of complexation in the gas-phase strictly corresponds to the difference in the electrostatic works accompanying the fixation of Lu^{3+} at $d_{LuRu} = 90.8$ pm from Ru^{II} in $[LuRu(\mathbf{L36})_3]^{5+}$, respectively, at $d_{LuCr} = 93.5$ pm from Cr^{III} in $[LuCr(\mathbf{L36})_3]^{6+}$ (Eq. (144)).

$$\begin{aligned}\Delta G^{\circ}_{c,gas}(LuCr) - \Delta G^{\circ}_{c,gas}(LuRu) &= W_{Lu,gas}(Cr) - W_{Lu,gas}(Ru) \\ &= 492\ kJ\ mol^{-1}\end{aligned} \tag{144}$$

This value can be thus compared with that computed from Coulomb's law (Eq. (145)), and the reasonable agreement, given the approximation made, confirms that solvation processes indeed overcome standard electrostatic repulsions for these d–f helicates in solution (Canard and Piguet, 2007).

$$W_{Lu,gas}(Cr) - W_{Lu,gas}(Ru) = \frac{3e^2 N_A}{4\pi\varepsilon_0}\left[\frac{2}{d_{LuRu}} - \frac{3}{d_{LuCr}}\right] = 419\ kJ\ mol^{-1} \tag{145}$$

Formation of RML_3 helicates with kinetically inert trivalent 3d-transition metal ions: Cr^{III} and Co^{III}

The syntheses of inert HHH-$[RCr^{III}\mathbf{L}_3]^{6+}$ and HHH-$[RCo^{III}\mathbf{L}_3]^{6+}$ take advantage of the lability of the chemically accessible parent Cr^{II} and Co^{II} precursors, for which standard self-assembly processes, similar to that described in Figure 113, lead to HHH-$[RCr\mathbf{L}_3]^{5+}$ and HHH-$[RCo\mathbf{L}_3]^{5+}$. Postmodification reactions under oxidative conditions eventually transform the M^{II} cations into inert M^{III} centers (Cantuel et al., 2002; Rigault et al., 1998). In the case of Cr^{III}, the initial thermodynamic self-assembly process starts from Cr^{II} triflate and the resulting blue-green solutions in degassed acetonitrile are diagnostic for the presence of the $3d^4$ metal ion in the helicates. Post-assembly oxidation by diffusion of air is fast and quantitative; the solutions turn yellow after a few minutes, owing to the low reduction potential of divalent chromium, for example, $E_{1/2}^{Cr^{III}/Cr^{II}} = -0.40$ V versus SCE for the tris (bipyridine) complex. The presence of Cr^{III} is ascertained by several analytical techniques including electronic absorption spectroscopy, ^{1}H-NMR, ES-MS, and X-ray crystallography (Cantuel et al., 2002). The known kinetic inertness of the $3d^3$ chromium cation allows the separation of enantiomerically pure helicates (see Section 7.6 below). For HHH-$[LnCo^{II}(\mathbf{L36})_3]^{5+}$ helicates, cyclic voltammograms in acetonitrile show a quasi-reversible Co^{II}/Co^{III} oxidation wave (+0.41 to 0.43 V vs SCE) compatible with the use of bromine as the outer sphere oxidative agent, which indeed yields the diamagnetic HHH-$[LnCo^{III}(\mathbf{L36})_3]^{6+}$ complexes (Ln = La, Lu; Rigault et al., 1998, 2000a).

Formation of RML_3 helicates with kinetically inert bivalent 4d- and 5d-transition metal ions: Ru^{II} and Os^{II}

For Ru^{II} and Os^{II}, there is no available parent labile oxidation states, and the self-assembly processes must include some poorly reversible elementary steps (Torelli et al., 2004). For the synthesis of HHH-$[RRu(\mathbf{L36})_3]^{5+}$, the procedure implies an intricate strategy, in which undesired coproducts are stepwise separated from the target helicate (Canard and Piguet, 2007; Figure 115).

For the more kinetically inert Os^{II} cation, the problem is even more challenging and the self-assembly reaction has to be performed in ethylene glycol at elevated temperature (160 °C) and under pressure (8–10 bar) to yield only a limited amount of a 3:1 mixture of HHH-$[Os(\mathbf{L36})_3]^{2+}$ and HHT-$[Os(\mathbf{L36})_3]^{2+}$. The targeted HHH-$[LuOs(\mathbf{L36})_3]^{5+}$ helicate is eventually obtained after several purification cycles by column chromatography on alumina (yield < 10%) followed by recombination with Lu^{III} (Riis-Johannessen et al., 2008).

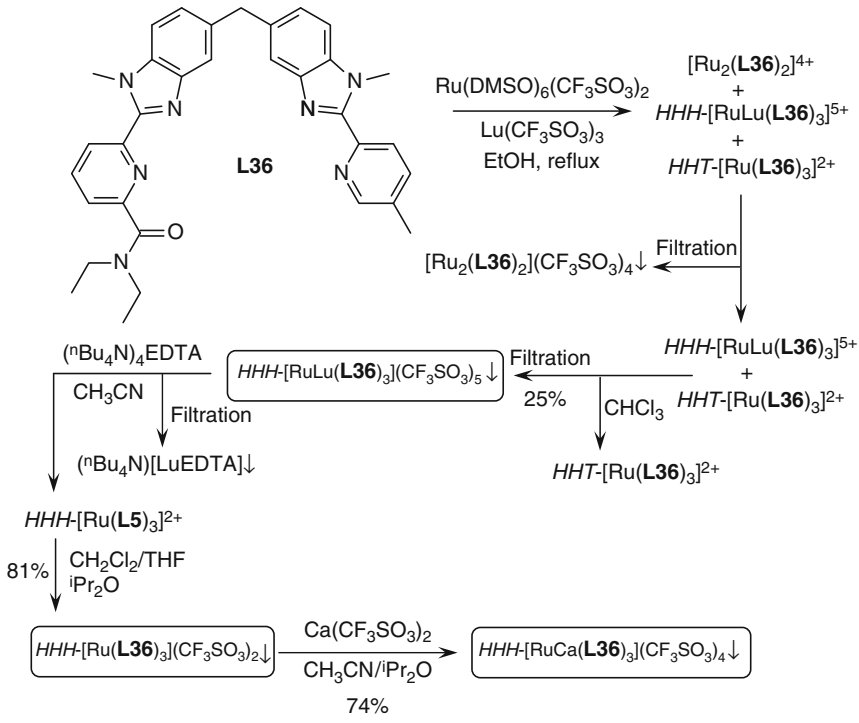

FIGURE 115 Synthesis of the inert HHH-[Ru(**L36**)$_3$]$^{2+}$ tripodal receptor and of its triple-stranded d–f HHH-[RuLu(**L36**)$_3$]$^{5+}$ and HHH-[RuCa(**L36**)$_3$]$^{4+}$ helicates (adapted from Canard and Piguet, 2007).

7.4 Solid state and solution structures

All of the reported molecular structures of crystals of *R*ML$_3$ helicates correspond to the HHH disposition of the ligands around the metal ions and have a pseudo-C_3-symmetry with the main axis going through the metal centers. With one exception, the available structures feature ligand **L36**. Generally speaking, the nine-coordinate lanthanide ion lies in a site with pseudotricapped-trigonal prismatic geometry while six-coordinate M^{II}/M^{III} ions display a more or less distorted pseudo-octahedral geometry, except for **EuZn**.[2] Selected structural parameters are listed in Table 21 and typical structures are shown in Figure 116.

In the **EuZn** structure (Piguet et al., 1996), five of the Zn–N bonds (2.01–2.19 Å) are close to the standard 2.11 Å value (Orpen et al., 1989) while the fifth one is much longer, 2.52 Å. The transition metal ion may thus be considered as being five-coordinate, with distorted trigonal prismatic geometry. Its ionic radius is then 0.62 Å, as compared to the

[2] For all the structures with L36, a simplified notation will be used, namely *RM* for [*RM*(L36)$_3$]$^{m+}$.

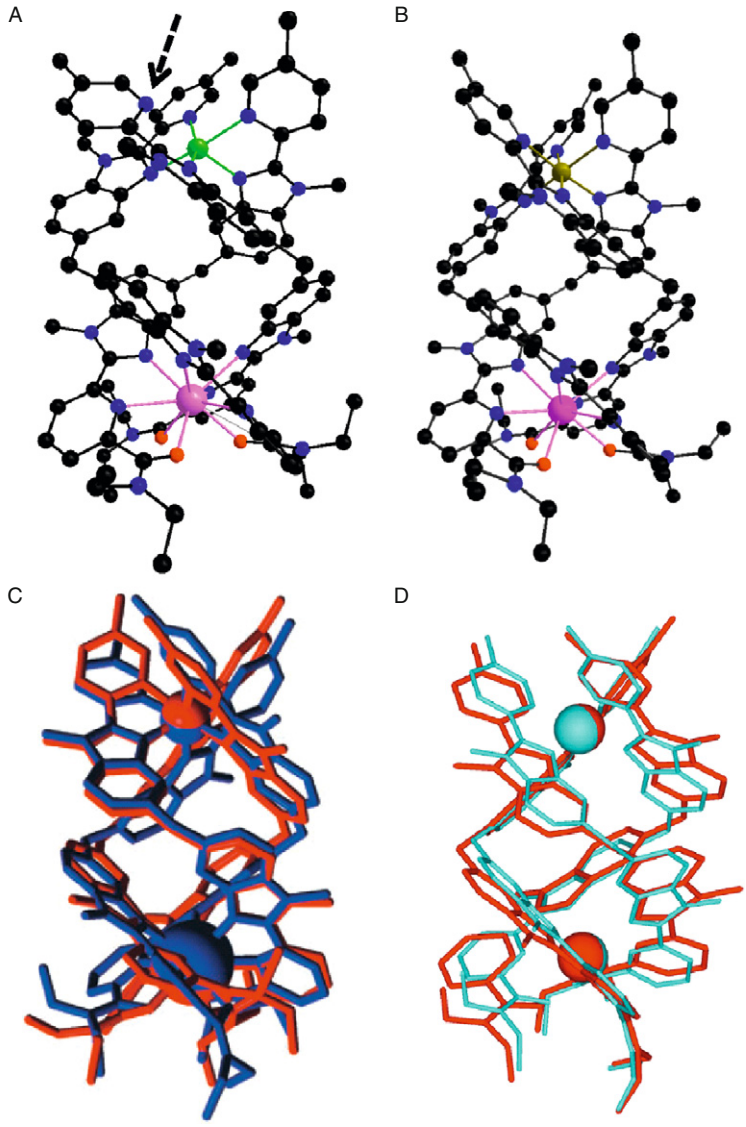

FIGURE 116 Typical structures of *RM* helicates with ligand **L36**: (A) **EuZn** (redrawn from Piguet et al., 1996); (B) **LaFe** (redrawn from Piguet et al., 1997b); (C) superposition of the structures of **EuCr** and **EuRu** (reproduced by permission from Torelli et al., 2005, © Wiley-VCH Verlag, 2005); and (D) superposition of the structures of **LuOs** and **LuRu** (redrawn from Riis-Johannessen et al., 2008).

expected 0.68 Å for a standard five-coordinate Zn^{II} ion (Shannon, 1976). Out of the three ligand strands, only one achieves a relatively symmetrical bidentate binding to the 3d ion. The distortion sustains by the two other ligand strands results from a close packing of the **EuZn** cations by pairs having opposite helicities in the unit cell, with intermolecular Zn...Zn contacts as short as 8.31 Å. Despite a significant deformation of the screw thread for the tridentate unit coordinated to Eu^{III}, the coordination polyhedron is close to the ideal tricapped-trigonal prism (TTP), with standard Eu–O and Eu–N distances. Interestingly, the Zn^{II} coordination sphere in $[EuZn(\mathbf{L37})_3]^{5+}$ is far less distorted and can be described as a octahedron flattened along the intermetallic axis while the 3d metal ion is now six-coordinate, as shown by its larger ionic radius (0.72 Å, reported standard value: 0.74 Å). This may be related to the effect of the SO_2NEt_2 substituent since the triple helices are now packed with their axis along the same direction, forming infinite columns compared to dimers for **EuZn**. The intramolecular intermetallic Eu...Zn contact distance is shorter by about 0.4 Å, but the Eu^{III} environment is unchanged (Edder et al., 2000). The crystal structure of **LaFe** has been determined at 170 K to ensure a maximum fraction of low-spin (LS) iron. The La^{III} environment is very similar to the pseudo-TTP structure evidenced for Eu^{III} in **EuZn** except for a larger twist between the two opposite facial tripods of the trigonal prism (17° versus 10°) and for the lengthening of the Ln-N and Ln-O bonds due to its larger ionic radius. On the other hand, the 3d metal ion is six-coordinate with an octahedral coordination polyhedron somewhat flattened along the C_3-axis. This is typical of a stereochemical demanding low-spin Fe^{II} ion which limits the deformation of the octahedral coordination despite the packing in pairs of opposite helicities, much as in **EuZn**. The Fe–N distances are standard and the calculated ionic radius (0.52 Å) is also in line with a LS divalent iron.

When iron is replaced by the low-spin, trivalent Co^{III} in ***R*Co**, the influence of the lanthanide ion is seen in the Co–N distances which are, on average, 0.05 Å shorter in **LuCo** compared to **LaCo.** This suggests that the Co–N bonds are stretched to accommodate the larger La^{III} ion in the nona-coordinate cavity, exemplifying the mechanical coupling between the two metal ions. As a result, The intramolecular *R*...Co contact distance increases by about 0.4 Å in going from **LaCo** to **LuCo** (Rigault et al., 2000b; Table 21). Examination of the series of structures ***R*Cr** (*R* = Nd, Eu, Yb, Lu) in which the Co^{III} ion is replaced slightly larger Cr^{III} ion points to the remarkable adaptability of the triple-stranded helical core to small variations in the ionic radii of either the 3d or the 4f transition metals. The overall structures with Co^{III} or Cr^{III} are very similar, the only noticeable difference being a somewhat longer intermetallic distance, ca. 9.3 Å versus ca. 9 Å, and a concomitant longer helical pitch (ca. 15.5 Å compared to ca. 13.5 Å) for ***R*Cr** helicates. On the other hand, variation of the R^{III} from

Nd to Lu induces only a 0.8% lengthening of the *R*-Cr contact distance and a 2% shortening of the helical pitch. These effects are smaller than the changes induced by the replacement of the 3d transition metal ion, despite that the variation in ionic radius between Nd^{III} and Lu^{III} (ca. 0.14 Å) is larger than the difference between Co^{III} and Cr^{III} (0.11 Å). The structural parameters are little affected when divalent Ru^{II} replaces Cr^{III} in **EuRu** and **LuRu**; the two ions have similar ionic radii but different charges and the intermetallic distance decreases to reach values similar to the one found in **LaFe** (Torelli et al., 2004, 2005). The structure of the helicate with the isoelectronic Os^{II} ion, **LuOs**, revealed an unusual distribution of the Os–N bonds, as well as bizarre anisotropic thermal parameters; careful examination of the data led to the conclusion that a preferential alignment of subdomains within the crystal may be responsible for this. In any case, averaged values do not deviate from those reported for **LuRu** (Riis-Johannessen et al., 2008).

The TTP coordination polyhedra of the R^{III} ions in the 12 reported structures are alike, as demonstrated by the geometrical analysis shown in Figure 117 and for which the relevant angles are reported in Table 21: all mean angles vary in short ranges, θ between 48° and 55°, ϕ between 178° and 179°, and ω between 50° and 56°.

Solution structure determination essentially relies on NMR data, via either a classical analysis of the number of signals and of their chemical shifts with the help of two-dimensional COSY, NOESY, and NOEDIF measurements, or the more sophisticated investigation of both lanthanide-induced shifts (LIS) and relaxation times (LIR). When the major species in solution is the heterobimetallic helicate, analysis of the ^{1}H-

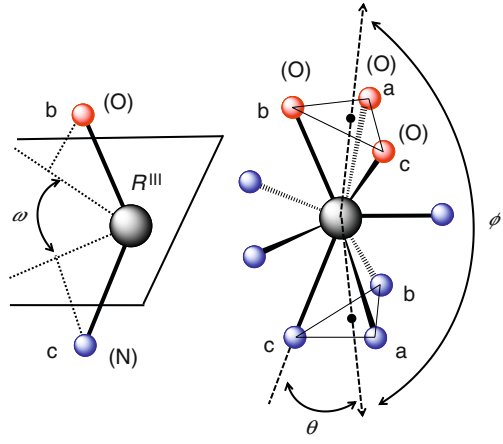

FIGURE 117 Definition of the angles for the analysis of the R^{III} coordination polyhedra in *R*M helicates (redrawn after Piguet et al., 1996).

NMR spectra is relatively simple. For instance, 26 and 23 signals are observed for the ***R*M** (M = Zn, Fe) helicates with ligands **L35** (Piguet et al., 1995d,e) and **L36** (Piguet et al., 1996, 1997b), respectively, pointing to the equivalence of the three ligand strands and therefore to C_3- or C_{3v}-symmetry for the molecular assembly, on the NMR timescale. The methylene protons of the bridge between the two chelating units of the ligands and of the dimethoxybenzyl or diethylamine substituents exhibit AB spin systems, precluding the presence of a mirror plane and therefore pointing to a HHH arrangement of the ligands with C_3-symmetry. The NOE effects observed, both intrastrand (Figure 118) and interstrand for a range of complexes (R = La, Ce, Nd, Sm, Eu, Yb, Lu, and Y) further confirm the helical twist of the ligands. Finally, analysis of the lanthanide-induced shift with separation of the contact and dipolar (pseudocontact) contributions according to Eq. (35) (see Section 3.6) substantiates the coordination of the lanthanide ion to the tridentate unit and of the 3d cation to the bidentate unit. For instance, small F_i values (<0.06) are observed for the protons of the bidentate unit in $[R\text{Zn}(\mathbf{L35})_3]^{5+}$ because of their large topological separation from the paramagnetic R^{III} ion. On the other hand, the F_i values are significantly larger for the protons of the tridentate binding unit and they increase to reach values as high as 0.25–0.33 when the protons are separated from the paramagnetic center by only three bonds, reflecting a large spin delocalization onto the bound tridentate unit. Similar conclusions hold for the Fe^{II} helicates with ligand **L35** (Piguet et al., 1997b), for Co^{II}, Co^{III} (Rigault et al., 1998), Ru^{II} (Torelli et al., 2004), and Os^{II} (Riis-Johannessen et al., 2008) helicates with ligand **L36**, as well as for Zn^{II} helicates with ligands **L36** (Piguet et al., 1996) and **HL38** (Edder

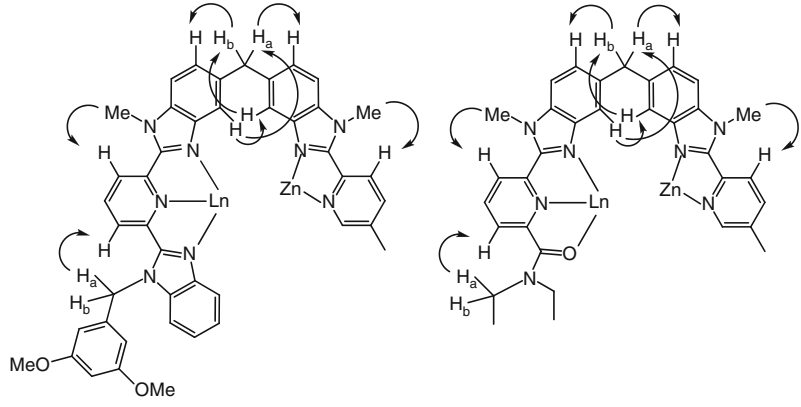

FIGURE 118 Intrastrand NOE effects observed for $[R\text{Zn}(\mathbf{L35})_3]^{5+}$ (left) and $[R\text{Zn}(\mathbf{L36})_3]^{5+}$ (right) in acetonitrile solution (R = La, Ce, Pr, Nd, Sm, Eu, Yb, Lu, Y) (redrawn after Piguet et al., 1995d, 1996).

TABLE 21 Selected structural parameter for the heterometallic *R*M helicates with ligands **L36** and **L37**

				R			M	
Ligand	*R*M	*R*. . .M (Å)	Pitch (Å)[a]	θ (°)[b]	ϕ (°)[b]	ω (°)[b]	r_i (Å)	References
L36	$EuZn^{II}$	8.96	15.4	55	178	50	0.62	Piguet et al. (1996)
L37	$EuZn^{II}$	8.58	14.6	48	179	55	0.72	Edder et al. (2000)
L36	$LaFe^{II}$	9.03	NA	52	179	52	0.52	Piguet et al. (1997b)
	$LaCo^{III}$	8.86	13.7	52	178	52	0.53	Rigault et al. (2000b)
	$LuCo^{III}$	9.23	13.5	49	179	55	0.48	Rigault et al. (2000b)
	$NdCr^{III}$	9.28	15.8	51	178	53	0.59	Torelli et al. (2005)
	$EuCr^{III}$	9.32	15.7	50	178	56	0.59	Cantuel et al. (2002)
	$YbCr^{III}$	9.33	15.4	49	179	52	0.59	Torelli et al. (2005)
	$LuCr^{III}$	9.35	15.4	49	179	56	0.59	Cantuel et al. (2002)
	$EuRu^{II}$	9.06	14.8	49	178	54	0.60	Torelli et al. (2005)
	$LuRu^{II}$	9.08	14.9	49	178	55	0.60	Torelli et al. (2004)
	$LuOs^{II}$	9.09	13.3	50	178	55[c]	0.63	Riis-Johannessen et al. (2008)

[a] Helical pitch corresponding to a 360° turn of the ligand strands.
[b] See Figure 117 for the definition of the angles.
[c] Individual values are highly dispersed, in the range 41–61°.

et al., 1997). When a fast-relaxing and highly paramagnetic 3d metal ion such as high-spin Co^{II} ($3d^7$, $\mu_{eff} \approx 4.9–5\mu_B$) is inserted into the triple-helical complexes, the NMR spectra span a 100 ppm range but are nevertheless fully interpretable (Rigault et al., 1998). In the case of **L36**, C_3-averaged values of the polar coordinates extracted from the crystal structure of **EuZn** have been used to recalculate the structural factors $(1–3\cos^2\theta)/r_i^3$, which significantly improved the fit of the experimental data. Values of the axial component χ_j^{zz} of the magnetic susceptibility tensor relative to Pr^{III} (Table 22) are in qualitatively good agreement with theoretical calculations for the larger ions (Ce, Nd, Eu) while they deviate more for Tm and Yb, although the general trend is maintained. These results not only point to the presence of C_3 triple-stranded helicates in solution but, also, to the **EuZn** crystal structure being a satisfying model for the averaged solution structures on the NMR timescale.

For the $[R\text{Fe}(\mathbf{L36})_3]^{5+}$ series of helicates, the signals of the protons belonging to the bidentate binding unit are very different from those of $[R\text{Zn}(\mathbf{L36})_3]^{5+}$ at room temperature, even for diamagnetic R^{III} ions, some of these protons being strongly shifted toward lower field as a result of the $^1A \rightleftarrows {}^5T_2$ spin-state equilibrium. The two NMR spectra become only similar when the temperature is lowered to 233 K, where iron is essentially in its diamagnetic low-spin state. The localization of Fe^{II} in the pseudo-octahedral site is further confirmed by cyclic voltammetry which shows the $[R\text{Fe}(\mathbf{L36})_3]^{5+}$ helicates being oxidized in a reversible one-electron process at $E_{1/2} \approx 0.82$ V (vs SCE), independent of the nature of the R^{III} ion (Piguet et al., 1997b).

Applying Reilley's method for the separation of contact and dipolar paramagnetic shifts to $[R\text{Co}^{III}(\mathbf{L36})_3]^{6+}$ helicates, that is, the linear forms of Eq. (35) (see Section 3.6):

$$\frac{\delta_{ij}^{\text{para}}}{\langle S_z \rangle_j} = F_i + G_i B_0^2 \frac{C_j}{\langle S_z \rangle_j} \tag{146}$$

TABLE 22 Comparison of theoretical and experimental values of the axial term of the magnetic susceptibility tensor relative to Pr^{III} for $[R\text{Zn}^{II}(\mathbf{L36})_3]^{5+}$ complexes (Piguet et al., 1996)

*R*Zn	Theoretical	Experimental	*R*Zn	Theoretical	Experimental
CeZn	0.57	0.63	EuZn	− 0.36	− 0.54
PrZn	1.00	1.00	TmZn	− 4.82	− 2.86
NdZn	0.38	0.47	YbZn	− 2.00	− 1.07

$$\frac{\delta_{ij}^{\text{para}}}{C_j} = F_i \frac{\langle S_z \rangle_j}{C_j} + G_i B_0^2 \tag{147}$$

leads to the plots reproduced on Figure 119A and B, in which a straight line is observed for R = Ce-Eu, but Tm and Yb are not included, pointing to a possible structural change between lighter and heavier lanthanide ions. When Tb, Dy, Ho, and Er are included in the plots, after succeeding in assigning the proton resonances for the paramagnetic heavier lanthanide ions, the Tb-Yb series fits a second straight line (Rigault and Piguet, 2000). This counterintuitive result, in view of the similarities in the crystal structures of $[R\text{Co}^{\text{III}}(\mathbf{L36})_3]^{6+}$ with R = La, Lu (Rigault et al., 2000a), can be corrected by applying the crystal-field independent method (Eq. (37), Section 3.6), as shown on Figure 119C so that the break resulting from the classical separation method is in fact due to a change in the ligand-field parameters along the lanthanide series, the ligand field being 1.6-fold smaller for the series Tb–Yb compared to Ce–Eu (Rigault et al., 2000a). A further comparison of the LIS and LIR data for the entire series of Co^{III} helicates with calculated data using the geometrical parameters of

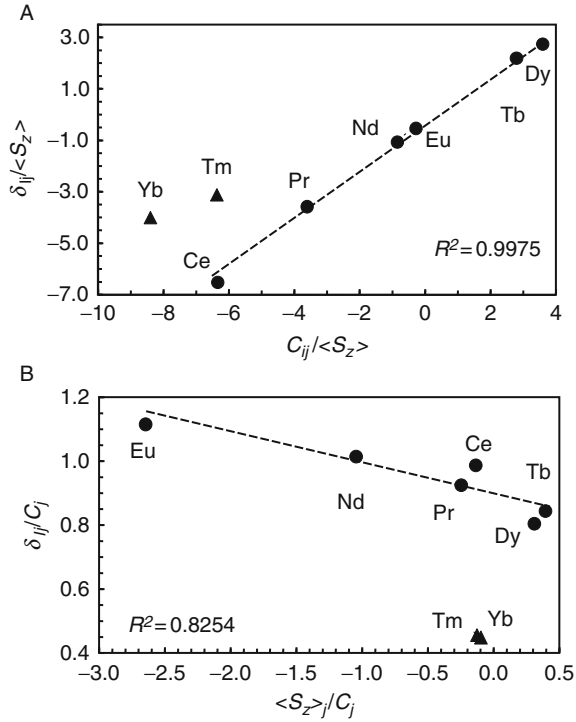

FIGURE 119 Continued

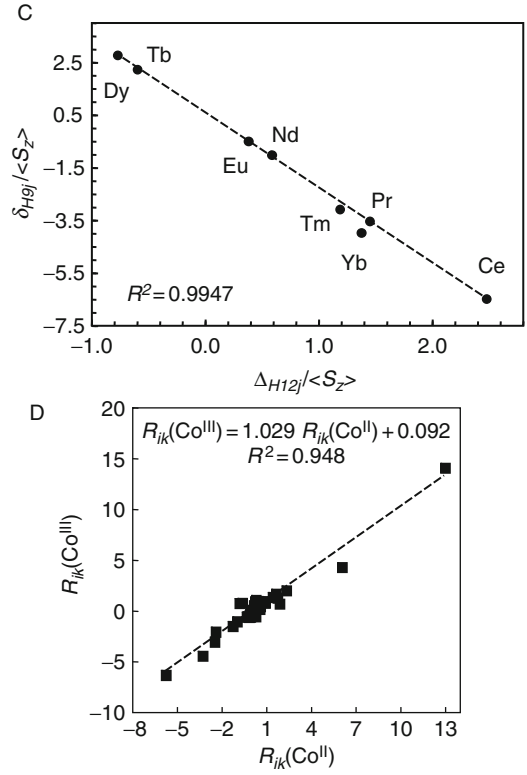

FIGURE 119 Plots of the paramagnetic-induced shifts for $[RCo^{III}(\mathbf{L36})_3]^{6+}$ in acetonitrile according to (A) Eq. (146), (B) Eq. (147), and (C) Eq. (37) (redrawn after Rigault et al., 2000a). (D) Plots of the structural factors $R_{ik} = G_i/G_k$ of the Co^{III} helicates versus those of the Co^{II} complex (redrawn after Rigault et al., 2000b).

the crystal structures for La and Lu confirms the isostructurality of the series, as well as a close match between the less-distorted crystal structure of the Lu helicate and the solution structure in acetonitrile, but for minor deviations due to a larger fluxionality in solution. A similar analysis on the Co^{II} helicates had to take into account the presence of two paramagnetic centers. However, the latter are magnetically independent, since the magnetic moments of the $\boldsymbol{RCo^{II}}$ helicate obey Eq. (148) with $\mu_{eff}^{Co^{II}} = 4.8$ MB, so that the LIS are identical in $\boldsymbol{RCo^{II}}$ and in $\boldsymbol{RCo^{III}}$. The complete NMR analysis yields similar results as for the trivalent cobalt compounds. This is illustrated in Figure 119D in which the structural factors $R_{ik} = G_i/G_k$ (see Eq. (37), Section 3.6) of RCo^{III} versus RCo^{II} plotted for 22 pairs of protons are indeed in linear relationship with a unit slope (Rigault et al., 2000a), consistent with the axial magnetic anisotropic susceptibilities reported in

TABLE 23 Comparison of theoretical and experimental values of the axial magnetic anisotropic susceptibility relative to the value for Dy^{III} ($C_j = -100$) for $[RCo^{II}(\mathbf{L36})_3]^{5+}$ and $[RCo^{III}(\mathbf{L36})_3]^{6+}$ helicates; data are corrected for ligand-field effects (Rigault et al., 2000b)

R	$C_j(RCo^{III})$	$C_j(RCo^{II})$	Theoretical	R	$C_j(RCo^{II})$	$C_j(RCo^{III})$	Theoretical
Ce	−5.2	−6	−6.3	Dy	−100	−100	−100
Pr	−8.0	−10	−11	Ho	−53	−57	−39
Nd	−3.8	−5.5	−4.2	Er	11	12	33
Eu	4.3	6	4.0	Tm	33	37	53
Tb	−91	−94	−86	Yb	13	13	22

Table 23 for the two series of complexes. That is both the Co^{II} and Co^{III} helicates have very similar rigid C_3 solution structure, exemplifying the ability of the $(\mathbf{L36})_3$ supramolecular receptor to adapt to 3d metal ions with various charges and ionic radii without disrupting the overall architecture of the final RML_3 helicates.

$$\mu_{\text{eff}}^{RCo^{II}} = \sqrt{(\mu_{\text{eff}}^{R})^2 + (\mu_{\text{eff}}^{Co^{II}})^2} \tag{148}$$

The structural studies by X-ray diffraction and NMR have been complemented by a high-resolution luminescence analysis of the Eu^{III}-containing complexes similar to the one conducted for the homometallic bioprobes (Section 6.3.1). Data are collected in Table 24. Firstly, the energy of the $^5D_0 \rightarrow {}^7F_0$ transition calculated with Eq. (19) (see Section 3.5) and the usual nephelauxetic parameters $\delta_{N(heter)} = -15.3$, $\delta_{O(amide)} = -15.7$, and $\delta_{O(carbox)} = -17.2\ cm^{-1}$ amounts to 17,236, 17,235, and 17,231 cm^{-1} for N_9, N_6O_3(amide), and N_6O_3(carbox) environments, respectively. The experimental data are in good agreement for **L35** but somewhat lower than predicted for **L36** and **L37** (17,224–17,229 cm^{-1}), possibly due to the large spin delocalization evidenced by NMR and causing a larger nephelauxetic effect. On the other hand, the experimental nephelauxetic effect for **HL38** is somewhat smaller (5 cm^{-1}) than calculated. All the emission spectra match an analysis based on a distorted ternary (C_3) symmetry as seen from the splitting of the $^7F_1$ level into two sublevels labeled A and E according to group-theoretical considerations. There are, however, large differences between the various helicates and, also, between solid state and solution samples, particularly in the case of **L37**. Looking at the ΔE (A–E) energy difference for the Zn^{II} helicates, which is directly proportional to the B_0^2 ligand-field parameter (Binnemans and Görller-Walrand, 1995), the strength of the ligand field induced by the various ligands at 10 or 13 K increases in the series **L35** (93 cm^{-1}) < **L37** (118) < **L36** (127) < **HL38**

TABLE 24 High-resolution analysis of the Eu($^5D_0$) emission to the $^7F_0$ and $^7F_1$ levels for $[EuM(\mathbf{L})_3]^{n+}$ and $[MEuM(\mathbf{L})_3]^{n+}$ helicates in solid state (s) or acetonitrile (as) solutions

					$^5D_0 \rightarrow {}^7F_1$		
Ligand	M	State	T (K)	$^5D_0 \rightarrow {}^7F_0$ E_{exp} (cm^{-1})	ΔE(A–E) (cm^{-1})	ΔE(E–E) (cm^{-1})	References
L35	Zn^{II}	as	10	17,224	94	43	Piguet et al. (1995d)
	Zn^{II}	as	295	12,236	NA	NA	
L36	Zn^{II}	s	10	17,220	127	21	Piguet et al. (1996)
	Zn^{II}	s	295	17,229	140	55	
	Zn^{II} [a]	s	295	17,226	134	63	
	Cr^{III}	s	10	17,216	100	48	Cantuel et al. (2002)
HL38	Zn^{II}	s	10	17,224	138	42	Edder et al. (1997)
	Zn^{II}	s	295	17,235	145	35	
	Zn^{II}	as	295	17,237	149	NA	
L37	Zn^{II}	s	10	17,221	118	37	Edder et al. (2000)
	Zn^{II}	s	295	17,225	117	NA	
	Zn^{II}	as	295	17,224	82	49	
L41	Zn^{II}	s	13	17,221	146	35	Edder et al. (2001)
	Zn^{II}	as	295	17,232	147	NA	
	Fe^{II}	s	13	17,221	144	37	
L42	$Zn^{II}Zn^{II}$	s	10	17,221	98	32	Cantuel et al. (2006)
	$Cr^{III}Cr^{III}$	s	10	17,218	80	34	

[a] Eu-doped (2%) $[GdZn(\mathbf{L36})_3]^{5+}$.

(138) < **L41** (146). This can be understood with respect to the inner sphere composition, a N_9 environment generating a weaker field than a N_6O_3 one. The weaker field induced by **L37** with respect to **L36** most probably arises from the less distorted coordination polyhedron in $[EuZn(\mathbf{L37})_3]^{5+}$ compared with $[EuZn(\mathbf{L36})_3]^{5+}$ (Edder et al., 2000) while the largest field observed for the helicate with **L41,** with respect to the carboxylic acid **HL38,** may be traced back to the weaker coordination of the 3d transition metal, allowing a tighter wrapping of the ligand strands around the lanthanide ion.

7.5 Intermetallic communication as a tool for tuning magnetic and photophysical properties

7.5.1 Tuning the spin-crossover parameters of Fe^{II}

Spin equilibria between the $^1A_1$ and $^5T_2$ states occur for all the Fe^{II}-containing helicates, that is, with ligands **L35-L37**. The effective magnetic moment of the iron partner is deduced from susceptibility measurements of $[R\mathrm{Fe}(\mathbf{L})_3]^{5+}$ and the corresponding $[R\mathrm{Zn}(\mathbf{L})_3]^{5+}$ helicates for assessing the diamagnetic contribution and the contribution from the lanthanide ions. The observed magnetic behavior of Fe^{II} allows the evaluation of the spin-crossover constant K_{sc} according to

$$\mu^2_{\mathrm{eff}}(\mathrm{Fe}) = \mu^2_{\mathrm{eff}}(R\mathrm{Fe}) - \mu^2_{\mathrm{eff}}(R\mathrm{Zn}) \tag{149}$$

$$^1\mathrm{A}_1(\mathrm{S}=0,\mathrm{LS}) \rightleftarrows {}^5\mathrm{T}_2(\mathrm{S}=2,\mathrm{HS})\ K_{\mathrm{SC}} \tag{150}$$

$$K_{\mathrm{SC}} = \frac{\mu^2_{\mathrm{eff}} - \mu^2_{\mathrm{LS}}}{\mu^2_{\mathrm{HS}} - \mu^2_{\mathrm{eff}}} = \frac{x_{\mathrm{HS}}}{1 - x_{\mathrm{HS}}} = \exp\left(-\frac{\Delta H_{\mathrm{SC}}}{RT} + \frac{\Delta S_{\mathrm{SC}}}{R}\right) \tag{151}$$

$$T_{\mathrm{SC}} = \frac{\Delta H_{\mathrm{SC}}}{\Delta S_{\mathrm{SC}}} \tag{152}$$

where μ_{LS} and μ_{HS} are the magnetic moments of the low and high-spin forms, taken as 5.0 and $0.3\mu_{\mathrm{B}}$, respectively (Sugiyarto et al., 1994), ΔH_{SC} and ΔS_{SC} are the corresponding thermodynamic parameters, while T_{SC} is the critical temperature for which $x_{\mathrm{HS}} = 0.5$. Relevant data obtained by either NMR or spectrophotometric determinations are collected in Table 25 while the high-spin mole fractions versus temperature are displayed on Figure 120 for helicates with **L37**. The temperature range investigated, 243–333 K, is limited by the physical properties of the solvent, acetonitrile, so that the spin transition cannot be directly evidenced, but its temperature can be calculated from Eq. (152). For **L35,**

TABLE 25 Parameters for the magnetic low-spin/high-spin equilibria of $[RFeL_3]^{5+}$ helicates in acetonitrile

L	*R*Fe	ΔH_{sc} (kJ mol^{-1})	ΔS_{sc} (J mol^{-1}K^{-1})	τ_{sc} (K)	x_{HS} (293 K)	References
L35	LaFe	20.6(6)	57(3)	361	0.16	Piguet et al. (1995e)
	CeFe	23.1(8)	66(4)	350	0.17	
	PrFe	22.2(8)	62(3)	358	0.16	
	NdFe	21.8(8)	60(3)	363	0.16	
	SmFe	20.0(9)	55(4)	364	0.15	
	EuFe	23.0(9)	64(3)	359	0.15	
L36	CaFe	30.3(3)	90(1)	336	0.17	Piguet et al. (1997b)
	LaFe	30.5(3)	92(1)	331	0.19	
	NdFe	30.2(3)	90(1)	334	0.18	
	EuFe	29.6(5)	89(1)	336	0.18	
	YFe	29.6(3)	88(1)	338	0.17	
	YbFe	28.3(4)	83(1)	342	0.16	
	LuFe	28.4(4)	82(2)	346	0.14	
	ScFe	25.8(7)	74(2)	349	0.16	
L37	LaFe	30.1(2)	94(1)	320	0.31	Edder et al. (2000)
	YFe	29.2(2)	89(1)	327	0.26	
	LuFe	29.8(2)	87(1)	331	0.24	

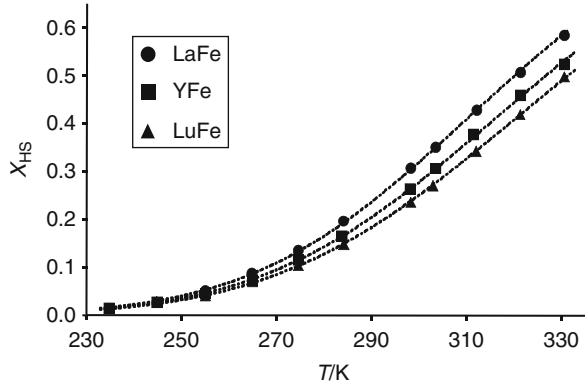

FIGURE 120 Mole fraction of high-spin Fe^{II} in $[R\text{Fe}(\textbf{L37})_3]^{5+}$ solutions in acetonitrile versus temperature (redrawn after Piguet et al., 1997b).

this temperature is relatively insensitive to the nature of the lanthanide ion (359–363 K), with the exception of Ce^{III}. On the other hand, there is smooth dependence of T_{SC} on the size of the metal ion for the **L36**

helicates, with an increase from 336 K (La) to 349 K (Sc), allowing a remarkable tuning of this parameter by the R^{III} ion (Piguet et al., 1997b). Replacement of the methyl substituent on the pyridine moiety (**L37**) has little consequence on the thermodynamic parameters, but lowers T_{SC} by a welcome 10 K, although the tuning range is somewhat reduced (320–331 K). The inner-sphere reorganization energy associated with the elongation of the Fe-N bond upon conversion from low-spin to high-spin Fe^{II} is in the range 8–25 kJ mol^{-1} and is expected to be the dominant contribution to ΔH_{SC}. The entropic factor encompasses a small electronic contribution associated with the difference in the degeneracy of the low- and high-spin states and larger ones arising from vibrational partition functions, the disorder of the high-spin state being more pronounced owing to longer Fe-N bonds.

Associating a luminescent R^{III} ion with paramagnetic Fe^{II} in the same supramolecular structure leads to materials with a fascinating combination of properties and tuning abilities thanks to a judicious ligand choice (Edder et al., 2001). For instance, the steric constraint linked to the introduction of a methyl group in the 6-position of the pyridine in **L41** results in the sole presence of high-spin HHH-$[EuFe(\mathbf{L41})_3]^{5+}$ helicate, both in solution and in the solid state (2–300 K) instead of the usual spin-state equilibrium, as observed for $[EuFe(\mathbf{L36})_3]^{5+}$; this is ascertained by the weak LMCT absorption band ($\varepsilon \approx 500\ M^{-1}cm^{-1}$) around 450 nm, responsible for the yellow color of the complex, and the faint d-d transitions at 910 (14 $M^{-1}cm^{-1}$) and 1130 nm (11 $M^{-1}cm^{-1}$). For comparison, the LMCT of the pure low-spin complexes $[LnFe(\mathbf{L36})_3]^{5+}$, accounting for their violet color, extends from 430 to 630 nm and is much more intense, with ε reaching 5800 $M^{-1}cm^{-1}$ at the maximum at 530 nm. As a result, the $^5D_0$ luminescence in $[EuFe(\mathbf{L36})_3]^{5+}$ is totally quenched in the range 10–400 K in view of the overlap between the Eu emission spectrum and this broad LMCT state (Piguet et al., 1997b). A similar quenching happens for $[EuFe(\mathbf{L35})_3]^{5+}$ as well (Piguet et al., 1995e). On the other hand, $[EuFe(\mathbf{L41})_3]^{5+}$ is luminescent, even at room temperature, yet less than the corresponding Zn^{II} complex, as indicated by the $Eu(^5D_0)$ lifetime which drops from 2.63 ms (ligand excitation, solid state, 13 K) in the zinc helicate to 0.28 ms in the iron complex due to partial directional $Eu^{III} \rightarrow Fe^{II}_{HS}$ energy transfer, the latter ion acting as a semitransparent partner (Figure 121).

7.5.2 Tuning visible lanthanide emission

The ligand-centered photophysical properties of the helicates with a spectroscopically silent nd-transition partner are not essentially different from those of the previously discussed homobimetallic helicates and will not be detailed here. When a nd-transition ion amenable to form MLCT states with the ligand strands is introduced into the helical edifices,

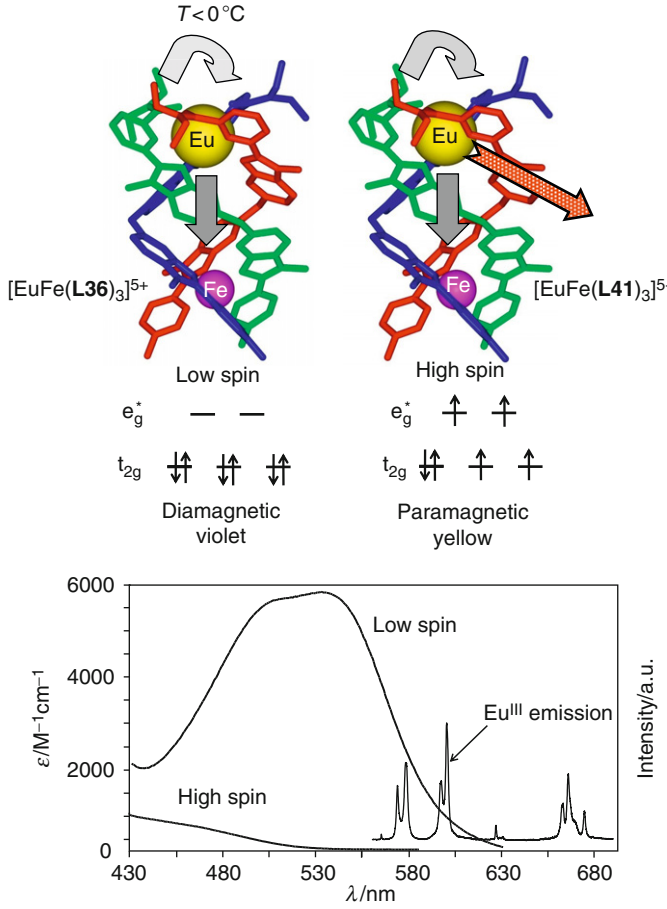

FIGURE 121 Top: schematic representation of energy transfer processes in low-spin $[EuFe(\mathbf{L36})_3]^{5+}$ (left) and high-spin $[EuFe(\mathbf{L41})_3]^{5+}$ (right). Bottom: absorption spectra at 295 K (left scale) of high-spin $[EuFe(\mathbf{L41})_3]^{5+}$ and of spin-crossover $[EuFe(\mathbf{L36})_3]^{5+}$ complexes in acetonitrile, as well as the overlapping Eu^{III} emission spectrum (right scale) of high-spin $[EuFe(\mathbf{L41})_3]^{5+}$ (solid state, 13 K) (redrawn after Edder et al., 2001).

specific absorption and, possibly, emission bands from these state are also observed, as well as d-d transitions. Relevant data are collected in Table 26 and show a relatively small influence of the lanthanide complexation on the ligand levels when M = Zn but a more pronounced one for the other ions. Lifetimes and quantum yields for lanthanide-centered luminescence are listed in Table 27. Except for $[EuCr(\mathbf{L36})_3]^{6+}$, in which Eu-to-Cr energy transfer is operating, and for $[EuFe(\mathbf{L41})_3]^{6+}$ for reasons discussed above, the Eu($^5D_0$) lifetimes are long, ca. 2.3–3.0 ms. This is

TABLE 26 Selected ligand-centered photophysical properties of the ligands and some of the $[RML_3]^{m+}$ and $[Cr^{II/III}RCr^{II/III}L_3]^{m+}$ helicates

L	*R*	M	State[a]	*T* (K)[b]	*E*(*π ← π) (cm^{-1})	*E*(MLCT) + *E*(d–d) (cm^{-1})	*E*($^1ππ^*$) (cm^{-1})	*E*($^3ππ^*$) (cm^{-1})	τ($^3ππ^*$) (ms)	References
L35			s	77	29,600, 28,600		25,000	19,200, 18,650	350, 88	Piguet et al. (1995d)
	La	Zn^{II}	s	77	29,600, 26,200		22,600	19,700, 18,900	124, 37	
	Lu	Zn^{II}	s	77	30,300, 25,650		22,200	19,700, 18,900	243, 79	
L35			$CHCl_3$	293	35,490, 31,450		NA	NA	NA	Piguet et al. (1995e)
	La	Fe^{II}	$CHCl_3$	293	30,550, 26,880	18,800	23,000[c]	19,000[c]	NA	
	Eu	Fe^{II}	$CHCl_3$	293	30,270, 27,020	18,870	23,000[c]	19,000[c]	NA	
L36			s	77	30,770		24,940	20,040, 18,870	560, 41[d]	Piguet et al. (1996)
	La	Zn^{II}	s	77	31,000		22,600	19,960, 19,050	250, 36[d]	
	Gd	Zn^{II}	s	77	31,250		22,600	19,960, 19,050	12, 5[d]	
L36			MeCN	293	33,320, 31,750		NA	NA	NA	Piguet et al. (1997b)
	La	Fe^{II}	MeCN	293	29,940, 28,570	19,050	22,220[c]	18,520[c]	NA	
	Lu	Fe^{II}	MeCN	293	29,940, 28,570	19,080	22,220[c]	18,520[c]	NA	
L36	La	Cr^{II}	MeCN	293	40,486, 30,121	23,640, 16,475, 14,368, 11,710, 9090, 8368				Cantuel et al. (2002)
	La	Cr^{III}	MeCN	293	40,486, 30,030	25,700, 22,800, 21,600, 20,000				
	Lu	Cr^{III}	MeCN	293	40,486, 29,940	25,700, 22,800, 21,600, 20,000				
L36	Lu	Ru^{II}	MeCN	296	39,525, 29,940	21,100	[e]	14,730[f]	0.38×10^{-3}[f]	Torelli et al. (2004)

(*continued*)

TABLE 26 (*continued*)

L	*R*	M	State[a]	*T* (K)[b]	$E(^*\pi \leftarrow \pi)$ (cm^{-1})	E(MLCT) + E(d–d) (cm^{-1})	$E(^1\pi\pi^*)$ (cm^{-1})	$E(^3\pi\pi^*)$ (cm^{-1})	$\tau(^3\pi\pi^*)$ (ms)	References
	Gd	Ru^{II}	MeCN	293	40,160, 30,120	21,185	25,800[g]	24,300, 20,700[g]	94[g]	Torelli et al. (2005)
L36	Lu	Os^{II}	MeCN	293	29,850	19,920, 14,500	[e]	12,400[f]	31×10^{-6}[f]	Riis-Johannessen et al. (2008)
L37			CH_2Cl_2	293	30,490					Edder et al. (2000)
	La	Zn^{II}	CH_2Cl_2	293	29,670					
	La	Fe^{II}	CH_2Cl_2	293	29,940	18,180, 17,270				
	Lu	Fe^{II}	CH_2Cl_2	293	29,670	18,180, 17,250				
L37			s	77	28,170		22,936	23,900, 22,650	68[d]	Edder et al. (2000)
	La	Zn^{II}	s	77	27,174		21,740	19,230, 18,250, 17,390	480[d]	
	Eu	Zn^{II}	s	77	26,675		21,645	[e]	[e]	
HL38	Eu	Zn^{II}	MeCN	293	41,000, 30,580		[e]	[e]	[e]	Edder et al. (1997)
L41			s	77	30,670		25,250	21,260, 19,690, 19,120, 16,550	605, 45[d]	Edder et al. (2001)
	La	Zn^{II}	s	77	30,210		23,700	20,920, 19,530, 18,140, 16,750	221	
	La	Fe^{II}	s	77	30,210	19,010	[e]	18,870[d]	261, 30	Cantuel et al. (2006)
L42	Lu	$Cr^{II}Cr^{II}$	MeCN	293	31,150, 27,300	16,690, 14,200, 11,765, 10,225, 8300		18,900[d]	2.45, 0.49[d]	
	Lu	$Cr^{III}Cr^{III}$	MeCN	295	31,350, 27,100	27,100, 20,000		24,450[d]	2.45, 0.49[d]	

[a] s, solid state.
[b] Except for $^*\pi \leftarrow \pi$ transitions of solid state samples, recorded by reflectance spectroscopy at room temperature.
[c] Very weak signal.
[d] At low temperature (77, 13, or 10 K).
[e] Luminescence quenched.
[f] From the ^{3}MLCT state.
[g] At 77 K.

TABLE 27 Quantum yields and lifetimes of the $[RML_3]^{n+}$ helicates, $R = Eu$, Tb upon ligand excitation

L	R	M	$\tau(^5D_J)$ (ms)[a]	c (M)	Q_L^{Ln} (%)[b]	References
L35	Eu	Zn	2.30(5)	10^{-4}	≈0.01	Piguet et al. (1995d, 1996)
	Tb	Zn	1.17(4)		NA	Piguet et al. (1995d)
L36	Eu	Zn	2.56	10^{-3}	4.2	Piguet et al. (1996)
			(10)	10^{-4}	9.3	
	Tb	Zn	1.89(6)		NA	
	Eu	Cr^{III}	0.55(4)[c]	10^{-4}	3.2	Cantuel et al. (2002)
L37	Eu	Zn	2.35(2)	10^{-3}	8.2	Edder et al. (2000)
HL38	Eu	Zn	2.99(9)	10^{-4}	32	Edder et al. (1997)
			2.43(2)[d]	10^{-4} [d]	15	
L41	Eu	Zn	2.63(1)	10^{-3}	7.4	Edder et al. (2001)
	Eu	Fe^{II}	0.28(1)	10^{-3}	0.03	

[a] Solid state sample, at 10 or 13 K, ligand excitation.
[b] In acetonitrile at room temperature; recalculated by using the most recent values reported for the $[R(terpyridine)_3]^{3+}$ internal references, 32 ± 1 (R = Eu) and 35 ± 1% (R = Tb) in acetonitrile (Comby, 2008); uncertainty: ± 10–15%.
[c] For $[EuCr(\mathbf{L36})_3](CF_3SO_3)_6 \cdot 4H_2O$; 0.75(1) ms for $[EuCr(\mathbf{L36})_3](CF_3SO_3)_6 \cdot 4MeCN$, and 0.87(4) ms for a solution 10^{-4} M in acetonitrile.
[d] 10^{-4} M in H_2O.

clearly in line with an inner coordination sphere devoid of water molecules. On the other hand, $Tb(^5D_4)$ lifetimes are shorter, probably due to some back transfer operating, the $^3\pi\pi^*$ states of the coordinated **L35** and **L36** ligands having an energy (≈19,000–20,000 cm^{-1}) close to the one of the $^5D_4$ level, 20,500 cm^{-1}. Quantum yields have only been determined for Eu^{III} helicates. They span a wide range, from 0.01% in $[EuZn(\mathbf{L35})_3]^{5+}$ because the N_9 environment made up of benzimidazolepyridine units is known to generate a rather low-lying and quenching LMCT state (Gonçalves e Silva et al., 2000; Petoud et al., 1999), to a high 32% for the sparingly soluble carboxylate $[EuZn(\mathbf{L38})_3]^{2+}$. The robustness of the triple-helical edifice is exemplified by the fact that adding up to 0.93 M water to $[EuZn(\mathbf{L36})_3]^{5+}$ does not alter either the $^5D_0$ lifetime or the quantum yield (Piguet et al., 1996). Similarly, the quantum yield of $[EuCr(\mathbf{L36})_3]^{5+}$ in acetonitrile (Q = 3.2%) remains unchanged up to 3 M added water (Cantuel et al., 2002). If the same experiment is conducted on the even more robust $[EuZn(\mathbf{L38})_3]^{2+}$ helicate in acetonitrile, the quantum yield slightly drops to reach 87% of its initial value up to 2 M of added water, probably in view of the second sphere effect of fast diffusing O–H

vibrators, and then further decreases slowly to reach about 80% of its initial value for a water concentration of 10 M. The quantum yield in pure water is about half that in acetonitrile and the lifetime is still long, 2.43 ms; with $\tau(D_2O) = 4.48$ ms, one calculate $q \approx 0$, using Supkowski and de Horrocks (2002) equation, a remarkable result in that even in pure water, there is no inner sphere interaction with the solvent (Edder et al., 1997).

When one metal ion plays the role of a donor for sensitizing the emission of a second accepting metal ion, the characteristic lifetimes τ of their excited states, which are related to their deactivation rates by $\tau_{em} = (k_{em})^{-1}$, are affected by the intermetallic communication process (Figure 122). If the energy transfer rate is much faster than the deactivation rate of the donor ion, the situation is very simple and assuming a Förster's dipole–dipolar mechanism, the yield of the transfer is given similarly to Eq. (77) by

$$\eta_{DA} = 1 - \frac{\tau^{D}_{obs}}{\tau^{D}_{0}} = 1 - \frac{Q^{D}_{obs}}{Q^{D}_{0}} = \frac{1}{\left(1 + \frac{R^{DA}}{R^{DA}_{0}}\right)^{6}} \tag{153}$$

where D stands for the donor and A for the acceptor, while subscript 0 for τ and Q denotes the situation without energy transfer; R^{DA} is the distance between the donor and the acceptor and R^{DA}_0 is the critical distance for 50% transfer. The experimental parameters corresponding to the situation without transfer are usually measured on $[RZnL_3]^{m+}$ or $[GdML_3]^{m+}$ complexes.

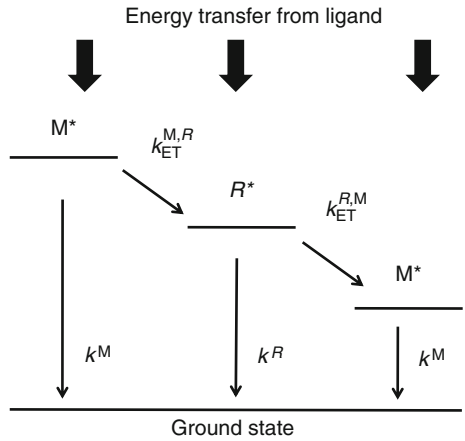

FIGURE 122 Schematic representation of a nd-to-4f energy transfer (left) and of a 4f-to-nd transfer (right) along with the definition of the rate constants.

The chromium helicate $[EuCr^{III}(\mathbf{L36})_3]^{6+}$ displays both $Cr(^2E \rightarrow {}^4A_2)$ and $Eu(^5D_0 \rightarrow {}^7F_j)$ emission. The lifetime of the latter is considerably shorter than in $[EuZn(\mathbf{L36})_3]^{5+}$, which is assigned to unidirectional $Eu \rightarrow Cr$ transfer along the C_3-axis (Cantuel et al., 2002). Determination of η_{CrEu} for two types of crystalline samples (hydrated and anhydrous, see Table 28) provides the same temperature-independent (10–295 K) efficiencies for this transfer, within experimental errors, $\approx 70 \pm 5\%$. The energy transfer yield is also insensitive to the nature of the sample, as shown by the same calculation carried out for 10^{-4} M solutions in acetonitrile using either quantum yields (see Table 27, $\eta_{CrEu} = 66\%$) or lifetimes (70%), a proof of the dipole–dipolar mechanism operating in these fairly rigid triple-helical structures (the calculated R_0 distance is ≈ 10.3 Å). In the case of Tb, the transfer is quantitative, no $^5D_4$ luminescence being observed even upon direct Tb excitation, because of the near resonance between the $Tb(^5D_4)$ and $Cr(^4T_2)$ electronic levels.

7.5.3 Tuning near-infrared lanthanide emission

Because of its transparency to biological tissue, NIR light is praised for bioprobes and many R^{III} ions seem to be ideally suited for this purpose. There are, however, two problems with these probes (Comby and Bünzli, 2007): (i) due to the small energy gap, the excited states are readily deactivated by all kind of vibrational oscillators, even by those residing in the outer coordination sphere, and (ii) the excited state lifetime is usually short, limiting the ease of application of TRD. The latter inconvenience may be remedied by populating the excited state of the NIR-emitting R^{III} ion by a slow emitting donor. Some transition metal ions such as Cr^{III} meet the necessary criteria and the triple-helical receptors dealt with in this chapter appear to be ideal hosts for facilitating such an energy transfer. The $[RCr^{III}(\mathbf{L36})_3]^{6+}$ and $[RRu^{II}(\mathbf{L36})_3]^{5+}$ complexes (R = Nd, Gd, Er, Yb), have been thoroughly tested for this purpose (Imbert et al., 2003; Torelli et al., 2005). The situation can be modeled as follows (Figure 122). In absence of energy transfer, the excited states of the isolated chromophores have deactivation rates k^R and k^M which are the sum of the radiative and nonradiative rate constants:

$$d[M^*]/dt = -\left(k_{ET}^{M,R} + k^M\right)[M^*] \tag{154}$$

$$d[R^*]/dt = k_{ET}^{M,R}[M^*] - k^R[R^*] \tag{155}$$

TABLE 28 Lifetimes, quantum yields, and energy transfer yields in microcrystalline samples of $[RZn(\mathbf{L36})_3]^{5+}$ and $[RCr^{III}(\mathbf{L36})_3]^{6+}$ helicates (data from Cantuel et al., 2002)

RM	*T* (K)	$\tau(^5D_J)$ (ms)[a]	$\tau(^2E)$ (ms)[a]	η_{RCr} (%)[b]	*RM*	*T* (K)	$\tau(^5D_J)$ (ms)[a]	$\tau(^2E)$ (ms)[a]	η_{RCr} (%)
GdCr	10	–	3.66(3)		GdCr	295		0.29(1)	
EuZn[b]	10	2.53(1)			EuZn[b]	295	1.67(2)		
EuCr[c]	10	0.55(4)	3.46(1)	78 (73)	EuCr[c]	295	0.59(1)	0.09(1)	65
EuZn[d]	10	2.19(1)			EuZn[d]	295	1.98(1)		
EuCr[e]	10	0.75(1)	3.12(1)	66 (70)	EuCr[e]	295	0.66(1)	0.05(1)	67
TbCr	10	[f]	3.39(1)	100	TbCr	295	[f]	0.17(1)[g]	100

[a] Upon ligand excitation.
[b] Values between parentheses are averages of data recorded at different excitation wavelengths.
[c] $[EuZn(\mathbf{L36})_3](ClO_4)_5 \cdot 2H_2O$.
[d] $[EuCr(\mathbf{L36})_3](CF_3SO_3)_6 \cdot 4H_2O$.
[e] $[EuCr(\mathbf{L36})_3](CF_3SO_3)_6 \cdot 4MeCN$.
[f] No $^5D_4$ luminescence.
[g] Direct excitation in the $Tb(^5D_4)$ level.

Integration gives:

$$[M^*] = [M_0^*] \cdot \exp\left\{-\left(k_{ET}^{M,R} + k^M\right)t\right\} \tag{156}$$

$$[R^*] = [M_0^*] \frac{k_{ET}^{M,R}}{k^R - \left(k_{ET}^{M,R} + k^M\right)} \left(\exp\left\{-\left(k_{ET}^{M,R} + k^M\right)t\right\} - e^{-k^R t}\right) \tag{157}$$

Equation (156) reveals that the decay rate of the excited state of the donor (in this case M*) increases, when energy is transferred onto the acceptor. The experimental decay of the donor metal ion thus corresponds to the sum of the two deactivation rate constants $k_{obs}^M = k^M + k_{ET}^{M,R}$, which translates into a reduced lifetime $\tau^M = (k_{obs}^M)^{-1} = (k^M + k_{ET}^{M,R})^{-1}$. Interpretation of Eq. (157) is complicated, because the magnitude of $k_{ET}^{M,R}$ controls the population rate of the R^* excited state. Therefore, the decay profile of R^* after initial excitation of the donor depends much on the relative magnitudes of the rate constants $k_{obs}^M = k^M + k_{ET}^{M,R}$ and k^R. Two limiting cases can be considered.

The first one refers to a situation for which $k_{obs}^M \gg k^R$, that is, the R^* level is almost completely populated before any significant lanthanide-centered deactivation occurs. As a consequence, the experimental deactivation rate k_{obs}^R mirrors the one found in absence of intermetallic communication, k^R. Introducing $k_{obs}^M \gg k^R$ into Eq. (157) produces Eq. (158), whereby the time dependence of the luminescence decay corresponds to an apparent rate constant $k_{app}^R = k^R$:

$$[R^*] = [M_0^*] \frac{k_{ET}^{M,R}}{k_{ET}^{M,R} + k^M} e^{-k^R t} \tag{158}$$

This situation is met for several d–f pairs, because the intrinsic deactivation rates of the d-block donors k^M are often considerably larger than the deactivation of the NIR-emitting R-centered excited states. This is for instance true for the Ru → Yb transfer in $[YbRu(\mathbf{L36})_3]^{5+}$ (Figure 123, top). As expected, the experimental decay rate of the donor $k_{obs}^{Ru} = 1.2 \cdot 10^5\,s^{-1}$ is larger than $k^{Ru} = 1.0 \cdot 10^5\,s^{-1}$ (measured for $[RuGd(\mathbf{L36})_3]^{5+}$), which is diagnostic for the existence of the Ru → Yb energy transfer. Since $k_{obs}^{Ru} = 1.2 \cdot 10^5\,s^{-1} > k^{Yb} = 5 \cdot 10^4\,s^{-1}$ (measured for $[ZnYb(\mathbf{L36})_3]^{5+}$), Eq. (158) predicts that the apparent (experimental) Yb-centered decay rate recorded for $[RuYb(\mathbf{L36})_3]^{5+}$ should roughly mirror k^{Yb}, which is the case, within experimental errors: $k_{app}^{Yb} = 4.4 \cdot 10^4\,s^{-1}$.

The second limiting case arises when $k_{obs}^M \ll k^{Ln}$, that is, when the R-centered excited state relaxes almost instantaneously upon being

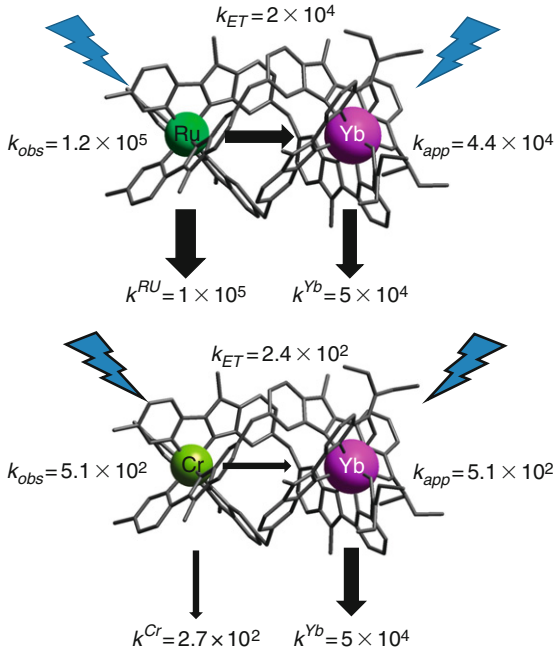

FIGURE 123 Schematic representation of the energy migration processes taking place in $[YbM(\mathbf{L36})_3]^{m+}$ helicates ($M = Ru^{II}$, Cr^{III}). Rate constants are given in s^{-1} (redrawn from Bünzli and Piguet, 2005).

populated by the slow-decaying d-block chromophore. Therefore, the deexcitation of the d-block ion ($k^{M}_{obs} = k^{M} + k^{M,R}_{ET}$) controls the overall deactivation process, and the apparent *R*-centered deactivation rate k^{R}_{app} should be equal to k^{M}_{obs}. Introduction of the condition $k^{M}_{obs} \ll k^{R}$ into Eq. (157), provides a simplified equation (159), showing that the time dependence of the *R** luminescence decay indeed corresponds to $k^{R}_{app} = k^{M}_{obs}$:

$$[R^*] = [M^*_0]\frac{k^{M,R}_{ET}}{k^R}\exp\left\{-\left(k^{M,R}_{ET} + k^{M}\right)t\right\} = [M^*_0]\frac{k^{M,R}_{ET}}{k^R}e^{-k^{M}_{obs}t} \qquad (159)$$

This situation is illustrated when Ru^{II} is replaced with Cr^{III} as the donor in $[CrYb(\mathbf{L36})_3]^{6+}$. Indeed, the combination of the intrinsic deactivation rate of the Cr-centered donor levels $k^{Cr} = 2.7 \cdot 10^2\,s^{-1}$ (measured for $[CrGd(\mathbf{L36})_3]^{6+}$), with the rate of energy transfer $k^{Cr,Yb}_{ET} = 2.4 \cdot 10^2\,s^{-1}$ gives $k^{Cr}_{obs} = k^{Cr} + k^{Cr,Yb}_{ET} = 5.1 \cdot 10^2\,s^{-1}$. The latter value is small compared to the inherent rate of deactivation of $Yb(^2F_{5/2})$, $k^{Yb} = 5 \cdot 10^4\,s^{-1}$ (measured for

$[ZnYb(\mathbf{L36})_3]^{5+}$), so that $k^{Yb} \gg k^{M}_{obs}$ (Figure 123, bottom). As predicted by Eq. (159), the experimental decay of the Yb-centered emission amounts to $k^{Yb}_{app} = 5.1 \cdot 10^2\ s^{-1}$, which exactly matches the slow deactivation rate of the Cr^{III} chromophore k^{Cr}_{obs}. These rate constants can be transformed into characteristic excited lifetimes, thus leading to $\tau^{Yb}_{app} = (k^{Yb}_{app})^{-1} = 23\ \mu s$, when Yb^{III} is sensitized by Ru^{II} in $[RuYb(\mathbf{L36})_3]^{5+}$, and $\tau^{Yb}_{app} = (k^{Yb}_{app})^{-1} = 1960\ \mu s = 1.96$ ms, when Yb^{III} is sensitized by Cr^{III} in the isostructural complex $[CrYb(\mathbf{L36})_3]^{6+}$. Such apparent lengthening of the lanthanide-centered NIR luminescence by two orders of magnitude demonstrates the tuning capacity of the binuclear supramolecular edifices and may be valuable for improving the sensitivity of time-gated bioanalyses, provided that a judicious choice of the donor chromophore is made. The relevant parameters for $R = Nd$, Er, Yb and $M = Ru$, Cr are listed in Table 29 for two temperatures, 10 and 295 K. At low temperature, at which phonon-assisted transfer would be minimized, Cr^{III} is a better donor than Ru^{II} and the efficiency of the process decreases in the order $Nd > Er > Yb$. The latter order is understandable in that the overlap integral between the emission spectrum of the donor and the absorption spectrum of the acceptor is largest for Nd owing to more lanthanide-centered excited states in the 13–15,000 cm^{-1} range as compared to Er and Yb. As a consequence, the largest critical distance for 50% transfer occurs for **NdCr**. It is also noteworthy that the apparent rate constants for the R ions are smaller by one to two orders of magnitude compared to the situation in which the lanthanide ion is not populated by the energy transfer (Torelli et al., 2005).

7.6 Enantiomerically pure lanthanide-containing helicates

The rationale for producing enantiomerically pure lanthanide-containing complexes lies in their potentiality for probing biological molecules or for sensing chiral substances (Shinoda et al., 2005). For instance, optically active lanthanide chelates with tetrapodal ligands intercalate selectively into DNA strands (Bobba et al., 2002) and their utility for live cell imaging has been proved (Poole et al., 2005). But the bioprobes need not to be optically pure in that the interaction of racemic mixtures with chiral substrates may stabilize one diastereomer, thus producing a diastereomeric excess which can be detected by circular dichroism (CD) or circularly polarized luminescence (CPL); this is for instance true for triple-helical $[Pr(2,2'\text{-dioxydiacetate})_3]^{3-}$ which interacts with L-proline in its ground state to generate a significant residual CD spectrum (Parac-Vogt et al., 2002).

When chirality is detected by CD, which probes the ground state chirality, either the coordinated chromophore absorption or the intraconfigurational f–f transitions are measured. The extent of the effect is

TABLE 29 Experimental deactivation rates (see text for definitions), calculated energy transfer efficiencies, Eq. (153), and critical distances for 50% transfer ($R_0^{M,R}$) in microcrystalline samples of $[RM(\mathbf{L36})_3]^{m+}$ helicates ($M = Cr^{III}$, Ru^{II}) (data from Torelli et al., 2005)

RM	*T* (K)	k_{obs}^{M} (s^{-1})	k^{M} (s^{-1})[a]	k_{app}^{R} (s^{-1})	k^{R} (s^{-1})[b]	$k_{ET}^{M,R}$ (s^{-1})	$\eta_{ET}^{M,R}$ (%)	$R_0^{M,R}$ (Å)
NdCr	10	2.13×10^3	2.73×10^2	2.13×10^3	6.84×10^5	1.86×10^3	87	12.8
YbCr	10	5.10×10^2	2.73×10^2	5.10×10^2	5.00×10^4	2.37×10^2	46	9.1
NdRu	10	1.55×10^5	1.04×10^5	1.65×10^5	6.84×10^5	5.10×10^4	33	8.1
ErRu	10	1.44×10^5	1.04×10^5	1.44×10^5	NA	4.00×10^4	28	7.7
YbRu	10	1.27×10^5	1.04×10^5	4.4×10^4	5.00×10^4	2.30×10^4	18	7.1
NdCr	295	8.33×10^3	3.45×10^3	8.33×10^3	6.25×10^5	4.88×10^3	59	12.8
YbCr	295	4.17×10^3	3.45×10^3	4.17×10^2	4.35×10^4	7.20×10^2	17	9.1
NdRu	295	3.45×10^6	1.16×10^6	6.94×10^5	NA	2.99×10^6	66	8.1
ErRu	295	1.85×10^6	1.16×10^6	1.85×10^6	NA	6.90×10^5	37	7.7
YbRu	295	1.68×10^6	1.16×10^6	5.71×10^4	NA	5.20×10^5	31	7.1

[a] Measured on GdM samples.
[b] Measured on *R*Zn samples.

characterized by the absorption dissymmetry factor defined from the difference in absorption between left (L) and right (R) circularly polarized light (Riehl and Muller, 2005):

$$g_{\text{abs}} = \frac{2\Delta\varepsilon}{\varepsilon} = \frac{2(\varepsilon_{\text{L}} - \varepsilon_{\text{R}})}{\varepsilon_{\text{L}} + \varepsilon_{\text{R}}} \tag{160}$$

CPL is the emissive pendent of CD and therefore probes the excited state chirality; it also reflects the molecular motions taking place between absorption and emission. In this case, the parameter of interest is the luminescence dissymmetry factor:

$$g_{\text{lum}} = \frac{2\Delta I}{I} = \frac{2(I_{\text{L}} - I_{\text{R}})}{I_{\text{L}} + I_{\text{R}}} \tag{161}$$

Theoretically, g_{lum} can be related to the electric and magnetic dipole transition moments μ^{gn} and m^{gn} (g denotes the ground state and n the excited state):

$$g_{\text{lum}}(\lambda) = 4\frac{f_{\text{CPL}}(\lambda)}{f_{\text{TL}}(\lambda)}\frac{\mu^{\text{gn}} m^{\text{gn}}}{(\mu^{\text{gn}})^2} \tag{162}$$

where $f_{\text{CPL}}(\lambda)$ and $f_{\text{TL}}(\lambda)$ are the line shapes for CPL and total luminescence (TL) signals. Since μ^{gn} is much larger than m^{gn}, CPL usually focuses on Laporte's allowed magnetic dipole transitions. For lanthanides, the best suited transitions are Sm($^4G_{5/2} \rightarrow {}^6H_J$, $J = 7/2$, $5/2$), Eu ($^5D_0 \rightarrow {}^7F_1$), Tb($^5D_4 \rightarrow {}^7F_J$, $J = 3$–5), Gd($^8S_{7/2} \rightarrow {}^6P_{7/2}$), Dy($^4F_{9/2} \rightarrow {}^6H_{11/2}$), and Yb($^2F_{5/2} \rightarrow {}^2F_{7/2}$). One advantage of lanthanide complexes over organic chiral probes is their often large luminescence dissymmetry factors, which can reach ± 0.5 (up to -0.78 for one of the common standards, tris(3-trifluoroacetyl-d-camphorato)europium) compared to $\pm 10^{-3}$ to $\pm 10^{-2}$ for organic molecules, including helicenes. CPL is not yet a very popular instrumental technique because of the weakness of the signals measured but substantial improvements are being made, particularly with respect to the excitation wavelength used for Eu^{III}, and instrumentation can be expanded to use TRD so that CPL may develop as a essential tool for the enantiomeric recognition of biological substrates (Do et al., 2008).

7.6.1 Mononuclear precursors

There are numerous examples of lanthanide chiral complexes, including many pseudo-C_3 compounds with tridentate receptors such as terpyridines (Muller et al., 2002a) or pseudo-C_4 chelates with tetrapodal hosts (Parker, 2004) but here we only briefly discuss the precursors of the binuclear helicates described in this chapter, namely derivatives of bis(benzimidazole)pyridine and of dipicolinic acid. A contribution to the understanding of the helical wrapping of the ligands around the

lanthanide ion on the chiroptical properties was gained by studying the 1:*n* complexes of Eu^{III} with ligand **L17**^{k} (Section 2.1, Figure 19): the measured weak CPL effect (attesting of the presence of a small diastereomeric excess in acetonitrile solution) of the 1:1 complex essentially arises from the influence of the remote asymmetric centers while for the 1:2 and 1:3 complexes, the structural contribution of the ligand wrapping intervenes as well, as confirmed by specific rotary dispersion measurements (Muller et al., 2003). Similar conclusions were reached for $[Eu(L)_3]^{3+}$, L = **L18**^{b} and **L18**^{c} (Section 2.1, Figure 21; Muller et al., 2001b, 2002b). In fact, isolation of pure enantiomers is difficult because of the usually large lability of the lanthanide ions.

7.6.2 Resolution of the PP and MM isomer of $[EuCr(\mathbf{L36})_3]^{6+}$

The synthesis of pure chiral nd–4f helicates requires the availability of facial noncovalent tripodal receptors $[M\mathbf{L}_3]^{n+}$ which feature an inert transition metal ion to avoid scrambling in solution. Within the range of investigated nd–4f compounds, both Co^{III} and Cr^{III} qualify, but the difficult oxidation of the former leaves traces of Co^{II} in solution which catalyzes the *fac*-$[Co(\mathbf{L36})_3]^{3+} \rightleftarrows$ *mer*-$[Co(\mathbf{L36})_3]^{3+}$ isomerization, so that Cr^{III} has been preferred (Figure 124). The inert receptors are obtained from the racemic 3d–4f helicate $[LaCr(\mathbf{L36})_3]^{6+}$ by removing the *R* ion with EDTA, followed by sorption onto a Sephadex® ion-exchange resin and elution with $Na_2Sb_2[(+)\text{-}C_4O_6H_2)]_2$. A careful examination of the Cotton effect experienced by the two separated isomers and comparison with M-(+)-$[CrL_3]^{3+}$ (L = phen, bipy) confirms the assignment of *P*-(+)-$[Cr(\mathbf{L36})_3]^{3+}$ and *M*-(-)-$[Cr(\mathbf{L36})_3]^{3+}$. Subsequent complexation with Eu^{III} affords the final chiral helicates *P*,*P*-(+)-$[EuCr(\mathbf{L36})_3]^{6+}$ and *M*,*M*-(-)-$[EuCr(\mathbf{L36})_3]^{6+}$.[3] The chiral isomers display mirror CD and CPL spectra, the latter for both the Eu ($^5D_0 \rightarrow {}^7F_J$, $J = 1$–4) and Cr($^2E \rightarrow {}^4A_2$) transitions and the crystal structure of the *M*,*M* isomer could be solved (Cantuel et al., 2004). Relevant chiroptical data are reported in Table 30.

Addition of R^{III} to the inert and chiral chromium podate *M*-$[Cr(\mathbf{L36})_3]^{3+}$ to self-assemble the *M*,*M*-$[RCr(\mathbf{L36})_3]^{6+}$ helicates (*R* = Eu, Gd, Tb) results in an inversion in the CD signal (Figure 125). The modeling of this effect by ZINDO calculations takes into account the exciton coupling model with three types of interaction, intranuclear between the ligand strands around each metal ions, and internuclear between ligand strands bound to different metal ions (Telfer et al., 2004). C_3-symmetry was assumed for the rigid CrN_6 chromophore in *M*,*M*-$[RCr(\mathbf{L36})_3]^{6+}$ and the results of the calculations show that a pair of oppositely signed rotational strengths appear in the range of the $^*\pi \leftarrow \pi$ transitions centered around 330–340 nm, with the positive rotational strength being of lower energy.

3 An alternate labeling for *M*,*M* is Λ,Λ while Δ,Δ is also used for *P*,*P*.

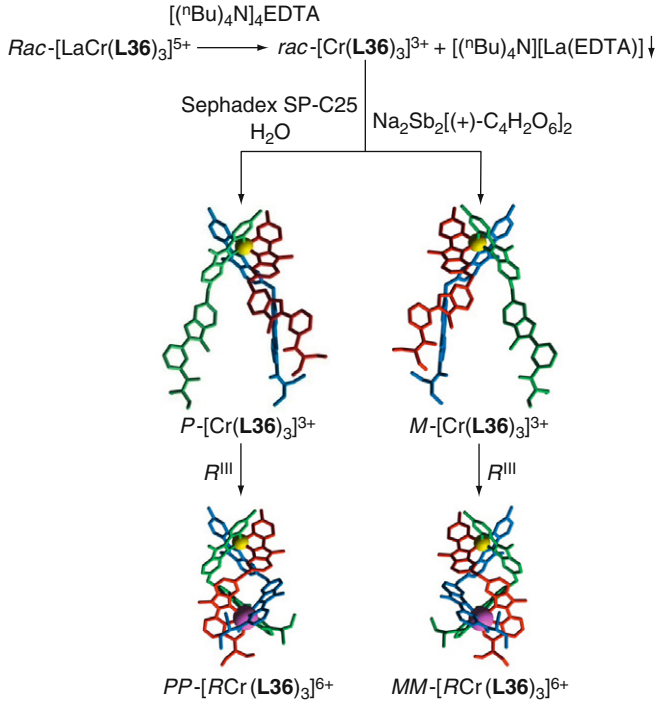

FIGURE 124 Chiral resolution of the tripodal receptor *rac*-[Cr(**L36**)$_3$]$^{3+}$ and formation of the pure chiral helicates *PP*-[*R*Cr(**L36**)$_3$]$^{6+}$ and *MM*-[*R*Cr(**L36**)$_3$]$^{6+}$ (redrawn after Telfer et al., 2004).

The RN_6O_3 center being more fluxional than CrN_6, prediction of the Cotton effect depends on the relative orientation of the chromophores; in particular, the CD signal inverses when the angle between two chromophores increases. This change in sign occurs without formal change in helicity! Taking a reasonable geometry into consideration though, the calculations predict that the ligands strands around the R^{III} ion give rise to CD signals of opposite phase compared to Cr^{III} despite the same absolute conformation they adopt.

The relative intensities of the CD spectra of the [*R*Cr(**L36**)$_3$]$^{6+}$ helicates are inversely proportional to the size of the R^{III} ion (Tb > Gd > Eu), supporting the assertion that chromophoric cavity around R^{III} produces a large negative exciton couplet, the coupling being strengthened when the ligand strands are tighter bound to the smaller R^{III} ions. A third contribution to the CD signal is the internuclear coupling giving rise to three excitons of moderate strength contributing to a negative signal at lower energy (i.e., in phase with the intranuclear *R* contribution). The relative contributions of these signals are depicted on Figure 125 (bottom). The computational model used excludes the metal ions, so that the

TABLE 30 Relevant chiroptical data for $[EuCr^{III}(\mathbf{L36})_3]^{6+}$ 1 mM in acetonitrile at 295 K (data from Cantuel et al., 2004)

Isomer	$\alpha^{20}(589)$ (deg mol^{-1} dm^2)	$\lvert\Delta\varepsilon^{340}_{max}\rvert$ ($M^{-1}cm^{-1}$)	g_{lum}(Cr) $^2E \rightarrow {}^4A_2$	g_{lum}(Eu) $^5D_0 \rightarrow {}^7F_1$	g_{lum}(Eu) $^5D_0 \rightarrow {}^7F_2$	g_{lum}(Eu) $^5D_0 \rightarrow {}^7F_3$[a]	g_{lum}(Eu) $^5D_0 \rightarrow {}^7F_4$[a]
M,M	−1239	74	+0.01	−0.154	+0.07	-9.2×10^{-4}	+0.033
P,P	+1146		−0.01	+0.163	−0.07	$+8.9 \times 10^{-4}$	−0.034

[a] From Gawryszewska et al. (2006).

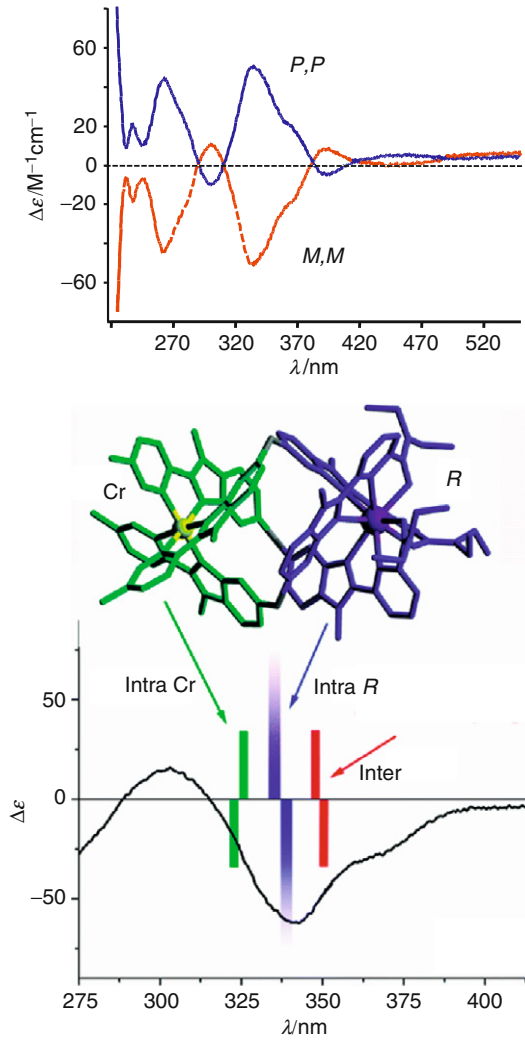

FIGURE 125 Top: CD spectra of *P,P*-[EuCr(**L36**)$_3$]$^{6+}$ and *M,M*-[EuCr(**L36**)$_3$]$^{6+}$ 1 mM in acetonitrile at 295 K (redrawn from Cantuel et al., 2004). Bottom: simulation of the 340-nm band with the exciton theory (redrawn from Telfer et al., 2004).

contribution of the MLCT state around 385 nm cannot be evaluated). The CPL spectra of *M,M*-[EuCr(**L36**)$_3$]$^{6+}$ and *P,P*-[EuCr(**L36**)$_3$]$^{6+}$ (Figure 126) have opposite values of g_{lum} for all four investigated transitions ($^5D_0 \rightarrow {}^7F_J$, $J = 1$–4); however, the signs are alternating, for example, for the *M,M* isomer, negative for $J = 1$ and 3 and positive for the other two

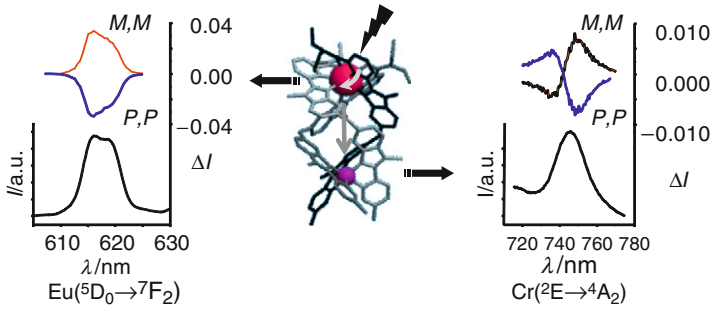

FIGURE 126 Parts of the CPL spectra of *P,P*-[EuCr(**L36**)$_3$]$^{6+}$ and *M,M*-[EuCr(**L36**)$_3$]$^{6+}$ 1 mM in acetonitrile at 295 K (redrawn from Cantuel et al., 2004).

transitions. A correlation between these signs and the structure of the helicate could not be established yet, probably because of a too large deviation from the idealized D_3-symmetry used for theoretical predictions (Gawryszewska et al., 2006).

7.7 Extension to polynuclear helicates: Pseudolanthanide cryptates

Associating Cr^{III} with R^{III} ions in binuclear triple-helical complexes leads to intramolecular energy transfers along the C_3-axis of the edifice, the directionality and yield of which depend on the nature of the R^{III} ion, $R \rightarrow Cr$ for Eu and Tb and $Cr \rightarrow R$ for the NIR-emitting Nd, Er, and Yb ions. In the latter case, the combination of the long-lived $Cr(^2E)$ level ($k_{em} \approx 300–3000\ s^{-1}$ depending on the temperature) with a comparable energy transfer rate ($k_{ET}^{Cr,R} \approx 200–5000\ s^{-1}$, depending on the temperature) results in the R^{III} ion being preferentially populated by the 3d-metal ion and having an apparent lifetime mirroring that of the $Cr(^2E)$ level. This apparent lengthening of the lifetime of the NIR emitting state is helpful for TRD analyses but does not improve the intrinsic quantum yield of the lanthanide ion. To boost the sensitivity of the overall sensitization process, without affecting the energy migration regime, several Cr^{III} chromophores would have to be connected to the lanthanide moiety. Expanding the binuclear helicate into a trinuclear molecule is an obvious first step in this direction and the tris(tridentate) ligand **L27** (Section 3.1, Figure 42) has been modified to the bidentate-tridentate-bidentate host **L42** (Section 7.2, Figure 110) thanks to a well established synthetic route (Section 7.2, Figure 112). An initial study has dealt with the resulting Eu and Tb trinuclear helicates [M*R*M(**L42**)$_3$]$^{m+}$ with both Zn^{II} and Cr^{III} (Cantuel et al., 2006). Although no stability constants could be determined, a fruitful combination of NMR, ES-MS and UV-vis spectroscopies

demonstrates that under strict stoichiometric conditions (2:1:3, M:*R*:L) and for a millimolar total ligand concentration, the target trinuclear helicate $[ZnRZn(\mathbf{L42})_3]^{7+}$ (R = La, Eu, Lu) is the major species in acetonitrile solution. Similarly to their binuclear counterparts, the helicates with Cr^{II} undergo an easy and rapid oxidation to $[Cr^{III}RCr^{III}(\mathbf{L42})_3]^{9+}$. Suitable crystals for X-ray structural determination could not be obtained, but high-resolution luminescence spectroscopy of $[ZnEuZn(\mathbf{L42})_3]^{7+}$ and $[CrEuCr(\mathbf{L42})_3]^{9+}$ is compatible with Eu^{III} located in a site with pseudo-D_3-symmetry (Figure 127, top). In particular both the energy of the $^5D_0 \rightarrow {}^7F_0$ transition and the splitting of the $^7F_1$ level matches very well those reported for $[EuZn(\mathbf{L35})_3]^{5+}$ (Table 24). In addition, analysis of the LIR for Zn*R*Zn complexes in acetonitrile (R = La, Eu, Tb, Lu, Y) shows that

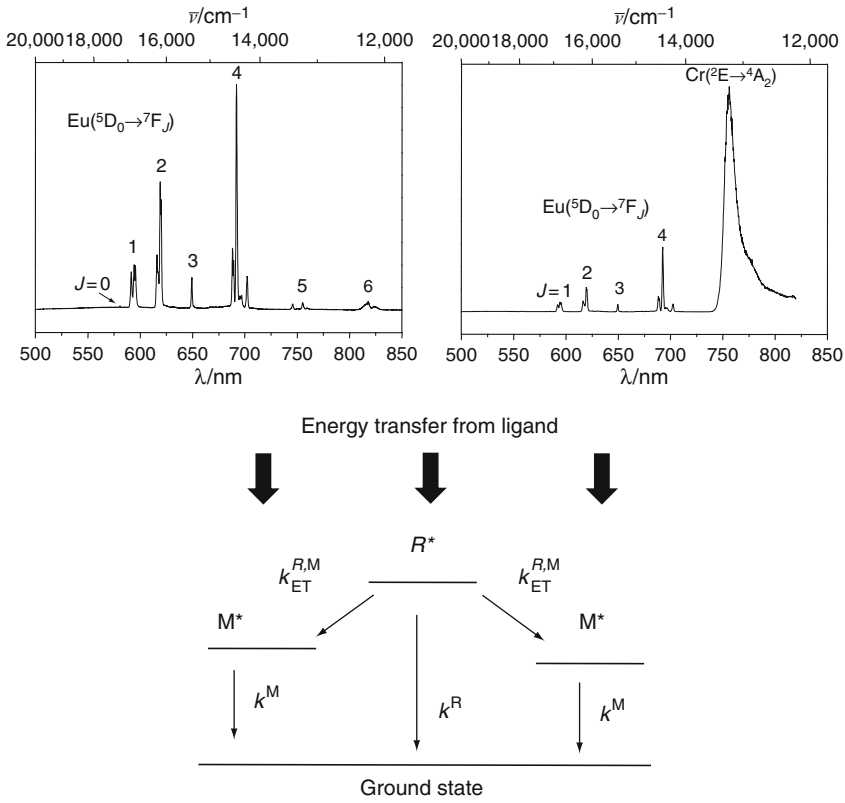

FIGURE 127 Top: luminescence spectra of $[MEuM(\mathbf{L42})_3]^{n+}$ (M = Zn^{II}, left; Cr^{III}, right). Bottom: rate constants used to model the divergent energy transfer in the CrEuCr edifice (redrawn from Cantuel et al., 2006).

the $[EuCr(\mathbf{L36})_3]^{5+}$ helicate is a reliable structural model for the solution structure of the trinuclear edifices.

The intramolecular communication along the C_3-axis generates two ''divergent'' $R \rightarrow Cr$ energy transfer processes, as exemplified by the dramatic decrease in the $Eu(^5D_0)$ lifetime (Table 31) which can be analyzed as follows, given the symmetry of the molecule and within the frame of the dipole–dipolar mechanism (Figure 127, bottom):

$$\eta_{tot}^{R,Cr} = \frac{2k_{ET}^{R,Cr}}{k^R + 2k_{ET}^{R,Cr}} \tag{163}$$

Assuming further that k^R is identical in the Zn^{II} and Cr^{III} helicates:

$$k_{obs}^{CrRCr} = \frac{1}{\tau_{obs}^{CrRCr}} = k^R + 2k_{ET}^{R,Cr} \tag{164}$$

and therefore:

$$k_{ET}^{R,Cr} = \frac{k_{obs}^{CrRCr} - k_{obs}^{ZnRZn}}{2} = \frac{(\tau_{obs}^{CrRCr})^{-1} - (\tau_{obs}^{ZnRZn})^{-1}}{2} \tag{165}$$

$$\eta_{tot}^{R,Cr} = 1 - \frac{\tau_{obs}^{CrRCr}}{\tau_{obs}^{ZnRZn}} \tag{166}$$

As expected, the efficiency of the $Eu \rightarrow Cr$ transfer increases from its value in the binuclear edifice $[EuZn(\mathbf{L36})_3]^{5+}$ (65% and 78% at 10 and 295 K, respectively) to reach values close to 90%, both in the solid state and in acetonitrile solution, at 10 or 295 K (Table 31), while the $Tb \rightarrow Cr$ transfer remains almost quantitative. The ratio of the rate constants for the total directional transfer, $k_{ET}^{Eu,Cr}(CrEuCr)/k_{ET}^{Eu,Cr}(EuCr)$ is 1.6(2) at 10 K and (surprisingly) 3.9(6) at 295 K. The critical distances for 50% transfer calculated assuming $R_{EuCr} = 9.32$ Å, as in $[EuZn(\mathbf{L36})_3]^{5+}$, are only marginally larger than those found in the binuclear analogue, reflecting a ≈2.5-fold increase in the overlap integral J (see Section 4.4, Eq. (78)).

For the time being, the trinuclear $[MRM(\mathbf{L42})_3]^{m+}$ helicates represent the first examples of supramolecular structures combining inert pseudo-octahedral Cr^{III} building blocks with the wrapping of three such ligand strands forming a cryptand-like, chiral cavity ideally suited for the complexation of lanthanide ions. In addition, these edifices have more flexibility than cryptands in that the cavity may be finely tuned to accommodate lanthanides ions with minute differences in size, a case study example of the induced fit principle at work! To our knowledge, the only other examples of binuclear 3d-transition metalloreceptors for R ions are {2}-metallacryptands based on 2,6-pyridyl-bis(β-diketones) which form

TABLE 31 Lifetimes, and energy transfer parameters in microcrystalline samples of $[MEuM(\mathbf{L42})_3]^{m+}$ ($M = Zn^{II}$, Cr^{III}), or their solution 1 mM in acetonitrile, under ligand excitation

Sample		T (K)	$\tau(^2E)$ (ms)	$\tau(^5D_J)$ (ms)	$k_{ET}^{Eu,Cr}$ (ms^{-1})	$\eta^{R,Cr}$ (%)	$R_0^{Eu,Cr}$ (Å)
CrGdCr	s	10	2.27(1)				
	s	295	0.031(1)				
ZnEuZn	s	10		1.96(1)			
	s	295		0.69(1)			
CrEuCr	s	10	2.08(2)	0.20(1)	2.2(1)	90(4)	11.9(2)
	s	295	0.033(1)	0.10(1)	4.3(4)	86(8)	11.2(4)
ZnTbZn	s	10		1.67(6)			
CrTbCr	s	10	1.8(2)	$1.75(4) \times 10^{-3}$	2.9×10^5	99.9	
ZnEuZn	MeCN	10		2.21(5)			
	MeCN	295		1.48(1)			
CrEuCr	MeCN	10	3.1(1)	0.24(1)	1.9(1)	89(6)	11.8(2)
	MeCN	295	0.012(1)	0.076(1)	6.2(5)	95(8)	13.5(3)

helical Fe_2L_3 host molecules able to incorporate K^I, Sr^{II}, or La^{III} (Saalfrank et al., 1998). Additionally, the group of K. Raymond has self-assembled GdFeGd macromolecular MRI contrast agents from the bis(bidentate) ligands 2,3-dihydroxyterephthalamide (TAM) and 1-methyl-2,3-dihydroxypyridone (HOPO), in which the Fe^{III} partner lies in the center of the cryptand-like cavity (Pierre et al., 2006). In these molecules, the ligand strands are arranged in a side-by-side fashion and therefore the assemblies cannot be termed helicates since they are achiral.

8. 4f- AND 5f-HELICATES WITH OTHER LIGANDS

8.1 Homo- and heterometallic polynuclear helicates

A combination of two venerable classes of ligands, β-diketonates (Binnemans, 2005) and bis(acylpyrazolonates) (Jensen, 1959), have produced some of the first characterized rare-earth $R_2\mathbf{L}_3$ triple-stranded helicates with the bis(bidentate) ligand $\mathbf{H_2L43^a}$ (Figure 128). The same year Piguet et al. (1992a,b) announced the isolation and structural characterization of $[Eu_2(\mathbf{L11})_3]^{6+}$, an initial report by a Chinese group (Xing et al., 1992) presented the isolation and full characterization of $[R_2(\mathbf{L43^a})_3] \bullet n H_2O$ (R = Y, La–Yb, except Ce, Pm; n = 3–8), including luminescence spectra for R = Pr, Sm, Eu, Tb, Dy, Tm, and Eu-doped Y and Gd. The crystal structure of the samarium helicate $[Sm_2(\mathbf{L43^a})_3(DMF)_4] \bullet DMF$, published 3 years later, reveals eight-coordinate Sm^{III} ions bound each to three bidentate units of each ligand strand and to two DMF molecules (Yang and Yang, 1995; Figure 129A). The coordination polyhedron is a distorted square antiprism, the oxygen atoms of two ligand strands forming one plane while the second plane consists of the two donor atoms of the third ligand strand and of the oxygen atoms of the two solvent molecules; the dihedral angle between these planes is small, ca. 1.5° for Sm1 and 3.3° for Sm2. The two coordination environment are not completely equivalent, distances between the Sm^{III} ions and the square planes being −1.27 and +1.27 Å for Sm1 and −1.22 and +1.32 Å for Sm2; the internuclear distance is 7.98 Å, considerably shorter than in $[Sm_2(\mathbf{L30^e})_3]^{6+}$ (9.18 Å; Jensen et al., 2008; see Section 3.2, Figure 48).

Increasing the bridge by one CH_2 unit ($\mathbf{H_2L43^b}$) does not change much the final products except for the coordination number of the R^{III} ion (Semenov et al., 2008). In $[Tb_2(\mathbf{L43^b})_3(H_2O)_2]$ (Figure 129B) and $[Tb_2(\mathbf{L43^b})_3(DMF)_2]$ for instance, Tb^{III} ions are only seven-coordinate being bound to only one ancillary ligand, with the oxygen atoms from these ligands lying on the pseudo-C_3 internuclear Tb-Tb axes. Both structures are very similar, with a helical pitch of approximately 21 Å that is considerably longer than those reported in Table 21.

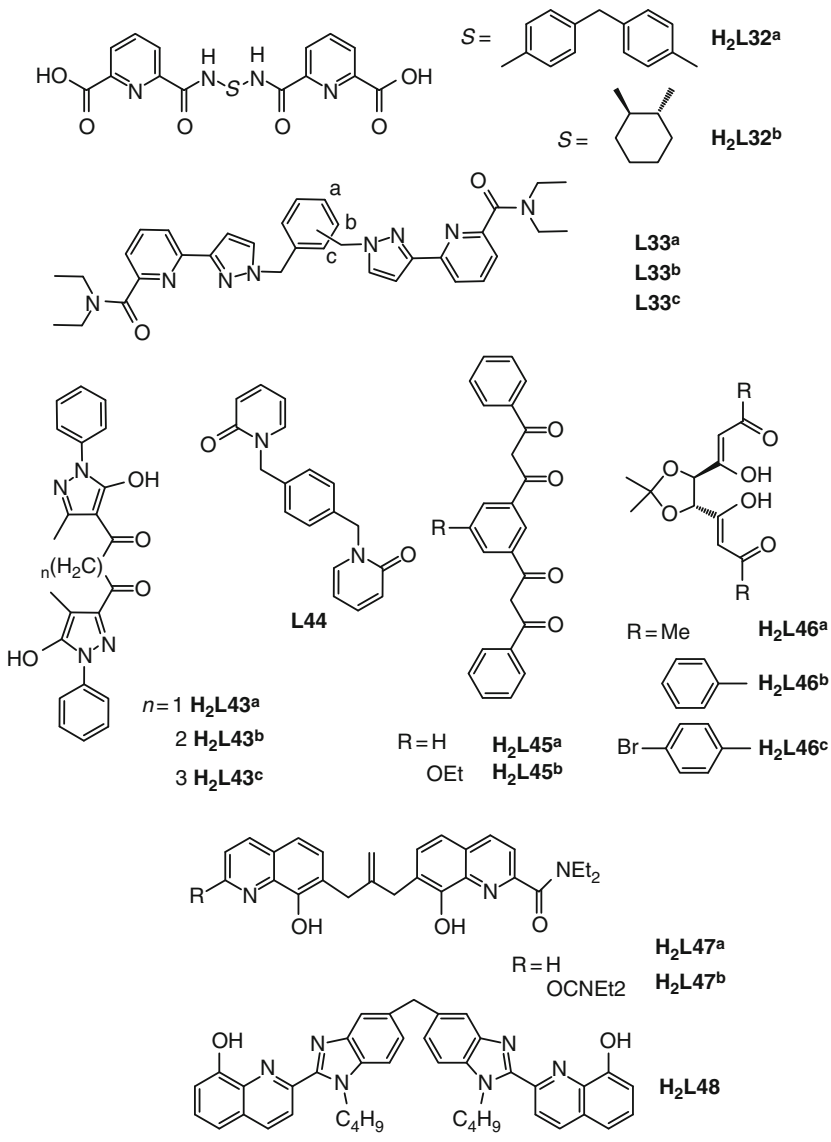

FIGURE 128 Ligands not based on bis(benzimidazole)pyridine for the self-assembly of homometallic binuclear helicates.

Obviously, the bis(monodentate) ligand **L44** cannot fulfill the coordination requirements of the R^{III} ions and the neodymium ion in the triple-stranded $[Nd_2(\mathbf{L44})_3(NO_3)_6]$ helicate (Figure 129C) is held outside the L_3 cavity, which is capped by ''stoppers'' made up of three bidentate nitrate

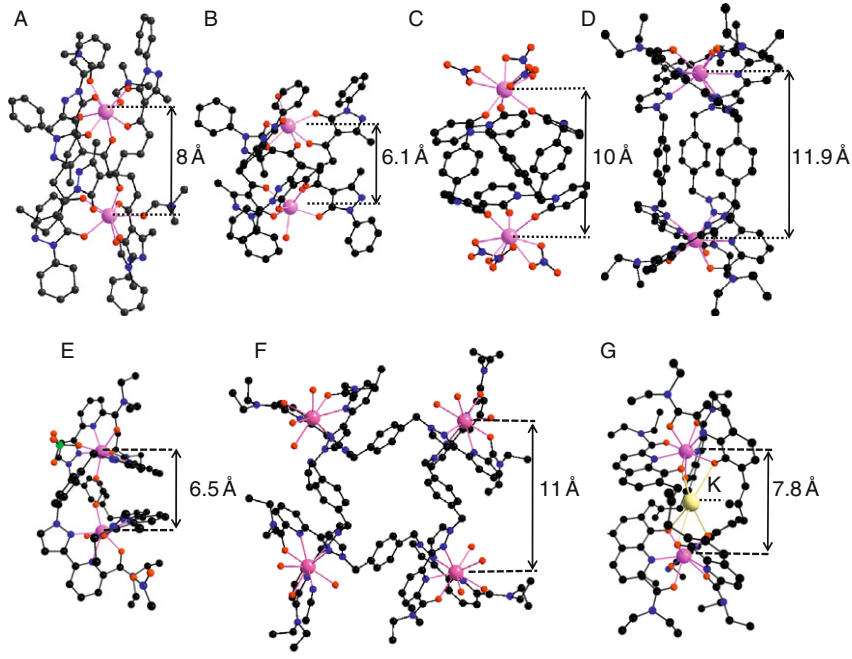

FIGURE 129 Molecular structures of (A) $[Sm_2(\mathbf{L43^a})_3(DMF)_4]\bullet DMF$ (redrawn from Yang and Yang, 1995), (B) $[Tb_2(\mathbf{L43^b})_3(H_2O)_2]$ (redrawn from Semenov et al., 2008), (C) $[Nd_2(\mathbf{L44})_3(NO_3)_6]\bullet 1.5MeCN$ (redrawn from Goodgame et al., 1993), (D) $[Nd_2(\mathbf{L33^a})_3]^{6+}$, (E) $[Yb_2(ClO_4)(\mu\text{-}HCO_2)(\mathbf{L33^b})_2]^{4+}$, (F) $[Nd_4(\mathbf{L33^a})_4(H_2O)_{11}(MeCN)]^{12+}$ (redrawn from Ronson et al., 2007), and (G) $[KYb_2(\mathbf{L47^a})_3]^{+}$ (redrawn from Albrecht et al., 2007a).

ions each. The resulting electrostatic attraction pulls the Nd^{III} ions far apart, the internuclear distance being 9.95 Å. The helix is substantially elongated in that it makes only one third of a turn between the two metal ions (Goodgame et al., 1993), that is, its pitch is on the order of 30 Å. Similarly to the parent diketones, the bis(bidentate) ligands $\mathbf{H_2L45^a}$ and $\mathbf{H_2L45^b}$ produce hexacoordinate environments upon wrapping in a helical fashion around two rare-earth ions ($R = Y$, Nd, Sm, Eu, Gd) which are easily completed with two water or methanol molecules (Basset et al., 2004). In organic solvents, ^1H NMR confirms the presence of three equivalent ligand strands with local C_2 symmetry and addition of Pirkle's reagent, {(*S*)-(+)-2,2,2-trifluoro-1-(9-anthryl)ethanol}, leads to the splitting of several resonances, indicating the presence of a racemic mixture of triple-stranded helices in solution. The bis(diketonate) ditopic ligand $(\mathbf{L45^a})^{2-}$ has singlet and triplet states with 0-phonon transitions at about 25,000 and 20,400 cm^{-1}, well suited for the sensitization of the Sm^{III}, Eu^{III}, and Nd^{III} ions. The quantum yield for $[Eu_2(\mathbf{L45^a})_3]$ in DMF amounts to 5%

and the $^5D_0$ lifetime is temperature dependent, increasing from 0.22 ms at room temperature to 0.46 ms at 77 K, pinpointing the probable presence of a thermally activated quenching by a relatively low-lying LMCT state, since the $\Delta E(^3\pi\pi^*-^5D_0)$ gap is too large ($\approx$3000 cm^{-1}) for substantial back transfer to occur. In methanol, use of the phenomenological equation (Beeby et al., 1999):

$$q_{MeOH} = 2.2[(k_{MeOH} - k_{MeOD}) - 0.125] \quad (167)$$

yields $q_{MeOH} = 3.7$, close to the expected value of 4 if the two Eu^{III} ions are octacoordinate. The quantum yields for the Sm^{III} helicate in DMF is smaller, 0.16%, with $\tau(^4G_{5/2}) = 13$ μs; the $Nd(^4F_{3/2})$ lifetime of $[Nd_2(\mathbf{L45^a})_3]$ in DMF is 1.5 μs, leading to a reasonable intrinsic quantum yield of 0.6%. A tetra-stranded helicate, $[Eu_2(\mathbf{L45^a})_4]^{2-}$ forms in presence of an excess ligand, as ascertained by ES-MS and NMR data, and it is more luminescent than the corresponding triple-stranded edifice. Introducing a chiral (*R*,*R*)-tartaric acid in the framework of bis(diketones) leads to ligands $\mathbf{H_2L46^{a-c}}$ which self-assemble under stoichiometric conditions with lanthanide chlorides in methanol and in presence of potassium carbonate into binuclear triple-stranded and neutral helicates: $[R_2(\mathbf{L46^a})_3] \cdot nH_2O$, $[R_2(\mathbf{L46^b})_3] \cdot nH_2O$ (R = La–Yb, except Pm), and $[R_2(\mathbf{L46^c})_3] \cdot nH_2O$ (R = La–Yb, except Pm and Gd), n = 2–5 (Albrecht et al., 2007b). The complexes are characterized by ES-MS in solution, as well as by their CD spectra. The ligands sensitize the luminescence of Eu^{III} and Tb^{III}, but no quantitative data are reported (lifetimes, quantum yields), except for $[Eu_2(\mathbf{L46^c})_3]$ for which $\tau(^5D_0)$ is equal to 0.1 and 0.5 ms in the solid state and in DMF solution, respectively, with an estimated quantum yield of 10% in solution. In addition, a tetra-stranded helicate can be obtained by reacting $\mathbf{H_2L46^c}$, $EuCl_3 \cdot 6H_2O$, and piperidine in a 4:2:2 ratio in chloroform-methanol, $(H\text{-}pip)_2[Eu_2(\mathbf{L46^c})_4]$. The latter has a longer $^5D_0$ lifetime (0.25 ms) than the corresponding triple-stranded complex but it dissociates into the triple-stranded helicate in DMF solution.

No crystal structure of the triple-stranded helicates with ligands $\mathbf{H_2L32^a}$ and $\mathbf{H_2L32^b}$ featuring two dipicolinic acid tridentate coordinating units is available either, but molecular mechanics calculations slightly favor R_2L_3 helicate formation with Δ,Δ or Λ,Λ configurations at the metal centers over ''side-by-side'' (meso)helicates in which the metal ions lie in sites with Δ,Λ configuration. The calculated stabilization energy of the ''true'' helicates over the meso species is –25 and –209 kJ mol^{-1} for $\mathbf{H_2L32^a}$ (Δ,Δ configuration) and $\mathbf{H_2L32^b}$, respectively (Lessmann and Horrocks, 2000). Internuclear Eu–Eu distances of 13.9 ($\mathbf{H_2L32^a}$) and 8.0 Å ($\mathbf{H_2L32^b}$) are estimated from these calculations. Titrations of

europium triflate with $\mathbf{H_2L32^a}$ and *R,R*-$\mathbf{H_2L32^b}$ in water and followed by high-resolution luminescence excitation spectroscopy of the $^5D_0 \leftarrow {}^7F_0$ transition clearly point to the formation of a preponderant 2:3 species under 2:3 *R*:**L** stoichiometric conditions: the hydration number *q* is strictly zero and the lifetimes of the main species amount to 1.48 and 1.56 ms for the complexes with $\mathbf{H_2L32^a}$ and *R,R*-$\mathbf{H_2L32^b}$, respectively, a value typical of a tris(dipicolinate) environment for the metal ion. The internuclear distances determined from Eu → Nd energy transfer experiments with the help of Eqs. (77) and (78) (Section 4.4) reproduce satisfyingly the theoretical calculations: 13.7(8), and 7.4(8) Å, for the helicates with $\mathbf{H_2L32^a}$ and *R,R*-$\mathbf{H_2L32^b}$, respectively. Finally, the conditional stability constant estimated for $[Eu_2(\mathbf{L32^a})_3]$ is large and comparable to those of the dicarboxylic helicates $[R_2(\mathbf{L13})_3]$ (Table 8).

The bis(tridentate) ligands $\mathbf{L33^{a-c}}$ are tailored for nonacoordination of R^{III} ions if three strands wrap around two metallic centers (Ronson et al., 2007). In reality, the branching of the second pyrazole–pyridine amide unit on the anchor benzene in *para*, *ortho*, or *meta* position plays a crucial role in the final structures of the polynuclear complexes obtained, few of them being helicates. For instance, $\mathbf{L33^a}$ with its para-substituted anchors lacks the required stereochemistry for inducing helical turns. As a consequence, it reacts with $R(ClO_4)_3$ (R = La, Nd) to produce, in acetonitrile and under 2:3 *R*:**L** stoichiometric ratio, achiral binuclear complexes in which the three ligand strands are arranged in a side-by-side configuration building a cylindrical molecule (Figure 129D). Both cylinder ends are topped by a nonadentate coordination pocket encapsulating a R^{III} ion in a chiral environment. However, there is a mirror plane between the two R^{III} ions which have therefore opposite configuration and which lie at a large distance of about 11.9 Å. When the stoichiometric ratio is reduced to 1:1, a rare example of circular helicate[4] self-assembles, with overall chemical formula $[Nd_4(\mathbf{L33^a})_4(H_2O)_{11}(MeCN)]^{12+}$ (Figure 129F). The structure is very close to D_4 symmetry with the four Nd^{III} ions lying approximately in a square with internuclear distances of ≈11 Å and defined by the four helically wrapped ligand strands. This tetranuclear species should in principle be entropically disfavored with respect to the formation of smaller oligomers and a possible explanation for its preferential formation is the occurrence of π–π stacking interactions between almost parallel pyridine-pyrazole units. Under the same synthetic conditions, but in nitromethane, La^{III} gives a nonhelicate binuclear complex with the two ligands in a side-by-side configuration while increasing the *R*:**L** ratio to 5:1 in acetonitrile leads to a one-dimensional coordination polymer with nonhelical chains. Nonhelical mono- and binuclear complexes are mainly

[4] Another recent example of circular helicate is the C_3-symmetrical pyramidal architecture with general formula $[Ln_4(L)_9(\mu_3\text{-}OH)](ClO_4)_2$ obtained from an enantiomerically pure monotopic pinene-bipyridine receptor (Lama et al., 2008).

obtained with the *meta* and *ortho* ligand **L33^{b}** and **L33^{c}** with the exception of the double-stranded binuclear helix $[Yb_2(\mathbf{L33^b})_2(\mu\text{-}HCO_2)(ClO_4)(H_2O)]^{4+}$ in which a bridging formate anion holds the two Yb^{III} metal ions at a short 6.5 Å distance (Figure 129E).

Another popular strongly chelating unit for rare-earth ions which, in addition, sensitizes the luminescence of NIR-emitting lanthanides is 8-hydroxyquinoline (Comby and Bünzli, 2007). The latter has been inserted in the bis(tridentate) and tridentate-bidentate host molecules **H_2L47^{a-b}**. Crystalline bimetallic and trimetallic trinuclear helicates are obtained, $[KYb_2(\mathbf{L47^a})_3]^+$, and $[KAlYb(\mathbf{L47^b})_3]$ which display sizeable luminescence with overall quantum yields of 1.0(1) and 1.2(1)% and lifetimes of the $^2F_{5/2}$ level of 18.9(1) and 22.6(2) μs, respectively (Albrecht et al., 2007a). It is noticeable that the green luminescence from the Al(quinoline)$_3$ moiety is totally quenched in the latter compound to the benefit of energy transfer onto the Yb chromophore. The templating potassium ion plays an unusual role in the structure of $[KYb_2(\mathbf{L47^a})_3]^+$ being connected to four oxygen atoms by standard distances (2.7–2.8 Å) and to others by longer bond lengths (3.4–3.6 Å); one vinylic group of a ligand strand is directed toward the potassium ion is such a way that a weak K. . .C = C η_2-interaction occurs. The K^I ion is encapsulated approximately at the center of the helicate, with K–Yb distances in the range 3.9–4.0 Å while the Yb^{III} ions are separated by 7.8 Å and bound to the three tridentate and syn-arranged amidoquinolate units (Figure 129G). Another interesting feature of these systems is that despite the prominent templating role played by potassium in the solid state structure, its presence does not seem to be required to form the $[R_2(\mathbf{L47^a})_3]$ helicate in solution: $\log(\beta_{2,3}^{R,L47a}) = 26.1(3)$ and 25.7(3) for R = Eu and Yb, respectively, while the 2:2 ($\log(\beta_{2,2}^{R,L47a}) \approx 19$), 1:3 ($\log(\beta_{1,3}^{R,L47a}) \approx 18$), and 1:2 ($\log(\beta_{1,2}^{R,L47a}) \approx 13$–14) species have much lower stability.

Using a similar coordination strategy, ligand **H_2L48** produces the triple-stranded helicates $[R_2(\mathbf{L48})_3] \bullet nH_2O$ (R = La, n = 3; R = Nd, n = 2); their structure in solution is proved by ^{1}H-NMR spectroscopy. The Nd^{III} complex is luminescent, with an overall quantum yield of 0.15% and a single exponential luminescence decay corresponding to a lifetime of 1 μs (Shavaleev et al., 2008). The connectivity in the solid state has also been established by X-ray diffraction (Terazzi et al., 2009).

In addition to the *R*K and *R*Al helicates described above, there are, to our knowledge, only two other examples of helical molecular structures encompassing both a 4f ion and a transition metal ion which could be included into the concept ''helicate.'' The first one features a trinuclear Zn^{II} metallohelicene $[Zn_3(\mathbf{L49})]$ (Figures 130A and 131A) as chiral receptor and was synthesized with the aim of investigating its inversion rate (Akine et al., 2006). The helical host contains a cavity that can easily incorporate a large spherical ion such as R^{III} or Ba^{II} which, in fact, acts

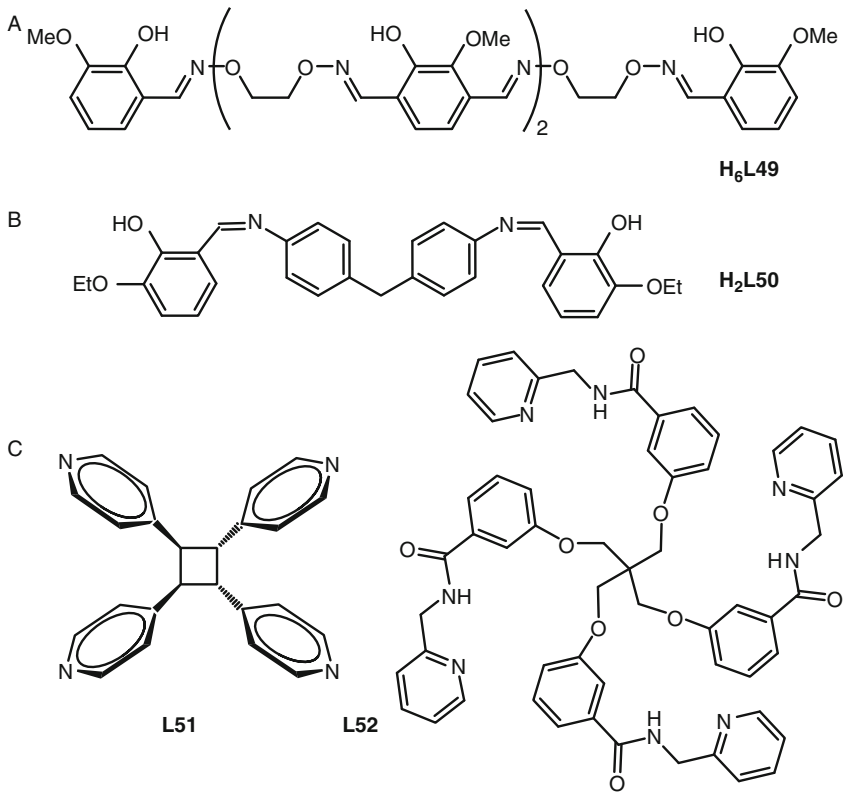

FIGURE 130 (A) Linear hexaoxime ligand $\mathbf{H_6L49}$ for building metallohelicenes, (B) segmental heterotopic ligand $\mathbf{H_2L50}$, (C) polytopic ligands for assembling lanthanide-containing helical metal–organic frameworks.

as templating ions, the reaction of $\mathbf{H_6L49}$ with zinc acetate alone giving rise to a mixture of complexes. The helical wrapping of the receptor around the R^{III} ion is clearly visible in the crystal structure of $[LaZn_3(\mathbf{L49})(OAc)_3(EtOH)]$ (Figure 132A), the metallohelicene accomplishing a 421° turn. The interconversion between the right-handed and left-handed configuration of the tetranuclear complex is slow (Figure 131B), the ^{1}H-NMR resonances of the three pairs of diastereotopic methylene protons remaining distinct even at 353 K, while if La^{III} is replaced by Ba^{II}, coalescence occurs at this temperature. The reason lies in a tighter helix with shorter La–O bonds compared to Ba–O and, possibly in the stronger electrostatic interaction created by the +3-charged lanthanum ion.

The second example is a tetranuclear double-stranded helicate $[Cu_2Gd_2(\mathbf{L50})_2(NO_3)_6(H_2O)_2]$ (Figures 130B and 132B) featuring quite

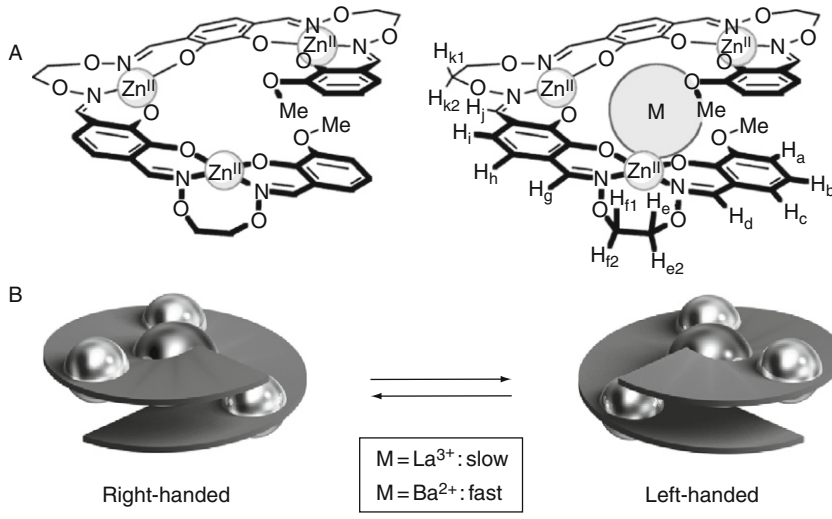

FIGURE 131 (A) Schematized structures of the trinuclear Zn^{II} metallohelicene and of the corresponding La^{III} metallohelicates. (B) Inversion process of the metallohelicates (reproduced by permission from Akine et al., 2006, © The Royal Society of Chemistry, 2006).

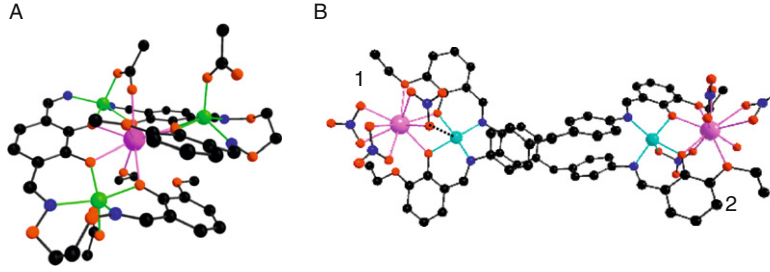

FIGURE 132 Molecular structures of (A) $[Zn_3La(\mathbf{L49})(Oac)_3(EtOH)]$ (redrawn from Akine et al., 2006) and (B) $[Cu_2Gd_2(\mathbf{L50})_2(NO_3)_6(H_2O)_2]$ (redrawn from Novitchi et al., 2008).

short Gd–Cu distances, 3.3–3.4 Å (Novitchi et al., 2008). Due to the helical arrangement of the two ligand strands, the Cu^{II} coordination polyhedron is different in the two compartments; Cu^{II} ions are primarily square planar with tetrahedral distortion of the N_2O_2 set of donor atoms but additionally, one nitrate ion is bridging the Cu and Gd atoms in a η^1,η^2, μ-mode for Cu1 with a long Cu–O bond (2.75 Å) and in a η^1,η^1,μ-mode for Cu^{II} with a shorter 2.5 Å Cu–O contact. The corresponding Gd^{III} ions are (somewhat unusually) ten-coordinate, Gd1 being bound to three

bidentate nitrates, one water molecule, two phenoxo, and one ethoxy oxygen atoms while for Gd2, one oxygen from a nitrate ion is replaced by an oxygen atom from a second ethoxy group.

The two Cu–Gd pairs are located at a distance long enough to be considered as isolated. When the susceptibility versus temperature data are modeled with the assumption that the magnetic interaction is the same within the two Cu-Gd pairs of the helicate, an interaction parameter $J = 4.5\ cm^{-1}$ is found. This model is substantiated by the weak intramolecular Cu...Cu interaction occurring when Gd^{III} is replaced with diamagnetic Y^{III}: $J = -0.44\ cm^{-1}$, using the isotropic Hamiltonian $H = -JS_{Cu1}S_{Cu2}$. Magnetization versus direct current (dc) field measurements for the corresponding Tb^{III} helicate $[Cu_2Tb_2(\mathbf{L50})_2(NO_3)_6)(H_2O)_2]$, in which ferromagnetic interactions also occur, reveals a single molecule magnet (SMM) behavior with a small hysteresis loop nearly sweep rate-independent. Substitution of the nitrate ions by hexafluoroacetylacetonate (hfa) ions in $[Cu_2Tb_2(\mathbf{L50})_2(hfa)_6)]$ ensures a better isolation of the tetranuclear helicates with respect to each other and amplifies the SMM behavior, the hysteresis loop being sweep-rate and temperature dependent.

8.2 Helical structures in coordination polymers and macrocyclic complexes

The assembly of a molecular helicate into a 1D coordination polymer has been reported recently (Semenov et al., 2008). The building block only differs from those mentioned earlier, $[Tb_2(\mathbf{L43^b})_3(L_2)]$ with $L = H_2O$, DMF, or $PPhe_3O$, by the nature of the ancillary ligand, diphenylphosphineethane dioxide ($dppeO_2$) replacing the monodentate donor. The bulkier ancillary ligand causes a slightly larger distortion from the idealized D_3-symmetry than the monodentate ligands. The helical units $[Tb_2(\mathbf{L43^b})_3(dppeO_2)_{1.5}]_n$ are connected through Tb^{III} ions by $dppeO_2$ bridges into infinite parallel chains, as shown on top of Figure 133.

There are two types of chains corresponding to the two different optical isomers. The length of the repetitive unit along the 1D chain is 16.3 Å with neighboring interchain Tb–Tb distances of 10.1 Å, somewhat longer than in the reference polymeric compound $[Ln(NO_3)_3(dppeO_2)_{1.5}]_n$ (9.2 Å). This distance can also be compared to the intramolecular Tb–Tb contacts of 6.5 Å. It is noteworthy that both the Tb^{III} molecular helicate $[Tb_2(\mathbf{L43^b})_3(H_2O)_2]$ and coordination polymer are highly luminescent, with quantum yields of $21 \pm 2\%$ ($\tau(^5D_4) = 0.45 \pm 0.05$ ms), despite the coordinated water molecule, for the former and $28 \pm 2\%$ (0.60 ± 0.05 ms) for the latter (S. Semenov and J.-C.G. Bünzli, 2008, unpublished results).

Numerous examples of supramolecular helical structures are documented for extended 1D, 2D, or 3D metal–organic frameworks, essentially built up from H-bond networks. An amazing variety of structures have

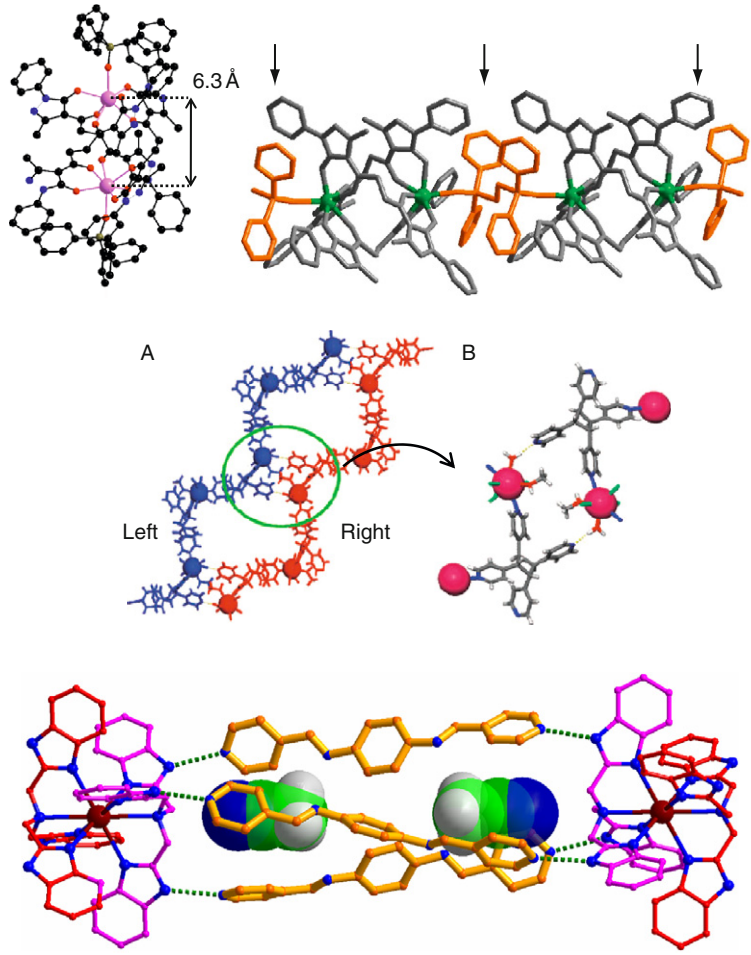

FIGURE 133 Top: structure of the first coordination polymer assembled from a helicate: (left) binuclear building block $[Tb_2(\mathbf{L43^b})_3(PPhe_3O)_2]$ (redrawn from Semenov et al., 2008), (right) fragment of the polymeric 1D chain with the bridging ligands indicated by arrows and colored (reproduced by permission from Semenov et al., 2008, © The Royal Society of Chemistry, 2008). Middle: perspective view of $\{[PrCl_3(\mathbf{L51})(MeOH)(H_2O)]\}_n$ (A) left- and right-handed helical chains and (B) the hydrogen-bonded polygon (reproduced by permission from Bucar et al., 2008, © The Royal Society of Chemistry (RSC) for the Centre National de la Recherche Scientifique and the RSC, 2008). Bottom: hydrogen-bonded triple-helical cylindrical motif of $\{[Pr(\mathbf{L53})_2(ClO_4)_3] \bullet (\mathbf{L54})_3 \bullet 2MeCN\}_n$ encapsulating acetonitrile guest molecules (reproduced in part by permission from Jiang et al., 2008, © American Chemical Society, 2008).

been reported including single-, double-, triple-, and even quadruple-stranded helices; in some instances, tubular channels walled with helical features are present in these materials and can host small molecules. We first present one recent example in which the authors have used the tetratopic molecule *crtt*-4,4′-tetrapyridyl-butane, **L51**, as the rigid bridging spacer acting as a bis(monodentate) ligand to assemble a single-stranded helical coordination polymer, $\{[PrCl_3(\mathbf{L51})(MeOH)(H_2O)] \cdot 2MeOH \cdot H_2O)\}_n$ (Bucar et al., 2008). The Pr^{III} cation is seven-coordinate in a pentagonal bipyramidal geometry (Figure 133, middle) being bound to three chlorides, two oxygen atoms from water and methanol, and two nitrogen atoms from pyridyl groups belonging to two different ligand molecules. This produces a single-stranded helical polymer along a 2_1 screw axis with a helical pitch of 20.1 Å. As in the previous example, helices of both hands are present and related by an inversion center. The self-assembly process is very sensitive to the nature of the anion: replacing chloride with nitrate ions gives rise to a 3D network consisting in a two-fold interpenetrated bimodal net with $(4.6^2)_2(4^2.6^{10}.8^3)$ topology for instance.

Developing luminescent materials for telecommunication or bioprobes, radiopharmaceuticals, MRI contrast agents, materials with special magnetic properties, or porous frameworks for the adsorption of small molecules are among the motivations often invoked for tailoring lanthanide-containing coordination polymers. Hydrothermal synthesis is the most common method for obtaining these materials also referred to as metal–organic frameworks (MOFs), or inorganic-organic hybrids. However, very few published works describe detailed physicochemical properties of the isolated materials, but for structural characterization. For instance, when R^{III}-centered luminescence is reported, only assignments are usually given, with no quantitative data such as lifetime or quantum yield, not to speak about the sensitization efficiency of the ligands. As a consequence, we have simply gathered in Table 32 the main characteristics of selected lanthanide-containing coordination polymers with helical structures published recently. When different types of structures, helical and nonhelical, were found in the investigated systems, only the helical structures are referred to in this table.

In the case of the porous $\{[R(phos)_3] \cdot 2H_2O\}_n$ networks, the adsorption isotherms have been recorded to test the intake capacity for N_2, H_2O, MeOH, and EtOH, of which 1.1, 1.76, 0.8, and 0 molecule(s) per formula unit can enter into the pores of the material, respectively. The network is stable to several dehydration/hydration cycles, maintaining its homochiral structure (Yue et al., 2006). Another clever approach to porous materials able to host small molecules starts by producing a mixture of monometallic helical complexes with different chirality from lanthanide perchlorate and tris(2-benzimidazoylmethyl)amine **L53** (Jiang et al., 2008):

TABLE 32 Structural and other characteristics of selected rare-earth containing coordination polymers with helical structures published in 2006–2008

Ligand[a]	*R*	Formula	Dim[b]	Helicity[c]	Other properties[d]	References
Homometallic coordination polymers						
L43[b]	Tb, Gd	$[R_2(\mathbf{L43^b})_3(dppeO_2)]_n$	1D	s, 16.3	Lum (Tb, τ, *Q*)	Semenov et al. (2008)
L51	Pr	$\{[PrCl_3(\mathbf{L51})_3(MeOH)(H_2O)]\}_n$	1D	s, 20.1	–	Bucar et al. (2008)
NTA	Eu	$\{[Eu(NTA)(H_2O)_2]H_2O\}_n$	1D	s, 8.1	Magn	Chen et al. (2008)
	Ho, Tm	$\{[R(NTA)(H_2O)_2]H_2O\}_n$	3D	t, 22.8	Magn	
pic	Nd, Sm	$[R(pic)_3]_n$	1D	s, 7.7	Magn (Nd, Sm); Lum (Sm)	Li et al. (2008)
ip	La, Pr, Nd, Dy	$\{Him[R(ip)_2(H_2O)]\}_n$	3D	s, 19.1; d, 9.5	Lum (NIR, Nd; vis, Dy)	Zhou et al. (2008)
	Y	$[Y(ip)_3(H_2O)_2]_n$	2D	s, 14.2; t, 42.7		
pydc	Y, Sm, Eu, Dy, Er, Yb	$[R_3(\mu\text{-}OH)_4(pydc)(Hpydc)_3(H_2O)_4]_n$	3D	d, NA	Lum (Sm, Eu, Dy; τ); Magn (all)	Huang et al. (2007)
imc	Eu, Dy	$[R(Himc)(SO_4)(H_2O)]_n$	2D	s, 6.5	Lum (Eu, Dy)	Sun et al. (2006a)
phos	Eu, Gd, Tb, Dy	$\{[R(phos)_3]\cdot 2H_2O\}_n$	3D	s, 18.8	Lum (Eu, Tb); Ads (all)	Yue et al. (2006)
L52	Er		1D	s, 14.8	–	

(*continued*)

TABLE 32 (*continued*)

Ligand[a]	*R*	Formula	Dim[b]	Helicity[c]	Other properties[d]	References
		{[Er(**L52**)$(NO_3)_3(H_2O)] \cdot H_2O\}_n$				Song et al. (2008c)
L53, **L54**	Pr	$\{[Pr(\mathbf{L53})_3(ClO_4)_3] \cdot (\mathbf{L54}) \cdot 2MeCN\}_n$	1D	t, NA	Thermal analysis, solution studies	Jiang et al. (2008)
Heterometallic coordination polymers						
$\mathbf{H_2L15^a}$	Er	$\{[ErAg_3(\mathbf{L15^a})_3(H_2O)]\}_n$	1D	t, 26.4	Lum (NIR, Er)	Zhou et al. (2008)
in	Nd, Eu	$[R Ag(OAc)(in)_3]_n$	3D	t, 27.4	Lum (Eu)	Gu and Xue (2006)
bpym	Nd, Sm, Gd	$\{[Ru(CN)_4(bpym)][R(NO_3)(H_2O)_5]_2\}_n$	1D	2, 12.5	Lum (NIR, Nd; τ)	Herrera et al. (2006a)
imdc	Y, Nd, Pr, Eu, Gd, Tb, Dy, Er, Yb	$\{[RCd(imcd)(SO_4)(H_2O)_3] \cdot 0.5H_2O\}_n$	1D	3, 10.5	Lum (Eu, Tb, Dy; τ, Eu, Tb)	Sun et al. (2006b)

[a] NTA, nitrilotriacetate; pic, picolinate; im, imidazole; ip, isophthalate; pydc, pyridine-2,5-dicarboxylate; imc, imidazolecarboxylate; phos, (*S*)-HO_3PCH_2–NHC_4H_7–CO_2H; $\mathbf{H_2L15^a}$, dipicolinic acid (Figure 17); in, isonicotinate; bpym, bipyrimidine; imdc, 4,5-imidazoledicarboxylate.
[b] Dimensionality of the network.
[c] Number of strands (s, single-stranded; d, double-stranded; t, triple-stranded; q, quadruple-stranded) and pitch in Å.
[d] Lum, luminescence (τ = lifetime, Q = quantum yield); Magn, magnetic susceptibility; Ads, adsorption isotherm.

$$R(ClO_4)_3 + \mathbf{L53} \rightarrow \Delta\Delta - [R(\mathbf{L53})_3](ClO_4)_3 \rightleftarrows \Delta\Lambda$$
$$-[R(\mathbf{L53})_3](ClO_4)_3 \rightleftarrows \Lambda\Lambda - [R(\mathbf{L53})_3](ClO_4)_3$$

Subsequent self-assembly with **L54** through hydrogen bonding leads to three types of chiral arrays, the two chiral species D_3-symmetry ($\Delta\Delta$,*P*, $\Delta\Delta$,*P*) and ($\Lambda\Lambda$,*M*, $\Lambda\Lambda$,*M*) as well as the *meso* form with inversion center ($\Lambda\Delta$,*M*, $\Delta\Lambda$,*P*) or ($\Delta\Lambda$,*P*, $\Lambda\Delta$,*M*). The one-dimensional channels of the former appear to be more permeable than those of the *meso* form and the two guest acetonitrile molecules (see bottom of Figure 133) can be removed but the framework then collapses.

Finally, some large macrocycles can wrap helically around two metal ions. Documented examples are the large Schiff base $\mathbf{H_2L55}$ (Kahwa et al., 1989, Figure 134) or $R^{III}Zn$ iminophenolate cryptates (Rodriguez-Cortias et al., 2002). This aspect is not further discussed here.

8.3 Actinide helicates

To our knowledge, there is a single report describing the synthesis and structural characterization of actinide helicates. By analogy with the first triple-stranded lanthanide helicates isolated (Piguet et al., 1992a; Xing

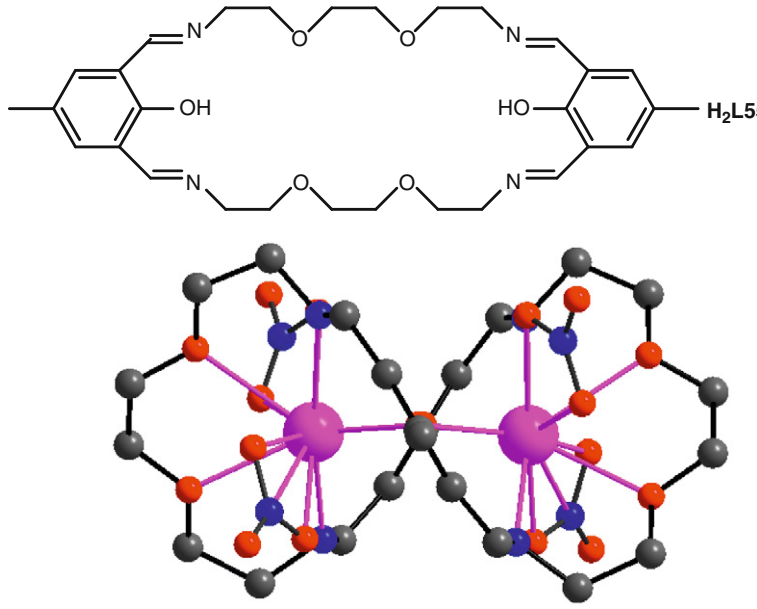

FIGURE 134 Structure of the ditopic Schiff base $\mathbf{H_2L55}$ and of its binuclear homometallic Gd^{III} complex (redrawn from Kahwa et al., 1989).

et al., 1992), Raymond and coworkers in Berkeley reasoned that the nine-coordinate tetravalent Th^{IV} ion would lead to quadruple-stranded helicates with ligands **H_2L43** (Figure 128) because the high charge of the actinide cation would favor four monoanionic bidentate pyrazolone ligand strands to bind at each metal ion (Xu and Raymond, 2006). MS and NMR data indeed point to the formation of such helicates upon reacting Th^{IV} acetylacetonate with **H_2L43^b** or **H_2L43^c** in MeOH/$CHCl_3$ 1/1. In both homochiral helicates, the Th^{IV} ions are nine-coordinate, the coordination sphere being completed by a bound DMF molecule; the coordination polyhedra are close to monocapped square antiprisms (C_{4v}). The helical pitch is 42.3 Å with a Th–Th internuclear distance of 8.30 Å in [Th_2(**L43^b**)$_4$(DMF)$_2$]; in the helicate with the ligand having a longer spacer, the Th–Th distance is about the same (8.15 Å) in [Th_2(**L43^c**)$_4$(DMF)$_2$], but the pitch is much shorter (29.6 Å). The explanation comes from the fact that the helicates are not palindromic; that is, the pitch is not constant all along the structure. The two subpitches of the capped square antiprisms are very similar in the two structures (ca. 19–22 Å) but the alkyl-bridge pitch is far longer in [Th_2(**L43^c**)$_4$(DMF)$_2$] (442 versus 50 Å!), which explains the larger overall pitch. As a comparison, the pitch of the terbium helicate with the short-bridged **H_2L43^a** ligand, [Tb_2(**L43^b**)$_3$(dppeO_2)] is much shorter, 16.3 Å (Figure 135).

9. CONCLUSIONS

The term ''helicate'' was introduced by Lehn et al. (1987) for metal complexes embedding two or more metal centers connected by one or more bridging ligand strands and since then the field has burgeoned and produced astonishing supramolecular structures (Albrecht, 2001; Piguet,

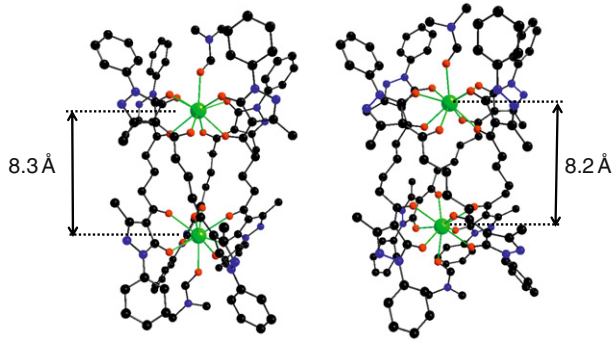

FIGURE 135 Molecular structures of the two characterized Th^{IV} helicates: [Th_2(**L43^b**)(DMF)$_2$] (left) and [Th_2(**L43^c**)(DMF)$_2$] (right) (redrawn from Xu and Raymond, 2006).

1999; Piguet et al., 1997a). Extension to the f-elements followed rapidly, with the first lanthanide binuclear helicates being reported in 1992 (Piguet et al., 1992a,b; Xing et al., 1992). The present chapter is a state of the art of this research domain 17 years after its debut and highlights how chemists have succeeded in taming the difficult programming of ligand strands for a selective recognition of the spherical rare-earth ions. Not only a suitable topological design of coordination sites has been achieved, for instance in C_2-symmetrical ditopic receptors derived from bis(benzimidazole)pyridine (Piguet et al., 1993b) but, also, introduction of subtle differences in the two tridentate chelating units allowed the preferential (if not unique) formation of heterobimetallic 4f–4f′ edifices (André et al., 2004). Increasing the number of coordinating unit according to a rationally thought design led to linear, triple-stranded tri- (Bocquet et al., 1992) and even tetranuclear 4f helicates (Zeckert et al., 2005). An innovative site-binding model mixing intra- and intermolecular connections, and taking advantage of the numerous stability constants published to date allows a close understanding of the thermodynamic stability of these helicates, despite the a priori large repulsion Coulomb's energy between the metal centers and, also the fact that some of these architectures are highly charged (+6 to +12). The mastering of these parameters makes the design of any 4f-metal containing helical edifice easily predictable.

Another crucial step has been the modification of the C_2-symmetrical bis(benzimidazole)pyridine ligands toward tridentate-bidentate host able to build nd–4f helicates (Piguet et al., 1995a). Indeed, easy modulation of the spectroscopic and magnetic properties of d-transition metal ions is achieved thanks to the large overlap of the d-orbitals with surrounding wave-functions. The unique combination of two nd and 4f ions into a cylindrical supramolecular architecture results in intermetallic communication which, in turn, materializes under the form of a tuning of one ion properties by the other. Demonstration of this effect in two particular cases, Fe^{II} spin-crossover parameters (Piguet et al., 1995e), and energy transfer modulating luminescent properties (Cantuel et al., 2002; Imbert et al., 2003) proved the feasibility of this approach and given that several different d-transition metal ions may be introduced into the helicates (to date: $Cr^{II/III}$, Fe^{II}, $Co^{II/III}$, Ni^{II}, Zn^{II}, Ru^{II}, Os^{II}) a whole range of molecular architectures having predetermined unique properties can be envisaged.

Modification of the C_2-symmetrical ligands to allow water solubility for the assembled helicate is another landmark (Elhabiri et al., 1999; Vandevyver et al., 2007) since it opens the way for the binuclear complexes to be used as lanthanide luminescence probes with a variety of applications ranging from cell imaging (Bünzli et al., 2008) to nucleic acid detection (Song et al., 2008b). The chemical robustness of the helicates, both thermodynamically and kinetically speaking, their inherent

chirality, as well as the ease with which they are taken into live cells and remain into them without affecting their biological functions are real advantages. Bioconjugation of the helicates should improve their specificity toward given cell lines and prove useful both in diagnostic and in the follow-up of cancer therapy, among others.

Future prospects for f-containing helicates seem to be incommensurable. Several subjects are not yet fully explored, for instance, 5f helicates are in their infancy (Xu and Raymond, 2006), 3d–4f constructions can be modulated almost at will, particularly when it comes to intermetallic communication, and the advent of extended networks constructed from helicate building blocks (Semenov et al., 2008) and/or incorporating helical features (Jiang et al., 2008) are promising. With respect to the latter, a mixture of nd and 4f ions could lead to interesting optical and/or magnetic materials (e.g., networks with large spin cross hysteresis) which are more and more needed for telecommunications, analytical and bioanalytical sensing, and storage of small molecules. In fact the present level of knowledge, particularly with respect to the modeling of the thermodynamic stability of these entities and to the various structural entities susceptible to be assembled, combined with the emergence of new types of ligands besides the archetypical, very efficient, and easily adjustable, bis(benzimidazole)pyridine framework, are an insurance for the unfolding of exciting science in the future.

REFERENCES

Addison, A.W., Burke, P.J., 1981. J. Heterocycl. Chem. 18, 803.
Addison, A.W., Rao, T.N., Wahlgren, C.G., 1983. J. Heterocycl. Chem. 20, 1481.
Aebischer, A., Gumy, F., Bünzli, J.-C.G., 2009. Phys. Chem. Chem. Phys. 11, 1346.
Akine, S., Taniguchi, T., Matsumoto, T., Nabeshima, T., 2006. Chem. Commun. 4961.
Albrecht, M., 2001. Chem. Rev. 101, 3457.
Albrecht, M., Osetska, O., Fröhlich, R., Bünzli, J.-C.G., Aebischer, A., Gumy, F., Hamacek, J., 2007a. J. Am. Chem. Soc. 129, 14178.
Albrecht, M., Schmid, S., Dehn, S., Wickleder, C., Shuang, Z., Basset, A.P., Pikramenou, Z., Fröhlich, R., 2007b. New J. Chem. 31, 1755.
Ali, H.D.P., Kruger, P.E., Gunnlaugsson, T., 2008. New J. Chem. 32, 1153.
An, Y., Berry, M.T., van Veggel, F.C.J.M., 2000. J. Phys. Chem. A 104, 11243.
André, N., Jensen, T.B., Scopelliti, R., Imbert, D., Elhabiri, M., Hopfgartner, G., Piguet, C., Bünzli, J.-C.G., 2004. Inorg. Chem. 43, 515.
André, N., Scopelliti, R., Hopfgartner, G., Piguet, C., Bünzli, J.-C. G., 2002. Chem. Commun. 214.
Anwander, R., 1999. Principles in organolanthanide chemistry. In: Kobayashi, S. (Ed.), Topics in Organometallic Chemistry, vol. 2. Springer-Verlag, Berlin, pp. 1–62.
Archer, R.D., Chen, H., Thomson, L.C., 1998. Inorg. Chem. 37, 2089.
Aspinall, H.C., 2002. Chem. Rev. 102, 1807.
Balzani, V., Credi, A., Venturi, M., 2002. Chem. Eur. J. 8, 5525.
Balzani, V., Credi, A., Venturi, M., 2008. Chem. Eur. J. 14, 26.
Barela, T.D., Sherry, A.D., 1976. Anal. Biochem. 71, 351.

Barta, C.A., Bayly, S.R., Read, P.W., Patrick, B.O., Thompson, R.C., Orvig, C., 2008. Inorg. Chem. 47, 2294.
Basset, A.P., Megennis, S.W., Glover, P.B., Lewis, D.J., Spencer, N., Parsons, S., Williams, R. M., De Cola, L., Pikramenou, Z., 2004. J. Am. Chem. Soc. 126, 9413.
Beeby, A., Clarkson, I.M., Dickins, R.S., Faulkner, S., Parker, D., Royle, L., de Sousa, A.S., Williams, J.A.G., Woods, M., 1999. J. Chem. Soc., Perkin Trans. 2 3, 493.
Benelli, C., 2002. Chem. Rev. 102, 2369.
Ben-Naim, A.J., 1998. J. Chem. Phys. 108, 6937.
Benson, S.W., 1958. J. Am. Chem. Soc. 80, 5151.
Benson, S.W., 1976. Thermochemical Kinetics, 2nd ed Wiley-Interscience, New York p. 37.
Bertini, I., Luchinat, C., 1996. Coord. Chem. Rev. 150, 1.
Binnemans, K., Görller-Walrand, C., 1995. Chem. Phys. Lett. 245, 75.
Binnemans, K., 2005. Rare earth β-diketonate complexes: functionalities and applications. In: Gschneidner, K.A. Jr., Pecharsky, V., Bünzli, J.-C.G. (Eds.), Handbook on the Physics and Chemistry of Rare Earths Vol. 35. Amsterdam: Elsevier Science. Chapter 225, pp. 107–272.
Blasse, G., 1976. Struct. Bond. 26, 45.
Bleaney, B.J., 1972. Magn. Reson. 8, 91.
Bobba, G., Frias, J.C., Parker, D., 2002. Chem. Commun. 8, 890.
Bocquet, B., Bernardinelli, G., Ouali, N., Floquet, S., Renaud, F., Hopfgartner, G., Piguet, C., 1992. Chem. Commun. 930.
Borkovec, M., Hamacek, J., Piguet, C., 2004. Dalton Trans. 4096.
Bornhop, D.J., Hubbard, D.S., Houlne, M.P., Adair, C., Kiefer, G.E., Pence, B.C., Morgan, D. L., 1999. Anal. Chem. 71, 2607.
Bornhop, D.J., Griffin, J.M.M., Goebel, T.S., Sudduth, M.R., Motamedi, M., 2003. Appl. Spectrosc. 57, 1216.
Boukhalfa, H., Crumbliss, A.L., 2000. Inorg. Chem. 39, 4318.
Brayshaw, P.A., Bünzli, J.-C.G., Froidevaux, P., Harrowfield, J.M., Kim, Y., Sobolev, A.N., 1995. Inorg. Chem. 34, 2068.
Brewster, J.H., 1974. Top. Curr. Chem. 47, 29.
Bucar, D.K., Papaefstathiou, G.S., Hamilton, T.D., MacGillivray, L.R., 2008. New J. Chem. 32, 797.
Bünzli, J.-C.G., 1989. Luminescent probes. In: Bünzli, J.-C.G., Choppin, G.R. (Eds.), Lanthanide Probes in Life, Chemical and Earth Sciences. Elsevier, Amsterdam, pp. 219–293 (Chapter 7).
Bünzli, J.-C.G., 1998. Coordination chemistry of the trivalent lanthanide ions: An introductory overview. In: Saez-Puche, R., Caro, P. (Eds.), Rare Earths. Editorial Complutense, Madrid, pp. 223–259.
Bünzli, J.-C.G., 2009. Chem. Lett. 38 (2), 104.
Bünzli, J.-C.G., Piguet, C., 2002. Chem. Rev. 102, 1897.
Bünzli, J.-C. G., Chauvin, A.-S., Vandevyver, C. D. B., Song, B., Comby, S., Ann. N.Y. Acad. Sci. 2008, 1130, 97.
Bünzli, J.-C.G., Piguet, C., 2005. Chem. Soc. Rev. 34, 1048.
Bünzli, J.-C.G., Petoud, S., Piguet, C., Renaud, F., 1997. J. Alloys Compd. 249, 14.
Burdick, G.W., Reid, M.F., 2007. $4f^n$–$4f^{n-1}5d$ transitions. In: Gschneidner Jr., K.A., Pecharsky, V., Bünzli, J.-C.G. (Eds.), Handbook on the Physics and Chemistry of Rare Earths, vol. 37. Elsevier Science, Amsterdam, pp. 61–98 (Chapter 232).
Cable, M.L., Kirby, J.P., Sorasaenee, K., Gray H.B., Ponce, A., 2007. J. Am. Chem. Soc., 129, 1474.
Cahn, R.S., Ingold, C., Prelog, V., 1966. Angew. Chem. Int. Ed. Engl. 5, 385.
Canada, R.G., 1983. Biochem. Biophys. Res. Commun. 111, 135.
Canada, R.G., 1988. Anal. Chim. Acta 205, 77.
Canada, R.G., Paltoo, D.N., 1998. Biochem. Biophys. Acta Mol. Cell Res. 1448, 85.

Canard, G., Piguet, C., 2007. Inorg. Chem. 46, 3511.
Canard, G., Koeller, S., Bernardinelli, G., Piguet, C., 2008. J. Am. Chem. Soc. 130, 1025.
Cantuel, M., Bernardinelli, G., Imbert, D., Bünzli, J.-C.G., Hopfgartner, G., Piguet, C., 2002. J. Chem. Soc., Dalton Trans. 1929.
Cantuel, M., Bernardinelli, G., Muller, G., Riehl, J.P., Piguet, C., 2004. Inorg. Chem. 43, 1840.
Cantuel, M., Gumy, F., Bünzli, J.-C.G., Piguet, C., 2006. Dalton Trans. 2647.
Capo, M., Saa, J.M., Alvarez, A., 2002. Chem. Commun. 1982.
Cargill Thompson, A.M.W., 1997. Coord. Chem. Rev. 160, 1.
Carrano, C.J., Raymond, K.N., 1978. J. Am. Chem. Soc. 100, 5371.
Carrano, C.J., Cooper, S.J., Raymond, K.N., 1979. J. Am. Chem. Soc. 101, 599.
Caulder, D.L., Raymond, K.N., 1997. Angew. Chem. Int. Ed. Engl. 36, 1440.
Caulder, D.L., Raymond, K.N., 1999. Acc. Chem. Res. 32, 975.
Chapman, R.D., Loda, R.T., Riehl, J.P., Schwartz, R.W., 1984. Inorg. Chem. 23, 1652.
Chapon, D., Husson, C., Delangle, P., Lebrun, C., Vottéro, P.J.A., 2001. J. Alloys Compd. 323–324, 128.
Chapon, D., Delangle, P., Lebrun, C., 2002. J. Chem. Soc., Dalton Trans. 68.
Charbonnière, L.J., Hildebrandt, N., 2008. Eur. J. Inorg. Chem. 3241.
Charbonnière, L.J., Williams, A.F., Frey, U., Merbach, A.E., Kamalaprija, P., Schaad, O., 1997. J. Am. Chem. Soc. 119, 2488.
Chauvin, A.-S., Tripier, R., Bünzli, J.-C.G., 2001. Tetrahedron Lett. 42, 3089.
Chauvin, A.-S., Gumy, F., Imbert, D., Bünzli, J.-C.G., 2004. Spectrosc. Lett. 37, 517 erratum 2007, 40, 193.
Chauvin, A.-S., Comby, S., Song, B., Vandevyver, C.D.B., Thomas, F., Bünzli, J.-C.G., 2007. Chem. Eur. J. 13, 9515.
Chauvin, A.-S., Comby, S., Song, B., Vandevyver, C.D.B., Bünzli, J.-C.G., 2008. Chem. Eur. J. 14, 1726.
Chen, X.-Y., Bretonnière, Y., Pécaut, J., Imbert, D., Bünzli, J.-C.G., Mazzanti, M., 2007. Inorg. Chem. 46, 625.
Chen, Z., Zhao, B., Zhang, Y., Shi, W., Cheng, P., 2008. Cryst. Growth Des. 8, 2291.
Choppin, G.R., 1989. Chemical properties of the rare earth elements. In: Bünzli, J.-C.G., Choppin, G.R. (Eds.), Lanthanide Probes in Life, Chemical and Earth Sciences. Elsevier, Amsterdam, pp. 1–41 (Chapter 1).
Choppin, G.R., Wang, Z.M., 1997. Inorg. Chem. 36, 249.
Comby, S., 2008. Ph.D.Dissertation No. 4052, École Polytechnique Fédérale de Lausanne. p. II-39.
Comby, S., Bünzli, J.-C.G., 2007. Lanthanide near-infrared luminescence in molecular probes and devices. In: Gschneidner Jr., K.A., Pecharsky, V., Bünzli, J.-C.G. (Eds.), Handbook on the Physics and Chemistry of Rare Earths, vol. 37. Elsevier Science, Amsterdam, pp. 217–470 (Chapter 235).
Comuzzi, C., Di Bernardo, P., Portanova, R., Tolazzi, M., Zanonato, P.L., 2002. Polyhedron 21, 1385.
Connally, R.E., Piper, J.A., 2008. Ann. NY Acad. Sci. 1130, 106.
Constable, E.C., 1992. Tetrahedron 48, 10013.
Constable, E.C., 1994. Prog. Inorg. Chem. 42, 67.
Constable, E.C., 1996. Atwood, J.L., Davies, J.E.D., MacNicol, D.D., Vögtle, F. (Eds.), Comprehensive Supramolecular Chemistry. Pergamon, Oxford (Chapter 6).
Constable, E.C., Ward, M.D., Tocher, D.A., 1991. J. Chem. Soc., Dalton Trans. 1675.
Costes, J.-P., Dahan, F., Wernsdorfer, W., 2006. Inorg. Chem. 45, 5.
Cotton, S., 2006. Lanthanide and Actinide Chemistry. John Wiley & Sons, Chichester.
D'Aléo, A., Pompidor, G., Elena, B., Vicat, J., Baldeck, P.L., Toupet, L., Kahn, R., Andraud, C., Maury, O., 2007. ChemPhysChem. 8, 2125.
D'Aléo, A., Picot, A., Baldeck, P., Andraud, C., Maury, O., 2008a. Inorg. Chem. 47, 10269.

D'Aléo, A., Picot, A., Beeby, A., Williams, J.A.G., Le Guennic, B., Andraud, C., Maury, O., 2008b. Inorg. Chem. 47, 10258.
Dalla Favera, N., Hamacek, J., Borkovec, M., Jeannerat, D., Ercolani, G., Piguet, C., 2007. Inorg. Chem. 46, 9312.
Dalla Favera, N., Hamacek, J., Borkovec, M., Jeannerat, D., Gumy, F., Bünzli, J.-C.G., Ercolani, C., Piguet, C., 2008. Chem. Eur. J. 14, 2994.
Dehnicke, K., Greiner, A., 2003. Angew. Chem. Int. Ed. Engl. 42, 1340.
Deiters, E., Song, B., Chauvin, A.-S., Vandevyver, C.D.B., Bünzli, J.-C.G., 2008. New J. Chem. 32, 1140.
Deiters, E., Song, B., Chauvin, A.-S., Vandevyver, C.D.B., Gumy, F., Bünzli, J.-C.G., 2009. Chem. Eur. J. 15, 895.
Denk, W., Strickler, J.H., Webb, W.W., 1990. Science 248, 73.
de Sá, G.F., Malta, O.L., Donega, C.D., Simas, A.M., Longo, R.L., Santa-Cruz, P.A., da Silva, E. F., 2000. Coord. Chem. Rev. 196, 165.
Dexter, D.L., 1953. J. Chem. Phys. 21, 836.
Di Bernardo, P., Zanonato, P.L., Melchior, M., Portanova, R., Tolazzi, M., Choppin, G., Wang, Z., 2008. Inorg. Chem. 47, 1155.
Do, K., Muller, F., Muller, G., 2008. J. Phys. Chem. A 112, 6789.
Dong, Y.-B., Wang, P., Ma, J.-P., Zhao, X.-X., Wang, H.-Y., Tang, B., Huang, R.-Q., 2007. J. Am. Chem. Soc. 129, 4872.
Durham, D.A., Frost, G.H., Hart, F.A., 1969. J. Inorg. Nucl. Chem. 31, 833.
Edder, C., Piguet, C., Bünzli, J.-C.G., Hopfgartner, G., 1997. J. Chem. Soc., Dalton Trans. 4657.
Edder, C., Piguet, C., Bernardinelli, G., Mareda, J., Bochet, C., Bünzli, J.-C.G., Hopfgartner, G., 2000. Inorg. Chem. 39, 5059.
Edder, C., Piguet, C., Bünzli, J.-C.G., Hopfgartner, G., 2001. Chem. Eur. J. 7, 3014.
Elhabiri, M., Albrecht-Gary, A.-M., 2008. Coord. Chem. Rev. 252, 1079.
Elhabiri, M., Scopelliti, R., Bünzli, J.-C.G., Piguet, C., 1999. J. Am. Chem. Soc. 121, 10747.
Elhabiri, M., Hamacek, J., Bünzli, J.-C.G., Albrecht-Gary, A.-M., 2004a. Eur. J. Inorg. Chem. 51.
Elhabiri, M., Hamacek, J., Humbert, N., Bünzli, J.-C.G., Albrecht-Gary, A.-M., 2004b. New J. Chem. 28, 1096.
Eliseeva, S.V., Ryazanov, M., Gumy, F., Troyanov, S.I., Lepnev, L.S., Bünzli, J.-C.G., Kuzmina, N.P., 2006. Eur. J. Inorg. Chem. 4809.
Ercolani, G., 2003. J. Am. Chem. Soc. 125, 16097.
Ercolani, G., 2006. Struct. Bond. 121, 167.
Ercolani, G., Piguet, C., Borkovec, M., Hamacek, J.J., 2007. Phys. Chem. B 111, 12195.
Evans, W.J., 2007. Inorg. Chem. 46, 3435.
Fatin-Rouge, N., Blanc, S., Leize, E., van Dorsselaer, A., Baret, P., Pierre, J.-L., Albrecht-Gary, A.-M., 2000. Inorg. Chem. 39, 5771.
Fatin-Rouge, N., Blanc, S., Pfeil, A., Rigault, A., Albrecht-Gary, A.-M., Lehn, J.-M., 2001. Helv. Chim. Acta 84, 1694.
Floquet, S., Ouali, N., Bocquet, B., Bernardinelli, G., Imbert, D., Bünzli, J.-C.G., Hopfgartner, C., Piguet, C., 2003. Chem. Eur. J. 9, 1860.
Floquet, S., Borkovec, M., Bernardinelli, G., Pinto, A., Leuthold, L.-A., Hopfgartner, G., Imbert, D., Bünzli, J.-C.G., Piguet, C., 2004. Chem. Eur. J. 10, 1091.
Flory, P.J., Suter, U.W., Mutter, M., 1976. J. Am. Chem. Soc. 98, 5733.
Förster, T., 1960. Burton, M., Kirby-Smith, J.S., Magee, L.L. (Eds.), Comparative Effects of Radiation. John Wiley & Sons, New York, p. 300.
Frey, S.T., Horrocks Jr., W.deW., 1995. Inorg. Chim. Acta 229, 383.
Frias, J.C., Bobba, G., Cann, M.J., Hutchison, C.J., Parker, D., 2003. Org. Biomol. Chem. 1, 905.
Frost, G.H., Hart, F.A., Hursthouse, M.B., 1969. J. Chem. Soc., Chem. Commun. 1421.
Fujita, M., Tominaga, M., Hori, A., Therrien, B., 2005. Acc. Chem. Res. 38, 371.
Fyles, T.M., Tong, C.C., 2007. New J. Chem. 31, 296.

Gargano, J.M., Ngo, T., Kim, J.Y., Acheson, D.W.K., Lees, W.J., 2001. J. Am. Chem. Soc. 123, 12909.
Garrett, T.M., Koert, U., Lehn, J.-M., 1992. Phys. Org. Chem. 5, 529.
Gassner, A.-L., Duhot, C., Bünzli, J.-C.G., Chauvin, A.-S., 2008. Inorg. Chem. 47, 7802.
Gawryszewska, P., Legendziewicz, J., Ciunik, Z., Esfandiari, N., Muller, G., Piguet, C., Cantuel, J.P., Riehl, J.P., 2006. Chirality 18, 406 and references therein.
Gonçalves e Silva, F.R., Longo, R.L., Malta, O.L., Piguet, C., Bünzli, J.-C.G., 2000. Phys. Chem. Chem. Phys. 2, 5400.
Gonçalves e Silva, F.R., Malta, O.L., Reinhard, C., Güdel, H.U., Piguet, C., Moser, J.E., Bünzli, J.-C.G., 2002. J. Phys. Chem. A 106, 1670.
Goodgame, D.M.L., Hill, S.P.W., Williams, D.J., 1993. J. Chem. Soc., Chem. Commun. 1019.
Görller-Walrand, C., Binnemans, K., 1996. Rationalization of crystal field parameters. In: Gschneidner, K.A., Eyring, L. (Eds.), Handbook on the Physics and Chemistry of Rare Earths, vol. 23. Elsevier Science, Amsterdam, pp. 121–283.
Görller-Walrand, C., Binnemans, K., 1998. Spectral intensities of f–f transitions. In: Gschneidner, K.A., Eyring, L. (Eds.), Handbook on the Physics and Chemistry of Rare Earths, vol. 25. Elsevier Science, Amsterdam, pp. 101–264.
Greenwald, M., Wessely, D., Goldberg, I., Cohen, Y., 1999. New J. Chem. 337.
Grenthe, I., 1961. J. Am. Chem. Soc. 83, 360.
Gu, X., Xue, D., 2006. Inorg. Chem. 45, 9257.
Guillaumont, D., Bazin, H., Benech, J.M., Boyer, M., Mathis, G., 2007. ChemPhysChem. 8, 480.
Hamacek, J., Piguet, C.J., 2006. Phys. Chem. B 110, 7783.
Hamacek, J., Blanc, S., Elhabiri, M., Leize, E., van Dorsselaer, A., Piguet, C., Albrecht-Gary, A.-M., 2003. J. Am. Chem. Soc. 125, 1541.
Hamacek, J., Borkovec, M., Piguet, C., 2005a. Chem. Eur. J. 11, 5217.
Hamacek, J., Borkovec, M., Piguet, C., 2005b. Chem. Eur. J. 11, 5227.
Hamacek, J., Borkovec, M., Piguet, C., 2006. Dalton Trans. 1473.
Hamacek, J., Bernardinelli, G., Filinchik, Y., 2008. Eur. J. Inorg. Chem. 14, 2994.
Hannon, M.J., Painting, C.L., Jackson, A., Hamblin, J., Errington, W., 1997. Chem. Commun. 1807.
Hannon, M.J., Moreno, V., Prieto, M.J., Moldrheim, E., Sletten, E., Meistermann, I., Isaac, C.J., Sanders, K.J., Rodger, A., 2001. Angew. Chem. Int. Ed. Engl. 40, 880.
Harris, C.M., McKenzie, E.D., 1969. J. Chem. Soc. A 746.
Harrowfield, J.M., Kim, Y., Skelton, B.W., White, A.H., 1995. Aust. J. Chem. 48, 807 and references therein.
Hasenknopf, B., Hall, J., Lehn, J.-M., Balzani, V., Credi, A., Campagna, S., 1996. New J. Chem. 20, 725.
He, C., Lin, Z., He, Z., Duan, C., Xu, C., Wang, Z., Yan, C., 2008. Angew. Chem. Int. Ed. Engl. 47, 877.
Hendersen, B., Imbusch, G.F., 1989. Optical Spectroscopy of Inorganic Solids. Clarendon Press, Oxford.
Herrera, J.-M., Pope, S.J.A., Adams, H., Faulkner, S., Ward, M.D., 2006a. Inorg. Chem. 45, 3895.
Herrera, J.-M., Ward, M.D., Adams, H., Pope, S.J.A., Faulkner, S., 2006b. Chem. Commun. 1851.
Hill, A.V., 1910. J. Physiol. (London) 4, 40.
Hopfgartner, G., Piguet, C., Henion, J.D., 1994. J. Am. Soc. Mass Spectrom. 5, 748.
Hopkins, T.A., Bolender, J.P., Metcalf, D.H., Richardson, F.S., 1996. Inorg. Chem. 35, 5356.
Huang, Y., Wu, B., Yuan, D., Xu, Y., Jiang, F., Hong, M., 2007. Inorg. Chem. 46, 1171.
Huck, W.T.S., Bowden, N., Onck, P., Pardoen, T., Hutchinson, J.W., Whitesides, G.M., 2000. Langmuir 16, 3497.
Huskowska, E., Riehl, J.P., 1995. Inorg. Chem. 34, 5615 and references therein.

Hutin, M., Schalley, C.A., Bernardinelli, G., Nitschke, J.R., 2006. Chem. Eur. J. 12, 4069.
Imbert, D., Cantuel, M., Bünzli, J.-C.G., Bernardinelli, G., Piguet, C., 2003. J. Am. Chem. Soc. 125, 15698.
Jacobson, H., Stockmayer, W.H., 1950. J. Chem. Phys. 18, 1600.
Jencks, W.P., 1981. Proc. Natl. Acad. Sci. USA 78, 4046.
Jensen, B.S., 1959. Acta Chem. Scand. 13, 1668.
Jensen, T.B., Scopelliti, R., Bünzli, J.-C.G., 2006. Inorg. Chem. 45, 7806.
Jensen, T.B., Scopelliti, R., Bünzli, J.-C.G., 2007. Chem. Eur. J. 13, 8404.
Jensen, T.B., Scopelliti, R., Bünzli, J.-C.G., 2008. Dalton Trans. 1027.
Jiang, J.-J., Zheng, S.-R., Liu, Y., Pan, M., Wang, W., Su, C.-Y., 2008. Inorg. Chem. 47, 10692.
Jocher, C.J., Moore, E.G., Xu, J., Avedano, S., Botta, M., Aime, S., Raymond, K.N., 2007. Inorg. Chem. 46, 9182.
Kahn, O., Kodjovi, E., 1999. Philos. Trans. R. Soc. Lond. A 354, 359.
Kahwa, I.A.K., Folkes, S., Williams, D.J., Ley, S.V., O'Mahoney, C.A., McPherson, G.L., 1989. J. Chem. Soc., Chem. Commun. 1531.
Ke, H.Y.D., Birnbaum, E.R., Darnall, D.W., Jackson, P.J., Rayson, G.D., 1992. Appl. Spectrosc. 46, 479.
Kleinerman, M., 1969. J. Chem. Phys. 51, 2370.
Koeller, S., Bernardinelli, G., Bocquet, B., Piguet, C., 2003a. Chem. Eur. J. 9, 1062.
Koeller, S., Bernardinelli, G., Piguet, C., 2003b. Dalton Trans. 2395.
Koeller, S., Bernardinelli, G., Piguet, C., 2006. C. R. Chimie 9, 1158.
Koert, U., Harding, M.M., Lehn, J.-M., 1990. Nature 346, 339.
Koper, G., Borkovec, M., 2001. J. Phys. Chem. B 105, 6666.
Krämer, R., Lehn, J.-M., Marquis-Rigault, A., 1993. Proc. Natl. Acad. Sci. USA 90, 5394.
Krämer, R., Fritsky, I.O., Pritzkow, H., Kovbasyuk, L.A., 2002. J. Chem. Soc., Dalton Trans. 1307.
Kröhnke, F., 1963. Angew. Chem. Int. Ed. 2, 225.
Kuhn, W., 1934. Kolloid Z. 68, 2.
Lakowicz, J.R., 2006. Principles of Fluorescence Spectroscopy, 3rd ed Springer-Verlag, New York.
Lama, M., Mamula, O., Kottas, G.S., Rizzo, F., De Cola, L., Nakamura, A., Kuroda, R., Stoeckli-Evans, H., 2007. Chem. Eur. J. 13, 7358.
Lama, M., Mamula, O., Kottas, G.S., de Cola, L., Stoeckli-Evans, H., Shoa, S., 2008. Inorg. Chem. doi:10.1021/ic7021006 (published on the web, December 12, 2008).
Lamture, J.B., Wensel, T.G., 1995. Bioconj. Chem. 6, 88.
Lamture, J.B., Zhou, Z.H., Kumar, A.S., Wensel, T.G., 1995. Inorg. Chem. 34, 864.
Latva, M., Takalo, H., Mukkala, V.M., Matachescu, C., Rodriguez-Ubis, J.-C., Kankare, J., 1997. J. Lumin. 75, 149.
Lawrence, D.S., Jiang, T., Levett, M., 1995. Chem. Rev. 95, 2229.
Lazarides, T., Sykes, D., Faulkner, S., Barbieri, A., Ward, M.D., 2008. Chem. Eur. J. 14, 9389.
Le Borgne, T., Bénech, J.-M., Floquet, S., Bernardinelli, G., Aliprandini, C., Bettens, P., Piguet, C., 2003. Dalton Trans. 3856.
Le Borgne, T., Altmann, P., André, N., Bünzli, J.-C.G., Bernardinelli, G., Morgantini, P.-Y., Weber, C., Piguet, C., 2004. Dalton Trans. 723.
Lehn, J.-M., 1988. Angew. Chem. Int. Ed. Engl. 27, 89.
Lehn, J.-M., 1995. Supramolecular Chemistry, Concepts and Perspectives. VCH, Weinheim.
Lehn, J.-M., 1999. Supramolecular Chemistry/Science: Some Conjectures and Perspectives. Kluwer Academic Publishers, Dordrecht.
Lehn, J.-M., 2007. Chem. Soc. Rev. 36, 151.
Lehn, J.-M., Eliseev, A.V., 2001. Science 291, 2331.
Lehn, J.-M., Rigault, A., 1988. Angew. Chem. Int. Ed. Engl. 27, 1095.

Lehn, J.-M., Sauvage, J.-P., Simon, J., Ziessel, R., Piccinni-Leopardi, C., Germain, G., Declerq, J.-P., van Meersche, M., 1983. Nouv. J. Chimie 17, 413.
Lehn, J.-M., Rigault, A., Siegel, J., Harrowfield, J., Chevrier, B., Moras, D., 1987. Proc. Natl. Acad. Sci. USA 84, 2565.
Leininger, S., Olenyuk, B., Stang, P.J., 2000. Chem. Rev. 100, 853.
Leonard, J.P., Jensen, P., McCabe, T., O'Brien, J.E., Peacock, R.D., Kruger, P.E., Gunnlaugsson, T., 2007. J. Am. Chem. Soc. 129, 10986.
Lessmann, J.L., Horrocks Jr., W.W., 2000. Inorg. Chem. 39, 3114.
Li, W., Wang, X.L., Song, X.Y., Li, L.C., Liao, D.Z., Jiang, Z.H., 2008. J. Mol. Struct. 885, 1.
Loukova, G.V., Huhn, W., Vasiliev, V.P., Smirnov, V.A., 2007. J. Phys. Chem. A 111, 4117.
Lukin, O., Vögtle, F., 2005. Angew. Chem. Int. Ed. Engl. 44, 1456.
Malta, O.L., 1997. J. Lumin. 71, 229.
Mammen, M., Choi, S.-K., Whitesides, G.M., 1998. Angew. Chem. Int. Ed. Engl. 37, 2754.
Mamula, O., Lama, M., Telfer, S.G., Nakamura, A., Kuroda, R., Stoeckli-Evans, H., Scopelliti, R., 2005. Angew. Chem. Int. Ed. Engl. 44, 2527.
Mamula, O., Lama, M., Stoeckli-Evans, H., Shova, S., 2006. Angew. Chem. Int. Ed. 45, 4940.
Manning, H.C., Goebbel, T., Thompson, R.C., Price, R.R., Lee, H., Bornhop, D.J., 2004. Bioconj. Chem. 15, 1488.
Manning, H.C., Smith, S.M., Sexton, M., Haviland, S., Bai, M.F., Cederquist, K., Stella, N., Bornhop, D., 2006. J. Bioconjugate Chem. 17, 735.
Marquis-Rigault, A., Dupont-Gervais, A., Van Dorsselaer, A., Lehn, J.-M., 1996. Chem. Eur. J. 3, 1395.
Martin, N., Bünzli, J.-C.G., McKee, V., Piguet, C., Hopfgartner, G., 1998. Inorg. Chem. 37, 577.
Martin, L.J., Hahnke, M.J., Nitz, M., Wohnert, J., Silvaggi, N.R., Allen, K.N., Schwalbe, H., Imperiali, B., 2007. J. Am. Chem. Soc. 129, 7106.
Matthews, C.J., Onions, S.T., Morata, G., Davis, L.J., Heath, S.L., Price, D.J., 2003. Angew. Chem. 115, 3274.
Maurizot, V., Linti, G., Huc, I., 2004. Chem. Commun. 924.
McKenzie, B.M., Miller, A.K., Wotjecki, R.J., Johnson, J.C., Burke, K.A., Tzeng, K.A., Mather, P.T., Rowan, S.J., 2008. Tetrahedron 64, 8488.
McMorran, D.A., Steel, P.J., 1998. Angew. Chem. Int. Ed. Engl. 37, 3295.
Meskers, S.C.J., Dekkers, H.P.J.M., 2001. J. Phys. Chem. A 105, 4589 and references therein.
Metcalf, D.H., Stewart, J.M.M., Snyder, S.W., Grisham, C.M., Richardson, F.S., 1992. Inorg. Chem. 31, 2445.
Meurer, K.P., Vögtle, F., 1985. Top. Curr. Chem. 127, 1.
Meyer, M., Kersting, B., Powers, R.E., Raymond, K.N., 1997. Inorg. Chem. 36, 5179.
Mitsunobu, O., Yamada, Y., 1967. Bull. Chem. Soc. Jpn. 40, 2380.
Moret, E., Nicolo, F., Bünzli, J.-C.G., Chapuis, G., 1991. J. Less-Common Met. 171, 273.
Motekaitis, R.J., Martell, A.E., Hancock, R.A., 1994. Coord. Chem. Rev. 133, 39.
Mulder, A., Huskens, J., Reinhoudt, D.N., 2004. Org. Biomol. Chem. 2, 3409.
Muller, G., Bünzli, J.-C.G., Schenk, K.J., Piguet, C., Hopfgartner, G., 2001a. Inorg. Chem. 40, 2642.
Muller, G., Schmidt, B., Jiricek, J., Hopfgartner, G., Riehl, J.P., Bünzli, J.-C.G., Piguet, C., 2001b. J. Chem. Soc., Dalton Trans. 2655.
Muller, G., Bünzli, J.-C.G., Riehl, J.P., Suhr, D., von Zelewsky, A., Mürner, H.-R., 2002a. Chem. Commun. 1522.
Muller, G., Riehl, J.P., Schenk, K.J., Hopfgartner, G., Piguet, C., Bünzli, J.-C.G., 2002b. Eur. J. Inorg. Chem. 3101.
Muller, G., Maupin, C.L., Riehl, J.P., Birkedal, H., Piguet, C., Bünzli, J.-C.G., 2003. Eur. J. Inorg. Chem. 4065.
Mürner, H.-R., Chassat, E., Thummel, R.P., Bünzli, J.-C.G., 2000. J. Chem. Soc., Dalton Trans. 2809.

Nasso, I., Galaup, C., Havas, F., Tisnes, P., Picard, C., Laurent, S., VanderElst, L., Muller, R.N., 2005. Inorg. Chem. 44, 8293.
Nielson, C.W., Koster, G.F., 1963. Spectroscopic Coefficients for p^n, d^n, and f^n Configurations. MIT Press, Cambridge.
Nishioka, T., Fukui, K., Matsumoto, K., 2007. Lanthanide chelates as luminescent labels in biomedical analyses. In: Gschneidner Jr., K.A., Pecharsky, V., Bünzli, J.-C.G. (Eds.), Handbook on the Physics and Chemistry of Rare Earths. Elsevier Science B.V., Amsterdam, p. 171ff (Chapter 234).
Novitchi, G., Costes, J.-P., Tuchagues, J.-P., Vendier, L., Wernsdorfer, W., 2008. New J. Chem. 32, 197.
Orpen, A.G., Brammer, L., Allen, F.H., Kennard, O., Watson, D.G., Taylor, R., 1989. J. Chem. Soc., Dalton Trans. S1.
Ouali, N., Bocquet, B., Rigault, S., Morgantini, P.-Y., Weber, J., Piguet, C., 2002. Inorg. Chem. 41, 1436.
Ouali, N., Rivera, J.-P., Morgantini, P.-Y., Weber, J., Piguet, C., 2003. J. Chem. Soc., Dalton Trans. 1251.
Ouali, N., Rivera, J.-P., Chapon, D., Delangle, P., Piguet, C., 2004. Inorg. Chem. 43, 1517.
Pandya, S., Yu, J.H., Parker, D., 2006. Dalton Trans. 2757.
Parac-Vogt, T.N., Binnemans, K., Görller-Walrand, C., 2002. J. Chem. Soc., Dalton Trans. 1602.
Parker, D., 2004. Chem. Soc. Rev. 33, 156.
Parker, D., Dickins, R.S., Puschmann, H., Crossland, C., Howard, J.A.K., 2002. Chem. Rev. 102, 1977.
Pauling, L., Corey, R.B., 1951a. Proc. Natl. Acad. Sci. USA 37, 235.
Pauling, L., Corey, R.B., 1951b. Proc. Natl. Acad. Sci. USA 37, 241.
Pauling, L., Corey, R.B., 1951c. Proc. Natl. Acad. Sci. USA 37, 251.
Pauling, L., Corey, R.B., 1951d. Proc. Natl. Acad. Sci. USA 37, 256.
Pauling, L., Corey, R.B., 1951e. Proc. Natl. Acad. Sci. USA 37, 261.
Pauling, L., Corey, R.B., 1951f. Proc. Natl. Acad. Sci. USA 37, 272.
Pauling, L., Corey, R.B., 1951g. Proc. Natl. Acad. Sci. USA 37, 282.
Perlmutter-Hayman, B., 1986. Acc. Chem. Res. 19, 90.
Petoud, S., Bünzli, J.-C.G., Renaud, F., Piguet, C., Schenk, K.J., Hopfgartner, G., 1997a. Inorg. Chem. 36, 5750.
Petoud, S., Bünzli, J.-C.G., Schenk, K.J., Piguet, C., 1997b. Inorg. Chem. 36, 1345.
Petoud, S., Bünzli, J.-C.G., Piguet, C., Xiang, Q., Thummel, R., 1999. J. Lumin. 82, 69.
Petoud, S., Cohen, S.M., Bünzli, J.-C.G., Raymond, K.N., 2003. J. Am. Chem. Soc. 125, 13324.
Pfeil, A., Lehn, J.-M., 1992. J. Chem. Soc., Chem. Commun. 838.
Phillips, M.A., 1928. J. Chem. Soc. 2393.
Phimphivong, S., Saavedra, S.S., 1998. Bioconj. Chem. 9, 350.
Picard, C., Geum, N., Nasso, I., Mestres, B., Tisnes, P., Laurent, S., Muller, R.N., Vander Elst, L., 2006. Bioorg. Med. Chem. Lett. 16, 5309.
Picot, A., Malvolti, F., Le Guennic, B., Baldeck, P.L., Williams, J.A.G., Andraud, C., Maury, O., 2007. Inorg. Chem. 46, 2659.
Picot, A., D'Aléo, A., Baldeck, P.L., Grichine, A., Duperray, A., Andraud, C., Maury, O., 2008a. J. Am. Chem. Soc. 130, 1532.
Picot, A., Feuvrie, C., Barsu, C., Malvolti, F., Le Guennic, B., Le Bozec, H., Andraud, C., Toupet, O., Maury, O., 2008b. Tetrahedron 64, 399.
Pierre, V.C., Botta, M., Aime, S., Raymond, K.N., 2006. J. Am. Chem. Soc. 128, 9272.
Piguet, C., 1996. Chimia 50, 144.
Piguet, C.J., 1999. Incl. Phen. Macrocycl. Chem. 34, 361.
Piguet, C., Bünzli, J.-C.G., 1996. Eur. J. Inorg. Chem. 33, 165.
Piguet, C., Bünzli, J.-C.G., 1998. Chimia 52, 579.

Piguet, C., Bünzli, J.-C.G., 1999. Chem. Soc. Rev. 28, 347.
Piguet, C., Geraldes, C.F.G.C., 2003. Paramagnetic NMR lanthanide induced shifts for extracting solution structures. In: Gschneidner Jr., K.A., Bünzli, J.-C.G., Pecharsky, V.K. (Eds.), Handbook on the Physics and Chemistry of Rare Earths, vol. 33. Elsevier Science, Amsterdam, pp. 353–463.
Piguet, C., Bernardinelli, G., Williams, A.F., 1989a. Inorg. Chem. 28, 2920.
Piguet, C., Bocquet, B., Müller, E., Williams, A.F., 1989b. Helv. Chim. Acta 72, 323.
Piguet, C., Bernardinelli, G., Williams, A.F., 1992a. Angew. Chem. Int. Ed. Engl. 31, 1624.
Piguet, C., Williams, A.F., Bernardinelli, G., Moret, E., Bünzli, J.-C.G., 1992b. Helv. Chim. Acta 75, 1697.
Piguet, C., Bochet, C.G., Williams, A.F., 1993a. Helv. Chim. Acta 76, 372.
Piguet, C., Bünzli, J.-C.G., Bernardinelli, G., Hopfgartner, G., Williams, A.F., 1993b. J. Am. Chem. Soc. 115, 8197.
Piguet, C., Bünzli, J.-C.G., Bernardinelli, G., Williams, A.F., 1993c. Inorg. Chem. 32, 4139.
Piguet, C., Bocquet, B., Hopfgartner, G., 1994. Helv. Chim. Acta 77, 931.
Piguet, C., Bernardinelli, G., Bünzli, J.-C.G., Petoud, S., Hopfgartner, G., 1995a. J. Chem. Soc., Chem. Commun. 2575.
Piguet, C., Bünzli, J.-C.G., Bernardinelli, G., Bochet, C.G., Froidevaux, P., 1995b. J. Chem. Soc., Dalton Trans. 83.
Piguet, C., Hopfgartner, G., Williams, A.F., Bünzli, J.-C.G., 1995c. J. Chem. Soc., Chem. Commun. 491.
Piguet, C., Rivara-Minten, E., Hopfgartner, G., Bünzli, J.-C.G., 1995d. Helv. Chim. Acta 1541.
Piguet, C., Rivara-Minten, E., Hopfgartner, G., Bünzli, J.-C.G., 1995e. Helv. Chim. Acta 1651.
Piguet, C., Bünzli, J.-C.G., Bernardinelli, G., Hopfgartner, G., Petoud, S., Schaad, O., 1996. J. Am. Chem. Soc. 118, 6681.
Piguet, C., Bernardinelli, G., Hopfgartner, G., 1997a. Chem. Rev. 97, 2005.
Piguet, C., Rivara-Minten, E., Bernardinelli, G., Bünzli, J.-C.G., Hopfgartner, G., 1997b. J. Chem. Soc., Dalton Trans. 421.
Piguet, C., Edder, C., Rigault, S., Bernardinelli, G., Bünzli, J.-C.G., Hopfgartner, G., 2000. J. Chem. Soc., Dalton Trans. 3999.
Piguet, C., Borkovec, M., Hamacek, J., Zeckert, K., 2005. Coord. Chem. Rev. 249, 705.
Platas, C., Avecilla, F., de Bas, A., Geraldes, C.F.G.C., Rodriguez-Blas, T., Adams, H., Mahia, J., 1999. Inorg. Chem. 38, 3190.
Platas-Iglesias, C., Elhabiri, M., Hollenstein, M., Bünzli, J.-C.G., Piguet, C., 2000. J. Chem. Soc., Dalton Trans. 2031.
Platas-Iglesias, C., Piguet, C., André, N., Bünzli, J.-C.G., 2001. J. Chem. Soc., Dalton Trans. 3084.
Poole, R.A., Bobba, G., Cann, M.J., Frias, J.C., Parker, D., Peacock, R.D., 2005. Org. Biomol. Chem. 3, 1013.
Poole, R.A., Montgomery, C.P., New, E.J., Congreve, A., Parker, D., Botta, M., 2007. Org. Biomol. Chem. 5, 2055.
Potts, K.T., Keshavarz-K, M., Tham, F.S., Gheysen Raiford, K.A., Arana, C., Abruña, H.D., 1993. Inorg. Chem. 32, 5477.
Puntus, L.N., Zolin, V.F., Puntus, L.N., Zolin, V.F., Kudryashova, V.A., Tsaryuk, V.I., Legendziewicz, P., Gawryszewska, P., Szostak, R., 2002. Phys. Sol. State (Engl. Transl.) 44, 1440.
Puntus, L.N., Chauvin, A.-S., Varbanov, S., Bünzli, J.-C.G., 2007. Eur. J. Inorg. Chem. 2315.
Raitsimiring, A.M., Gunanathan, C., Potapov, A., Efremenko, I., Martin, J.M.L., Milstein, D., Goldfarb, D., 2007. J. Am. Chem. Soc. 129, 14138.
Rapenne, G., Patterson, B.T., Sauvage, J.-P., Keene, F.R., 1999. Chem. Commun. 1853.
Reisfeld, R., Jørgensen, C.K., 1977. Lasers and Excited States of Rare Earths. Springer-Verlag, Berlin.

Renaud, F., Piguet, C., Bernardinelli, G., Bünzli, J.-C.G., Hopfgartner, G., 1997a. Chem. Eur. J. 3, 1646.
Renaud, F., Piguet, C., Bernardinelli, G., Bünzli, J.-C.G., Hopfgartner, G., 1997b. Chem. Eur. J. 3, 1660.
Renaud, F., Piguet, C., Bernardinelli, G., Bünzli, J.-C.G., Hopfgartner, G., 1999. J. Am. Chem. Soc. 121, 9326.
Renaud, F., Decurnex, C., Piguet, C., Hopfgartner, G., 2001. J. Chem. Soc., Dalton Trans. 1863.
Richardson, F.S., Metcalf, D.H., Glover, D.P., 1991. J. Phys. Chem. 95, 6249.
Riehl, J.P., Muller, G., 2005. Circularly polarized luminescence spectroscopy from lanthanide systems. In: Gschneidner Jr., K.A., Pecharsky, V., Bünzli, J.-C.G. (Eds.), Handbook on the Physics and Chemistry of Rare Earths, vol. 34. Elsevier Science, Amsterdam, pp. 289–357 (Chapter 220).
Rigault, S., Piguet, C., 2000. J. Am. Chem. Soc. 122, 9304.
Rigault, S., Piguet, C., Bernardinelli, G., Hopfgartner, G., 1998. Angew. Chem. Int. Ed. Engl. 37, 169.
Rigault, S., Piguet, C., Bünzli, J.-C.G., 2000a. J. Chem. Soc., Dalton Trans. 2045.
Rigault, S., Piguet, C., Bernardinelli, G., Hopfgartner, G., 2000b. J. Chem. Soc., Dalton Trans. 4587.
Riis-Johannessen, T., Dupont, N., Canard, G., Bernardinelli, G., Hauser, A., Piguet, C., 2008. Dalton Trans. 3661.
Riis-Johannessen, T., Dalla Favera, N., Todorova, T.K., Huber, S.M., Gagliardi, L., Piguet, C., 2009. Chem. Eur. J. (in press, DOI 10.1002/chem.200900904).
Rodriguez-Cortias, R., Avecilla, F., Platas-Iglesias, C., Imbert, D., Bünzli, J.-C.G., de Blas, A., Rodiguez-Blas, T., 2002. Inorg. Chem. 41, 5336.
Ronson, T.K., Adams, H., Harding, L.P., Pope, S.J.A., Sykes, D., Faulkner, S., Ward, M.D., 2007. Dalton Trans. 1006.
Ruiz-Martinez, A., Casanova, D., Alvarez, S., 2008. Chem. Eur. J. 14, 1291.
Saalfrank, R.W., Seitz, V., Caulder, D.L., Raymond, K.N., Teicher, M., Stalke, D., 1998. Eur. J. Inorg. Chem. 1313.
Sabbatini, N., Guardigli, M., Manet, I., 1996. Antenna effect in encapsulation complexes of lanthanide ions. In: Gschneidner, K.A., Eyring, L. (Eds.), Handbook on the Physics and Chemistry of Rare Earths, vol. 23. Elsevier Science, Amsterdam, pp. 69–120 (Chapter 154).
Samuel, A.P.S., Moore, E.G., Melchior, M., Xu, J.D., Raymond, K.N., 2008a. Inorg. Chem. 47, 7535.
Samuel, A.P.S., Xu, J., Raymond, K.N., 2008b. Inorg. Chem. 47, 7535.
Sato, S., Wada, M., 1970. Bull. Chem. Soc. Jpn. 43, 1955.
Sayre, A., 1975. Rosalind Franklin and DNA. W.W. Norton and Company, New York.
Scaff, W.L., Dyer, D.L., Mori, K., 1969. J. Bacteriol. 98, 246.
Scarrow, R.C., White, D.L., Raymond, K.N., 1985. J. Am. Chem. Soc. 107, 6540.
Schneider, H.-J., Yatsimirsky, A.K., 2008. Chem. Soc. Rev. 37, 263.
Schoentjes, B., Lehn, J.-M., 1995. Helv. Chim. Acta 78, 1.
Selvin, P.R., 2000. Nat. Struct. Biol. 7, 730.
Semenov, S.N., Rogachev, A.Y., Eliseeva, S.V., Pettinari, C., Marchetti, F., Drozdov, A.A., Troyanov, S.I., 2008. Chem. Commun. 1992.
Semenova, L.I., Sobolev, A.N., Skelton, B.W., White, A.H., 1999. Aust. J. Chem. 52, 519.
Senegas, J.-M., Bernardinelli, G., Imbert, D., Bünzli, J.-C.G., Morgantini, P.-Y., Weber, J., Piguet, C., 2003. Inorg. Chem. 42, 4680.
Senegas, J.-M., Koeller, S., Piguet, C., 2005. Chem. Commun. 2235.
Shannon, R.D., 1976. Acta Crystallogr. Sect. A 32, 751.
Shavaleev, N.M., Scopelliti, R., Gumy, F., Bünzli, J.-C.G., 2008. Inorg. Chem. 47 (19), 9055.
Shen, Q., Hu, J.-Y., Jin, Z.-S., 1990. Zhongguo Xitu Xuebao (J. Chin. Rare Earth Soc.) 8, 359.

Shinoda, S., Miyake, H., Tsukube, H., 2005. Molecular recognition and sensing via rare earth complexes. In: Gschneidner Jr., K.A., Pecharsky, V., Bünzli, J.-C.G. (Eds.), Handbook on the Physics and Chemistry of Rare Earths, vol. 35. Elsevier Science, Amsterdam, pp. 276–331 (Chapter 226).
Siitari, H., Hemmilä, I., Pettersson, K., Lövgren, T., 1983. Nature 301 (5897), 258.
Smith, E.B., 2004. Basic Chemical Thermodynamics, 5th ed Imperial College Press, London p. 31.
Smith, V.C., Lehn, J.-M., 1996. Chem. Commun. 2733.
Song, B., Vandevyver, C.D.B., Chauvin, A.-S., Bünzli, J.-C.G., 2008a. Org. Biomol. Chem. 6, 4125.
Song, B., Vandevyver, C.D.B., Deiters, E., Chauvin, A.-S., Hemmilä, I., Bünzli, J.-C.G., 2008b. Analyst 133, 1749.
Song, X., Zhou, X., Liu, W., Dou, W., Ma, J., Tang, X., Zheng, J., 2008c. Inorg. Chem. doi:10.1021/ic8008267 (published on the web, November 8, 2008).
Sonogashira, K., Tohda, Y., Hagihara, N., 1975. Tetrahedron Lett. 50, 4467.
Steemers, F.J., Verboom, W., Reinhoudt, D.N., Vandertol, E.B., Verhoeven, J.W., 1995. J. Am. Chem. Soc. 117, 9408.
Stoddart, J.F., Philp, D., 1996. Angew. Chem. Int. Ed. Engl. 35, 1154.
Su, X.C., Man, B., Beeren, S., Liang, J., Simonsen, S., Schmitz, C., Huber, T., Messerle, B.A., Otting, G., 2008a. J. Am. Chem. Soc. 130, 10486.
Su, X.C., McAndrew, K., Huber, T., Ottong, G., 2008b. J. Am. Chem. Soc. 130, 1681.
Sugiyarto, K.H., Craig, D.C., Rae, D.A., Goodwin, H.A., 1994. Aust. J. Chem. 47, 869.
Sun, Y.Q., Zhang, J., Yang, G.Y., 2006a. Chem. Commun. 1947.
Sun, Y.Q., Zhang, J., Yang, G.Y., 2006b. Chem. Commun. 4700.
Supkowski, R.M., de Horrocks Jr., W., 2002. Inorg. Chim. Acta 340, 44.
Takalo, H., Mukkala, V.M., Merio, L., Rodriguez-Ubis, J.C., Sedano, R., Jusnes, O., Brunet, E., 1997. Helv. Chim. Acta 80, 372.
Tancrez, N., Feuvrie, C., Ledoux, I., Zyss, J., Toupet, L., Le Bozec, H., Maury, O., 2005. J. Am. Chem. Soc. 127, 13474.
Telfer, S.G., Tajima, N., Kuroda, R., Cantuel, M., Piguet, C., 2004. Inorg. Chem. 43, 5302.
Terazzi, E., Rivera, J.-P., Ouali, N., Piguet, C., 2006. Magn. Reson. Chem. 44, 539.
Terazzi, E., Guénée, L., Bocquet, B., Lemonnier, J.-F., Dalla Favera, N., Piguet, C., 2009. Chem. Eur J. (in press) ; DOI 10.1002/chem.20090226.
Thalladi, V.-R., Schwartz, A., Phend, J.N., Hutchinson, J.W., Whitesides, G.M., 2002. J. Am. Chem. Soc. 124, 9912.
Torelli, S., Delahaye, S., Hauser, A., Bernardinelli, G., Piguet, C., 2004. Chem. Eur. J. 10, 3503.
Torelli, S., Imbert, D., Cantuel, M., Bernardinelli, G., Delahaye, S., Hauser, A., Bünzli, J.-C.G., Piguet, C., 2005. Chem. Eur. J. 11, 3228.
Tripier, R., Hollenstein, M., Elhabiri, M., Chauvin, A.-S., Zucchi, G., Piguet, C., Bünzli, J.-C. G., 2002. Helv. Chim. Acta 85, 1915.
Vandevyver, C.D.B., Chauvin, A.-S., Comby, S., Bünzli, J.-C.G., 2007. Chem. Commun. 1716.
Van Holde, K.E., 1985. Physical Biochemistry, 2nd ed Prentice Hall, Englewood Cliffs, NJ.
Vögtle, F., 1991. Supramolecular Chemistry. John Wiley & Sons, Chichester (Chapter 2).
Walsh, B.M., 2006. Judd–Ofelt theory: Principles and practices. In: Di Bartolo, B. (Ed.), Advances in Spectroscopy for Lasers and Sensing: Part 1. Springer-Verlag, Berlin, pp. 403–433.
Wang, C.-C., Lo, W.-C., Chou, C.-C., Lee, G.-H., Chen, J.-M., Peng, S.-M., 1998. Inorg. Chem. 37, 4059.
Watson, J.D., 1968. The Double Helix. Atheneum, New York.
Watson, J.D., Crick, F.H.C., 1953. Nature 171, 737.
Weissman, S.I., 1942. J. Chem. Phys. 10, 214.
Werts, M.H.V., Jukes, R.T.F., Verhoeven, J.W., 2002. Phys. Chem. Chem. Phys. 4, 1542.

Wilkins, M., 2003. The Third Man of Double Helix: An Autobiography. Oxford University Press, New York.
Williams, A.F., Piguet, C., Bernardinelli, G., 1991. Angew. Chem. Int. Ed. Engl. 30, 1490.
Winnik, M.A., 1981. Chem. Rev. 81, 491.
Wright, J.B., 1951. Chem. Rev. 48, 397.
Xing, Y., Li, Y., Yan, L., Yang, R., 1992. Gaodeng Xuexiao Huaxue Xuebao 13, 14.
Xu, J., Raymond, K.N., 2000. Angew. Chem. Int. Ed. Engl. 39, 2745.
Xu, J., Raymond, K.N., 2006. Angew. Chem. Int. Ed. Engl. 45, 6480.
Yang, L., Yang, R., 1995. Polyhedron 14, 507.
Yu, J.H., Parker, D., Pal, R., Poole, R.A., Cann, M.J., 2006. J. Am. Chem. Soc. 128, 2294.
Yue, Q., Yang, J., Li, G.H., Li, G.D., Chen, J.S., 2006. Inorg. Chem. 45, 4431.
Zeckert, K., Hamacek, J., Rivera, J.-P., Floquet, S., Pinto, A., Borkovec, M., Piguet, C., 2004. J. Am. Chem. Soc. 126, 11589.
Zeckert, K., Hamacek, J., Senegas, J.-M., Dalla-Favera, N., Floquet, S., Bernardinelli, G., Piguet, C., 2005. Angew. Chem. Int. Ed. Engl. 44, 7954.
Zhou, R.S., Cui, X.B., Song, J.F., Xu, X.Y., Xu, J.Q., Wang, T.G., 2008. J. Solid State Chem. 181, 1565.
Zohar, O., Ikeda, M., Shinagawa, H., Inoue, H., Nakamura, H., Elbaum, D., Alkon, D.L., Yoshioka, T., 1998. Biophys. J. 74, 82.
Zong, R., Thummel, R.P., 2005. Inorg. Chem. 44, 5984.